# Thermal spraying of novel composite coating compositions for wear resistance applications

By

Kerem Derelizade

Supervisors : Professor Tanvir Hussain & Professor Andrei Khlobystov

Thesis submitted to the University of Nottingham for the degree of Doctor of Philosophy


Department of Mechanical, Materials and Manufacturing

Faculty of Engineering

May 2022

# Table of Contents

# Table of Figures

# Acknowledgements

I would like to acknowledge the Engineering and Physical Sciences Research Council (EPSRC) and Rolls – Royce plc for funding my research. I would like to express my gratitude to my supervisors Professor Tanvir Hussain and Professor Andrei Khlobystov for their support and sharing their experience and knowledge. I would also like to thank Dr Federico Venturi for his assistance and the whole Coatings and Surface Engineering (CSE) research team.

The work presented in this thesis would have not been possible without the help of the John Kirk and Rory Screaton at Wolfson and Graham Rance at the Nanoscale and Microscale Research centre (nmRC).

Finally, I would like to thank my family for always supporting me and my friends from Cyprus and the ones I met in Nottingham throughout my journey, who helped me to feel like I am not alone during the hard times.

## Declaration

I Kerem Derelizade declare that this thesis and the work reported has been composed entirely by myself.

# List of Publications

• K. Derelizade, F. Venturi, R. G. Wellman, A. Khlobystov, and T. Hussain, “Structural changes of thermal sprayed graphene nano platelets film into amorphous carbon under sliding wear,” *Applied Surface Science*, vol. 528, p. 146315, Oct. 2020, doi: 10.1016/j.apsusc.2020.146315.

• K. Derelizade, F. Venturi, R. G. Wellman, A. Kholobysov, and T. Hussain, “Wear performance of graphene nano platelets incorporated WC-Co coatings deposited by hybrid high velocity oxy fuel thermal spray,” *Wear*, vol. 482–483, p. 203974, Oct. 2021, doi: 10.1016/j.wear.2021.203974.

• K. Derelizade, A. Rincon, F. Venturi, R. G. Wellman, A. Kholobystov, and T. Hussain, “High temperature (900 °C) sliding wear of CrNiAlCY coatings deposited by high velocity oxy fuel thermal spray,” *Surface and Coatings Technology*, vol. 432, p. 128063, Feb. 2022, doi: 10.1016/j.surfcoat.2021.128063.

# Abstract

Friction and wear are ongoing problems in various industrial applications including aerospace, automotive and power generation. Any form of sliding or rotational contact between surfaces generates friction and heat, leading to surface deformation and material removal, hence the failure of the components in the long term. Coatings are used to improve the mechanical properties and the life cycle of the components hence cutting down the maintenance cost. Thermal spray is a popular and widely used coating deposition technique in the industry for the deposition of wear-resistant coatings. Amongst all thermal spray techniques, high-velocity oxy-fuel (HVOF) thermal spray offers a cost-effective and reliable way to deposit dense and superior quality coating with various microstructures at different thickness ranges and from different feedstock options including powders, suspensions, solutions and even nanostructured 2D materials. 2D materials with nanostructured chemistry are becoming popular for wear-resistant and friction reduction applications. These can be used either as solid-state lubricants on their own or as a reinforcement material for composite coatings. This thesis describes the deposition and characterisation of novel coating compositions including 2D nanomaterials via HVOF thermal spray. Graphene nano-platelets (GNP) and hexagonal boron nitride (hBN) were chosen as the 2D materials for room temperature (~20 °C), and high temperature (~900 °C) wear applications, respectively.

A unique graphene nano-platelets thin film was deposited onto stainless steel from an aqueous GNP suspension (1wt. %) via suspension high-velocity oxy-fuel (SHVOF) thermal spray, which uses suspension as the feedstock as opposed to powder. The GNP film reduced the coefficient of friction (CoF) by 7 times compared to an uncoated stainless-steel sample, even for a discontinuous film. The deposited film acted to a greater extent like a solid lubricant and protected the surface until the structural integrity of the GNP film was observed. The effectiveness of the GNP film was dependent on the oxidation behaviour and structural integrity instead of bonding strength between the substrate and the film, the thickness, and the area coverage of the film.

Two different novel composite coatings, WC-Co + GNP1 and WC-Co + GNP2 were deposited via a hybrid HVOF thermal spray technique, where GNP1 and GNP2 refer to graphene nano-platelets with different dimensions and surface area. This technique allows in-situ mixings of radially injected sub-micron sized GNPs in the suspension and axially

injected micro-sized WC-Co powder inside the flame. The wear performance of the system was improved due to the alteration of mechanical properties such as microhardness and porosity as a result of GNP addition. The incorporation of both GNP1 and GNP2 into the WC-Co coating improved the wear performance of the whole system (combined wear rate of the coatings and the counter body) against the both alumina and WC-Co counter body.

A composite CoCrAlY + hBN (1 wt. %) powder was produced then deposited as a high-temperature wear-resistant coating via HVOF thermal spray. The hBN was chosen due to its self-lubricative abilities and high-temperature properties as CoCrAlY coatings are used in high-temperature applications. The hBN incorporation did not affect microstructure and microhardness, but both the thickness and the fracture toughness of the deposited coating were reduced due to the changes in heating and cooling characteristics during the thermal spray process. The wear mechanism was altered from a plastic deformation dominant mechanism into a brittle deformation dominant one as a result of hBN addition. The addition of hBN changed the flame chemistry and eliminated the formation of surface oxides. Therefore, hBN can be used to protect the powders during thermal spray that are sensitive to oxidation, phase segregation or decarburisation and deposit coatings without surface oxides.

A recently developed and unique CrNiAlCY metal powder was characterised and tested as a possible feedstock material for high-temperature wear-resistant coating deposition via HVOF thermal spray. A study of spray parameters showed coatings with lower porosity and higher microhardness deposited with higher oxygen flow rates. The microstructure and phase integrity of the metal powder was conserved during the thermal spray processes and were not affected by oxygen flow rates. Room temperature wear tests showed that a 10 N load is not high enough for a complete uniform wear track formation. At 30 N and 60 N, uniform wear tracks were obtained. The wear mechanism involves the oxidation of wear debris which is pushed towards the edges of the wear track. On the other hand, the whole worn surface was oxidised and covered with the protective $C_2O_3$ oxide layer at higher temperature wear tests. The same wear mechanism was demonstrated at both 10 N and 30 N tests. However, increasing the load to 60 N changed the wear mechanism; the protective $Cr_2O_3$ could not withstand the load and started to crack.

# Chapter 1: Introduction

## 1.1 Overview

Tribological contacts between components create friction and wear, which are severe problems for engineering applications in various industries such as; aerospace, automotive and power generation. Friction generates heat which can lead to oxidation, energy consumption and deformation of the surfaces and can be detrimental to the mechanical properties. On the other hand, wear is more critical as it causes the failure of the components and operational breakdown, hence increasing the cost and energy consumption. Figure 1 shows the global energy consumption, cost and $CO_2$ emissions because of friction and wear. A study performed in 2017 showed that approximately 23% of the world's total energy consumption was due to tribological contacts. 20% of this energy was consumed to overcome the friction, while the rest was used during remanufacturing and maintenance phase of the components [1]. Therefore, there has been extensive research to find new tribological developments and solutions to improve the performance and efficiency of the current systems. Figure 2 shows the estimated annual savings in the four main sectors for energy consumption, cost and $CO_2$ emissions if advanced tribology implementation is applied. Lubricants and coatings are the main tribological implementations used to reduce the coefficient of friction and wear.

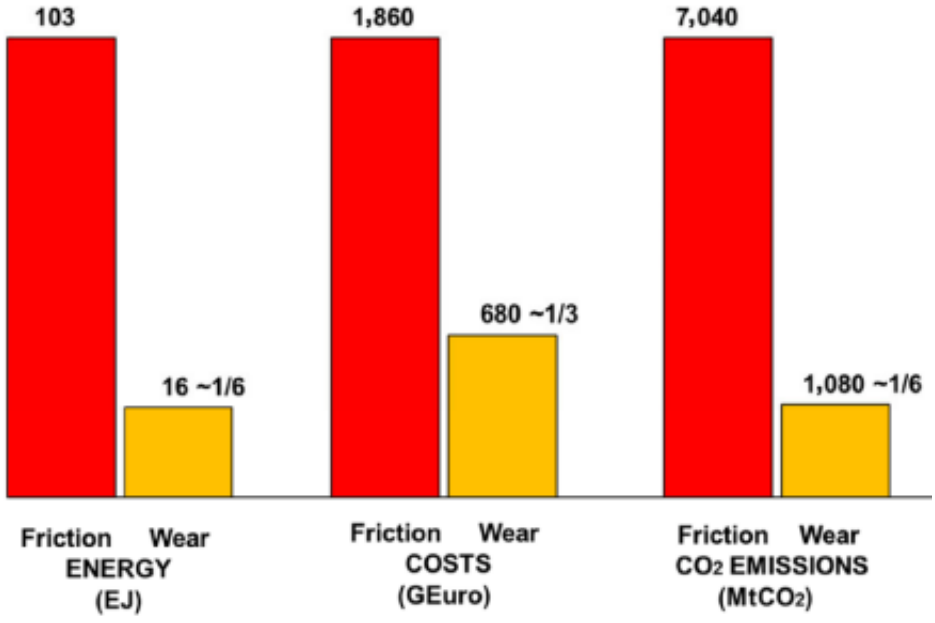


*Figure 1: Global energy consumption, cost and $CO_2$ emissions as a result of friction and wear [1].*

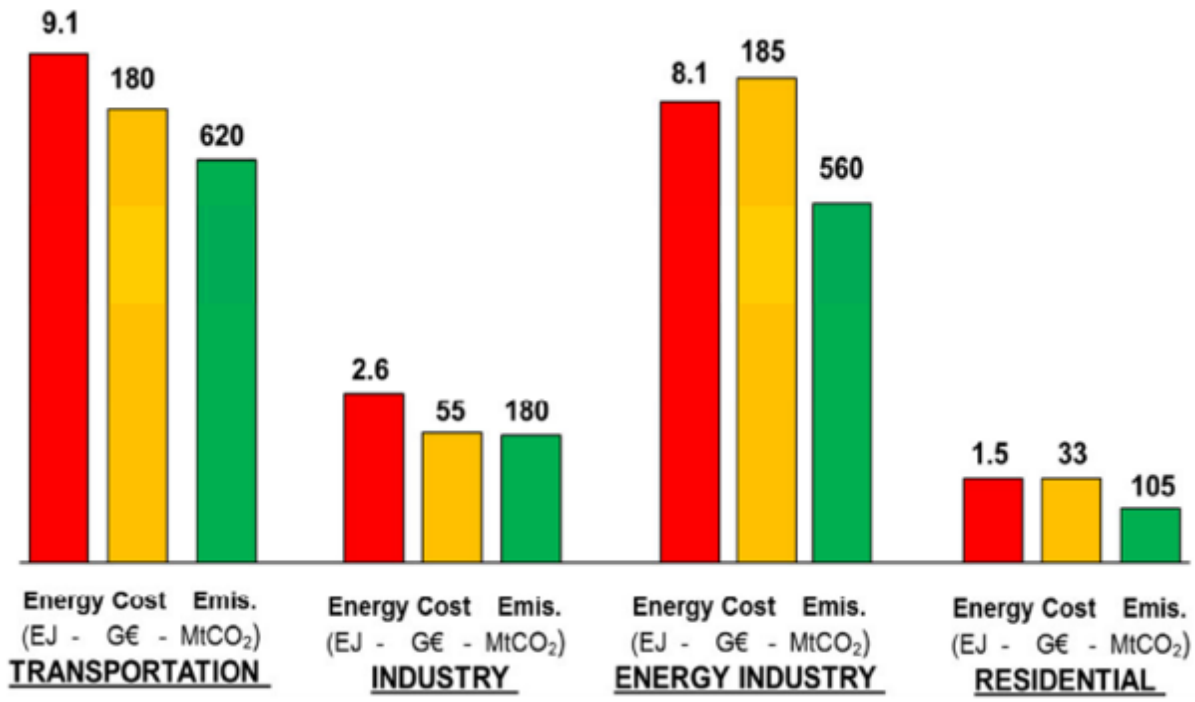


*Figure 2: Potential annually savings in energy, cost and CO2 emissions in different sectors after 8 years of intensive advanced tribology implementations [1].*

Coatings from sub-micron to millimetres thick are deposited on the surface of the tribological contacts for extra protection without altering the properties of the underlying materials. Deposited coatings improve the mechanical properties and life cycle of components hence cutting down the maintenance cost and energy consumption. Coatings can be deposited via different processes such as electroplating, thermal spray, and physical and chemical vapour deposition. The thermal spray technique offers fast and efficient deposition of reliable thick coatings from different feedstock types over large surface areas. Therefore, it is the preferred technique and becoming increasingly popular for coating deposition in many industrial applications over the other methods. The global thermal spray market was valued at nearly USD 10,000 million in 2020, and thermal spray coating, powder and equipment markets are all expected to achieve a compound annual growth rate (CAGR) of over 7% by 2026 [2]. The thermal spray offers a wide range of material forms to be used as feedstocks. Powder, wires, rods and even suspensions or solutions can be used as a feedstock option to deposit metal, ceramic and cermet coatings with the thermal spray technique. Figure 3 shows the industrial applications where the thermal spray was issued and the regional

interest in this technology. WC-Co and MCrAlY + CrC (M is for the metal) coatings have been the most conventional coating compositions used in wear-resistant coatings for decades. WC-Co coatings are preferred for applications where the maximum operating temperature does not exceed 500 °C. In temperatures above this, the wear performance of the WC-Co coatings decreases significantly due to the decarburisation [3]. On the other hand, MCrAlY (M can be cobalt, nickel or a combination of both) based coatings such as MCrAlY + cBN and MCrAlY + CrC is preferred for applications where the operating temperature is much higher than 500 °C. These coating compositions have better high-temperature characteristics than the WC-Co coating composition. MCrAlY coating is a softer coating than the others used for oxidation resistance purposes. However, the CrC and cBN phases into the base MCrAlY matrix improve the hardness and wear resistance of the coatings. Both WC-Co and MCrAlY coatings have been the most effective compositions for decades, and there is an urgent need to improve their performance or develop better performing options.


*Figure 3: Thermal spray market distribution around the globe and the industrial application where the thermal spray is used* [4].

Lubricants increase the load-carrying capacity of the systems by reducing the shear force between the contacts. Oil-based lubricants have been used for decades and the recent

developments in technology have led to new nanotechnology-based additives. The Invention of the first 2D material graphene, in 2004 [5] opened new areas of interest for researchers, especially for wear and friction-related applications. Graphene became an emerging solid lubricant as a result of its self-lubrication ability, chemical inertness and enhanced surface properties. In addition, graphene was also used as a reinforcement material in composite manufacturing for improved mechanical properties such as hardness, young's modulus, yield strength and ultimate tensile strength. Hexagonal boron nitride (hBN) is another 2D material with the same structure and properties as graphene and is referred to as white graphene. hBN is also used as a solid-state lubricant for tribological contacts, especially at higher temperatures (~500 °C). Graphene cannot be used at temperatures higher than ~500 °C in air. Graphene is formed from carbon atoms bonded to each other in a hexagonal matrix, so it combusts in air atmospheres once the required temperature is reached. Once all the mechanisms responsible for both improved tribological performance and failure of the 2D lubricants are understood, they can be engineered to produce wear-resistant coatings or incorporated into other existing wear resistance materials to form composite coatings. Therefore, in this study, graphene film deposition via HVOF thermal spray was investigated, and the wear and friction performance was analysed. Later on, composite WC-Co + GNP coatings were deposited. The effects of GNP incorporation on the mechanical properties, microstructure and wear performance were investigated. A composite CoCrAlY + hBN powder was also produced, which was sprayed via HVOF thermal spray. The effect of hBN addition on the mechanical properties, microstructure and wear performance at 900 °C was analysed. In addition to works on 2D materials, a unique and recently developed CrNiAlCY powder was characterised and used to deposit wear-resistant coatings for high-temperature applications (900 °C).

## 1.2 Aims & Objectives

The main aim of this study was to deposit unique coating compositions with 2D materials via a high velocity oxy-fuel thermal spray for improved wear performance at both room temperature and high temperature (900 °C) applications. 2D Graphene nanoplatelets (GNP) films and composite WC-Co + GNP coatings were deposited for room temperature applications to replace WC-Co coatings. CoCrAlY + hBN composite coatings were deposited to improve the hardness and wear resistance of the CoCrAlY coatings which are used for

oxidation resistance. For high-temperature applications, a recently developed bespoke CrNiAlCY powder was used to deposit a new coating composition. The aim of this study was achieved by using the following four objectives:

• Produce a 2D graphene nano-platelet film via Suspension high-velocity oxy-fuel (SHVOF) thermal spray and investigate the effect of spray parameters (suspension flow rate, standoff distance, flame power) on the film deposition and thickness of the deposited films. Discuss the coefficient of friction behaviour of the film by analysing the unlubricated ball on the disc sliding wear test. Analyse the structural changes of the GNPs throughout the thermal spray and wear tests were by advanced characterisation techniques such as Raman Spectroscopy, field emission gun scanning electron microscopy (FEG-SEM), transmission electron microscopy (TEM) and electron energy-loss spectroscopy (EELS) to understand the mechanism responsible for improved CoF and failure of the film afterwards.

• Produce a WC-Co + GNP composite coatings via hybrid high-velocity oxy-fuel thermal spray to combine impressive hardness and wear performance of WC-Co with self-lubricating and outstanding CoF behaviour of GNPs. Investigate the effect of GNP incorporation on the mechanical properties and microstructure of the coatings. Analyse the CoF and wear performance of the system via unlubricated ball on disc sliding wear test, and how the GNP incorporation and mechanical properties affect these performances. Investigate the effect of wear test parameters (load, counter body and sliding distance) on the wear performance and wear mechanisms.

• Produce CoCrAlY + hBN composite powder and deposit this composition via liquid-fuelled HVOF thermal spray to combine the high-temperature properties of the CoCrAlY with the self-lubricating and outstanding COF behaviour of hBN at elevated temperatures. Investigate the effect of hBN incorporation on the microstructure and mechanical properties of the deposited coating. Analyse the CoF and wear performance of the system via unlubricated ball on disc sliding wear test, and how the hBN incorporation and mechanical properties affect these performances.

• Produce and characterise CrNiAlCY coating via liquid-fuelled HVOF thermal spray from a recently developed unique powder. Investigate the effect of spray parameter (oxygen flow rate) on the coating microstructure and mechanical properties. Analyse the wear performance of the coatings at both room temperature and higher temperature via unlubricated ball ion disc sliding wear tests and corresponding wear mechanisms. Investigate the possible usage of this recently developed unique powder as a feedstock material alternative for wear-resistant coating deposition via HVOF thermal spray.

## 1.3 Scope of the thesis

This thesis has seven chapters and is presented in a Published Works Thesis format. Four journal papers (three published and one under review) make up Chapters 4, 5, 6 and 7 and form the core of this thesis. A list of publications and a summary of each chapter are given below.

Chapter 2 is the literature review and has six subsections. This chapter starts by reviewing the thermal spray processes and then focuses on the HVOF thermal spray. In the following subsections, 2D materials graphene and hBN were reviewed. Their effects on mechanical properties, microstructure and wear performance of the composites are summarised. Followed by the current knowledge about WC-Co and MCrAlY coatings which are chosen as the main matrix materials for graphene and hBN incorporation for room temperature and high-temperature applications, respectively. This chapter was concluded with a summary and gaps in the literature.

Chapter 3 describes the experimental methods used throughout this thesis.

Chapter 4 explains the deposition of GNP films via HVOF and the structural changes of the GNP film during the unlubricated sliding wear tests.

Chapter 5 presents a study on WC-Co + GNP composite coating deposition via hybrid HVOF thermal spray using WC-Co powder and GNP suspension simultaneously. The wear performance of the deposited composite coatings was studied extensively, effects of various test parameters and GNP addition was analysed and compared to a reference WC-Co coating.

Chapter 6 explains composite CoCrAlY + hBN powder production and deposition of composite CoCrAlY + hBN coatings via HVOF thermal spray. The effect of hBN addition on the coating microstructure, mechanical properties and wear performance was studied.

Chapter 7 presents a study on a recently developed unique CrNiAlCY powder. The powder was characterised and analysed as a possible feedstock option for HVOF thermal spray to deposit high-temperature wear-resistant coatings.

Chapter 8 discusses the findings of this thesis and connects the results provided in the experimental chapters.

Chapter 9 concludes the finding of this thesis and includes recommendations for future work.

# Chapter 2: Literature review

## 2.1 Thermal spray

### 2.1.1 Introduction

Thermal spray is the general term for a group of processes used to deposit coatings. It is widely used in industry to deposit metallic, ceramic, cermet, and polymer coatings from a wide range of feedstock materials. Thermal spray can deposit wear, environmental barrier, thermal barrier, electrically conductive/insulative, medical abradable and abrasive coatings [6]. Feedstock materials in the form of wires, rods, powder, suspension, and solution are all can be used to deposit coatings. During the process, the feedstock materials are subjected to elevated temperatures and velocities supplied by either electrical or chemical methods. Elevated temperatures convert the feedstock materials into a molten and/or semi-molten state, while the high velocities accelerate these particles towards the surface of interest. Upon impact, the molten materials deform plastically as they flatten and form splats. Rapid solidification and successive build-up of these splats form a coating on the surface [7,8]. Figure 4 shows a schematic diagram of a thermal spray process and a typical microstructure of a deposited coating. Coatings deposited via thermal spray usually have some unmolten particles, oxides, and porosity up to 10 % [9].

The thermal spray has various advantages compared to other coating deposition techniques. It is a versatile process as various feedstock types in different forms can be used. It is a low energy input process as the energy required for the heating and acceleration is generated inside the system. The ability to deposit thick coatings for a wide range of applications in a short amount of time is another appealing advantage of the thermal spray. In addition, parts can be stripped off, coated and reuse repetitively, which makes the thermal spray a cost-effective process. However, being a line of sight process is a limitation of the thermal spray as it cannot coat the small and deep cavities [9].

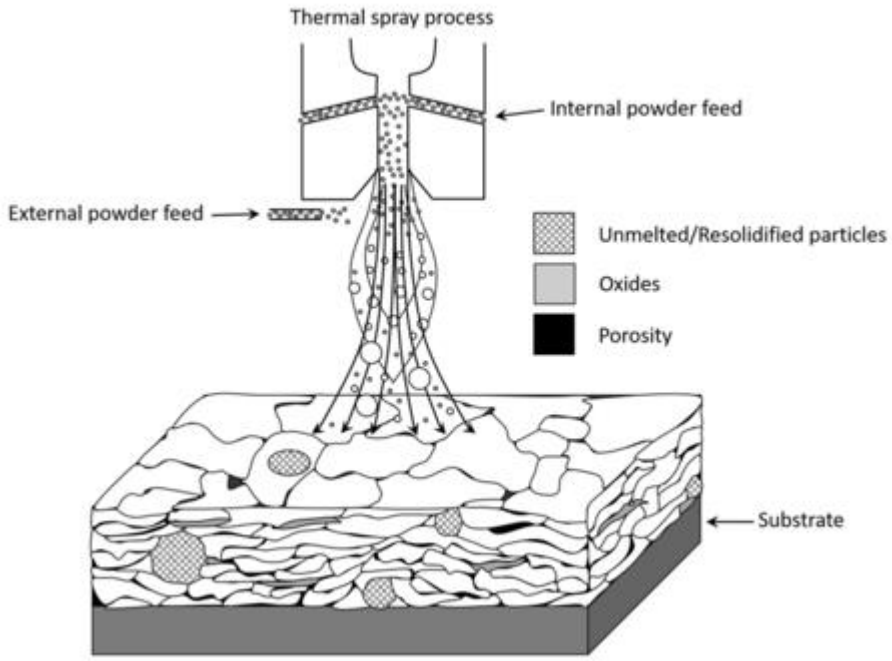


*Figure 4: Schematic diagram showing the thermal spray process and the typical microstructure of a deposited coating* [10].

### 2.1.2 Classification of thermal spray processes

The thermal spray process is classified into four main categories by way of supplying the energy and the velocity via chemical or electrical methods to the feedstock materials. These groups are plasma arc, electric arc, flame, and kinetic spray. The kinetic spray is also known as cold spray and differs from the other three categories. Cold spray relies on the supply of kinetic energy instead of thermal energy to the feedstock materials. There are no melting and solidification processes during cold spray, bonding to the surface of interest and coating deposition obtained only by the impact of high kinetic energy particles with the surface. Figure 5 shows four main categories of thermal spray processes and their subsets. Both plasma and arc spray use electrical heating for the feedstock materials. During an electric arc spray, materials are heated directly. Two consumable wires are used as a feedstock and a direct current (D.C) electric source is used to supply energy for heating. An electric arc is produced between the tips of the two wires which are continuously fed together. Electric arc causes the melting of the wire tips, and a high-velocity air jet is used to accelerate and direct molten droplets from the arc zone towards the surface of interest. A jet of gas at plasma

temperatures is used in a plasma arc spray. Plasma is usually known as a fourth state in which free moving electrons and ions are present under an electric field. Once the electric field is removed, heat and light energy are released due to the combination of electrons and ions. Plasma for this spraying process is generated by ionising the gas. Sufficient energy for the ionisation of the gas is supplied by a dc electric arc. Then feedstock particles are injected into the plasma flame by an inert carrier gas. Followed by heating, and acceleration of particles towards the surface to be coated. The flame spray uses a chemical method which is the combustion of fuels with oxygen or air to produce thermal energy. In addition, the production of an expanding gas flow with additional gases is used to accelerate the feedstock materials towards the surface.

Velocities and temperatures reached inside the flame or gas stream during the coating deposition process vary according to the type of the thermal spray as can be seen in Figure 6. Cold Spray has the lowest flame temperature (300-1000 °C) and the highest particle velocity (800-1200 m/s) range out of 4 main categories [10,11]. Plasma spray has the highest flame temperatures that can go up to ~12000 °C and the particle velocities vary from 150 m/s to 600 m/s depending on the type of plasma spray and the particle size [8,10–13]. Wire arc spraying has the second-highest flame temperatures of ~4000 °C with a particle velocity range of 100 to 130 m/s [8,10,11]. Furthermore, flame temperatures reached by flame spray are 3000 °C. On the other hand, the particle velocities vary depending on the type of flame spray. Combustion flame spray has the lowest particle velocities, even lower than arc spray with 40 – 100 m/s. However, particle velocities from 500 m/s to 1000 m/s are reachable via a high velocity oxy-fuel thermal spray or detonation gun flame spray [8,10,11,14,15].

The main aim of this study was to deposit unique coating compositions via various modified high velocity oxy-fuel thermal spray deposition techniques. Therefore, the following sub heading in this chapter are focused on these HVOF thermal spray setups.

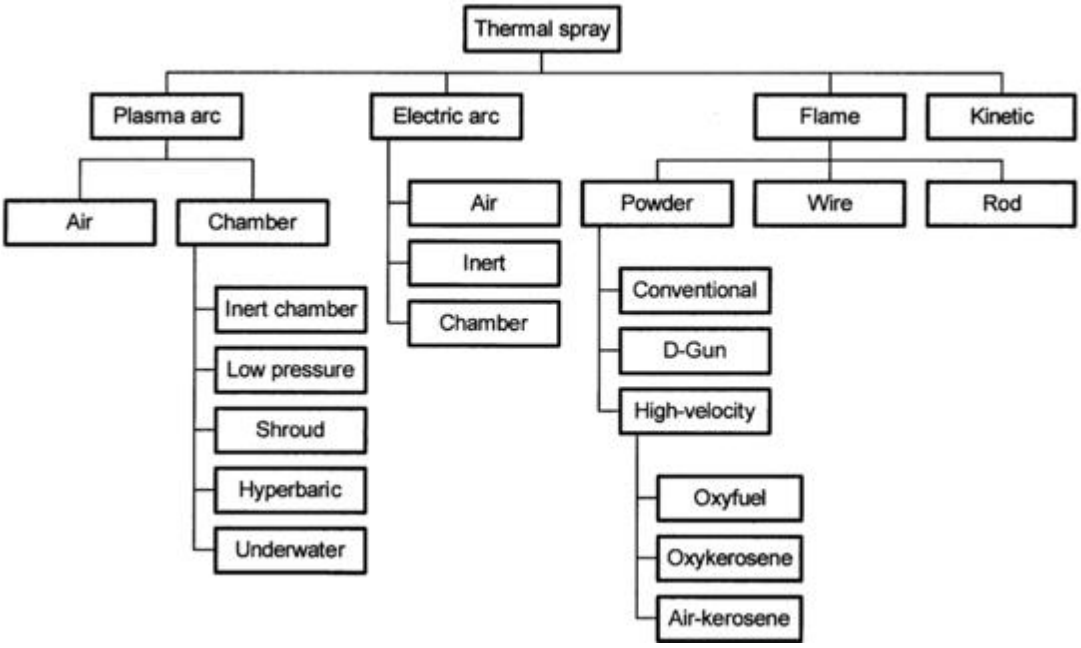


*Figure 5: Different classes of thermal spray techniques and their subsets* [16].

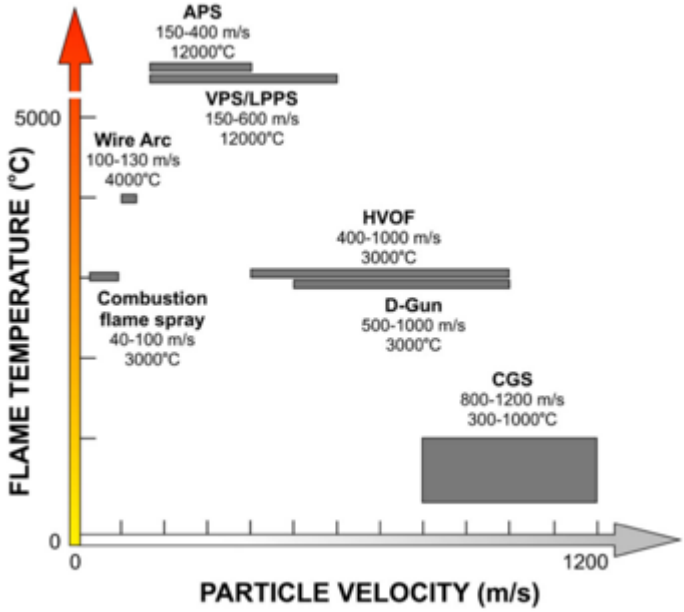


*Figure 6: Flame temperatures and particle velocities reached in wire arc, combustion flame spray, atmospheric plasma spray (APS), vacuum or low-pressure plasma spray (VPS/LPPS), high-velocity oxy-fuel (HVOF), Detonation Gun (D-Gun) and cold gas spray (CGS)* [11].

### 2.1.3 High-Velocity Oxy-Fuel (HVOF) Thermal Spray

High-velocity oxy-fuel thermal spray is a type of thermal spray where internal confined combustion is used to supply thermal energy and velocities to the feedstock materials. High volumes of pressurised oxygen gas together with fuel are injected into the water- or air-cooled combustion chamber. Both gas and liquid fuels can be used, and common fuel types include kerosene, hydrogen, propane, propylene, and acetylene. Combustion and constant gas flow create elevated temperatures and pressures. Following the combustion chamber, combustion gases are fed into a small diameter nozzle, 8- 30 cm in length [8], where they are accelerated and directed towards the substrate through a supersonic expansion. Figure 7 shows the schematic of the HVOF thermal spray system together with basic features. Different powder injection points can be used in various HVOF thermal sprays. A carrier gas is used to supply the powder feedstock either radially into the combustion chamber together with the gases, or axially to the exit of the combustion chamber [8,17,18].

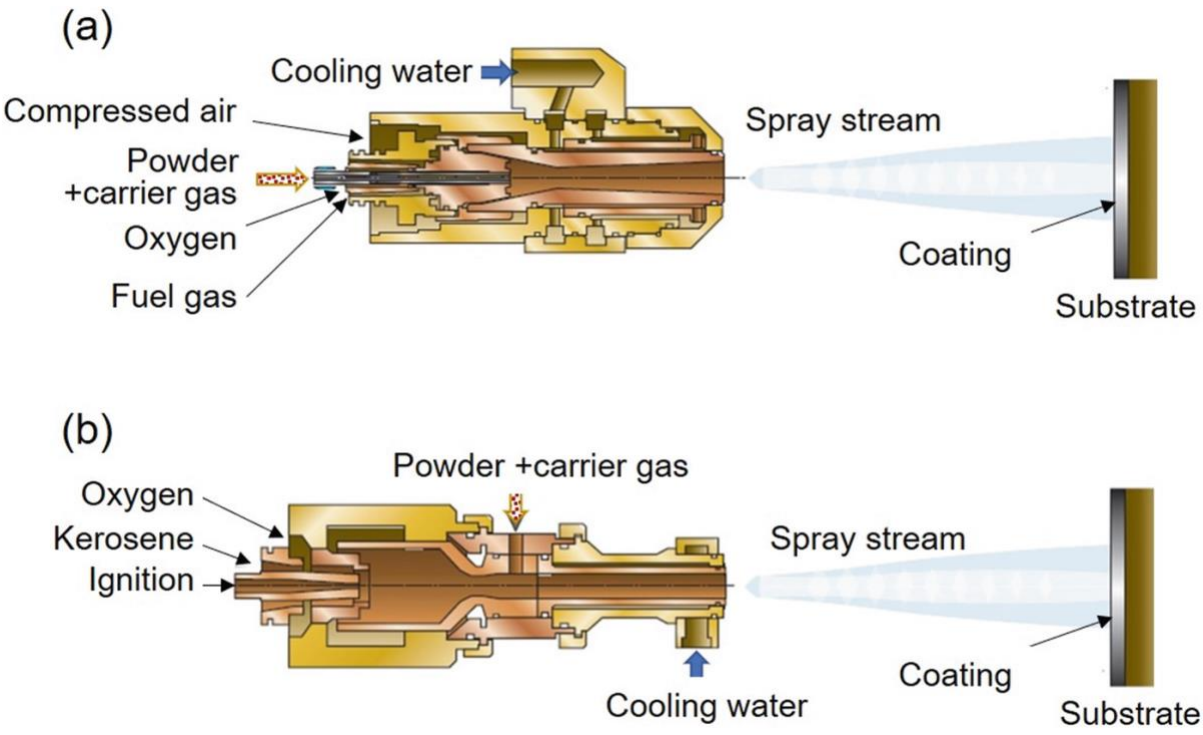


*Figure 7: Shows a schematic diagram of HVOF thermal spray systems with different powder injection points. Powder feedstock can be injected either into the combustion chamber together with gases (a) or exit the combustion chamber (b)* [17].

### 2.1.4 Suspension and Solution Precursor Thermal Spray

Suspension or solution thermal spray is an emerging and slightly modified version of a standard thermal spray where the feedstock is in the form of suspension or solution. Using suspension or solution as a feedstock allows the micro and nano-sized particles to be used for coating deposition via thermal spray [19]. Finer feedstock particles lead to tailored coating microstructures with superior mechanical properties compared to conventional coatings [19–22]. Suspension and solution precursor feedstocks have been used in the plasma and HVOF thermal spray setups so far. They are referred to as suspension plasma spray (SPS), solution precursor plasma spray (SPPS), suspension high-velocity oxy-fuel (SHVOF) thermal spray and solution precursor high-velocity oxy-fuel (SPHVOF) thermal spray. The principle of the operation of the suspension and solution thermal spray is still the same as a classic thermal spray. In a classic thermal spray, the powder feedstock is supplied to the system via a carrier gas. In a suspension thermal spray, suspensions of fine powders are uniformly distributed in an aqueous or alcoholic solution, while in a solution thermal spray, liquid precursors are dissolved in water or organic solvents. Both suspension and solution feedstocks are fed to the system by a pressurised vessel. Figure 8 shows a schematic diagram of a SHVOF thermal spray process together with pictures of the instruments used. As mentioned in the previous sections, the thermal spray process relies on the impact of high velocity, molten and semi-molten particles on the surface. Fine particles have smaller momentum / thermal inertia. Therefore, finer particles can be heated and accelerated more rapidly compared to the thicker ones. However, they cannot sustain this as much as larger particles [23,24]. Sharp reductions in particle velocity and temperatures are obtained for finer particles, so they cannot follow up the gas stream till the substrate. Even if they do, their momentum is not high enough to create the necessary flattening and hence the bonding with the substrate. Using micro/nano-sized powders in a suspension or solution solves this problem. Suspension and solution enter the flame or the gas jets as droplets or continuous liquid jets depending on the type of injection mode. The liquid breaks down into smaller droplets due to the drag force created between the suspension/solution and the flame or gas jet. In suspension thermal spray, the liquid inside the droplets evaporates, and the sintering process of the suspended fine particles starts. The process is followed by the formation of splats from the dried fine particles and the agglomerates upon impact. In solution precursor thermal spray, fine solid particles precipitate

from the liquid droplets inside the flame/gas jet, which is followed by the melting of the particles, hence the formation of splats upon impact with the surface [10,25]. A schematic diagram showing the in-flight particle transformation and splat formation for both suspension and solution thermal spray is shown in Figure 9.

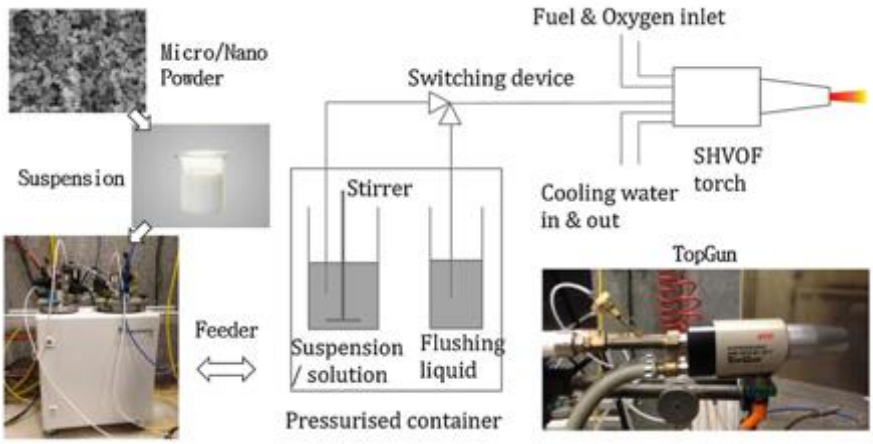


*Figure 8: Schematic drawing of a suspension high-velocity oxy-fuel (SHVOF) thermal spray with basic features and the equipment pictures* [26].

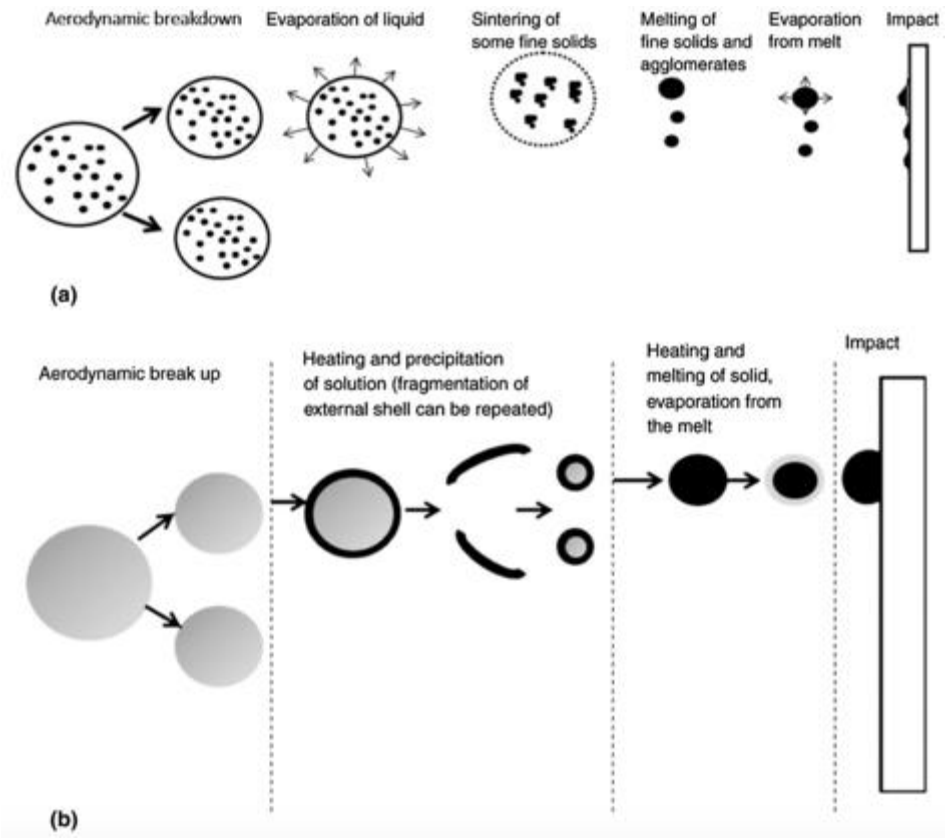


*Figure 9: Schematic of in-flight particle transformation and splat formation for suspension thermal spray (a) and solution precursor thermal spray (b)* [25].

### 2.1.5 Hybrid Thermal Spray

Hybrid thermal spray is a recently developed concept after extensive studies and promising coating compositions obtained from suspension and solution feedstocks. The initial concept was developed in 2011, where an atomizer was used to inject the solution feedstock simultaneously, while the powder feedstock was fed through the conventional powder feeder of a plasma spray gun [27,28]. This concept was later applied to other thermal spray systems and different hybrid feedstock combinations studied, which are listed below.

- Axial injection of both feedstocks to the centre of the flame/gas jet
- Radial injection of both feedstocks downstream to the flame/gas jet
- Radial and axial injection of both feedstocks simultaneously to the flame/gas jet

This concept allows simultaneous injection of different feedstock types with separate flow rate controls. Changing the flow rates of the feedstocks independently during the spray also allows the deposition of layered, composite and functionally graded coatings [29]. Pre powder mixing is eliminated as the in-situ mixing is obtainable via this approach. In addition, depending on the position and angle of the suspension/solution injection, oxygen and temperature-sensitive materials such as graphene can be used as a feedstock as well [30–33]. The benefits obtained from a hybrid thermal spray concept open a door to new coating compositions.

### 2.1.6 Thermal Spray Coating Microstructure

Thermal spray coatings have a lamellar microstructure due to successive build-up of splats. In addition to the splats formed from molten powders, oxides, unmolten / resolidified particles, and pores can be present inside a thermally sprayed coating microstructure. The presence of oxides, pores and different phases are all dependent on the spray parameters used to deposit the coatings. The process parameters need to be optimised to obtain the best possible microstructure and performance for the target application. The power of the thermal spray, the distance between the surface and the nozzle (stand-off distance), feedstock flow rate and the particle size have an influence on the acceleration, heating, and cooling profiles and hence on the splat formation.

#### 2.1.6.1 Splats

Splats can be referred to as the building blocks of the lamellar structure of a thermal sprayed coating and can be up to 20 µm thick [9]. As described above, splats are formed as the accelerated molten or semi-molten particles flatten upon impact with the surface. Sufficient melting and acceleration and hence splat formation are crucial to obtain a dense, thick and well-bonded coating. Increasing the power of thermal spray can increase particle temperatures and velocities. In addition, lowering the flow rate of the feedstock is another option to enhance the melting and acceleration of the particles as the same amount of energy can be used to heat up and accelerate a smaller volume of particles. Feedstock particle size also contributes to the splat formation. Particles with a smaller size have a high surface area to volume ratio. Hence, feedstocks with smaller particle sizes have faster heating and acceleration rates compared to the thicker ones. However, they also have faster cooling and deceleration rates compared to the larger particles.[23,24]. On the other hand, the distance

between the nozzle and the surface (stand-off distance) needs to be adjusted accordingly to obtain an enhanced particle melting and heating at the point of impact. If the nozzle is too close to the surface, particles will impact the substrate before reaching a molten or semi-molten state and with lower velocities. If the nozzle is further away, particles will slow down and start to solidify before reaching the substrate [34,35].

#### 2.1.6.2 Oxides

Oxides are formed due to the exposure of the heated materials to air and the heating of the coating surface during the deposition process. The presence of oxides in the microstructure can be useful depending on the application type. Oxides have higher hardness than metals. Therefore, a microstructure involving both metals and metal oxides improves the hardness of the deposited coatings [36–40] in some conditions. However, increased hardness comes with a cost of reduced fracture toughness and creates more brittle coatings as oxides weaken the boundaries [37,39,41]. Different methods can be used to reduce the number of oxides in a coating, if necessary. Lower dwell times reduced particle temperatures, and reduced substrate surface temperature can be used to minimise the oxide content. Shrouding gasses such as nitrogen or argon can be used to minimise the contact with air to eliminate the oxide formation. In addition, increasing the particle size can reduce the oxide content as larger particles have a lower surface area to volume ratio.

#### 2.1.6.3 Porosity

Pores are generally produced as a result of poor bonding between the splats and unmolten or resolidified particles. These particles become trapped between the splats inside the coating microstructure, and pores are formed around them. Similar to oxides, porosity can be a useful feature depending on the application, such as thermal barrier coatings (TBCs) for gas turbine engines. Pores are incorporated inside these coating microstructures to improve the thermal insulation and shock resistance (high strain tolerance) of the coatings [42–44]. However, in general, pores in a coating microstructure represents poor bonding between the splats and degraded mechanical properties. Pores can function as stress risers, which initiate crack formation and growth. This can reduce the hardness and fracture toughness of the coatings, which are detrimental for wear resistance applications. In addition, this can lead to the pull-out of coating fragments which can act as a third body abrasive wear and can increase the wear rate even more [6,45].

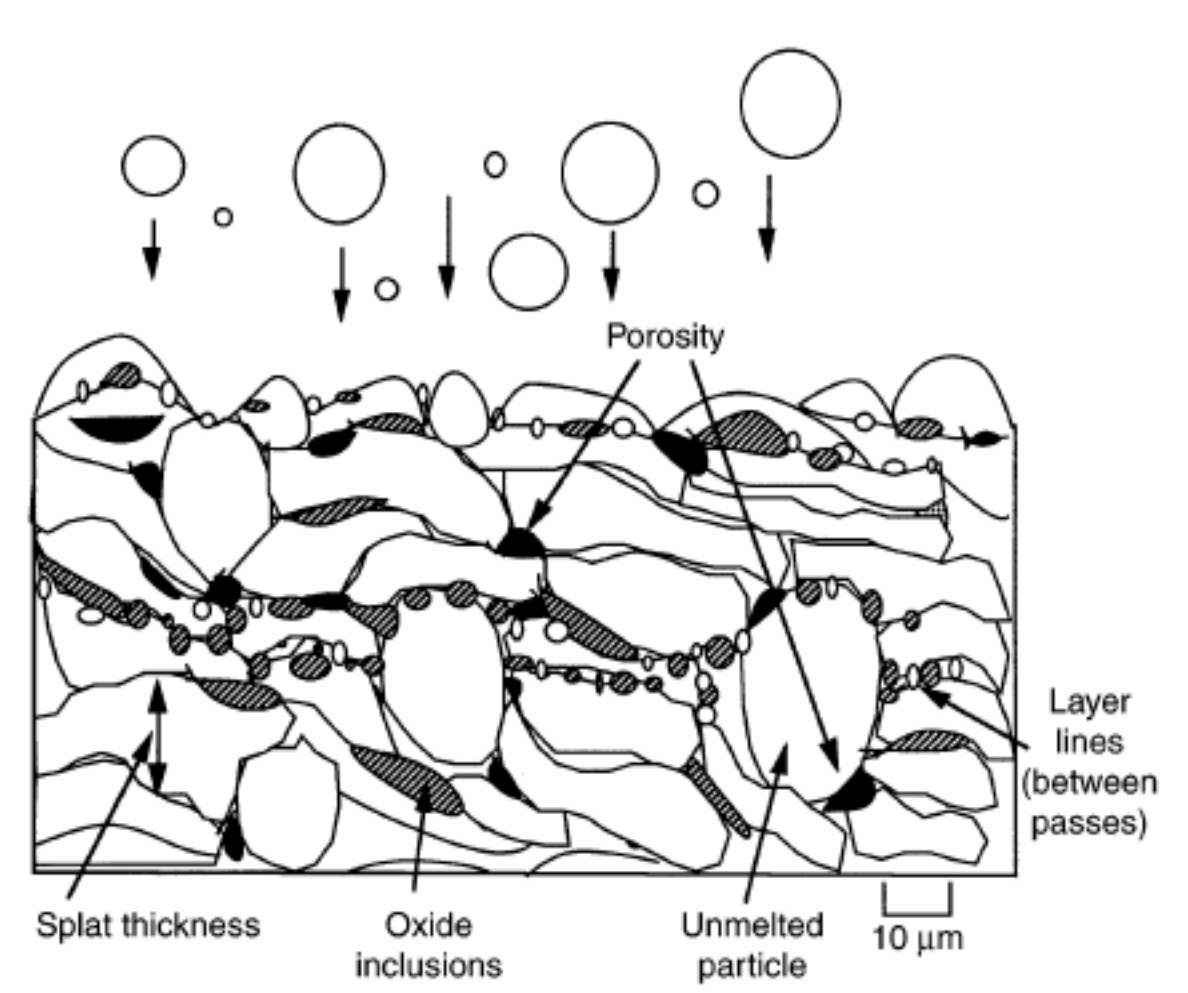


*Figure 10: Shows a schematic representation of a coating cross section deposited by thermal spray* [46].

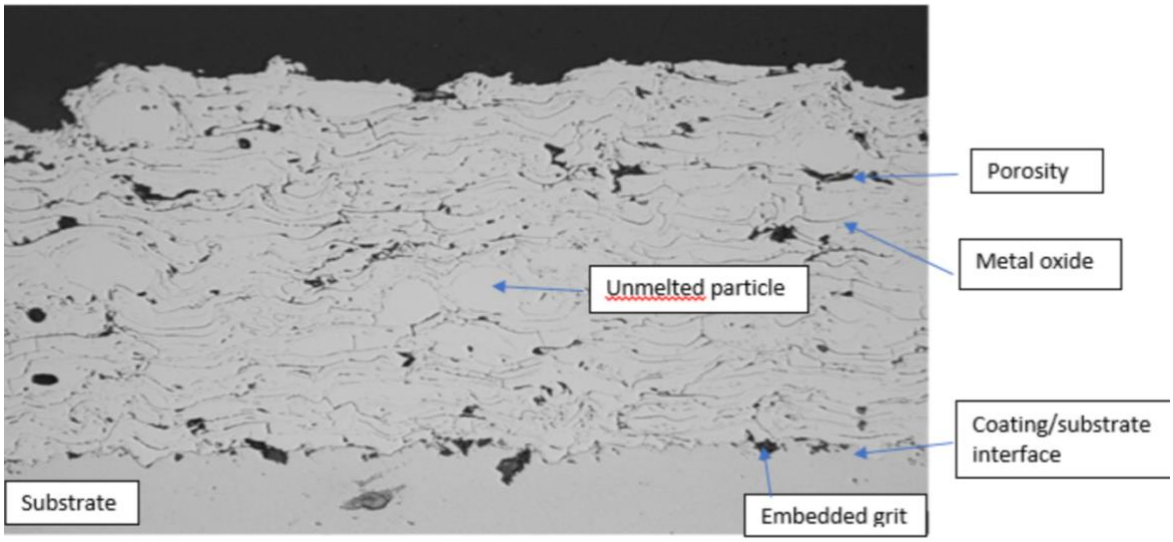


*Figure 11: Shows a cross section of a thermal spray metal alloy coating* [47].

## 2.2 Reinforcement

### 2.2.1 Graphene

#### 2.2.1.1 Introduction

Graphene is a form of (allotrope) carbon atoms which, is also a basic structural unit of carbon nanotubes (CNT), graphite, fullerenes etc. It has a 2D layered structure in which a network of carbon atoms bonded to each other in a hexagonal lattice, as can be seen in Figure 12. Graphene is referred to as a single layer, and more than one layer is known as graphite. Although, many people use graphene containing names such as graphene nanoplatelets (GNPs) or multilayer graphene (MLG) to define a few layers (usually up to 10) of graphene. More than ten layers are usually referred to as thick graphene sheets. Graphene is known as the strongest material present so far, and that's why it attracted the interest of surface engineers [48,49]. Also, it has good thermal conductivity, electrical conductivity, inertness, lubricative ability and surface properties due to its 2D structure [50–53]. Its extreme strength, shearing ability and chemical inertness give rise to impressive tribological behaviour and makes graphene a strong candidate for friction and wear-resistant applications [54]. In addition to those outstanding properties, graphene is also impermeable to liquids and gases. Therefore the rate of corrosion and oxidation processes are slower as those processes are dependent on water and oxygen [55]. Its thermal stability also makes it available to use in various applications where the operating temperature is not exceeding 600 °C. Graphene was extensively studied as a reinforcement material for composite manufacturing. The main aim of graphene, multi-layer graphene or graphene nanoplatelets addition is to increase the strength and to improve the mechanical properties of the main matrix materials.

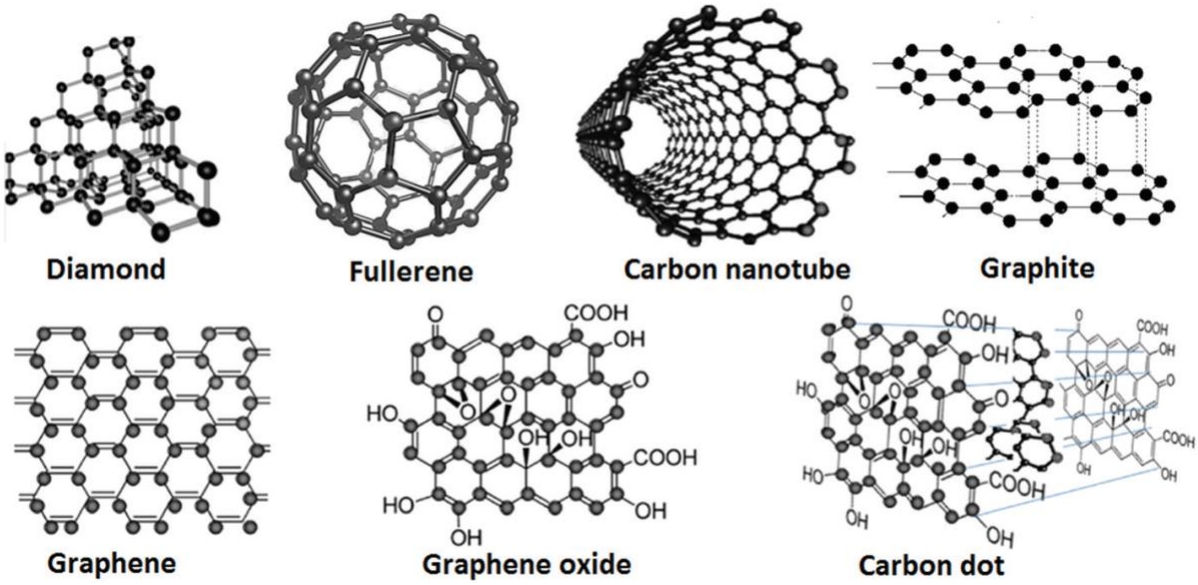


*Figure 12: Different allotropes of carbon that differ in crystalline structures such as diamond with cubic lattice and graphite with hexagonal lattice* [56].

The outstanding properties of graphene are dependent on the number of layers, defects and presence of functional groups attached to it if there are any. Scientists can get information about the presence of defects, and the number of layers in multi-layer graphene or graphitic structure by referring to the bands in Raman Spectroscopy. Raman Spectroscopy is a major tool for scientists working on carbon-containing nanomaterials and is widely used to characterise graphitic structures. It is a method in which laser light is used to measure the vibrational and/or rotational energy in the test specimen. It relies on the inelastically scattered light from the observed material and produces a spectrum with bands. Raman spectra of graphitic structures consist of 3 bands shown in Figure 13. Those bands are referred to as, the D, G and 2D or G' bands. Each of those bands and their positions depends on the relative position of atoms and the nature of bonding between them [57]. Intensity, shape and the position of the bands are used to determine the structure and the chemical changes or modifications that graphitic materials undergo due to any process.

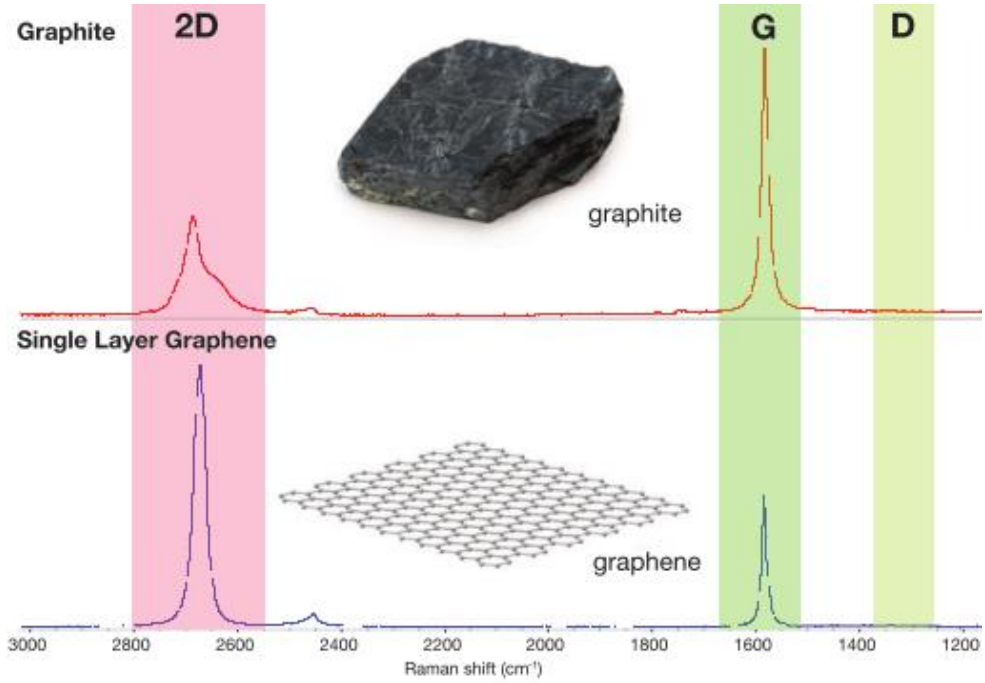


*Figure 13: The Raman spectra of single-layer graphene and graphite, collected with 532 nm excitation* [57].

The D band, in other words, is a disorder or defect band which represents the expansion and contraction occurring to the carbon rings. However, there should be a defect or graphene edge near the ring to make it active. This band represents defects and disorders present in the hexagonal carbon ring lattice structure present in every single layer of the graphitic structure. That is the reason why the D band is very weak in both high-quality graphite and graphene in Figure 13. The position and shape of the D band vary with the frequency of the laser used in the spectroscopy. Therefore, the same laser frequency should be used for all measurements [57]. The G band can be seen in the range between 1575 $cm^{-1}$ and 1600 $cm^{-1}$, and it represents the vibrational energy of $sp^2$ hybridized carbon-carbon bonds, which form the hexagonal carbon chains and rings. The intensity of the G band is strongly dependent on the number of graphene layers. Increasing the number of layers, which means moving from graphene to a more graphitic structure, there will be the presence of more $sp^2$ hybridized carbon-carbon bonds in the structure. As a result, the intensity of the G band increases with the number of graphene layers [57]. The directly proportional relationship between the number of layers and the G band intensity can be seen in Figure 14, which shows the intensity of the G band for single, double and triple layer graphene.

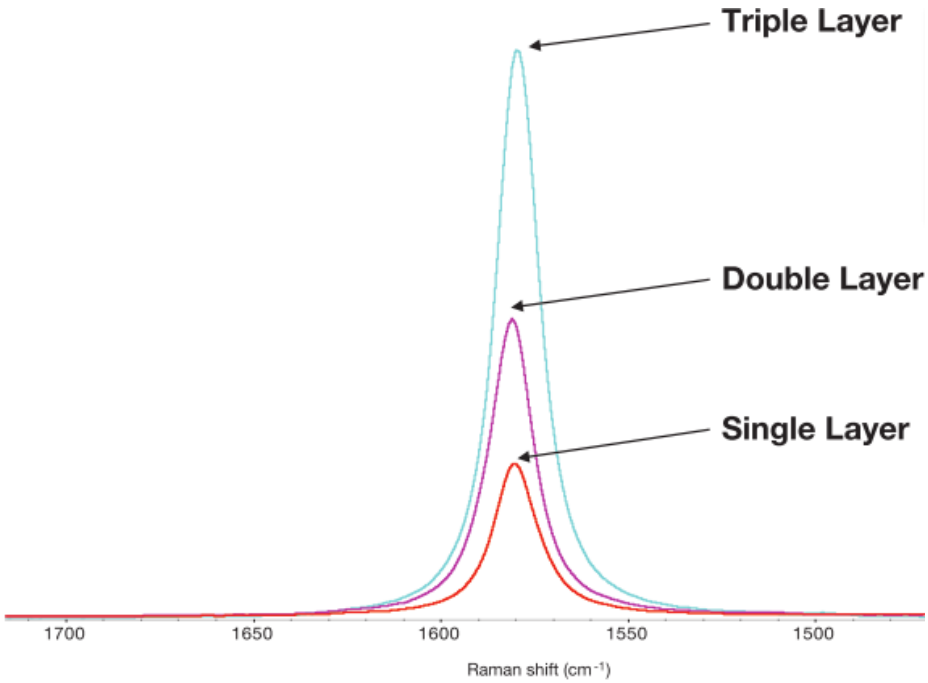


*Figure 14: Variations in the G band intensity with the number of graphene layers, collected with 532 nm excitation* [57].

Position of the G band shifts with changing the number of graphene layers, in addition to the change in the intensity. The position of the G band shifts to a lower frequency (energy) as the number of layers increases, as shown in Figure 15. Heavy atoms and light bonds have lower Raman shifts, therefore it is expected to see a shift to a lower frequency band position while moving from graphene to a graphitic structure [58]. Although both band position and band intensity can be used to distinguish the number of layers, the intensity method is more reliable. The position of the G band can be affected by environmental factors such as temperature, strain and doping but the intensity of the G band is less sensitive to those factors.

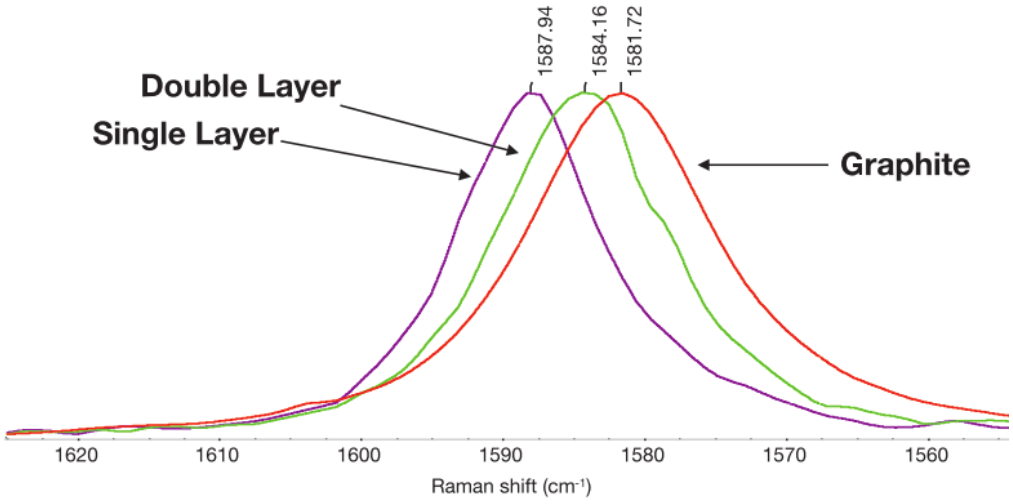


*Figure 15: The G band position as a function of layer thickness, collected with 532 nm excitation* [57].

The 2D or G' band is the band formed between the 2600 and 2800 $cm^{-1}$ range. It is the second order of the D band, but its presence is not related to the presence of the D band. The 2D band is related to the band structure of the graphene and indicates the amount of disorder between the hexagonal layers. As the 2D band represent the band structure of the graphene, moving from single-layer graphene into a graphitic structure, decreases the intensity and broadens the 2D band [57]. This phenomenon is shown in Figure 16.

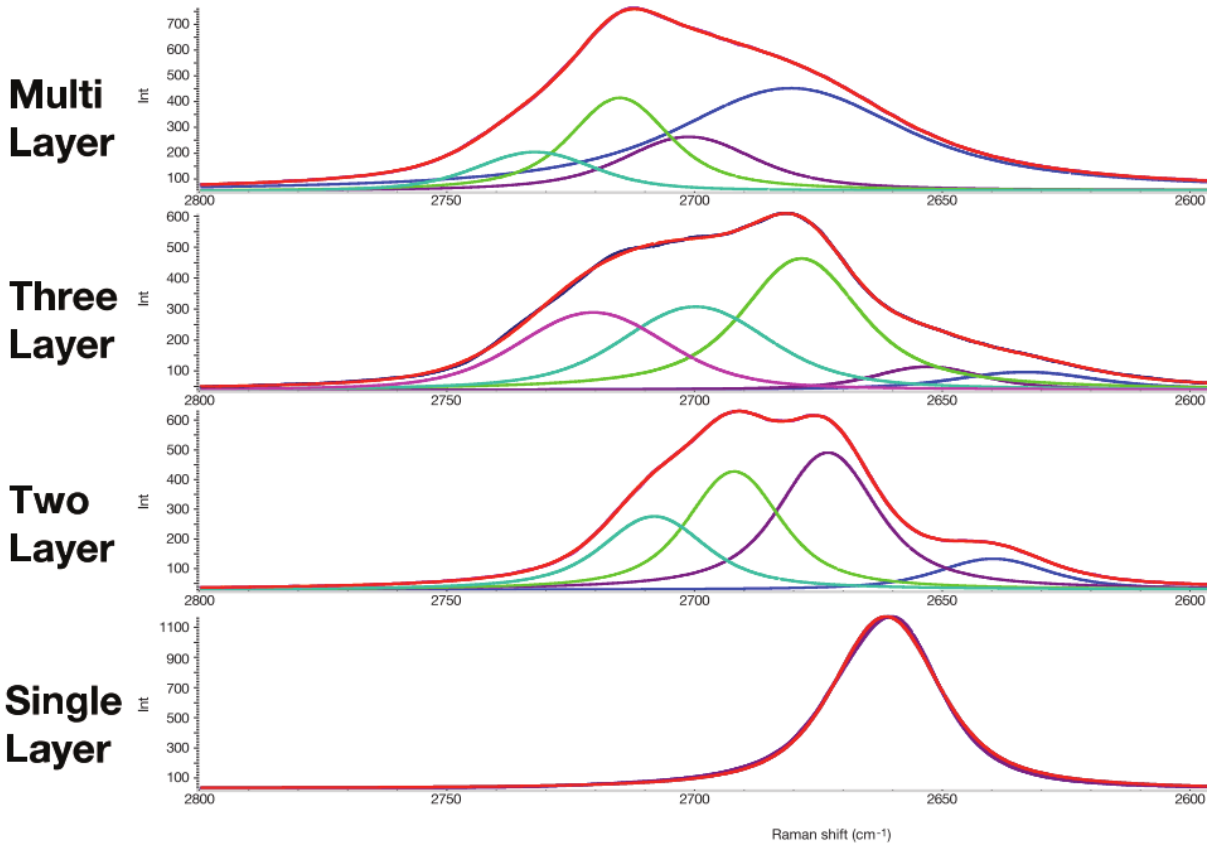


*Figure 16: Shape of the 2D band as a function of layer thickness* [57]

To sum up, both G and 2D bands can be used to determine the layer thickness, defects, and disorders present between the hexagonal layers of the structure. Some studies also use the ratio between the intensities of those bands ($I_{2D}/I_G$). According to [57] a high ratio of around 2 represents a defect-free high-quality single-layer graphene but moving from single-layer graphene to a graphitic structure the ratio is decreasing. That ratio result represents an intensity reduction in the 2D band while an increase of intensity in the G band as we move from single-layer graphene to multi-layer graphene or a graphitic structure. In addition, the ratio between the D and the G bands, ($I_D/I_G$) can be used to determine the defects and disorders present inside the hexagonal carbon rings or chains.

### 2.2.1.2 Graphene and Metal Matrix Composite Systems (MMCs)

#### *2.2.1.2.1 Aluminium – GNP Composites*

Aluminium is a widely used metal in the aerospace and automotive industry due to its ductility, strength, low weight and good corrosion and oxidation resistance [59,60]. Therefore, studies were performed to investigate the effect of GNP addition to the aluminium

matrix. Table 1 shows a brief summary of the studies performed on aluminium matrix and changes to mechanical properties associated with GNP incorporation. Usually, Al – GNP composites are produced by metallurgical processes such as hot extrusion, hot rolling and mechanical alloying. Different concentrations of GNP solutions were incorporated (≤ 0.13 vol. %, ≤ 1.28 vol. % and ≤ 6.34 vol. %) by various techniques and parameters in different studies [54]. ≤ 1.28 vol. % GNP addition led to improvements in hardness, yield strength, ultimate tensile strength, failure strain by more than half and both compressive strength and flexural strength also increased by nearly 50%. When the GNP concentration was increased to ≤ 6.34 vol. %, the tensile strength of the composite decreased by 20 %. On the other hand, both flexural and compressive strength still increased by 20%. However, the improvements obtained are lower than those obtained by ≤ 1.28 vol. % of GNP [61,62]. Lower GNP concentrations such as ≤ 0.13 vol. % and ≤ 0.34 vol. % were also examined, and both concentrations diminished hardness and compressive strength values. The main reason for the decrease in mechanical properties, especially for higher GNP concentrations is due to the agglomeration of the GNP particles. Agglomeration creates larger particles which result in increased porosity and also act as stress risers, which initiate the crack formation and growth. Processing techniques and parameters also affect mechanical properties. The hot extrusion method was reported to encourage the formation of carbides which lowers the hardness [56]. In addition, higher sintering times and temperatures also encourage carbide formation and lead to grain growth. On the other hand, they also increase the diffusion rates which is essential for better bonding between reinforcement and matrix materials and also for consolidation [63,64]. To sum up, the addition of around ≤ 1.28 vol. % of GNPs into an aluminium metal matrix looks like the optimal GNP concentration which leads highest improvements in mechanical properties. Both higher and lower GNP concentrations do not create significant improvements. In lower concentrations, there are not enough GNP particles to bond with the matrix. In higher concentrations, GNP agglomerates result in the reduction of mechanical properties. In addition, processing parameters should be in the right balance to harvest the advantages of higher sintering times and temperatures but at the same time minimise the disadvantages created by them.

| Main Matrix Material | GNP concentration ( wt. %) | Mechanical properties (percentage change compared to unreinforced ) | Reference |
|---|---|---|---|
| Al | 1 | Vickers Hardness (HV) = +36%<br>Compressive Strength (CS) = +13% | [61] |
| | 2 | HV= + 50%<br>CS = +16% | |
| | 3 | HV= + 50%<br>CS = +19% | |
| | 0.5 | Ultimate tensile strength (UTS) = +15%<br>Yield Strength (YS) = +8% | [65] |
| | 1 | UTS= +50%<br>YS = +43% | |
| | 1.5 | UTS= +35%<br>YS= na. | |
| | 2 | UTS= +18%<br>YS= na. | |
| | 0.3 | YS = +36% | [66] |
| | 0.5 | YS = +47% | |
| | 0.7 | YS = +55% | |
| | 0.39 | YS= +14.7%<br>UTS= +11.1%<br>HV= +11.8%<br>Failure Strain = -28.8%<br>UCS= - 7.8% | [67] |

*Table 1: A brief summary of the various studies performed on Graphene incorporated aluminium matrix systems, showing graphene concentrations used and changes in the mechanical properties of the system.*

*2.2.1.2.2 Magnesium – GNP Composites*

Magnesium is another lightweight material and one of the most abundant metals on earth. The main issue of magnesium is its lower strength and ductility [68]. Therefore, GNPs are incorporated into the magnesium metal matrix to overcome the strength and ductility related problems. Table 2 shows a brief summary of the studies performed on magnesium matrix and changes to mechanical properties associated with GNP incorporation. Incorporating GNPs into magnesium was performed by either wet chemistry, ball milling or ultrasonication powder mixing method followed by solid-state stirring, spark plasma sintering or metallurgical methods for consolidation. When the wet chemistry method was used for powder mixing, microspores were created at the final composite and oxidation products can be seen, which lowers the strength of bonding between GNPs and the metal matrix [69]. However, this is only an exceptional study. Composites manufactured by ultrasonication followed by solid-state stirring shows better bonding of GNPs to the matrix, and there was no sign of porosity but still, oxidation product was present [70,71]. Furthermore, higher densification was achieved when metallurgical processing routes were preferred but those are directional processing techniques that cause even distribution of GNPs and non-uniform grain size distribution at the final product. Research performed so far showed that the addition of GNP to a magnesium metal matrix is beneficial for improving mechanical properties. The addition of ≤ 2 vol. % GNP improves hardness, elastic modulus, yield strength and ultimate tensile strength by 78 %, 131 %, 117 % and 58 %, respectively [69–74].

| Main Matrix Material | GNP concentration ( wt. %) | Mechanical properties (percentage change compared to unreinforced ) | Reference |
|---|---|---|---|
| Mg | 1 | HV= +20% | [75] |
| | 2 | HV= +34% | |
| | 5 | HV= +8% | |
| | 0.3 | YS= +5%<br>E= +22%<br>UTS= +8%<br>HV= +17% | [71] |
| | 1.2 | HV= +78% | [76] |

*Table 2: A brief summary of the various studies performed on Graphene incorporated magnesium matrix systems, showing graphene concentrations used and changes in the mechanical properties of the system.*

*2.2.1.2.3 Copper – GNP Composites*

Copper is another commonly used metal in the industry due to its thermal and electrical conductivity and corrosion resistance. However, it has a low hardness, like aluminium and magnesium [77]. Therefore, GNPs incorporated into the copper metal to achieve higher hardness and improved mechanical properties. Table 3 shows a brief summary of the studies performed on copper matrix and changes to mechanical properties associated with GNP incorporation Studies show that copper–GNP composites have also behaved similarly to both magnesium - and aluminium - GNP composites. The addition of GNP particles to the metal matrix improves the mechanical properties. Further increase in GNP concentration causes the formation of pores and a reduction in both density and mechanical properties due to the agglomeration. Although Cu – GNP composites behave very similar to both Al – GNP and Mg – GNP composites, agglomeration of the particles is not a problem till ≤ 8 vol. % GNP [54]. Studies showed the addition of ≤ 8 vol. % GNP improves hardness, yield strength, ultimate tensile strength and young's modulus by 50 %, 114 %, 42.8 % and 61 %, respectively [78–81]. However, the improvements also depend on the fabrication technique and parameters used.

One of the studies reported a decrease in mechanical properties as dispersion of GNPs was not enough throughout the copper matrix [54,81].

| Main Matrix Material | GNP concentration ( wt. %) | Mechanical properties (percentage change compared to unreinforced ) | Reference |
|---|---|---|---|
| Cu | 3 | YS= +25%<br>Youngs Modulus, E = +9% | [78] |
| | 5 | YS= +53%<br>E = +24% | |
| | 8 | YS= +75%<br>E = +34% | |
| | 12 | YS= +40%<br>E = +25% | |
| | 0.5 | YS= +3%<br>UTS= +4% | [80] |
| | 1 | YS= +14%<br>UTS= +10% | |
| | 2.5 | YS = +80%<br>E= +30% | [82] |

*Table 3: A brief summary of the various studies performed on Graphene incorporated copper matrix systems, showing graphene concentrations used and changes in the mechanical properties of the system.*

*2.2.1.2.4 Strengthening Mechanisms Induced by GNPs*

Studies performed on GNP incorporated aluminium, magnesium and copper metal composites show sufficient improvements in mechanical properties, although a relatively small amount of GNPs used. Figure 17 represents the variation in mechanical properties of different metal matrix composites with different GNP concentrations. A general upward trend

with some exceptions in mechanical properties can be seen. The addition of GNPs up to a point improves the mechanical properties. Once the GNP concentration starts to go over a specific limiting point, there are no more improvements in mechanical properties. When high concentration GNPs were used, they tend to agglomerate. GNP agglomerates act as stress concentrators and initiate crack growth. In addition, they also contribute to the formation of pores, hence lowering the density and mechanical properties [54].

The improvements obtained in mechanical properties by GNP incorporation can be explained by 4 different strengthening mechanisms. These mechanisms are grain refinement, Orowan strengthening, the efficiency of load transfer from matrix to GNP and strain hardening. Grain refinement takes place during the fabrication process of the composites, as the GNPs wrap around the grains and prevent the growth. Therefore, produced composites have finer grains hence, more grain boundaries. Grain boundaries act as a barrier for dislocation motions. In addition, finer grains mean less dislocation pile up at the grains and hence lower stress generated by them in each grain. While the GNPs located at the grain boundaries cause the formation of finer grains, GNPs located inside the grains are responsible for Orowan strengthening. When dislocations move inside the grains and interact with GNP particles, they bow out between particles and form Orowan loops around them. Those loops inhibit the motion of dislocations. When a load is applied to the GNP – metal composite, it is transferred from the metal matrix to the GNPs. Therefore, the high strength and ductility of GNPs can be effectively used for enhanced mechanical properties. To obtain an efficient load/stress transfer from the matrix to the GNPs a strong interface is a must. Fabrication methods and parameters are the strongest factors affecting the strength of the interface. First of all, GNPs must be distributed and dispersed evenly for strong interfacial bonding between them and the matrix. Some studies used flake morphology [83] to obtain high contact areas, while others involved GNPs decorated with metal nanoparticles for higher aspect ratios [81]. Moreover, the addition of the GNPs leads to the dislocation pile-up and increased dislocation density. Therefore, dislocations start to interact with each other and impede further dislocation motions which are known as strain hardening.

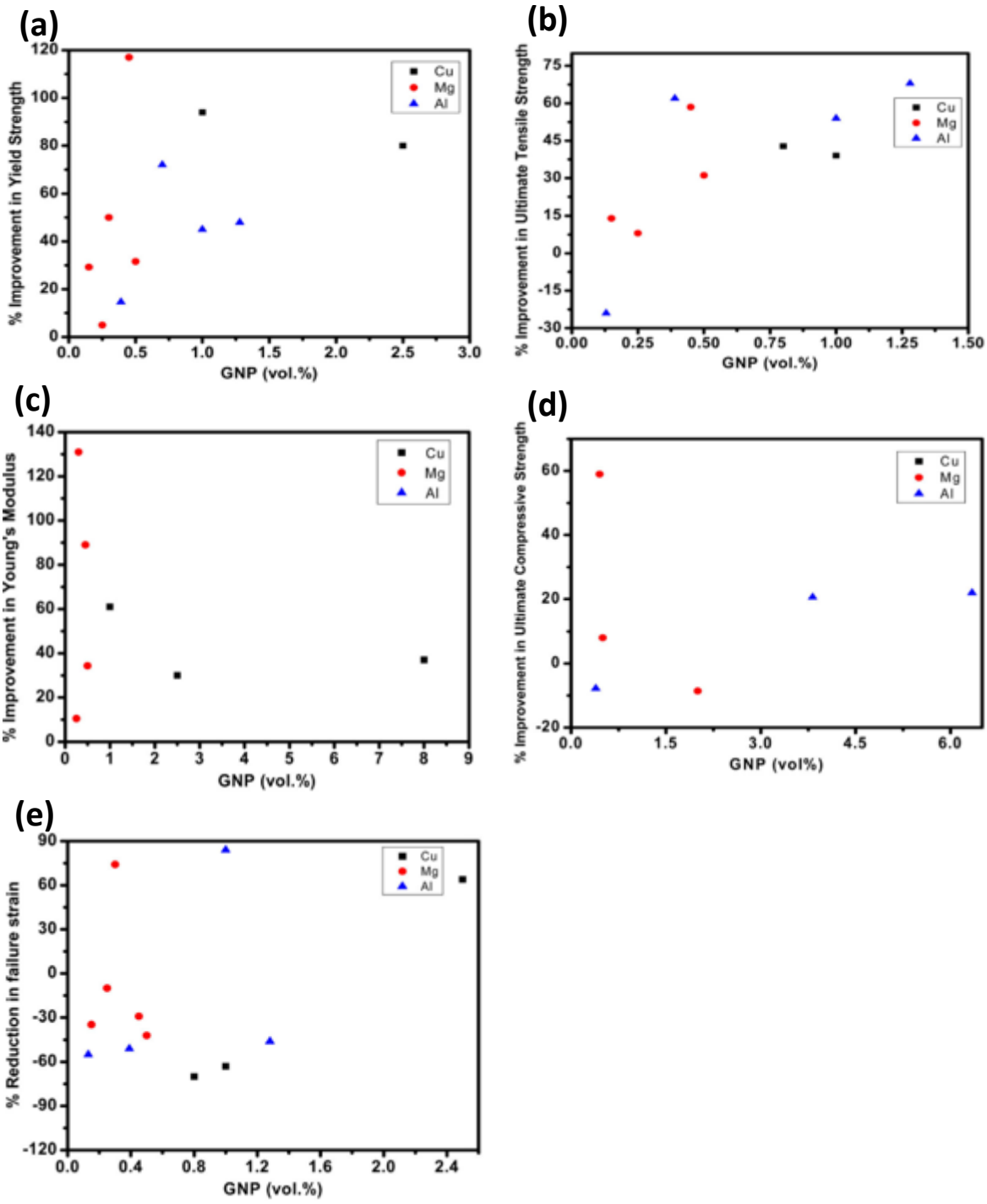


*Figure 17: Graphs above represent an improvement in yield strength (a), ultimate tensile strength (b), young's modulus (c), ultimate compressive strength (d) and reduction in failure strain (e) with GNP vol. -% for different metal matrix composites (MMCs)* [54].

*2.2.1.2.5 Tribological Performance*

The most common form of failure in moving and rotating parts is mechanical failure due to the wear and friction generated during the motion. High strength layered structure with weak van der Waals forces between the graphene layers and its chemical inertness makes graphene an emerging lubricant. In addition, due to its outstanding strength and chemical inertness, graphene is not affected by environmental and loading conditions while conventional lubricants do [54]. Therefore, using it as a reinforcement material in composites creates a continuous in situ solid lubricant supply during the operation and the improved mechanical properties of the system. Wear tests were performed on pure Mg and Mg – GNP composites with varying GNP concentrations. Pure magnesium undergoes abrasive wear. A high number of scratches and cracks present on the wear surface shown in Figure 18 (a and b), indicates high wear rates. On the other hand, Mg – GNP composite showed reduced wear and presence of GNP on the wear track, which pulled out during the test and act as a solid lubricant shown in Figure 18 (c and d). Wear surface analysis showed a 40 % and 60 % reduction in depth and width of the wear tracks, respectively [75]. Intermetallics such as TiAl and $Ni_3Al$ are widely used in structural applications due to their high strength, low density and structural stability at high temperatures; however, low wear resistance is a major drawback for them. GNPs were incorporated into these intermetallics (TiAl / GNP and $Ni_3Al$ – GNP) to improve the wear performance. GNP incorporation reduces both the coefficient of friction and the wear rates at room temperature compared to base intermetallic materials. The amount of reduction varies depending on the material of the counter surface chosen. Wear characteristics of GNP incorporated intermetallics at higher temperatures were also studied. Studies showed that the wear rates stayed low till the temperatures were up to 500 °C. Further increase in temperature causes a sharp increase in wear rates due to oxidation. Figure 19 represents SEM images of TiAl / GNP worn surface at 2 different temperatures. When the wear test was performed at 550 °C, a small number of oxidation sites is present on the worn track surface. As the wear test temperature increased to 600 °C, rich oxides were formed in presence of GNPs which causes a drastic increase in wear rate [54,84].

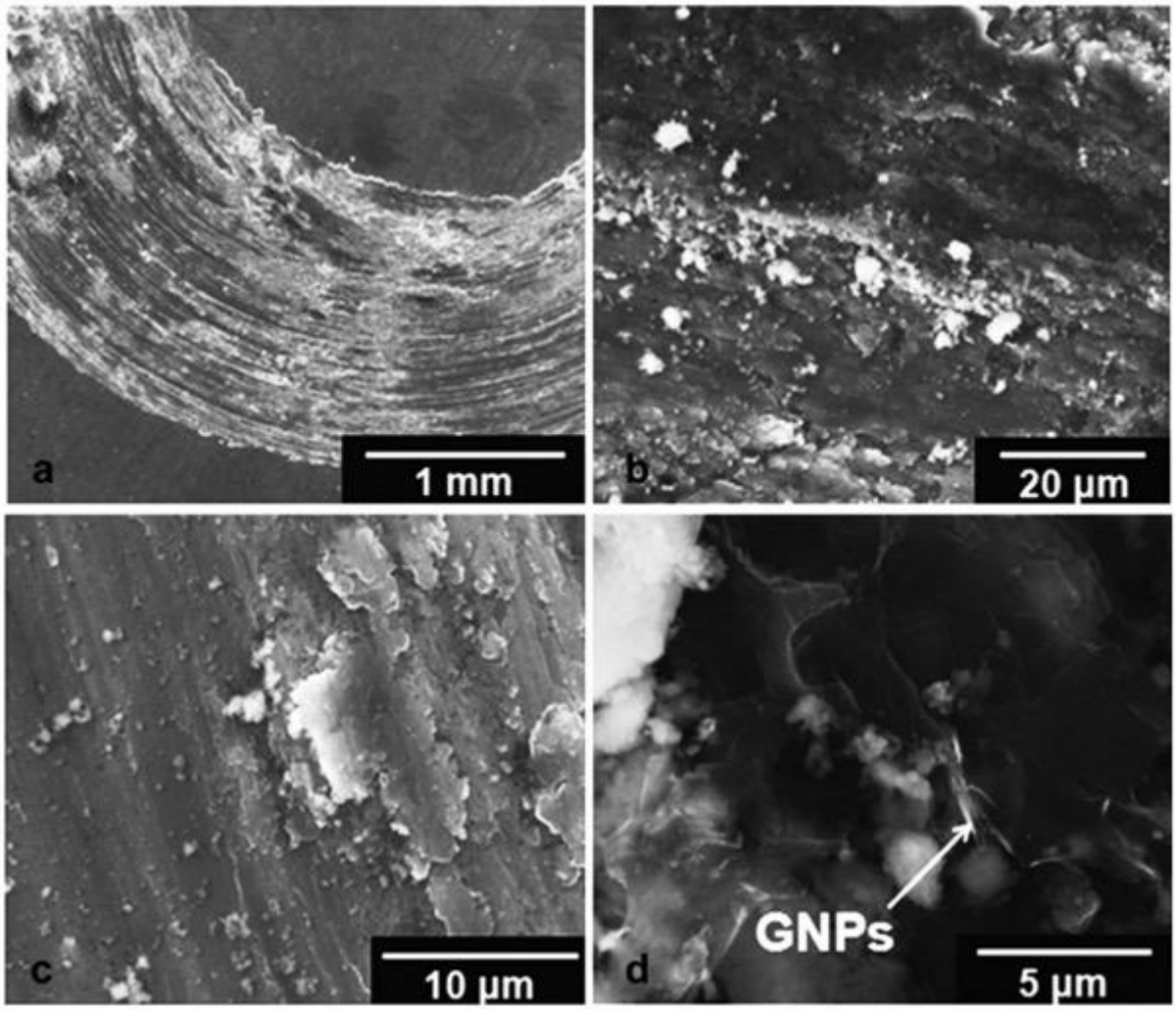


*Figure 18: SEM images from worn surfaces of (a and b) pure Mg show typical abrasive wear with wear debris in the deformed region and GNP in worn surfaces of (c) Mg - 2 vol. % GNP and (d) Mg - 5 vol. % GNP composite* [75].

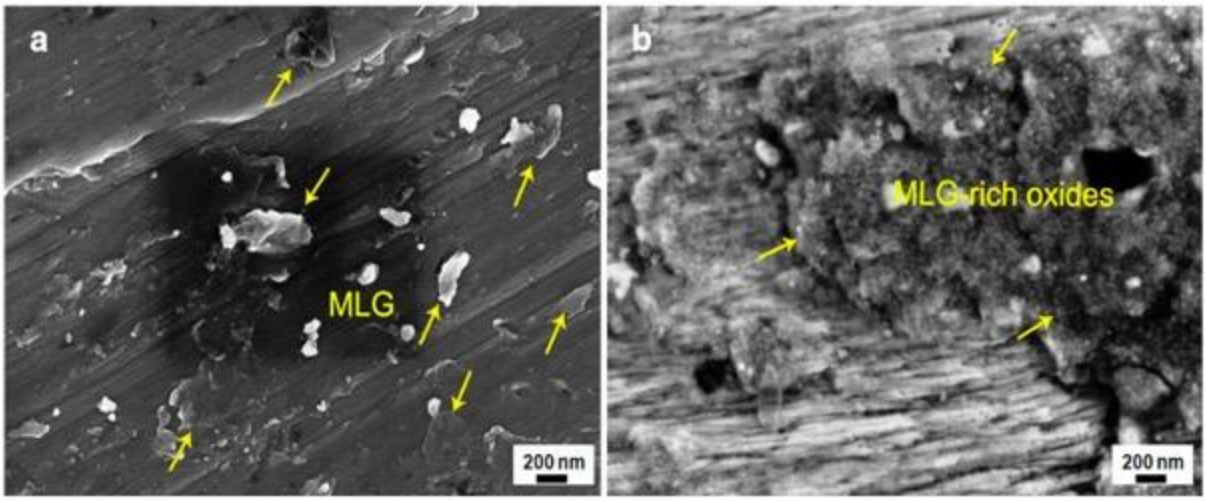


*Figure 19: SEM images of the worn surfaces of TiAl / GNP at 550 °C (a) and at 600 °C (b)* [54].

### 2.2.1.3 Graphene and Ceramic Matrix Composite Systems (CMCs)

#### *2.2.1.3.1 Alumina – GNP Composites*

Alumina is the first ceramic material used in a ceramic – GNP composite material fabrication, which was performed by the SPS method and proved that ceramic – GNP composites could be producible [85]. Alumina ($Al_2O_3$) is a very practical ceramic that is widely used in the aerospace, automotive and biomedical industries. Therefore, many studies were performed to analyse the addition of GNPs as a reinforcement material to the alumina matrix. The effect of various GNP concentrations was investigated and the results showed a 53 % and 94 % increase in fracture toughness with the addition of 3.5 vol. % and 2 vol. % GNPs respectively [54,86]. Another study shows the performance of alumina – GNP composite under bending. According to it, the addition of 0.78 vol. % GNPs increase both flexural strength and flexural toughness by 31 % and 27 %, respectively [54,87]. In addition to improvements in mechanical properties, alumina composites also benefit from the electrical conductivity of graphene. Similar improvements were also reported with CNT reinforcement, but they are inferior compared to the GNPs. This is due to the structure of materials as there are more contact points available in a GNP structure compared to a CNT [88,89]. Another study was performed at the University of Nottingham by fabricating alumina – GNP (1 vol. %) composite coating by using HVOF thermal spray. The mean fracture toughness of the composite coating was calculated as nearly 2 times higher than a pure alumina coating. However, there is a large standard deviation of results due to the phase change of alumina during fabrication [90].

#### *2.2.1.3.2 Silicon Nitride – GNP Composites*

Silicon nitride ($Si_3N_4$) is another widely used structural ceramic after alumina. It is mostly preferred for applications at elevated temperatures due to its thermal stability. Graphene incorporation to silicon nitride matrix was performed to achieve improved mechanical and electrical properties. A significant increase of around 135 % in fracture toughness was obtained by the addition of nearly 1.5 vol. % GNP [54,91]. Another study was performed to compare the improvements obtained by another carbon-based material, CNTs. The same concentration (5 vol. %) of both GNPs and CNTs were added to a silicon nitride matrix. Results show that GNPs dispersion was better than CNTs due to their higher aspect ratio. As a result, silicon nitride – GNP composite has enhanced mechanical properties than silicon nitride – CNT

composite [54,92]. In addition to mechanical improvements, electrical properties were also improved by adding GNPs up to 24 vol. % [93,94]. However, enhancement in electrical conductivity is dependent on fabrication methods. For example, spark plasma sintering (SPS), aligns GNPs in a preferred direction, which gives rise to an anisotropic electrical response [54].

*2.2.1.3.3 Toughening and Energy Dissipation Mechanisms Induced by GNPs*

Hardness, elastic modulus, compressive and tensile strength are the main mechanical properties studied for metal – GNP composites. However, fracture toughness and flexural strength are the mechanical properties studied in detail for ceramic – GNP composites. Because both flexural strength and fracture toughness are the mechanical properties that limit the structural applications of ceramics.

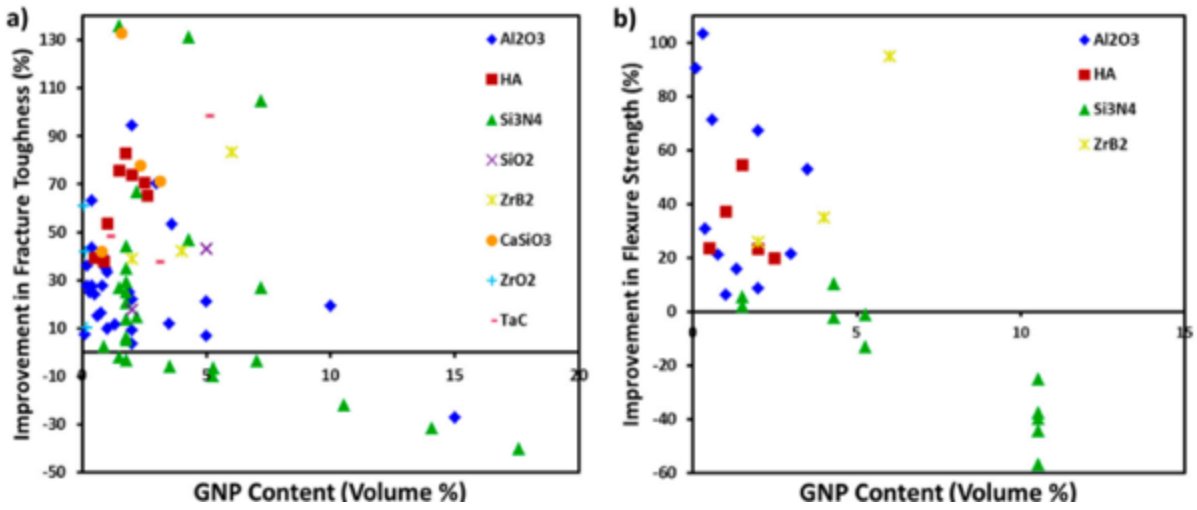


*Figure 20: Fracture toughness (a) and flexure strength (b) improvements versus GNP content in a volume percentage of various ceramic matrix composites* [54].

Figure 20 shows the improvements obtained in both fracture toughness and flexural strength of various ceramic matrixes due to the incorporation of GNPs with various concentrations, Generally, the addition of GNPs has a positive effect on both fracture toughness and flexure strength of ceramic composites. Most of the studies are concentrated around < 3 vol. % GNP additions. Some studies used higher GNP contents, but both fracture toughness and flexural strength decrease after a specific point, or the improvements can also be achievable by lower GNP contents. Therefore, there is no point in increasing GNP content after a specific amount. High GNP contents make dispersion harder and cause the formation of agglomerates.

Enhanced fracture toughness and flexure strength of ceramic composites are due to the toughening mechanisms induced by the presence of GNPs. Three different toughening mechanisms take place in the order of crack deflection, crack bridging and GNP pull-out. Figure 21 shows the GNPs wrapping around the grains, deflecting and bridging the cracks which later lead to the pull out of the GNPs. When a growing crack faces a GNP inside the microstructure, it cannot propagate through the GNP due to the significantly high in-plane strength of graphene. In addition, as graphene has a high aspect ratio, the crack cannot even enclose the GNP. Therefore, GNPs act as a barrier to crack propagation and cause the deflection of cracks (Figure 21 (a)). If the growing crack has enough energy to propagate through the GNP, high in-plane strength still does not allow graphene to break, so GNP acts as a bridge between two grains and prevents further widening of the crack (Figure 21 (b)). If the propagating crack has enough energy, it can pull the GNP off the bridged grains (Figure 21(c)). The energy used to pull out GNP is energy that would have otherwise been released through crack propagation. Toughening mechanisms are described depending on the matrix material choice and the bonding between the matrix and the GNPs. In addition to the added toughening methods to the matrix materials, GNPs also have intrinsic energy dissipation methods, which conventional reinforcement materials such as fibre or whisker do not have. Studies performed on bulk GNP structures show exceptional bending and kinking without fracturing up to angles of 180° [95]. This remarkable flexibility of the GNPs allows them to absorb energy and hinder crack propagation. Furthermore, due to the high surface areas of GNPs and the presence of week van der Waals bonding between graphene layers, they can easily slide and slip past each other. This creates high friction forces, which can be used to dissipate energy [54].

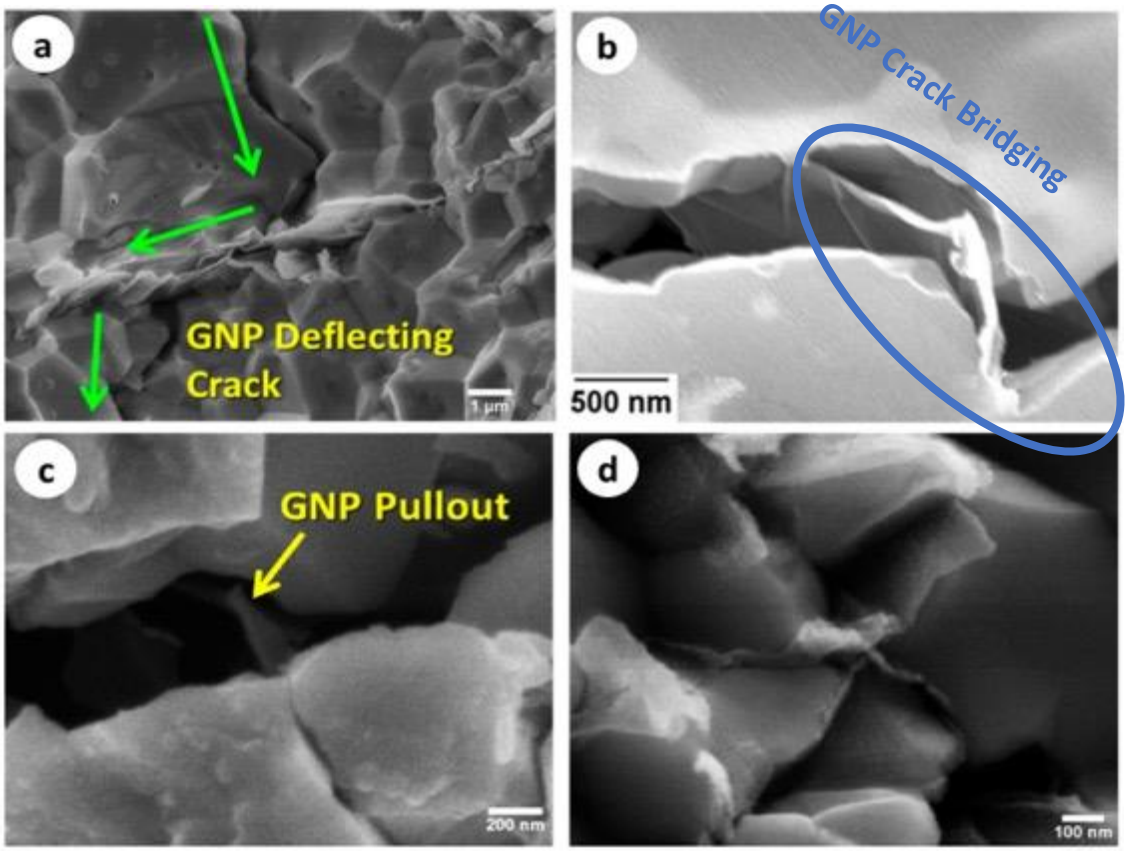


*Figure 21: Toughening Mechanisms induced by the presence of GNPs; (a) Crack deflection, (b) crack bridging, (c) GNP pull - out and (d) GNP grain wrapping* [54]

#### *2.2.1.3.4 Tribological Performance*

The tribological behaviour of ceramic–GNP composites at different loading conditions was investigated at both room temperature and elevated temperatures. Both dry and lubricated by the presence of isooctane sliding wear tests were performed at room temperature. Studies show that both coefficients of friction and wear rates depend on the GNP content and the loading conditions. Generally, the addition of graphene nano-platelets does not have a significant effect (only small improvements in some studies) on the coefficient of friction at lower loading conditions. However, as the load increases, the COF value decreases [54,96–98]. Wear rates show a more dependent behaviour on the GNP content than the loading. Studies investigated the effect of different GNP concentrations from 0.25 vol. % till up to 17 vol. %. Results show that the wear resistance of composites increases with the addition of low GNP contents. As the GNP content increases, wear resistance behaves similar to other mechanical properties and starts to decrease because of agglomeration. One of the studies illustrates the effect of 0.5 vol. % and 5 vol. % GNP content

on wear characteristics. Although COF decreases in both GNP contents wear volume was only reduced when 0.5 vol. % GNP was added [99]. The coefficient of friction is not following the same trend as wear rates. Although, wear resistance starts to drop due to agglomeration when GNP content is more than 1-5 vol. %, improvements in COF are still obtainable. As the GNPs are known as solid lubricants, increasing the amount of GNPs lead to lower CoF. However, density and the structural integrity of the composites reduce due to the agglomeration of GNPs which leads to degradation in mechanical properties and an increase in wear rates. For example, wear characteristic of silicon nitride–GNP composite with GNP content up to 17 vol. % was investigated in a study and the highest wear resistance was achieved by the addition of 1.7 vol. % GNP. However, in the same study, the lowest coefficient of friction was achieved by incorporating 8 vol. % GNP into the silicon nitride matrix [97].

The wear performance of the GNP incorporated ceramic composites at elevated temperatures was not extensively studied compared to the room temperature wear performance. Silicon nitride is one of the ceramic matrixes that have enough data and information to comment on the effect of GNP additions on wear characteristics at elevated temperatures. Data present so far investigates the wear rate and coefficient of friction of two silicon nitride–GNP composite samples with different GNP contents. Wear tests were performed at 300 °C, 500 °C and 700 °C with 1 wt. % / 1.7 vol. % and 3 wt. % / 5 vol. % GNP contents. The coefficient of friction did not show any improvements throughout the study. As the temperature increased, for 1 wt. %, CoF were similar to unreinforced, pure silicon nitride, but it is increased for 3 wt. % GNP content. In the case of wear rates, at 300 °C wear rate for the sample containing 1 wt. % GNP decreased by an order of magnitude but increased for 3 wt. % GNP content. As the temperature increased, the wear rate for 1 wt. % increased and became similar to unreinforced pure silicon nitride. Silicon nitride reinforced with 5 wt. % GNP content still has poor wear resistance than others at increased temperatures. To sum up, the addition of GNPs only improved wear resistance up to 300 °C and only with 1 wt. % GNP content [54,96] .

The mechanisms responsible for the improved wear resistance due to the addition of GNPs vary in different studies. So far, there are two different theories present to explain the phenomena. In some studies, investigations on worn surfaces show a graphene-containing protective and lubricating tribolayer [96,100]. However, few other studies did not report the

formation of a tribolayer but still managed to get improved wear resistance. So, it is believed that the improvements are due to the toughening mechanisms induced by the GNPs and their lubricative ability between the grains [98,101]. In one study, Archard's equation was used to prove the theory of wear rate improvements due to the toughening mechanisms. Calculations were made to see if the improvements in wear rate were just dependent on hardness difference which is obtained by GNP addition. The theoretical result showed a 21.7 % increase in wear resistance as a result of hardness. However, the experimental result showed an increase of around 65 % [100] which suggests a combined effect of an increase in hardness and lubricative ability of GNPs took place in that study.

### 2.2.2 Hexagonal Boron Nitride

#### 2.2.2.1 Introduction

2D materials became an emerging area of study after the invention of graphene and the developments in large scale 2D material production methods [102,103]. 2D materials have unique characteristics and outstanding properties which attract interest. Hexagonal boron nitride (hBN) is one of these 2D materials, which has a layered structure. Alternating boron and nitrite atoms are covalently bonded ($sp^2$ hybridised) to each other to form a hexagonal honeycomb structure within layers. The strength of $sp^2$ hybridised covalent bonds gives rise to extreme in-plane strength and thermal conductivity. In addition, layers are connected with van der Waals forces, weaker than the in-plane covalent bonds [104]. The structure of hBN is similar to multi-layered graphene/graphite; hence it is referred to as white graphite. A schematic representation of the hexagonal boron nitride structure can be seen in Figure 22.

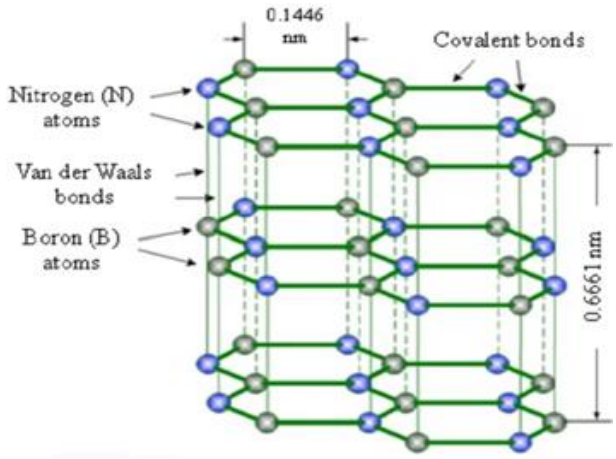


*Figure 22: Schematic of a hexagonal boron nitride structure, showing the bonding, atoms and spacing* [105].

The properties of the hBN are also similar to the graphene as a result of the similarities in the structure. hBN has a very low density (2.1 g/cm$^3$), chemical inertness, hardness, thermal conductivity (predicted in-plane at room temperature is 550 W m$^{-1}$ K$^{-1}$) and thermal stability. In contrast to graphene, hBN is electrically insulating due to the large bandgap (5.97 eV) and the presence of a minimum number of dangling bonds and charge carriers [106–109]. In addition, hexagonal layers can easily slide over each other due to the weaker van der Waals forces of attraction between the layers compared to the in-plane covalent bonds. When this is combined with the thermal conductivity hBN can easily dissipate the energy away from the tribological contacts. Hence, it is widely used as a solid lubricant for high-temperature applications. When compared with other solid lubricants, hBN outperforms them in high-temperature applications to reduce the wear rate and the coefficient of friction (CoF) [38,110]. In addition, the combination of solid lubricant abilities with low density, hardness, corrosion and oxidation resistance makes the hBN a promising additive for composite manufacturing to improve the performance of the main matrix alloy [38,103,111–116]. Coatings incorporated with hBN are also deposited via various techniques such as electrodeposition, laser cladding and thermal spray.

#### 2.2.2.2 Mechanical and Tribological Performance

The high-temperature properties of the hBN mentioned in the previous section made it a promising material for incorporating into high-temperature matrix materials. Nickel-based materials such as NiCr, Ni60, NiCr/$Cr_3C_2$ and $Ni_3Al$ were studied extensively as the main matrix materials for hBN incorporation [111–114]. In addition to the high-temperature matrix materials, polyetheretherketone (PEEK) and hydroxyapatite/chitosan (HA/CTS) are two other matrix materials used and studied for hBN incorporation in the literature [103,117–119]. The addition of hBN increases the mechanical properties of the composites including the elastic modulus, and micro- and nano-hardness. However, improvements in the mechanical properties are dependent on the hBN concentration achieved in the final composite microstructure. There is a critical point depending on the deposition technique and main matrix material used, where the addition of more hBN reduces the rate of improvements in the mechanical properties due to the agglomeration. The agglomeration of finer hBN particles creates a non-uniform distribution, introduces pores and weakens the bonding strength. Figure 23 (a) shows the effect of varying hBN concentrations in the final matrix on the

mechanical properties including elastic modulus, and micro- and nano-hardness. On the other hand, two studies performed Nickel-based hBN incorporated coatings deposited by plasma spray, showed no improvements in the mechanical properties. The authors reported the lower hardness of hBN compared to the main nickel matrix and increased porosity content around the hBN additives inside the composites [113,114].

The tribological performance of the hBN incorporated composite systems has a similar trend to the mechanical properties, explained above. The van der walls forces of attraction allow the hBN layers to slide over each other and enable the formation of tribofilms. In addition to the energy dissipation via sliding of layers, the high thermal conductivity of the hBN allows the heat generated at the tribological contacts to dissipate faster. The combination of these two mechanisms as a result of the hBN addition reduces the coefficient of friction between the tribological contacts. In addition, the combination of lubricative abilities and the improved mechanical properties as a result of hBN incorporation improves the wear resistance of the materials. Studies showed that the wear rate was reduced significantly by the addition of the hBN into the matrix. Similar to the mechanical properties and the CoF, after a critical point, the addition of hBN did not improve the performance further; however, it is still performing better than the main matrix material. Figure 23 (b) shows the CoF and wear rate behaviour of the composites as a function of the hBN concentration. Wear debris produced at higher levels of hBN incorporation includes agglomerates of hBN and the worn surfaces were covered with more pores. In addition, hexagonal boron nitride offers corrosion resistance and improved performance at elevated temperatures compared to other 2D additives such as graphene and molybdenum disulfide ($MoS_2$) due to its thermal stability. In contrast to the mechanical properties and the wear performance, corrosion resistance does not affect by the agglomeration of the hBN particles. In summary, the addition of hBN improves the properties and the performance of the main matrix both at room and elevated temperatures; however, the composite microstructures should be optimised for the desired mechanical properties, corrosion and wear resistance.

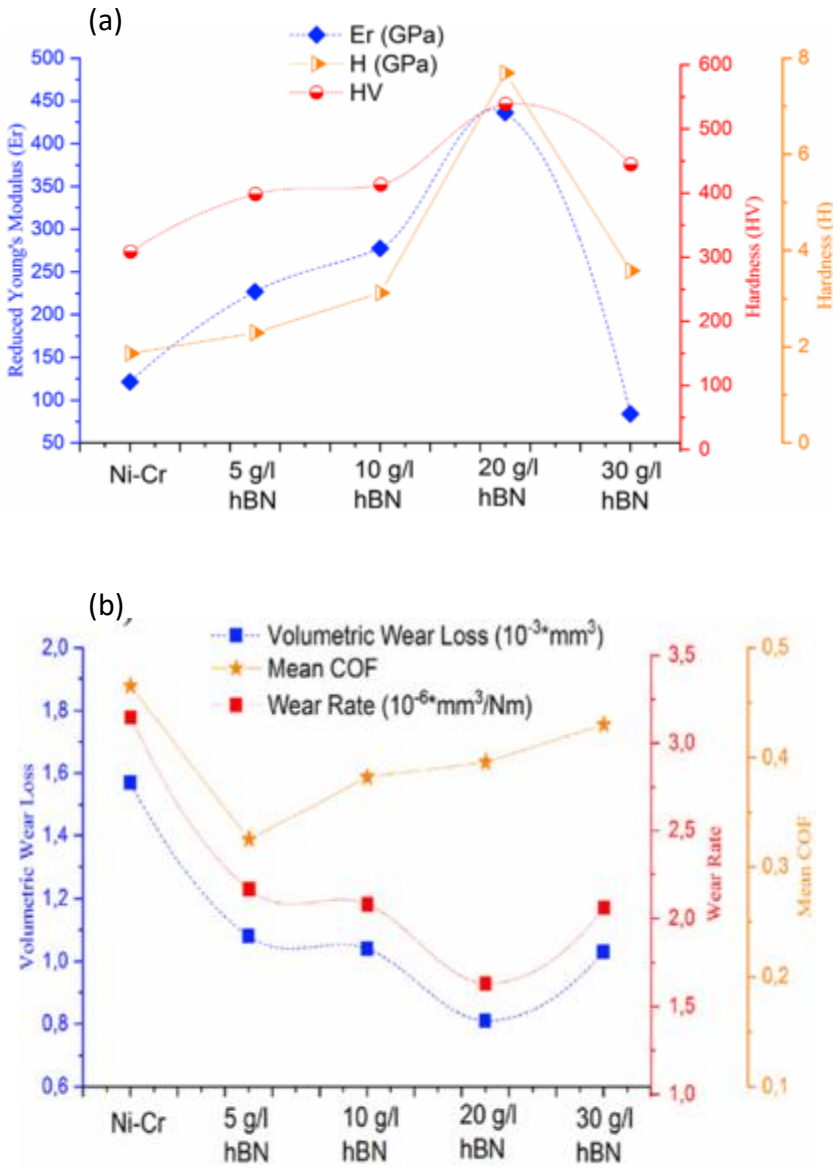


*Figure 23: Plots show elastic modulus, microhardness and nano hardness values (a) of pure Ni-Cr and different amounts of hBN incorporated Ni-Cr coatings and volumetric wear loss, mean CoF and wear rate for each sample (b)* [111].

## 2.3 Matrix

Two different main matrix compositions were chosen to carry out the objectives of this thesis. These compositions are WC-Co and MCrAlY. WC-Co was chosen for room temperature wear performance analysis. In aerospace industry, thermal sprayed WC-Co coatings are widely used to protect the surfaces from wear [120] due to outstanding mechanical properties such as, hardness, strength and wear resistance, [121,122]. WC-CrCo is also another popular material. However, as there was not any other work done on incorporation

of graphene into any WC-Co matrix and to prevent further complexity in the microstructure and the performance analysis, WC-Co was chosen over WC-CrCo.

Presence of carbon inside this composition prevents its usage at higher temperatures due to the decomposition of carbides. Hence, MCrAlY compositions were chosen for higher temperature applications. Thermal sprayed MCrAlY coatings are widely used in the applications where, high-temperature oxidation and corrosion resistance are required. M refers to a metal that can be Nickel, Cobalt or a combination of both [123–125].

### 2.3.1 WC-Co Thermal Spray Coatings

#### 2.3.1.1 Introduction

Thermal sprayed WC-Co composite coatings are extensively used in a wide range of industries such as the aerospace and power generation industry. WC-Co coatings are well known for their hardness, strength and wear resistance, so they are used for applications requiring sliding, rolling, fretting, abrasion and erosion resistance [121,122,126]. Impeller shafts, aircraft flap tracks, land-based turbine blades, pump housings and expansion joints are some of the specific areas coated with WC-Co to protect the surfaces without affecting the bulk mechanical properties of the materials [120]. Depending on the application, different carbide grains sizes (from nano to micro) and cobalt contents (e.g. WC-12Co, WC-15Co and WC-17Co) are used in the coatings. Plasma spray was the preferred thermal spray method used to deposit WC-Co coatings till the 1980s. However, HVOF thermal spray methods have become the popular option to deposit WC-Co cermet coatings nowadays. Plasma spray has high processing temperatures that led to decarburization of the WC phase and formation of the $W_2C$ phase. HVOF thermal spray methods have lower processing temperatures compared to plasma spray, and coatings deposited by HVOF thermal spray have a minimal $W_2C$ phase [120,127,128]. Although the $W_2C$ phase is harder than the WC phase, it is an undesirable phase due to its brittle nature, and lower wear resistance properties.

#### 2.3.1.2 Coating Microstructure

Thermal sprayed WC-Co coating microstructure mainly consisted of angular WC grains embedded in the cobalt binder matrix. In addition to the WC and cobalt phases, $W_2C$, W and $C_xW_yC_z$ phases can also be present inside the coating microstructure. WC grains cannot melt completely during the HVOF thermal spray process as a result of their high melting point.

However, the cobalt matrix melts, WC dissolves in the molten cobalt, and C releases from the system due to oxidation. As a result of this carbon loss during the deposition, $W_2C$, $C_xW_yC_z$ and W phases precipitates [129–132]. In addition, an amorphous and or nanocrystalline phase rich in the binder can also form due to the fast-cooling rates. The phases present in the microstructure are distinguishable in a backscattered electron (BSE) micrograph. The cobalt binder phase has a dark grey contrast. The light grey contrast represents the WC phase, and the contrast becomes lighter in the order of WC, $W_2C$ and W, as a result of the increased heavier tungsten content. In addition, the $W_2C$ phase has a dendritic morphology compared to the angular morphology of the WC phase, as the $W_2C$ is growing epitaxially on the WC surfaces [133,134]. Figure 24 shows a WC-Co coating microstructure with WC and $W_2C$ phases and shows their morphology. The microstructure of the deposited coatings is dependent on the feedstock, the type of the thermal spray and the spray parameters used. The size of carbide grains of the deposited coatings is directly proportional to the carbide grain sizes of the feedstock. Grain sizes can also influence the heating of the particles. Finer grains have a higher surface area to volume ratio; hence a higher rate of heating, decomposition and formation of undesirable phases can be obtained. In addition, feedstock powder size has an effect on the in-flight particle velocity and temperature during the deposition process. Finer particle size increases the in-flight particle temperature and velocity and creates a more uniform heat distribution. Therefore, denser and less porous coatings can be deposited. On the other hand, as a result of higher temperatures, the rate of oxidation, decomposition and decarburization increases, which can lead to the formation of more undesirable phases. Furthermore, cobalt content also affects the heating of the particles and hence decarburization. WC-Co coatings with higher cobalt contents can have fewer undesirable phases. The higher specific heat value of the cobalt is higher than the WC, therefore in-flight particle temperatures will be lower in a cobalt-rich mixture [135–139].

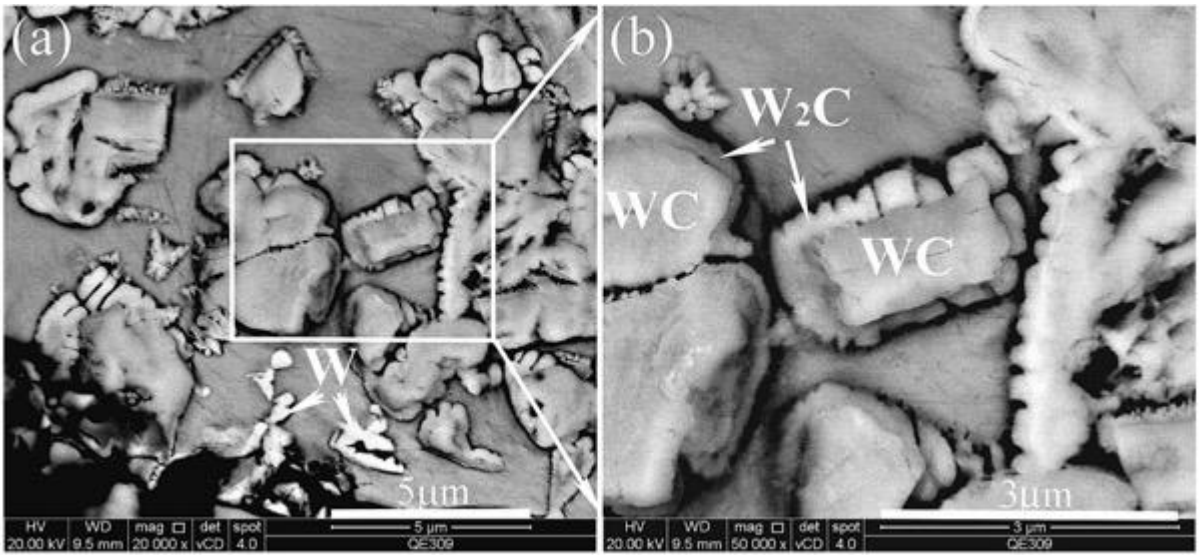


*Figure 24: Show a BSE micrograph of a WC-Co coating cross-section in low (a) and high (b) magnification. Angular WC phases and dendric $W_2C$ phases are labelled* [133].

### 2.3.1.3 Coating Mechanical Properties & Wear Performance

WC grains are responsible for the higher hardness and strength of the microstructure as cobalt is the relatively soft phase compared to the WC. However, cobalt has higher fracture toughness and flexural strength and keeps the WC grains together as a result of its excellent carbide wetting and adhesion properties. Cobalt content and the carbide grain size are the main contributors to the mechanical properties and hence the wear performance of the composite WC-Co system. Increasing the cobalt content of a WC-Co composite coating reduces the hardness and Young's modulus. On the other hand, both fracture toughness and flexural strength increase as cobalt is a ductile phase and has a higher energy absorption capacity compared to the WC grains [135–138]. However, WC-Co coatings with lower cobalt contents have higher wear resistance due to their higher hardness and young's modulus. WC-Co coatings with finer carbide grains have improved mechanical properties and wear performance compared to medium or coarse carbide grains [132,140–142]. Finer carbide grains lead to increased density of grain boundaries, more surface bonding with the binder and reduced binder mean free path due to increased surface area to volume ratio. These lead to an increase in fracture toughness and hardness for the WC-Co coatings as the carbide grain size decreases. Improved hardness and fracture toughness with finer carbide grains decrease the wear rate of the coatings. In addition, improved bonding with the cobalt binder matrix due to finer grains reduces the WC grains pull out and third body abrasive behaviour of these

grains which in turn reduces the wear rate. On the other hand, a few studies reported inconsistent results on the mechanical properties and the wear performance of the WC-Co coatings with extremely fine or nanostructured WC grains. As mentioned in the previous section, finer grain size can promote decomposition and the formation of undesirable phases. Hardness and fracture toughness reduction is reported due to a higher rate of decomposition and formation of the $W_2C$ phase which is more brittle (lower fracture toughness). The wear performance of these coatings is varying depending on the testing condition and the type of wear mechanism. The wear rate can still be lower if the mechanism is depending on WC grains pull-out and acting as an abrasive particle. Finer grains are still providing better bonding with the cobalt binder matrix. However, if the mechanism is dependent on the hardness and fracture toughness of the coatings, degraded mechanical properties of WC-Co coatings with finer grains increase the wear rates [130,131,140,141,143–145].

## 2.3.2 MCrAlY Thermal Spray Coatings

### 2.3.2.1 Introduction

MCrAlY coatings are used for the components that are exposed to high temperatures in both aero-jet propulsion and land-based power generation engines. M refers to a metal that can be Nickel, Cobalt or a combination of both [123–125]. Engine components exposed to elevated temperatures are usually made up of Nickel-based superalloy due to the outstanding properties and performance of the nickel alloys at elevated temperatures. However, these alloys are prone to oxidation and high-temperature corrosion. Therefore, MCrAlY coatings are applied to the components due to their oxidation and corrosion resistance properties. When MCrAlY coatings are exposed to elevated temperatures in the air atmosphere, a thermally grown oxide (TGO) layer forms due to the outward or inward diffusion of metal or oxygen ions respectively. Alumina ($Al_2O_3$) and chromia ($Cr_2O_3$) are the main oxide layers that form on metal surfaces. However, the formation of chromia is not desirable as chromia can volatilise at temperatures above 1000°C. In addition, chromia has a fast growth rate which can cause residual stresses and failure of the coating. Therefore, aluminium in the MCrAlY coating composition is used for the formation of the continuous oxide layer on the coating top surface. The formation of Alumina improves the corrosion resistance of the coatings, and alumina is thermally stable and acts as a protective layer [123,146]. Nickel and cobalt compositions present inside the MCrAlY coating help with the

adaptation of the coating to the properties of base nickel superalloy, control the activity of aluminium and hold the oxide layer in place [146]. MCrAlY coatings can be deposited via various thermal spray techniques, including air plasma spray, low-pressure plasma spray, vacuum plasma spray, high-velocity oxy-fuel (HVOF) thermal spray, and cold spray. However, HVOF thermal spray is favourable over plasma spray for MCrAlY coating deposition due to higher bond strength, fewer defects, and oxide content [147–151]. NiCoCrAlY coating compositions usually have higher oxidation and corrosion resistance than the NiCrAlY and CoCrAlY compositions. Furthermore, CoCrAlY composition is also used for cobalt-based superalloys to improve sulphur corrosion resistance [147,152].

#### 2.3.2.2 Coating Microstructure

MCrAlY coatings have the conventional lamellar microstructure and splat like morphology of the thermal spray coatings. Phases present in the coating microstructure are strongly dependent on the spray parameters and the microstructure of the feedstock powder. Figure 25 shows a BSE micrograph of a conventional NiCrAlY coating cross-section deposited by HVOF thermal spray. Figure 26 shows both cross-section and top surface SEM micrographs of NiCoCrAlY coating deposited via high-velocity air fuel (HVAF) thermal spray. Both NiCoCrAlY and NiCrAlY coatings have same the microstructure. The microstructure consists of two main phases [153–158]. Light grey contrast represents either ductile $\gamma$-Ni (rich in Ni, Cr and or Co depending on the feedstock composition) and/or $\gamma'$ -Ni ($Ni_3Al$) phases. Dark grey contrast represents another nickel phase referred to as the brittle $\beta$ – NiAl phase which is rich in aluminium. $\beta$ phase is acting as an aluminium supply and offers oxidation resistance while $\gamma$ / $\gamma'$ phases improve the ductility [159]. The microstructure of the CoCrAlY coating is slightly different from the other two. This light grey contrast represents $\gamma$-Co (rich in Co and Cr) and or $\gamma'$ -Co($Co_4Al_{13}$) phases. Dark grey contrast represents the $\beta$ – CoAl phase (rich in Al) [147]. In addition, oxide phases can be formed by oxidation of the metal particles, either in the flame or after the splat formation on the surface. The formation of oxides is dependent on the thermal spray parameters and the microstructure of the powder feedstock used. Oxide phases are dark contrast stringers, which suggests inter splat oxide formation [153,160,161]. Oxides formed during the thermal spray and after heat treatments are usually (Cr, Ni)O, $Al_2O_3$, $Cr_2O_3$ and spinel oxides of (Co, Ni)(Cr, Al)$_2O_4$. The presence of cobalt, nickel or both in the spinel oxides is dependent on the MCrAlY powder feedstock composition. However, the

formation of spinel oxides can be detrimental to the coatings' operation life. The fast rate of growth of the oxides can create residual stresses in the coating which can lead to failure.

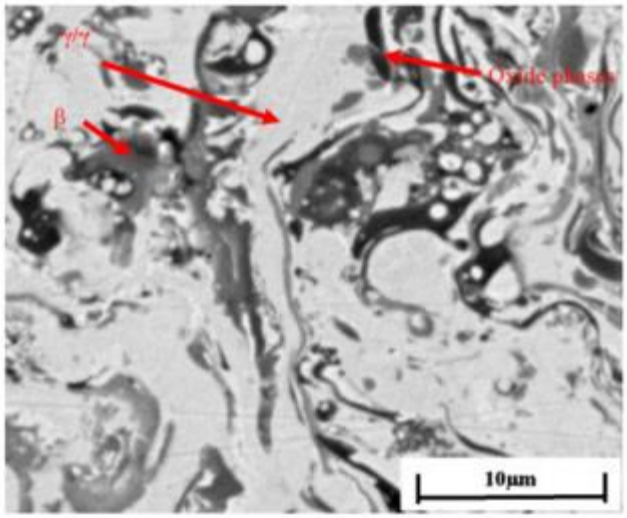


*Figure 25: Shows a BSE micrograph of a NiCrAlY thermal spray coating microstructure*[153].

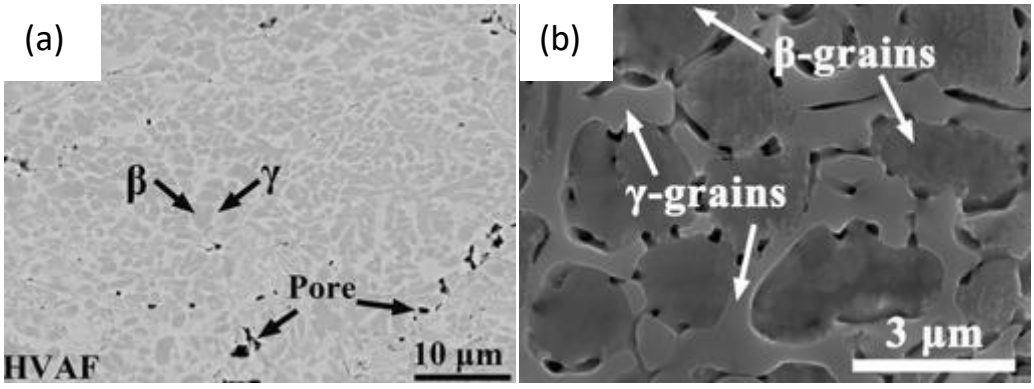


*Figure 26: Shows cross-section and top surface SEM micrographs of a NiCoCrAlY coating deposited by high-velocity air fuel (HVAF) thermal spray* [162].

The microstructure of the CoCrAlY coating is slightly different from the other two, which is shown in Figure 27. This light grey contrast represents $\gamma$-Co (rich in Co and Cr) and or $\gamma'$ - Co($Co_4Al_{13}$) phases. Dark grey contrast represents the $\beta$ – CoAl phase (rich in Al) [147]. In addition, oxide phases can be formed by oxidation of the metal particles, either in the flame or after the splat formation on the surface. The formation of oxides is dependent on the thermal spray parameters and the microstructure of the powder feedstock used. Oxide phases are dark contrast stringers, which suggests inter splat oxide formation [153,163,164]. Oxides formed during the thermal spray and after heat treatments are usually (Cr, Ni)O, $Al_2O_3$, $Cr_2O_3$ and spinel oxides of (Co, Ni)$(Cr, Al)_2O_4$. The presence of cobalt, nickel or both in the

spinel oxides is dependent on the MCrAlY powder feedstock composition. However, the formation of spinel oxides can be detrimental to the coatings' operation life. The fast rate of growth of the oxides can create residual stresses in the coating which can lead to failure.

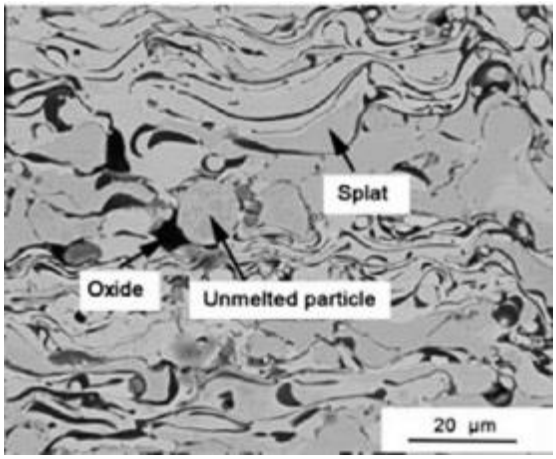


*Figure 27: BSE micrograph showing the CoCrAlY coating cross-section deposited by HVOF thermal spray* [147].

## 2.4 Summary & Gaps in the Literature

Friction and wear are the main contributors to the surface deformation of components. Surface deformation leads to reduced life span and increased downtime, hence increased cost and energy for remanufacturing. Application of coatings on the surface from microns to millimetres is a common tribological solution for surface protection. Thermal spray is a cost-effective, fast and reliable coating deposition method widely used in the industry. Dense, thick and different superior coating microstructures can be deposited for a wide range of applications via thermal spray. Ceramic and metal-based oxidation, corrosion and wear-resistant coatings such WC-Co and MCrAlY form the biggest market for the thermal spray industry at the moment. The powder is the conventional form of feedstock used in thermal spray. However, it limits the type and size of feedstock materials that can be used. The current developments in the thermal spray industry, such as suspension and hybrid thermal spray techniques, open the door to deposit new coating compositions and the ability to tailor conventional coating microstructures. The microstructure hence the properties and the performance of the conventional thermal sprayed coatings can be tailored by using suspension feedstock which is made up of smaller particles compared to the conventional powder. In addition, the suspension allows the sub-micron sized particles such as graphene

and hexagonal boron nitride to be used as a feedstock which was not possible before. The ability to use new materials and alter the microstructures via hybrid suspension and solution thermal spray requires further detailed studies to investigate the possible new coating microstructures, properties and performances.

Graphene became an area of interest after its invention as a result of its outstanding properties. The addition of graphene into a system improves the properties and the wear performance once the concentration of the graphene is optimised. Graphene was studied extensively as a solid lubricant and an additive during composite manufacturing. However, the thermal spray technique was not studied in detail as a graphene deposition and incorporation technique; hence requires further studies. Graphene was extensively studied as an additive to improve the performance of composites. However, GNP films alone have not been studied in detail. The real fundamental mechanism behind the improved wear performance of GNP incorporated coatings was not present in the literature yet. Different mechanisms were suggested for improved wear performance. Some studies reported the formation of GNP tribofilms, while others claimed the improvements were obtained due to improved mechanical properties. A few studies also to claim that the improvements were obtained as a combination of both tribofilm formation and enhanced mechanical properties. Studying GNP films alone can help the community to understand this mechanism, how the GNPs behave under the load and the reasons for failure. Once all the mechanisms and reasons for failure are understood, GNP incorporated coatings can also be engineered accordingly for improved performance. Although GNPs were added to various metal and ceramic matrices, there was not a study performed on WC-Co so far. WC-Co is the conventional wear-resistant coating used in many engineering applications. Therefore, a study of GNP incorporation into a WC-Co system and analysing the wear performance will contribute to the community.

Similar to graphene, hBN is also extensively used as a solid lubricant and as an additive for improved wear performance of composites for higher temperature applications. hBN has similar structure and properties to graphene and has better high-temperature properties than graphene. In addition to self-lubricative ability, thermal stability and conductivity of the hBN allow the dissipation of heat energy from the tribological contacts. Studies showed improved hBN addition improves the mechanical properties, and reduces the coefficient of friction and wear rate once the hBN concentration was optimised for the desired application.

Advances in thermal spray technology allow usage of hBN for coating deposition. So far, hBN was used to improve the performance of the wear-resistant coatings such as MCrAlY + CrC, but not used to convert an oxidation-resistant coating (MCrAlY) into a wear-resistant coating.

# Chapter 3: Experimental Methods

This chapter covers the methods used throughout this work. The working principle and theories behind the methods are covered here. More detailed explanation about the specific parameters, measurements and materials used are given in the experimental section of each chapter individually.

## 3.1 Coating Deposition

Coatings are deposited on the AISI 304 stainless steel (SS) substrates with a nominal composition of Fe-19.0Cr-9.3Ni-0.05C (all in wt. %), which have dimensions of 60 x 25 x 2 mm. Substrate surfaces were grit blasted with a blast cleaner from Guyson (Dudley, United Kingdom) with F100 brown aluminium oxide particles (0.125-0.149 mm). Prior to thermal spray, the substrate surfaces were cleaned with industrial methylated spirit (IMS) and compressed air. The prepared suspensions for thermals spray was stirred by using a FB-505 Ultrasonic Processor (Fischer scientific, United Kingdom). Substrates were attached to a rotating carousel with a diameter of 260 mm. The carousel rotates with a speed of 73 rpm during the spray runs which gives rise to a 1 m/s linear velocity for the attached substrates. In the meantime, the spray gun moves vertically with a traverse speed of 5 mm/s, which leads to a 4 mm overlap between tracks from subsequent passes. Two different thermal spray guns were used in this work. TopGun (GTV, Luckenbach - Germany) operates with hydrogen and suspension feedstocks can be used. Feedstock materials are injected axially into the combustion chamber in this setup. On the other hand, the Metjet IV (Metallisation, Dudley – United Kingdom) system operates with kerosene and the powder feedstock radially injected into the exit of the combustion chamber. Figure 28 shows the thermal spray guns and the setup used in this work.

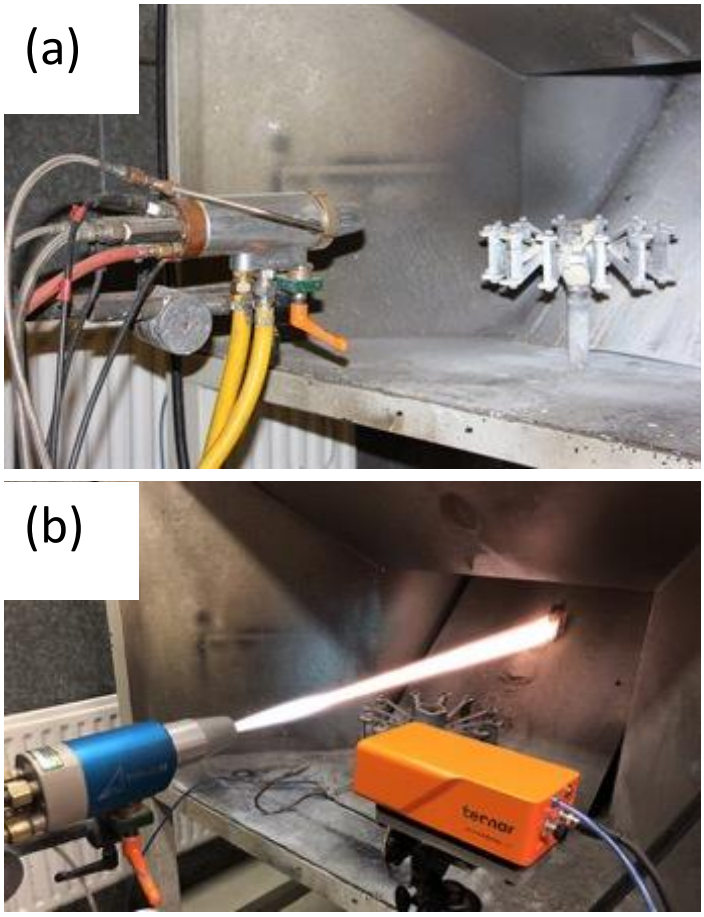


*Figure 28: Thermal spray setups used in this work. MetJet IV (a) and GTV TopGun (b).*

## 3.2 Material Characterisation

### 3.2.1 X-Ray Diffraction (XRD)

XRD is a non-destructive characterisation technique used to identify the materials and their crystalline structures. Monochromatic X-rays are directed towards the samples and X-rays are diffracted in different directions with various intensities and diffraction angles as a results of interactions with the atoms of the sample. These diffracted waves can be destructive and cancel each other out. On the other hand, some of them are constructive according to Bragg's law of diffraction which creates the peaks in the XRD diffractogram. Bragg's law of diffraction is explained by the following equation and the schematic of the diffraction mechanism can be seen in Figure 29;

$$2dsin\theta = n\,\lambda$$

Where d is the lattice spacing, $\theta$ is the angle of diffraction and $\lambda$ is the X-ray wavelength and *n* is an integer, referred to as the order of diffraction, and is often unity. The obtained peaks

in an XRD diffractogram are matched against a database of various diffraction patterns for phase identification.

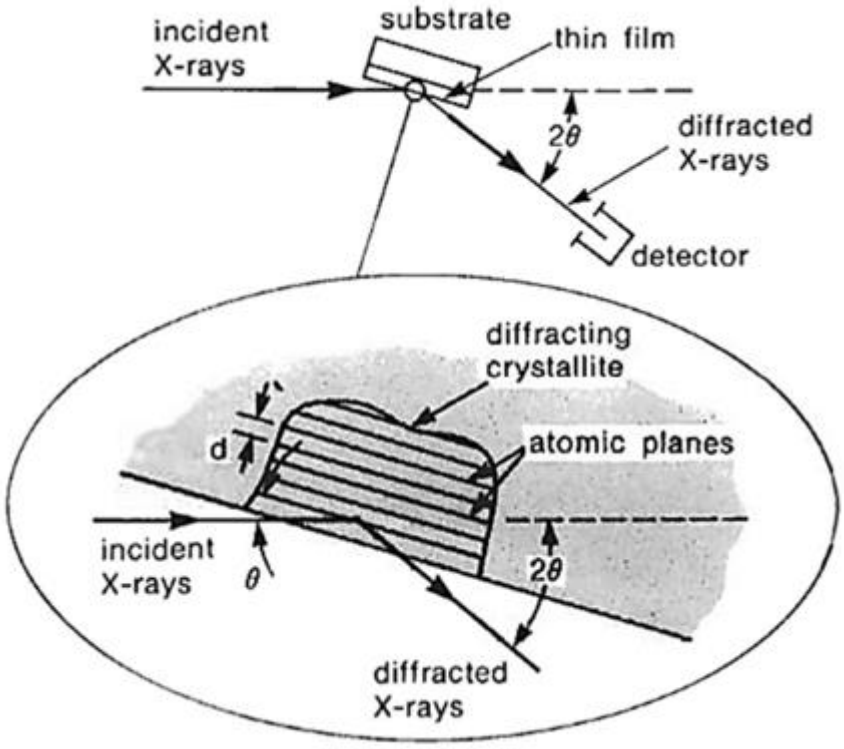


*Figure 29: A schematic diagram of X-ray diffraction according to the Braggs law of diffraction* [165].

### 3.2.2 Scanning Electron Microscopy (SEM)

Scanning electron microscopy is a high-resolution imaging technique which uses the kinetic energy of the electrons (1 to 50 keV) to scan the surface of interest. An electron source and electromagnetic lenses are used to create a dense beam of electrons that are directed towards the specimen. The interaction of the electron beam with the atoms of the specimen produces signals. These signals are collected via various detectors to produce two different micrographs, which show surface topography and compositional information. Figure 30 shows the interaction volume created between the electron beam and the specimen, during the SEM. Secondary electron (SE) micrographs are produced by the signals generated from the inelastic scattering of the electrons. As a result of inelastic scattering, these electrons have lower energy and can only escape from the top surface of the specimen. Therefore, SE micrographs are preferred for surface topography analysis [166]. Backscattered electron (BSE) micrographs are produced by the signals generated from the reflected electrons via elastics scattering. These electrons have higher energy and can emerge from deeper parts of

the specimen. In addition, heavier materials have bigger atomic structures hence more electrons can be reflected elastically and more signals generated. Therefore, heavier elements appear brighter in the BSE micrographs compared to lighter elements. BSE micrographs are used to differentiate between the different phases and compositional information [166].

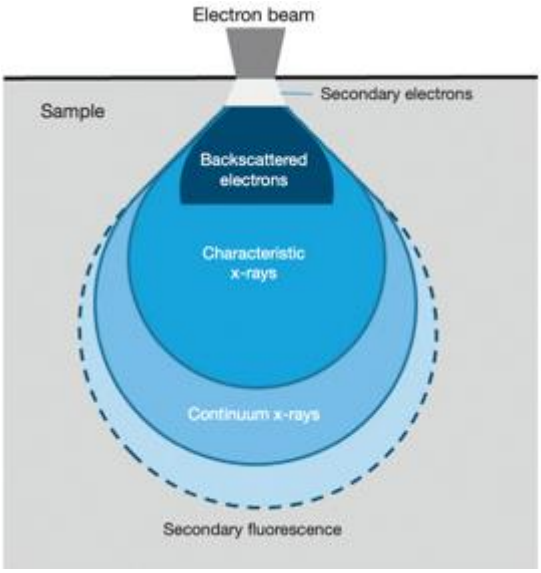


*Figure 30: Interaction volume between the beam and the sample with approximate areas where backscattered and secondary electrons can be generated* [167].

### 3.2.3 Energy Dispersive X-Ray Spectroscopy (EDXS)

Energy-dispersive X-ray analysis is used to qualitatively identify the presence of elements and quantitatively define the concentration of the elements in the specimen. Figure 31 shows a schematic diagram which represents the working principle of the EDX analysis. The interactions between the electron beam and the specimen knock off the electrons from the shells. This creates an unstable atomic structure, and electrons from higher energy levels move to lower energy levels to fill the space left behind. During this movement, the difference in energy is released in the form of X-rays.

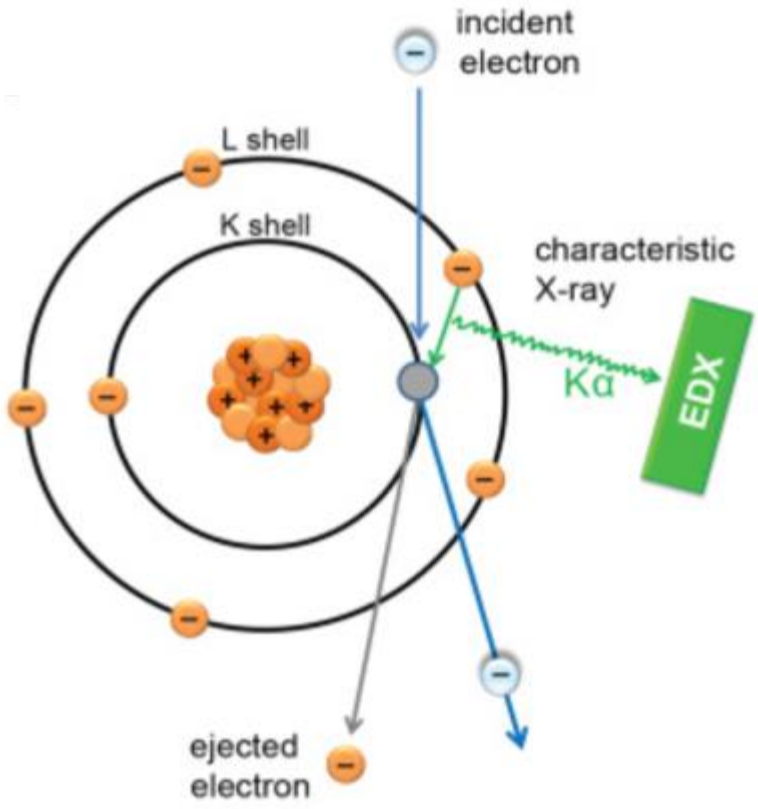


*Figure 31: The schematic showing the principle of operation of the EDX* [168].

### 3.2.4 Transmission Electron Microscopy (TEM)

TEM is a microscopy technique that is very similar to SEM. An incident electron beam is used to interact with a very thin (less than 100 nm or a suspension on a grid) sample and the transmitted electrons are used for imaging. Different objective apertures are used to obtain various images of the specimen, knows as bright field (BF) or dark field (DF) image. For bright film image, only non-deflected incident beam was allowed to pass through the aperture, while for the dark field image only diffracted beams were allowed to pass. Contrast of the BF image can be used to determine the thickness hence the weight of the sample as the heavier areas scatter the electrons with bigger angles, they appear darker. In addition, diffraction patterns can be generated by using the right objective apertures as the incident beam of electrons undergoes to Bragg's scattering (explained above). Single crystalline samples appears as a pattern of dots while polycrystalline and amorphous samples appear as a set of rings.

### 3.2.5 Raman Spectroscopy

Raman spectroscopy is a light (photon) scattering method used to measure the vibrational energy of the molecules. When the photon interacts with the molecule, the molecule moves to a virtual higher energy state as a result of energy transfer between the incident photon and the molecule. The virtual energy state is not stable so photons are re-emitted to release the energy. Usually the incident and the emitted photon have the same energy which is known as the Rayleigh scattering. When the molecule gains or lost energy during the process, the wavelength of the scattered photons changes. This is referred to as Raman scattering. Figure 32 shows a schematic description of Rayleigh scattering and Raman scattering.

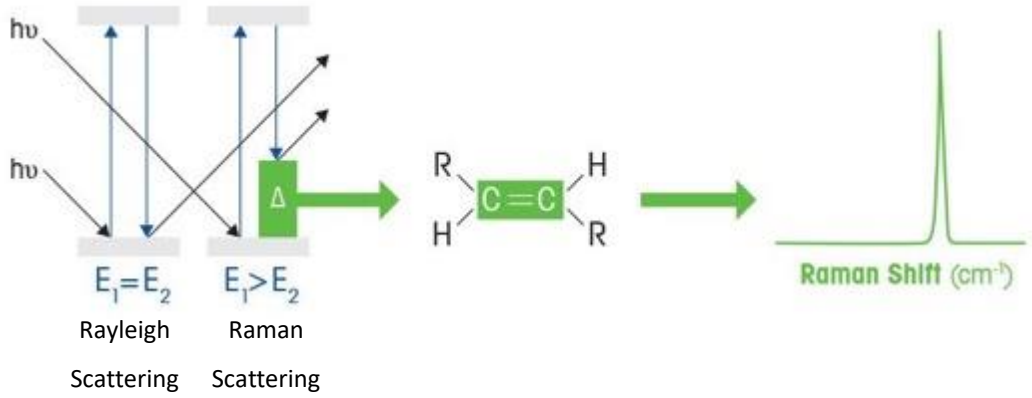


*Figure 32: Schematic explanation of Rayleigh scattering, Raman scattering and the detection of the molecule via Raman shifts* [169].

### 3.2.6 Surface Profilometry

A stylus profilometer was used to measure the 2D vertical displacements over the specimen surface via an inductive (LVDT) gauge. A diamond stylus tip with a radius of 2µm was moved over the surface at a speed of 0.25 mm/s. Surface roughness (Ra) values are measured from the transverse 2D line profiles via Mountains Map software. In addition, the depth of the wear tracks is measured from the line profiles, which are converted into the specific wear rate values. Detailed explanations about how to obtain specific wear rate values from the wear track depth are given in the following chapters.

## 3.3 Mechanical Properties Testing

### 3.3.1 Microhardness

A Vickers indenter was used to measure the microhardness of the coatings. The indenter has a diamond-shaped tip with a 136° angle and creates pyramidal indents on the surface of interest as a result of the plastic flow of material. A schematic representation of the indenter and the indents created on the specimen are given in Figure 33. The Microhardness of the specimen is calculated using the geometry of the indenter, indent and the applied load. The following equation was used, where HV is Vickers hardness, P is the indentation load in grams and d is the diameter length in mm [170];

$$HV = \frac{2Psin(\frac{136}{2})}{d^2}$$

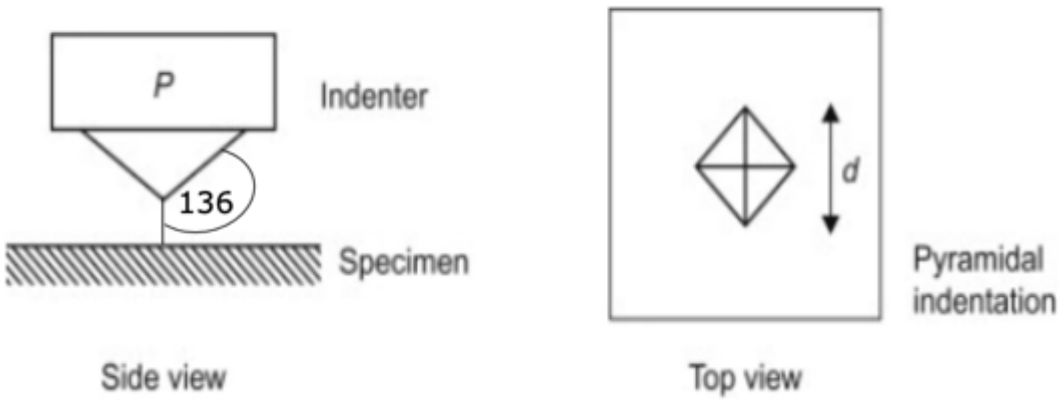


*Figure 33: Schematic representation of the indenter used in this work and the shape of indents created on the specimen* [171].

### 3.3.2 Fracture Toughness

The indentation method described above was used for fracture toughness measurements as well. Loading was increased till the indent obtains cracks at the edges parallel to the coating cross-section, as shown in Figure 34. During the loading, cracks are initiated at the surface (radial crack) or inside the material (median crack) and grow into full size (half penny) during the unloading phase as a result of the mismatch between the outer elastic zone and the inner, rigid plastic zone [172]. For this crack growth model (Palmqvist) to

be valid, the ratio between the length of crack from the centre of the indent and the half diagonal length (c/a) must be in the range of 0.6 to 5. If this criterion is valid, the following equation is used to calculate the fracture toughness;

$$K_{IC} = 0.079(\frac{P}{a^{(3/2)}})\log(\frac{4.5a}{c})$$

Where $K_{IC}$ is fracture toughness in $MPa.m^{0.5}$, P is the loading in N, a is the half indentation diagonal length in m, and c is the length of crack from the indent centre in m.

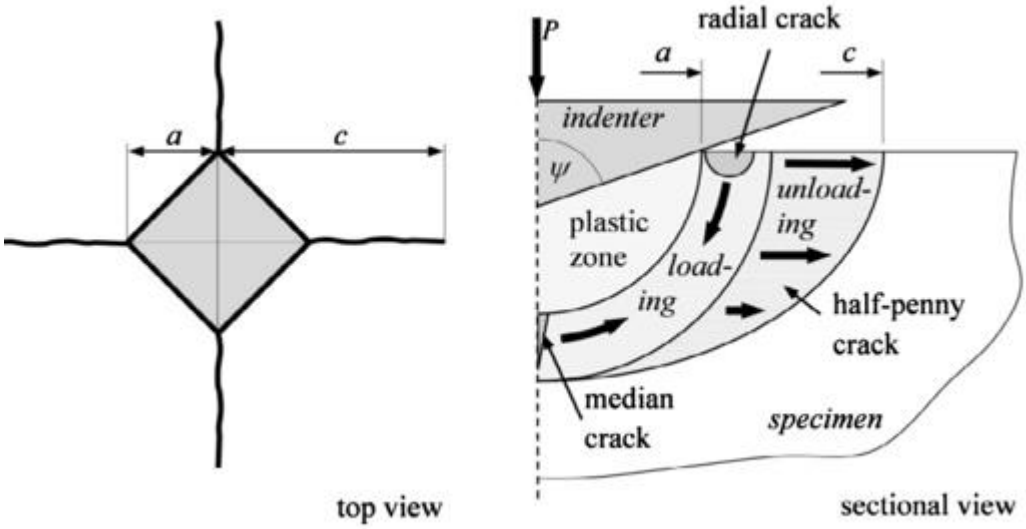


*Figure 34: A schematic showing the indent used for fracture toughness calculations and the palmqvist crack growth model* [172].

## 3.4 Wear Testing

### 3.4.1 Room Temperature Sliding Wear Test

A ball on a disc rotatory tribometer was used for dry sliding room temperature wear tests. The sample was attached to a rotating shaft while the counter body was fixed with rectangular jaws. The load is directly applied on top of the counter body. The equipment has a friction force sensor to measure the real-time coefficient of friction between the surfaces in contact. Figure 35 shows a 3D schematic of the room temperature tribometer and a magnified schematic representing the rotational sliding contact between the sample and the counter surface.

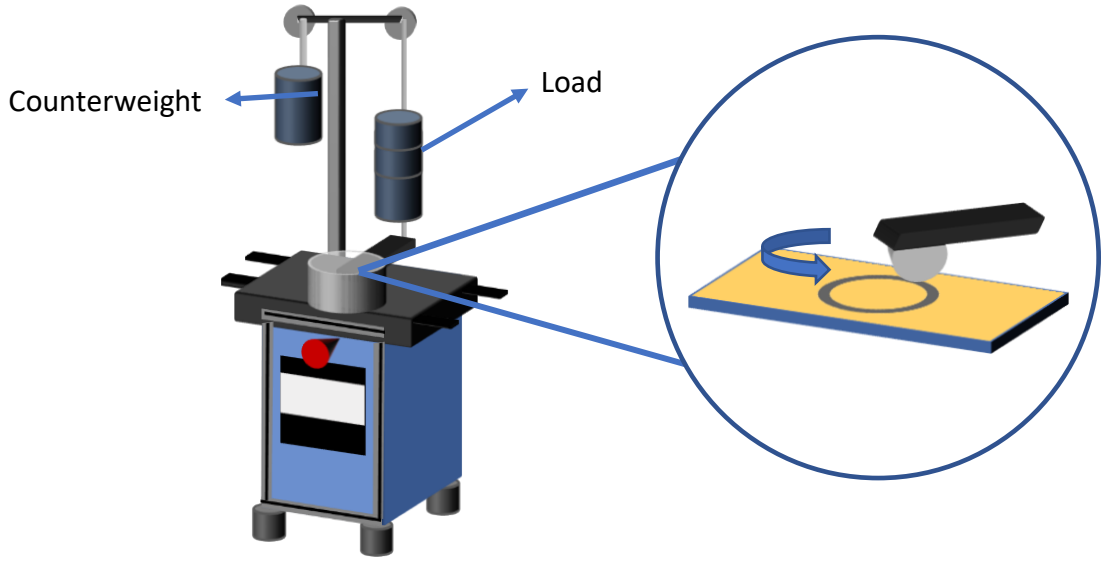


*Figure 35: 3D schematic of room temperature  tribometer*

### 3.4.2 High-Temperature Sliding Wear Test

A tribometer with a built-in furnace was used for the high-temperature wear tests. The tribometer has a ball on disc arrangement and dry sliding wear tests were performed. The sample was attached to a rotating shaft while the counter body was attached to a stationary lever arm. The load was applied to the other end of the lever arm. Thermocouples were used inside the furnace to check the temperature of the test atmosphere.

Figure 36 shows the setup inside the built-in furnace of the high-temperature tribometer. Furthermore, the equipment has a friction force sensor and LVDT sensor to measure the coefficient of friction and the vertical displacement of the lever arm, respectively. Figure 37 shows the lever arm, sensor and the loading part of the high-temperature tribometer which is outside of the built-in furnace.

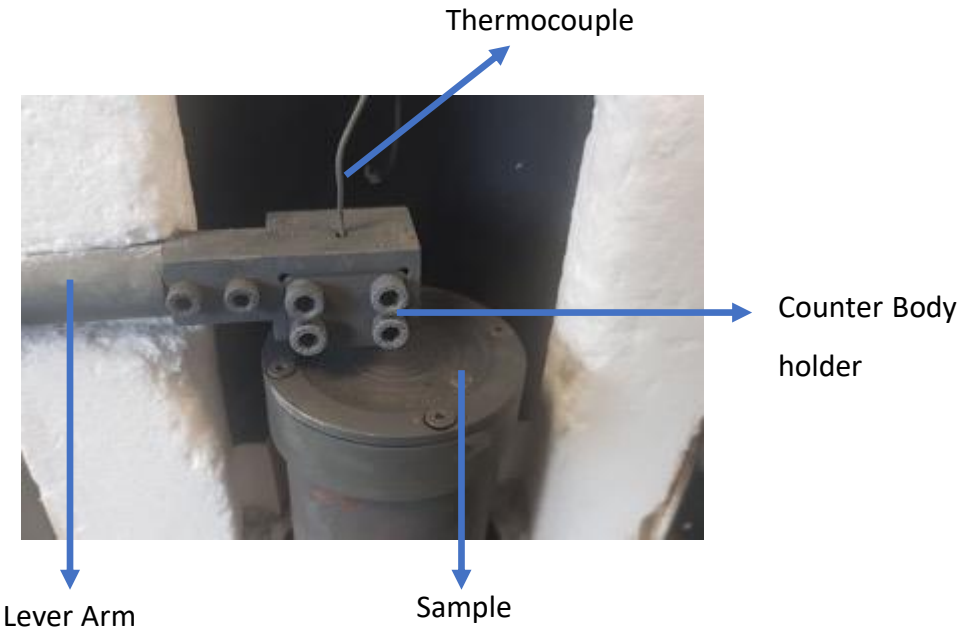


*Figure 36: Inside of the built-in furnace of high-temperature tribometer.*

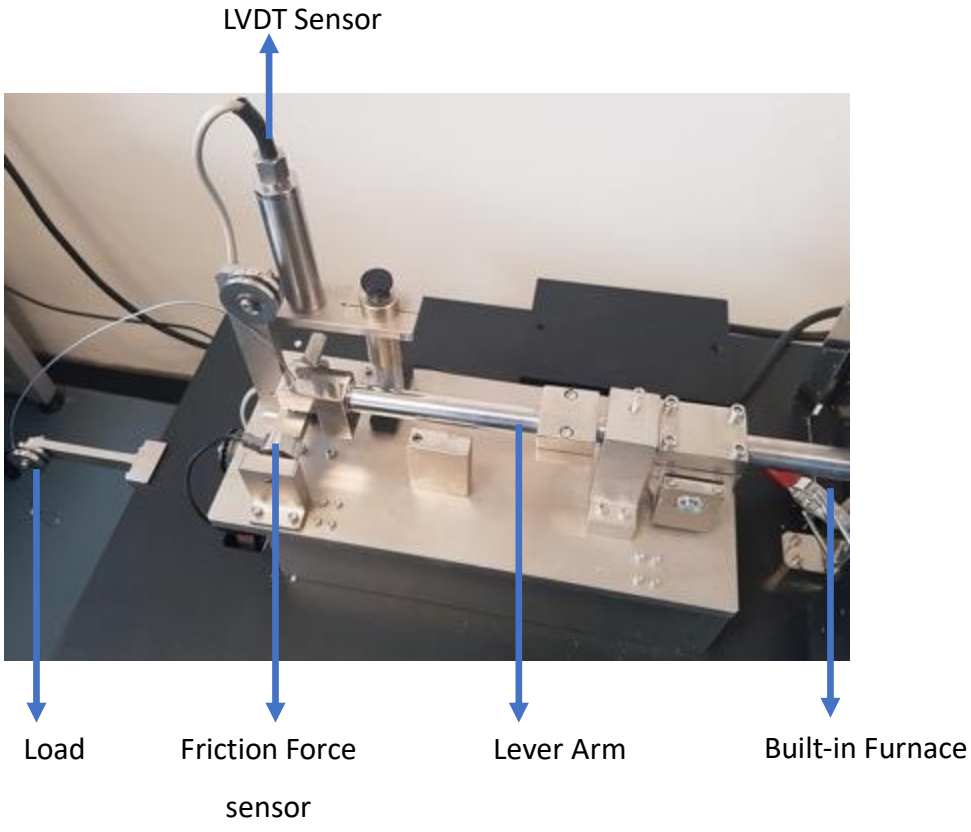


*Figure 37: Outside of the built-in furnace on the high-temperature tribometer.*

# Chapter 4: Structural Changes of thermal sprayed graphene nano platelets film into amorphous carbon under sliding wear

Publication number = Applied Surface Science 528 (2020) 146315

## 4.1 Abstract

Graphene has become a promising candidate to protect surfaces against friction due to its strength and lubricating ability. In this study, graphene nano platelets (GNP) thin films have been deposited onto stainless steel substrates by axially injecting GNP suspension through high velocity oxy fuel thermal spray gun. The tribological performance of the films under dry sliding wear was investigated through unlubricated ball on disc sliding wear test against a sintered alumina counter body ball under 5 N load. The understanding of the behaviour of the GNPs under sliding wear will be useful for improving the performance of graphene-based coatings which are in demand for wear resistant applications. A film was deposited showing significant improvements in friction with coefficient of friction value reduced by 7 times compared to uncoated stainless steel, even for a discontinuous film. A morphological analysis shows sliding wear led to change in particle shape from angular flakes into randomly oriented circles. Interatomic bonding and structural analysis performed reveals oxidation defect formations during wear test. Structural degradation and oxidation of GNPs during the process led to formation of amorphous carbon from graphene. Amorphous carbon formation reduces the lubricating ability and strength of the film, leading to failure.

**Keywords**: Thermal spray; SHVOF; Graphene nanoplatelets; Wear; Nanoparticles; Tribology

## 4.2 Introduction

Graphene is an allotrope of carbon atoms characterized by a 2D network of $sp^2$ hybridised carbon atoms bonded to each other in a hexagonal lattice. Graphene is also the basic structural unit of carbon nanotubes (CNT), graphite and fullerenes. From chemistry point of view, the term graphene is used to refer to a single layer only and particles with more than one layer are known as graphite. However, many researchers use graphene containing names such as graphene nano-platelets (GNPs) or multilayer graphene (MLG) to define a few layers (usually up to 20) of graphene according to the convention in their respective field. Stacks of more than more than 20 layers are usually referred as thick graphene sheets [50].

Graphene is known as the strongest material discovered so far and that is why it attracted the interest of surface engineers. Studies performed on elastic properties and intrinsic strength of pristine graphene via atomistic simulations and atomic force microscopy (AFM) showed that the in plane Young's modulus is ≈ 1 TPa and the tensile strength value is higher than 100 GPa [54,173,174]. Depending on the production method of graphene, it can be polycrystalline and have grain boundaries which might lead to weakness compared to pristine graphene. A study performed on chemical vapour deposition (CVD) grown graphene shows that the elastic stiffness is the same as pristine graphene and strength is only reduced by approximately 20 GPa [175]. Also, graphene has good thermal conductivity and electrical conductivity. Molecular dynamic simulations, Raman spectroscopy and thermal conductivity measurements performed on graphene in different studies led to a broad range of values from 1000 to 5000 W/mK [176–178]. Assumptions about the absorbance of graphene and dimension of the samples used during the studies are the main factors that yield this broad range of values. The electrical conductivity of graphene also depends on the shape of samples tested and the packing density. According to studies performed on graphene compacted into various shapes and with different pressure electrical conductivity varies from ≈ 100 S/m to ≈ 1000 S/m [179,180]. In addition, graphene has lubrication ability, enhanced surface properties and chemical inertness due to its low reactivity once dangling bonds are passivated. Outstanding properties of GNPs mentioned above made them a promising reinforcement material for composite manufacturing. After their discovery, GNPs have been added to metal, ceramic, cermet (metal & ceramic) and polymer matrices via various manufacturing methods to improve the mechanical properties of the matrix material. Hardness, yield strength and ultimate tensile strength are a few of the improved mechanical properties reported due to the addition of GNPs. Range of improvements in mechanical properties are varied form 20% to even more than 100% depending on the concentration of the GNPs [69–74,86,87,91].

GNP strength, shearing ability and chemical inertness also give rise to enhanced wear resistance in addition to improved mechanical properties of composites. Mechanical failure due to wear and generation of friction are the most common form of failure in moving and rotating parts. Hence, wear resistance and tribology properties have high importance for composites used in moving parts. Incorporation of GNPs into ceramic and metal matrices

improve the wear resistance via combination of two different mechanisms. Improved wear performance has been linked to both improvements in fracture toughness and hardness, and formation of protective tribofilms due to the exfoliation of GNPs. A major contributor mechanism to the improved wear resistance has not been identified yet; some studies reported fracture toughness as the main contributor while other studies did not. Two different studies investigate the tribological performance of alumina / GNP composites via unlubricated ball on disc tests and wear resistance improved by two order of magnitude at 10N load against alumina counter-body [90] and one order of magnitude at 25N against tungsten carbide counter-body [98]. According to the first study, the main reason behind the improved wear performance is the improved localised mechanical properties and fracture toughness rather than a tribofilm formation. Silicon nitride is another ceramic which was investigated in both lubricated (isooctane) and unlubricated conditions. Wear performance of SiN / GNP composites against a silicon nitride counter-body in the presence of isooctane shows that the wear resistance was increased. It has been also reported that due to the exfoliation of GNPs a protective tribofilm was produced [96]. Wear performance of silicon nitride in unlubricated conditions also shows improvements in wear resistance by 5.5 times against an alumina counter surface and by 8.5 times against borosilicate counter surface [101]. In a study performed on wear performance of alumina / GNP composite at 40 N load against a ceramic counter-body, Archard wear equation was used to calculate the theoretical wear loss and hence wear rate. The Archard wear equation relates the volume worn per unit sliding distance to the normal load and the hardness of the softer surface [181]. Theoretical results showed a 21.7 % increase in wear resistance as a result of hardness. However, experimental results showed an increase around 65 % [100]. The formation of a tribofilm was also observed during the test and this is reported to be the dominant mechanism for improved wear resistance in this case. Improvements in wear resistance for the metal matrix were also obtained. Incorporation of GNPs into a magnesium matrix lead 40 % and 60 % reduction in depth and width of the wear track respectively compared to pure magnesium. GNP particles were pulled out during the test and acted as a solid lubricant [75].

GNP incorporated composites have been studied extensively, however, wear or tribological performance of GNP films alone have not been studied in detail, which might help to understand the mechanisms responsible for improved wear properties in composites.

Atomic force microscopy (AFM) and friction force microscopy (FFM), micro tribometer and micro stracth test methods were used to investigate the tribological performance of graphene at the nano and micro scale level [55,182–188]. Test were performed on either single or few layers of deposited or grown graphene films for applications in electronic devices mostly and analysis was carried out in atomic scale. However, macro scale tribological performance was not investigated in detail where a bulk amount of graphene film subjected to larger loads (in Newtons, N instead of mN) over a bigger contact area than a FFM or AFM tip. There are a few studies involving graphene spread over a surface contact area, as a solid lubricant in which bonding between surface and graphene was not aimed. Although there was not any mechanical or chemical bonding between the graphene and the applied surface, results showed promising improvements in coefficient of friction (down to around 0.2) and wear performance [189,190]. In recent studies, GNP films were deposited using a thermal spray flame to achieve a film on the surface, which again led to a reduction in coefficient of friction down to 0.1 as a result of a GNP tribofilm formation [32,191].

In this study a pure GNP film was produced by using suspension high velocity oxy fuel (S-HVOF) thermal spray technique. S-HVOF is a modified version of HVOF thermal spray which requires the use of liquid suspension feedstock instead of powder. Suspension feedstock allows the usage of nano and sub-micron sized particles to be sprayed through HVOF thermal spray system and is a promising technique to form films with tailored microstructures. HVOF thermal spray technique is widely used in industry, as it leads to the production of coatings with lower porosity, higher bonding strength and hardness in shorter period of time. It is a fast and effective method to deposit GNPs over extended surfaces. Potential usage of the deposited film as a protective layer against wear is discussed by analysing sliding wear test results and structural changes of graphene throughout the test. Once all the mechanisms responsible for failure and the main reason for improved tribological performance are understood, GNPs can be engineered to improve the service life or performance of GNP films and GNP incorporated composites.

## *4.3* Experimental

### 4.3.1 Feedstock Preparation

GNP suspension in deionised water was prepared using 1 wt. % GNPs (product no. AB 304022, ABCR, Germany) which have 6-8 nm nominal thickness and 5 µm average lateral size. Figure 38 shows the morphology of the GNP particles used in this study. Sodium dodecyl sulphate, SDS (product no. 71725, Sigma –Aldrich, United Kingdom) was added as a surfactant to promote dispersion of GNPs. The amount of surfactant added was 1 wt. % of the GNPs used. The prepared suspension was stirred by using a FB-505 Ultrasonic Processor (Fischer scientific, United Kingdom) which operates at 20 kHz with two seconds pulse every five seconds for one hour (in total one hour but with intervals).

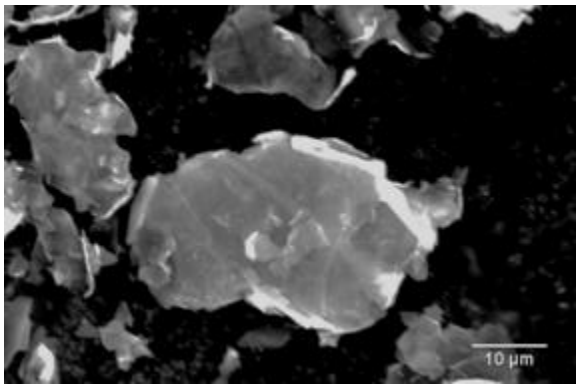


*Figure 38: SE micrograph of as - received GNP powder before forming suspension in deionised water.*

### 4.3.2 Substrate Surface Preparation

AISI 304 stainless steel (SS) substrates with nominal composition of Fe-19.0Cr-9.3Ni-0.05C (all in wt. %) were used, which have dimensions of 60 x 25 x 2 mm. Substrates were grinded by using sequential silicon carbide (SiC) grinding pads which had grit sizes P240, P400, P800 and P1200, respectively. This surface treatment was followed by polishing, utilising diamond polishing pads of average particle diameter of 6 µm and 1 µm, respectively. Prior to spray, the substrate surfaces were cleaned with industrial methylated spirit (IMS).

### 4.3.3 Thermal Spray Preparation

GNPs were deposited onto the polished SS substrates by using a TopGun SS (GTV gmbh, Germany) S-HVOF thermal spray system. This suspension spray gun utilises hydrogen gas as fuel which combusts with oxygen in a 22 mm long combustion chamber. Suspension was injected axially into the combustion chamber through an injector of 1 mm diameter from a

mechanically stirred reservoir by a pressurised suspension feeder. Substrates were attached to a rotating carousel with a diameter of 260 mm. The carousel rotates with a speed of 73 rpm during the spray runs which gives rise to a 1 m/s linear velocity for the attached substrates. In the meantime, the spray gun moves vertically with a traverse speed of 5 mm/s, which leads to a 4 mm overlap between tracks from subsequent passes. [26]. Four different thermal spray runs were performed to investigate the effect of spray parameters, flame power, stand-off distance and suspension flow rate on the deposition efficiency. Flow rates of suspension, oxygen and hydrogen were varied for different runs depending on the required flame power and suspension input. Flame powers were calculated from combustion calculations by using flow rates of oxygen and hydrogen gases. Each run was performed until 10 passes of the gun were completed. Compressed nitrogen gas directed to the carousel was used to prevent overheating of the samples. Here, nitrogen was chosen instead of air to minimise the possibility of oxidation of GNPs once deposited on the substrates and still hot and reactive. An overview of the runs and parameters used in each run are given in Table 4. The runs and parameters shown below are chosen to summarise and explain the main findings of this study. However, there were more thermal spray runs performed to achieve a film with better coverage and durability. For those tests and results please check the appendix.

| Spray runs | Spray parameters | | |
|---|---|---|---|
| | Flame power (kW) | Stand-off distance (SoD) (mm) | GNP suspension flow rate (ml/min) |
| Run #1 (baseline) | 25 | 85 | 70 |
| Run #2 (Effect of flow rate) | 25 | 85 | 125 |
| Run #3 (Effect of SOD) | 25 | 100 | 125 |
| Run #4 (Effect of Flame Power) | 50 | 100 | 125 |

*Table 4: Spray parameters used to perform each S-HVOF thermal spray run.*

### 4.3.4 Wear Testing

A ball on disc unlubricated rotational sliding wear test was performed by using a rotary tribometer (Ducom Instruments, The Netherlands). Microscale tribological performance of deposited films was investigated at 5 N load. 10 mm diameter circular wear tracks were created by using 6 mm diameter alumina (99.9% aluminium oxide) counter body balls (Dejay distributions, United Kingdom). The Samples rotated at 57 rpm for 30 minutes giving rise to 29.8 mm/s sliding linear speed and 53.7 m sliding distance.

### 4.3.5 Material Characterisation

#### 4.3.5.1 Scanning Electron Microscopes (SEM)

Surface morphology imaging of deposited coatings and worn surfaces after the tribology tests was performed by using a Quanta 600 SEM (FEI, The Netherlands) in SE mode with 10 kV accelerating voltage and 12 mm working distance. The average coverage obtained was estimated by applying threshold to SEM micrographs on imageJ (NIH, USA) software. A 7100F field emission gun scanning electron microscope (FEG–SEM) (JEOL, Japan) was used for high resolution imaging of worn areas in SE mode with 5 kV accelerating voltage and 10 mm working distance. SE mode was chosen as detected electrons originate mainly from the

surface and allow a better topography analysis of the samples, especially in the case of thin GNP films.

#### 4.3.5.2 Raman Spectroscopy

A Jobin YVON LabRAM HR spectrometer (Horiba, Japan), modified by addition of an automated xyz stage (Märzhäuser, Germany) was used to perform Raman spectroscopy. Before the spectra collection, the instrument was calibrated using a standard Si (100) reference band at 520.7 $cm^{-1}$ and the Rayleigh line at 0 $cm^{-1}$. Spectra were obtained by using a red laser with wavelength of 660 nm together with 300 µm pinhole and an objective yielding 100X magnification. A 1% laser filter was applied to attenuate the intensity at the sample, as normally used to prevent damaging of carbon based samples. A 300 lines/mm rotatable diffraction grating was employed for scanning a range of Raman shifts during each acquisition. The detection of signals to create spectra was done by using a Synapse detector (Horiba, Japan). Each individual spectrum was collected for 180 seconds and repeated for 3 times to eliminate artefacts generated by cosmic rays and to improve signal to noise ratio. Raman spectra from 5 different points were obtained and averaged for each spectrum here reported. Spectra were corrected by applying linear baseline subtraction to eliminate fluorescence and normalised to the intensity of the characteristic carbon G band by using Labspec 6 software (Horiba jobin YVON, Japan).

#### 4.3.5.3 Field Emission Gun – Transmission Electron Microscopy (FEG-TEM)

As-received GNP powder and worn GNP particles (wear debris formed after the wear test mentioned at section 2.4) from the wear track was collected and suspended into propan-2-ol solution. Suspension was then transferred onto holey carbon TEM grids and left to dry. A 2100F FEG-TEM (JEOL, Japan) operated at 200 kV was used for bright field imaging for both powders. Electron energy-loss spectroscopy (EELS) was performed using an Enfinium detector (Gatan, USA) with 2 mm aperutre and an acquisition time of 0.262 s. Gatan Microscopy Suite software (GMS3) was used to analyse EELS spectra and subtract background signal. Furthermore, Fast Fourier's Transform function of the software (Live FFT) was applied to high magnification TEM micrographs to analyse the crystal structure of the sample in chosen areas.

#### 4.3.5.4 Atomic Force Microscopy

Atomic force microscopy (AFM) measurements were performed via an Asylum Research MFP-3D (Oxford instruments ltd., UK) instrument in amplitude modulated tapping mode (AC). Scratches were made onto the GNP film / substrate surface with tweezers in order to remove GNPs from the surface and variation of height across the scratches was measured to estimate the thickness of the film.

#### 4.3.5.5 Surface Analysis

Alicona G5 infinite focus (alicona imaging GmbH, Austria) instruments was used to perform surface texture measurements. Data was obtained from 161 µm x 161 µm square areas via a 100x objective lens followed by noise and tilt corrections. Surface texture measurements obtained were used to estimate the thickness of the film.

## 4.4 Results

### 4.4.1 Coating Characterisation

Figure 39 shows surface morphology of the deposited films for each run at both high and low magnification. Both angular and tiny GNP flakes and bigger randomly shaped agglomerated GNP blocks are present on the surface. A uniform film was not achieved by any of the runs and GNP particles have a random distribution on the surface. Table 5 shows the area coverage obtained by each run, Run #1 was performed by injecting suspension at a rate of 70 ml/ min into a 25 kW flame and substrates were positioned 85 mm away from the gun exit. This configuration leads to a 31.5 % area coverage (as estimated from Figure 2 a, e). The flow rate of the suspension was increased to 125 ml/min for Run #2 which gives rise to an increase in coverage by more than 50% (Figure 2 b, f). Run #3 was performed by keeping the flow rate at 125 ml/min and increasing the stand-off distance to 100 mm. The area coverage of GNPs increased from 49.5% to 58% as a results of the increase in stand-off distance (Figure 2 c, f). In the last run, Run #4, the effect of flame power was studied by increasing the power from 25 kW to 50 kW. The area coverage of GNPs reduced significantly compared to the other 3 runs, down to 7%. As the sample produced by Run #3 has highest area coverage, it has been chosen for wear / tribology test and further analysis with Raman spectroscopy, TEM and EELS. Thickness of this deposited film was estimated via AFM by the procedure described in section 4.3.5.4 is 482 ± 155 nm. Furthermore, surface texture measurements obtained from alicona

were used to estimate the thickness as well. As the surface is only partially covered, height of the highest peak was assumed to be the thickest point of the film whereas the uncovered areas were considered the zero points. Thickness estimated from this method is 483 ± 160 nm. In addition average roughness of the film/substrate surface is 0.020 ± 0.004 µm.

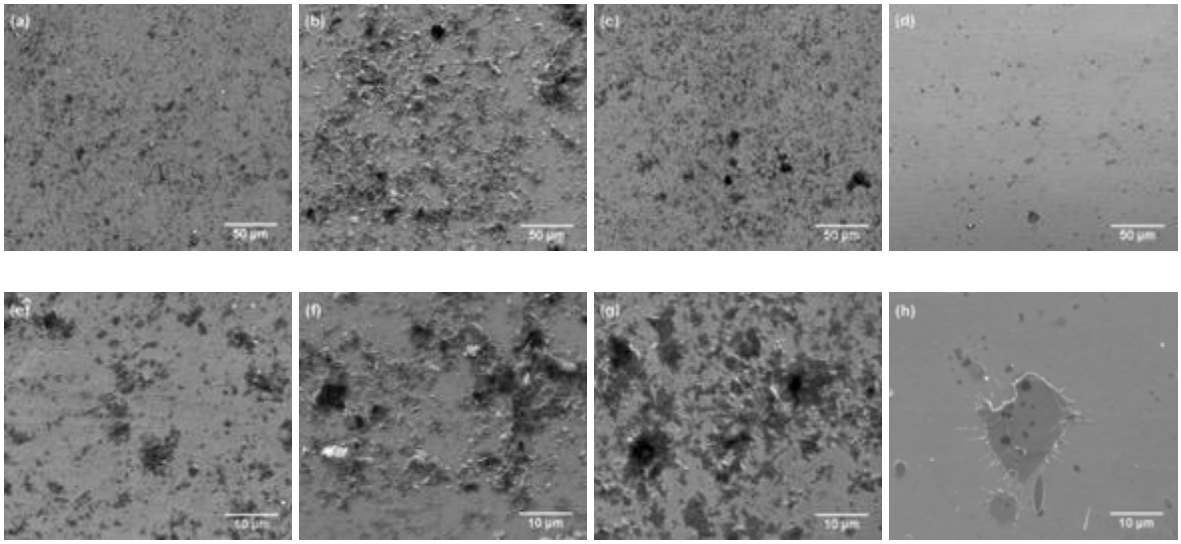

*Figure 39: Low and high magnification SE micrographs showing the surface morphology of GNP films produced by Run #1 (a,e), Run #2 (b, f), Run #3 (c, g), Run #4(d, g).*

| Samples | Area Coverage (%) |
|---|---|
| Run #1 | 31.5 ± 2.6 |
| Run #2 | 49.5 ± 0.5 |
| Run #3 | 58.0 ± 4.0 |
| Run #4 | 7.0 ± 0.6 |

*Table 5: Percentage area coverage by the deposited film for each run estimated by applying contrast threshold to SEM micrographs and measuring the area fraction via ImageJ software. The associate error is the standard error of the mean.*

Raman spectroscopy was performed on both as-received GNP particles and on the chosen deposited GNP films. Data was collected from five different areas for both specimens and spectra intensity averaged to form a single spectrum for each sample. Average Raman spectra obtained exhibit three main bands showed in Figure 40, which are fingerprints of graphitic structure. Those are the G, D and 2D bands. The G band is located at ~1580 $cm^{-1,}$

and arises from the in plane vibrations (stretching) of $sp^2$ hybridized carbon-carbon bonds in hexagonal carbon rings and chains. The D band – observed at ~1350 $cm^{-1}$ arises due to ring breathing mode (expansion / contraction) from $sp^2$ hybridized carbon hexagonal rings, is related to disorder and defects present in each single layer and is used to measure the amount of defects present in the hexagonal carbon ring lattice structure. The 2D band – the third characteristic band, appears at ~2700 $cm^{-1}$, is the second order of the D band and is related to the band structure of graphene [192,193]. Therefore, this band is related to the multi layered structure of GNPs and yields an indication of the amount of disorder between the layers. The comparison between Raman band intensity ratios ($I_D/I_G$ and $I_{2D}/I_G$) was also performed and is shown in Figure 41 to highlight the effect of the processes on the GNP structure integrity. The spectrum of the GNP film resembled the spectrum of the as-received GNPs suggesting there was minimal structural change during thermal spray. This is also proved by the consistent $I_D/I_G$ ratios (0.39 ± 0.03 and 0.37 ± 0.11 for as received GNP and GNP film, respectively). Alongside $I_{2D}/I_G$ ratios are 0.44 ± 0.07 and 0.54 ± 0.08 representing increasing defects in the layered structure of GNPs upon thermal spray.

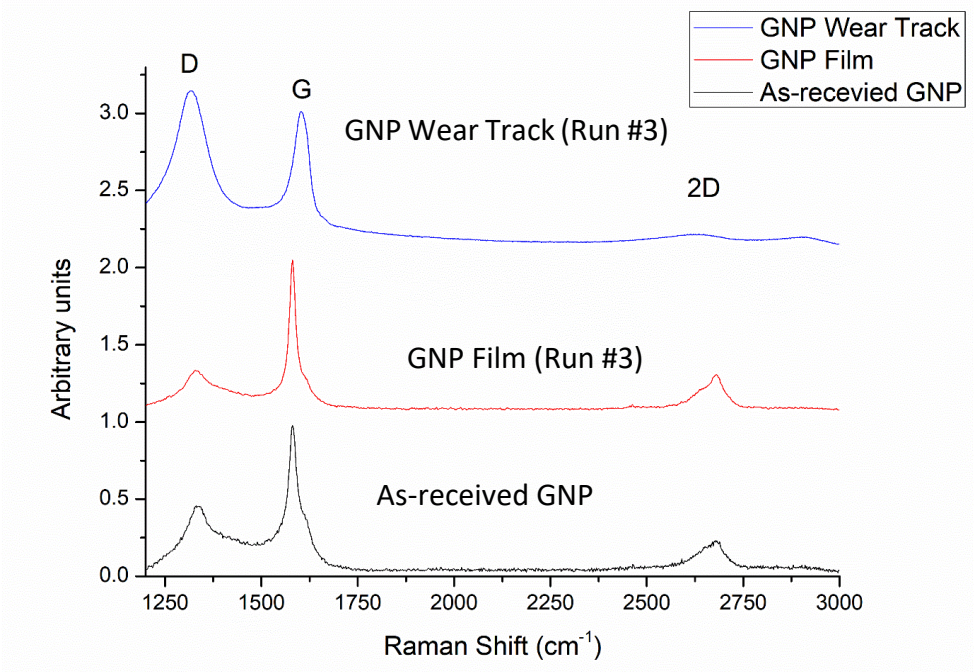


*Figure 40: Average Raman Spectra for as-received GNP, SHVOF thermal sprayed GNP film and GNP films inside the wear track obtained at 5N Load. Spectra have been baseline corrected for fluorescence, normalised to the intensity of the G band for ease of comparison and shifted along the y-axis for clarity.*

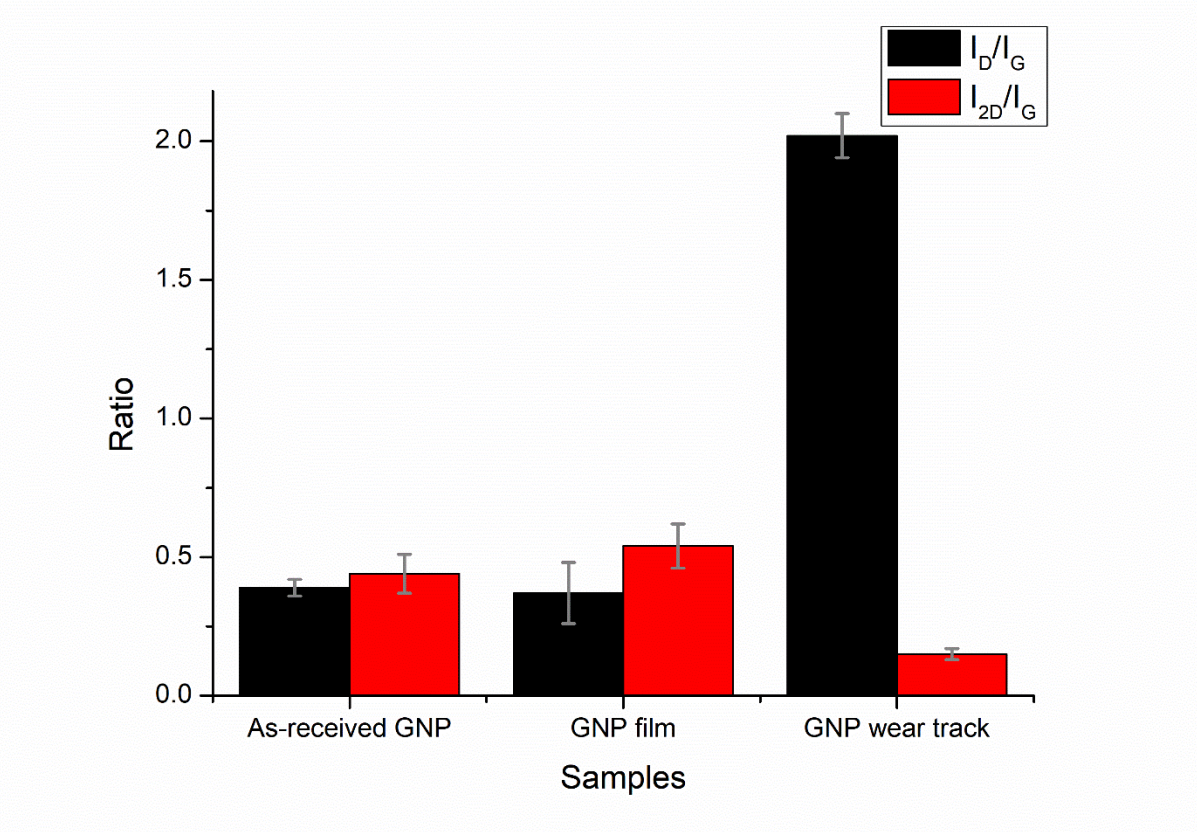


*Figure 41: Intensity ratios of Raman bands obtained for as received GNP, GNP film and GNPs inside the wear track*

### 4.4.2 Tribological Performance

The deposited GNP film leads to remarkable improvement in wear performance by reducing the coefficient of friction (CoF) significantly, even if a uniform film was not deposited. Figure 5 shows CoF against cycles for a GNP deposited surface and a bare stainless steel surface for comparison. Each cycle represents one complete circular revolution (10 mm diameter) of the counter-body, and the accuracy of coefficient of friction measurements is 0.02 ± 1% measured frictional force. In the bare stainless steel case, CoF increases sharply to ~0.5 in only ~100 cycles. Then, it raises up to ~0.7 gradually with the number of cycles. In the GNP film case, the CoF remains at 0.1 up to ~875 cycles and then sharply increases to 0.5 in a few cycles. Afterwards, it follows the trend as the no film scenario by gradually increasing with the number of cycles. Repeated wear tests shows the same trend. The only slight difference obtained is at the transition point, where the coefficient of friction increases from 0.1 to 0.7. This point slightly shifts earlier or later in cycles depending on the amount of GNPs present at the contact point.

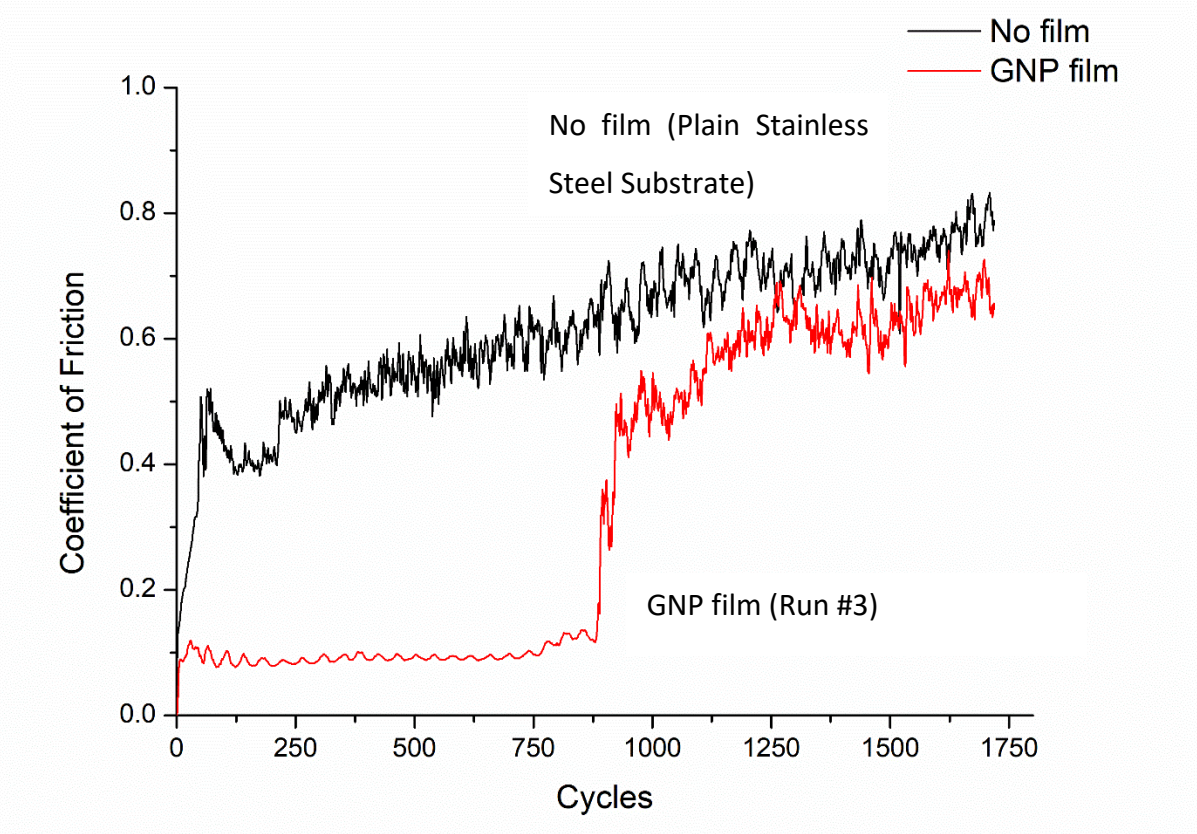


*Figure 42: Coefficients of friction against cycles for GNP film sample and a bare stainless steel substrates.*

### 4.4.3 Worn Surface Characterisation

The worn surfaces were characterised by SEM, TEM, Raman and EELS to study the wear mechanism and deformation of the deposited film. Figure 43 shows low magnification micrographs of wear tracks when CoF is ~0.1 (a) after ~500 cycles and ~0.7 (b) after 1700 cycles. When CoF is ~0.1, a two-body abrasive wear mechanism takes place. There is no significant damage or material removal (mild wear regime) from the substrate surface; material was shifted to the edges of the wear track indicating ploughing wear mechanism and abrasive grooves are also present. The wear track width is ~185 µm and the surface is relatively smooth. When the CoF is 0.7, the wear track is ~ 7 times wider and the surface is rougher. Severe damage happened to the surface, wear debris was produced and wear grooves due to material removal can be seen. This is a clear indication that the film is no longer present on the surface and a severe wear regime took place. Removal of material leads to a change of wear mechanism from two body abrasive wear to three body abrasive wear. Figure 44 shows high magnification FEG- SEM micrographs of wear tracks when CoF is ~0.1

(a) after ~500 cycles and ~0.7 (b) after 1700 cycles. Alignment of GNPs in the direction of motion and tribofilm formation can be seen when CoF is ~ 0.1. When CoF is ~ 0.7, tribofilm is no longer present inside the wear tracks. Agglomerated chunks of GNPs got stuck inside the wear grooves or were trapped between the wear debris produced. Delamination of the surface due to severe wear regime was followed by fragmentation and led to the formation of wear debris flakes. Further analyses by TEM, Raman and EELS were performed on the wear track for CoF ~0.1, the high roughness of the wear track for CoF 0.7 prevents the calibration and usage of Raman spectroscopy. The produced films were destroyed and removed from the wear track at the stage when CoF is 0.7 therefore TEM and EELS could not be performed.

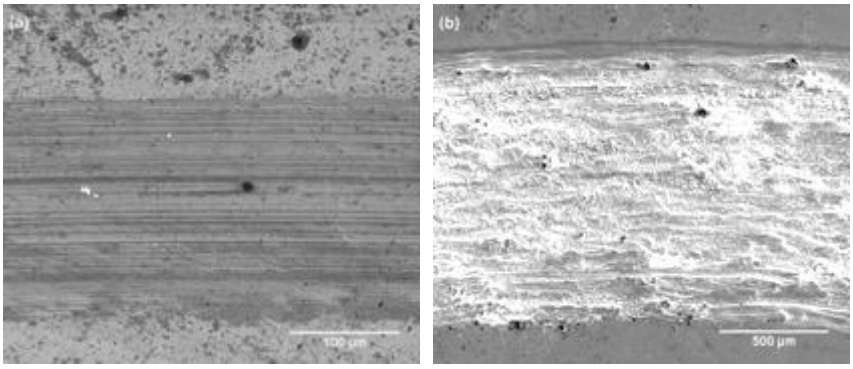


*Figure 43: Low magnification SEM SE micrographs showing the surface morphology of the wear tracks when CoF is around 0.1 (a) and 0.7 (b)*

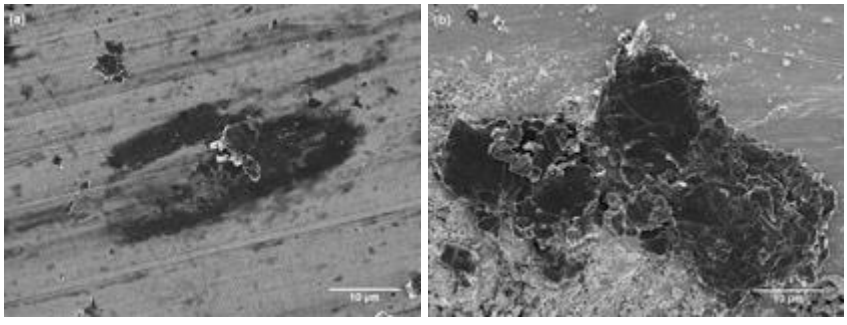


*Figure 44: High magnification FEG-SEM SE micrographs showing the surface morphology of the GNP particles inside the wear tracks when CoF is around 0.1 (a) and 0.7 (b). Tribofilm formation is shown in (a) as dark grey patches generated by GNPs exfoliated upon wear testing.*

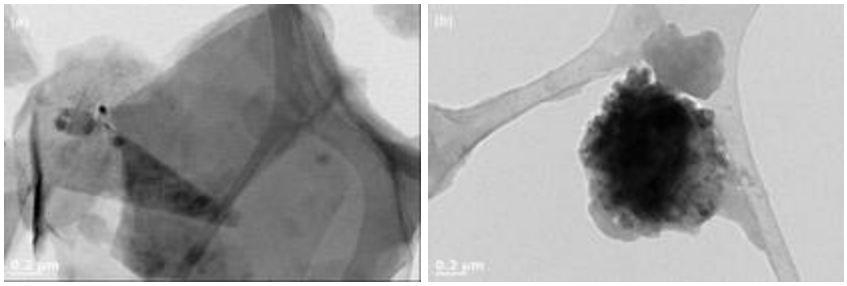

*Figure 45: TEM Micrographs of unprocessed GNPs (a) and GNPs after wear tests of 5N while CoF is 0.1 (b).*

Raman spectra from five different points were obtained for GNP films inside the wear track after ~500 cycles, when the CoF was ~0.1. The spectra were averaged into a single spectrum which this time is dominated by 2 bands the G and D bands, as shown Figure 3. The intensity of the D band increased sharply, while broadening and slight shifting of the G band occurs. $I_D/I_G$ ratio for GNPs inside wear track is 2.02 ± 0.08, which is five times higher than the as received and deposited GNPs, suggesting that a significant amount of structural defects was introduced. The 2D band decreased significantly as can also be seen from the $I_{2D}/I_G$ ratio (0.15 ±0.02), that indicates a disordering of the layered structure of GNPs.

Figure 45 shows TEM micrographs of as-received GNPs (a) and GNPs collected from the wear track after ~500 cycles (CoF ~0.1). Initially, GNP particles were angular and wide flakes were present in the as-received condition. After ~500 cycles they turned into round, irregularly shaped narrow particles. In addition, GNP particles were thinner before the application of load and turned into thicker particles, which explains the contrast difference in TEM micrographs. High magnification TEM micrographs of two different areas from GNP films inside the wear track after of ~500 cycles with diffraction patterns obtained from the marked areas are presented in Figure 46. FFTs are used to comment on the crystal lattice structure of the particles on those specific areas. In one of the areas, angular edges completely transformed into rounded edges (Figure 46 (a)).The FFT obtained from this area shows a ring pattern which corresponds to amorphous carbon. On the other hand, individual GNP flakes with angular edges can be seen in the second area of interest (Figure 46 (b)). The FFT obtained from this area has both a ring and a hexagonal pattern showing that crystal lattice structure of the GNPs conserved so far, with smaller presence of amorphous carbon. After ~500 cycles,

not all of the GNPs have deformed as CoF remains at ~0.1 and the presence of undeformed ones survive until ~875 cycles are reached (when CoF reaches ~0.7).

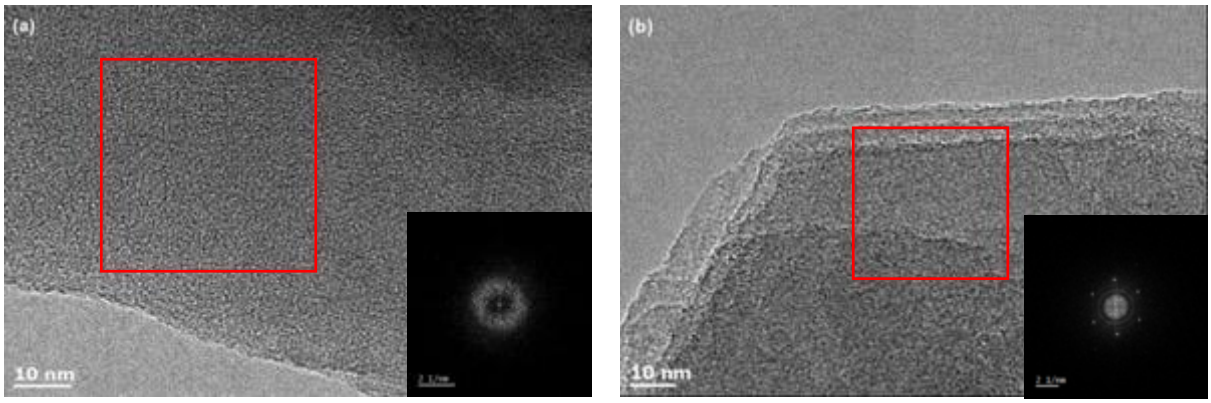


*Figure 46: High magnification TEM micrographs of GNPs after wear test and FFTs of the marked areas obtained by Gatan GMS 3 software.*

EELS spectra for as-received GNPs and GNPs collected from the wear track after ~500 cycles (CoF ~0.1) are shown in Figure 47. The EELS spectrum of as-received GNPs resemble a graphite EELS spectrum as given in literature [194]. A broad band representing sigma (σ) bonding at ~300 eV loss followed by a shoulder is present. The band present at ~284 eV corresponds to pi ($\pi$) bonding [195] . The sigma bond is the bonding between $sp^2$ hybridized orbitals, while the pi bond is the bonding between unhybridized *p* orbitals in graphene [196] . On the other hand, the EELS spectrum of deformed GNPs is similar to the spectrum of amorphous carbon with an oxygen peak appearing at ~540 eV [194]. The band representing the pi bonding is undistinguishable, and the sigma bond band is getting narrower while the shoulder disappears.

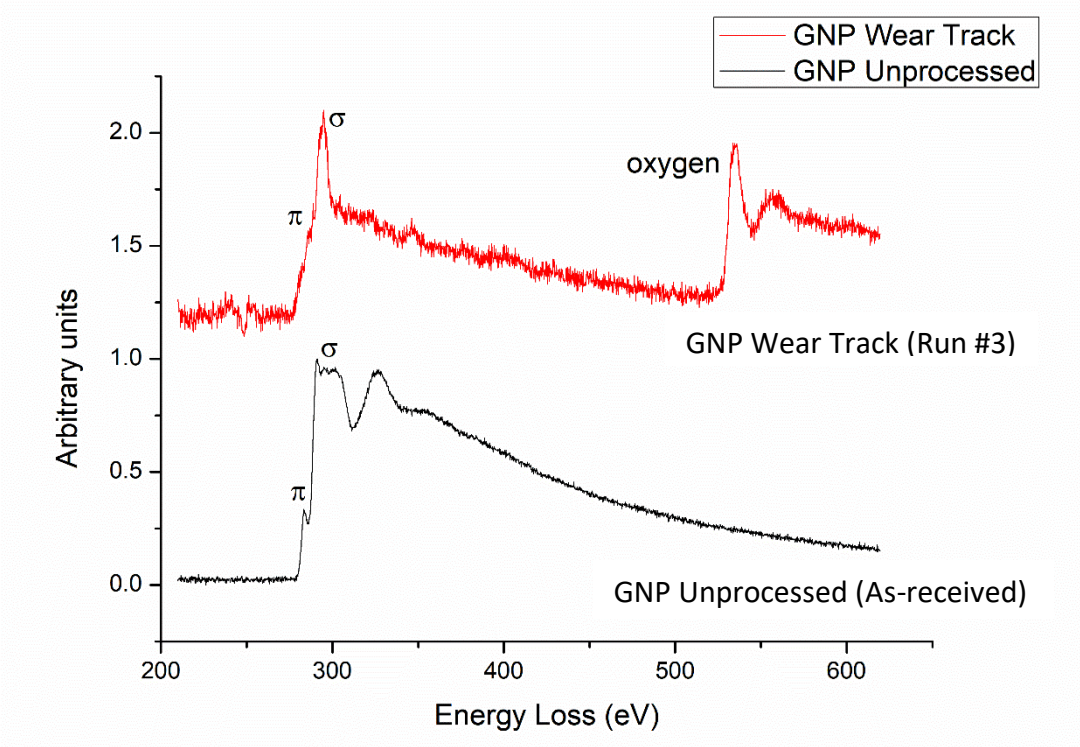


*Figure 47 : EELS Spectra of the unprocessed GNPs and spectra from the wear track of the 5 N when CoF is 0.1. Spectra heave been baseline corrected for background signal, normalised to the intensity of the highest peak for ease of comparison and shifted on the y-axis for clarity.*

## 4.5 Discussion

### 4.5.1 Film Deposition & Transformation of GNPs in Flame.

From the material characterisation, it was clear that GNPs had random distribution and orientation on the surface. Some degree of melting of feedstock material is key for the formation of a strong bond between the coating and substrate [197]; however, GNPs fully oxidise and combust at 600 °C before any form of melting can take place [198,199]. This prevents the formation of a strong bond with the substrate and as the process continues loosely bonded particles are removed from the surface due to the high gas velocity. Significant reduction in the GNP amount inside the wear tracks also indicates the presence of weak bonding between the coating and the substrate surface as the loosely bonded GNPs were removed due to the load exerted by the counter-body. Spray parameters used during the deposition have influence on the area coverage of the film. Instead, suspension flow rate and flame power have a major effect on coverage. Increasing flow rate leads to a higher area coverage as a result of increased number of particles sprayed per unit time. Conversely, the

flame power increase has an adverse effect on deposition, leading to less than 10% area coverage at 50 kW. Higher temperature and velocity at 50 kW compared to 25 kW, lead to more combustion and removal of GNPs from the surface. The stand-off distance has a minor effect on the area coverage, only leading to less than 10 % increase. The GNP deposited on substrates that are further away from the flame are protected more against removal due to high gas velocities. However, stand-off distance cannot be increased significantly as the particles would lose their momentum before reaching the substrate. In similar studies performed via radially injecting the GNP suspension into the thermal spray flame instead of axially into the combustion chamber, led to better deposition efficiency (92% coverage) [32,191]. Radial injection reduces the degradation of GNPs inside the flame as they are subjected to the heat for a reduced amount of time. In addition higher suspension flow rate (170 ml/min) and larger standoff distance (300 mm) were used. In our study, it has been seen that increasing both flow rate and standoff distance increases the area coverage. However, the radial injection doesn't allow the full exploitation of the thrust from the thermal spray flame. Also, a too long stand-off distance could lead to a reduction of the particles velocity and raise problems of gas turbulence. These effects would ultimately lead to a poorer bonding with the substrate.

Raman spectra obtained from as-sprayed region have all three characteristic bands (D, G and 2D) of graphene which confirms the survival of GNPs throughout the suspension preparation and thermal spray. Both suspension preparation and thermal spray processes did not induce significant defects into the graphene (no change in $I_D/I_G$) and did not lead to a change in the layered structure (no change in $I_{2D}/I_G$). Small differences in both $I_D/I_G$ and $I_{2D}/I_G$ ratios for as–received GNP and GNP films can be explained by inhomogeneity of GNP particles. Another study performed using the same equipment for GNP suspension preparation followed by GNP incorporation in ceramic nanocomposite coatings produced by S-HVOF thermal spray also confirmed the survival of GNPs [90].

### 4.5.2 Structural Changes in GNPs during Wear

Although a thick and uniform film was not achieved, conservation of the structure of GNPs during S-HVOF thermal spray leads to promising improvement in coefficient of friction during the unlubricated sliding wear tests. Layers of GNPs slid over each other when the load was applied, due to the presence of weak van der Waals bonds between the layers. Layers

positioned themselves next to each other in the direction of motion and formed tribofilms, as observed inside the wear track, [100]. The tribofilm formation provides optimal wear performance even if the initial coverage was not 100%. In addition, loosely bonded GNPs transferred onto the counter-body surface. Both tribofilm formation and transfer of GNP film from the substrate to counter-body surface contributed to the low CoF values. The presence of polishing lines inside the wear track and the low CoF values indicate the surface was protected. Coefficient of friction values in between 0.1 and 0.2 were also observed in some studies where graphene was used as a solid lubricant between stainless steel bodies [55,189,190]. Generation of heat due to the contact pressure between the two surfaces led the film to fail after passing through a transition stage, which led to a sudden increase in CoF from ~0.1 to ~0.7. This pattern in dry air only observed in study [190], where solution processed graphene was used as lubricant and lasted less than 100 cycles. However, constant addition of graphene usually prevents this failure but it is not possible in all applications. Deposited GNP film in our study outperformed the solution processed graphene lubricant layer even at higher sliding speed and load used to test the GNP film. The mechanism leading to failure of the film starts with the formation of oxygen bonds in between the graphene layers. Oxidation of the GNPs was confirmed by the presence of the oxygen bond peak at ~540 eV loss obtained from EELS of deformed and worn GNPs collected from wear track after ~500 cycles (CoF 0.1) [194]. The presence of oxygen bonds in between the layers changes the uniformity of the structure and introduces extrinsic defects via change of bonding type from $sp^2$ to $sp^3$ hybridization [192,200]. The change in hybridization also can be seen from the EELS spectra as the peak for pi (280 eV) bond, which corresponds to $sp^2$ hybridization, disappears after the wear test. Change in bonding and hybridization lead to formation of interatomic hydrogen bonding between the layers in oxidised graphene. As hydrogen bonding is a stronger interatomic bonding than van der Waals forces, layers lose their ability to slide over each other to dissipate the frictional force [55,201]. The reduction in lubrication ability causes the GNP layers to experience higher in-plane and shear stresses which induce further defects in the hexagonal structure of graphene as the wear test proceeds. In a study performed in hydrogen atmosphere in comparison to nitrogen, the wear performance of graphene improved significantly, as the hydrogen passivates the dangling carbon bonds generated by graphene rupture during wear and stabilizes the atomic shape of graphene [189]. These phenomena also prove the formation of oxygen bonds and deformation of the unique

structure of graphene in air atmosphere. This phenomenon explains the sharp increase of the D band and disappearance of the 2D band, which is the characteristic band for graphitic structures, when comparing Raman spectrum of the worn GNPs to the Raman spectra of both as-sprayed and as-received GNPs. In addition, broadening of the Raman bands after wear test and formation of a D+G peak illustrates the increase in disorder of the GNPs [193]. The loss of order in the crystal structure, therefore of crystallinity, can also be seen from change in morphology during the wear test which lead to formation of irregular spheres from cornered flakes. Once the defects reach a significant amount to deform the structure of graphene, amorphisation of GNP particles occurs and also amorphous carbon in the EELS spectrum and amorphous ring patterns in the FFT appear. Figure 11 shows schematic diagram explaining the formation mechanism of amorphous carbon from GNPs under sliding wear.

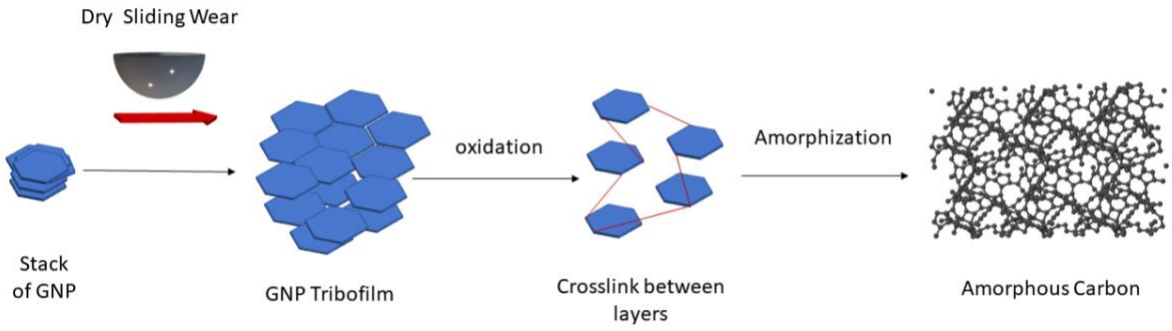


*Figure 48: Schematic diagram showing the formation of amorphous carbon from GNPs under dry sliding wear.*

## 4.6 Conclusion

A GNP film was deposited for the first time by axially injecting GNP suspension through a high velocity oxy-fuel thermal spray system. This is a quick and efficient method of depositing GNP films over an extended surface. A uniform film was not achieved due to weak bonding between the substrate and the film and removal of loosely bonded particles from the surface by incoming high velocity gas jet. However, significant improvements in CoF (decrease from 0.7 to 0.1) and unlubricated sliding wear (protection of the substrate) performance was observed due to tribofilm formation and lubricating ability of GNPs. The produced film acted to a greater extent like a solid lubricant instead of a wear resistant film during the tribological analysis. The film protected the surface up to 750 cycles under a load of 5 N. A mechanism for amorphous carbon formation from graphene under sliding wear was

observed. Generation of heat as a result of friction led to oxidation of GNP films and oxygen bonds formed in between the layers. The presence of those bonds changed the bonding type and reduced the lubrication ability of the film. Once those changes reach a critical level which is enough to cause the hexagonal structure of the graphene to change into amorphous carbon, the film fails.

Findings of this study suggest, oxidation of the GNPs during the wear process and deformational of the hexagonal structure is critical for surface protection and lubrication. Therefore, if the oxidation during the wear and deformation of the unique hexagonal structure can be prevented or delayed in a GNP containing composite coating or film, the operation life and the performance can be improved.

## 4.7 Acknowledgements

This work was supported by the Engineering and Physical Sciences Research Council [Grant Number EP / M50810X/ 1]. This work was supported by Rolls – Royce plc; in the form of a CASE Ph.D. studentship. The authors thank the Nanoscale and Microscale Research Centre (nmRC) for providing access to instrumentations and Dr Graham Rance for valuable technical discussion and Dr Michael Fay for performing TEM & EELS. The authors also acknowledge John Kirk at the University of Nottingham for conducting the HVOF thermal spray.

# Chapter 5: Wear Performance of graphene nano platelets incorporated WC-Co coatings deposited by hybrid high velocity oxy fuel thermal spray

Publication number = Wear 482-483 (2021) 203974

## 5.1 Abstract

WC-Co coatings have been used as wear resistant coatings in aero engines for decades, and research is still ongoing to further improve the performance of these coatings through compositional modifications to reduce wear. The coatings are used for unlubricated sliding wear protection in aero compressor parts such as; compressor, disc mid-span stiffeners and compressor aerofoils. In this study, two different graphene nanoplatelets (GNPs) were introduced into the WC-Co (88-12 wt. %) coating through a hybrid thermal spray technique. Under the correct injection conditions, hybrid HVOF thermal spray leads to in-situ powder mixing which eliminates the need for premixed powder. The addition of GNPs into the WC-Co coating led to an increase in the porosity of coatings. Both GNPs improved the wear performance of the system against alumina and reduced damage to the counter surface. Against the WC-Co counter body, although in a few cases the GNP incorporated coatings had a higher wear rate, lower deformation on counter bodies were obtained. When wear of counter surfaces and coatings were combined, GNPs improved the wear performance of the system as a whole.

Keywords: thermally sprayed; wear; friction; WC-Co; graphene

## 5.2 Introduction

In engineering applications, the friction force between moving parts causes wear and subsequent material loss from the surfaces, which leads to degradation and loss of function. In many cases, it is neither possible nor economic to replace parts frequently and hence wear resistant coatings are used. Thermal sprayed WC-Co cermet coatings are widely used especially in the aerospace industry and land based turbine blades to protect the surfaces from wear without affecting the bulk mechanical properties of the materials [120]. WC-Co is well known for its hardness, strength, wear resistance, [121,122] Plasma spray methods have been used until the 1980s for WC-Co cermet coating deposition. High processing

temperatures during plasma spray led to decarburization and formation of the $W_2C$ phase which has lower wear resistance properties than the WC phase. HVOF thermal spray methods have become more popular to deposit WC-Co cermet coatings nowadays, as they have lower processing temperatures compared to plasma spray and coatings have minimal $W_2C$ phase [120]. In addition to the type of thermal spray process, particle sizes carbide grain size, and binder to carbide ratio are the other important factors that affect the microstructure and hence the mechanical properties of the deposited coatings. Cobalt binder is a relatively soft phase compared to carbides. Therefore, increasing the cobalt content reduces the hardness and Young's modulus of the deposited WC-Co coating. On the other hand, fracture toughness and flexural strength increase slightly as cobalt is a ductile phase and has higher energy absorption capability. In addition to the effect on mechanical properties, increasing the cobalt content reduces the decarburization and formation of the $W_2C$ phase. Cobalt has a higher specific heat value compared to WC, therefore in-flight particle temperatures are lower [135–138]. Feedstock powder size has an effect on velocity and temperature reached by the particles in flight during the deposition process. Studies performed showed that reducing the powder size, increases the temperatures of the particles and creates a more uniform heat distribution. This increases the deformation upon impact which leads to denser, less porous and harder coatings. However, as a result of higher temperatures oxidation, decomposition and decarburization happen at a higher rate which lead to the formation of undesirable phases that can affect the performance of the coatings [140,202,203]. Furthermore, carbide grain sizes also affect the mechanical properties and hence performance of the deposited coatings. WC-Co coatings with finer carbide grains perform better compared to medium or coarse carbide grains [132,140,141]. However, once the carbide grain sizes are in an extremely fine or nanostructured level, inconsistent results were reported on mechanical properties and performances of the coatings. Most studies reported a higher degree of decomposition as a result of higher surface area to volume ratio in smaller grains. However, morphology of the powder feedstocks can also influence the surface area to volume ratio and hence heating of the particles. In some studies fracture toughness and hardness are reported to be increased in nanostructured carbide grains as a result of increased density of grain boundaries, surface bonding with binder material and reduced binder mean free path. However, some studies reported a reduction in hardness and fracture toughness as a result of higher decomposition rates. Higher decomposition rates of WC phase leading to higher loss

of C and dissolution of WC in the molten Co binder phase. In addition, it favours the $W_2C$ phase which has lower fracture toughness (more brittle) than WC phase. Furthermore, wear performance of these coatings varies as the wear regime depends on the testing conditions and the type of wear mechanism taking place. Finer carbide grains can reduce the wear rate when the wear is dominated by WC grains pull out and third body abrasive behaviour of these grains. On the other hand, reduced hardness and fracture toughness increases the wear rate of these coatings as well under the dry sliding and three body abrasive wear [130,131,140,141,143,144]. Both mechanical properties and wear performance of WC-Co coatings on its own and combined with other metals have been studied extensively in the literature. However, these have not been studied using WC-Co together with the solid lubricant graphene. Graphene has promising results on friction and wear when it is used as a solid-state lubricant or reinforcement material for composite materials.

In 2004, Novoselov *et al.* managed to obtain a single layer of $sp^2$ hybridized carbon atoms inside a hexagonal lattice by mechanically exfoliating graphite [5] which was later on named as graphene. Graphene became an important and promising material since its discovery, as it is currently the strongest material known and has high Young's modulus and good thermal and electrical conductivity. In addition graphene also has chemical inertness, enhanced surface properties and self-lubrication ability, which makes it a promising material to reduce friction hence to improve wear resistance [54,55]. Graphene nano platelet (GNP) is a common name used to refer a few layers of graphene (usually up to 20) [50]. Extensive studies were performed on GNPs and their incorporation into ceramic, polymer, metal and cermet matrix materials via various manufacturing methods. Mechanical properties of the materials and hence their performances are reported to increase as a result of GNP incorporation. However these improvements are dependent on the GNP concentration, manufacturing techniques and main matrix materials [69–74,86,87,91]. Wear resistance of the GNP incorporated materials are also improved, as a result of improved mechanical properties such as hardness and fracture toughness which are important factors in wear processes. In addition, in some studies a tribofilm formation was also observed as a result of GNP pull out [54,75,90,96,98,100,101]. In other studies HVOF thermal spray methods were also used to produce pure GNP coatings, where massive reductions in coefficient of friction (down to around 0.1) and hence protection of the surfaces was observed [32,204,205].

In this study, composite coatings of WC-Co and graphene nanoplatelets have been produced using a hybrid HVOF thermal spray. This technique allowed *in–situ* mixing of the submicron sized GNPs with the micro sized WC-Co inside the flame. Hardness and wear resistance of the WC-Co and self-lubrication ability of GNP with its ability to improve mechanical properties of composites have been combined in a single coating. Wear performance of coatings has been investigated by using the ball on disc wear test to analyse the effect of GNP incorporation, microstructure and mechanical properties of the coatings. The ball on disc wear test was chosen as it is a simple but elegant wear test technique in laboratory settings that provides reliable values of coefficient of friction (CoF) during the test. Here, the tracking of CoF is important for observing the formation of self-lubricating GNP tribofilms during the test.

## 5.3 Materials & Methods

### 5.3.1 Feedstock Materials

Three different feedstock materials, WC-Co (Amperit 518, H.C. Starck, Germany), graphene nanoplatelets (product no. AB 304022, ABCR Germany) and graphene nanoplatelets aggregates (product no. AB304025, ABCR, Germany), were used in this study. Amperit 518 was used in the powder form, while the other two were used to prepare suspensions.

Amperit 518 powder consists of agglomerated and sintered tungsten carbide (WC) particles with medium grain size (~ 2.5 µm), in a cobalt (Co) binder. This composite powder was formed from 88 wt.% tungsten carbide and 12 wt.% cobalt, WC-12Co. Back scattered electron (BSE) micrographs of WC-12Co in both low (a) and high (b) magnification are shown in Figure 49. From the low magnification BSE micrograph, spherical powder morphology and a homogenous distribution of powder particles can be seen. On the high magnification BSE micrograph, particles are seen as porous and tungsten carbide grains can be discerned from the cobalt matrix based on the contrast. Brighter areas, as marked with a blue arrow, represent WC grains, while dark grey areas, as marked with a red arrow, represent the cobalt binder matrix. WC-Co particles have a nominal size range of 15 - 45 micron with D90, D50 and D10 values of 48-58, 29-37 and 18-22 µm respectively, as stated by the manufacturer. Stated chemical composition of this tungsten-based powder is 11-13 wt. % Cobalt, 5.2-5.6 wt. %

Carbon (C) and 0.2 wt. % Iron (Fe). The powder was dried overnight inside a drying cabinet at ~100°C before the thermal spray to eliminate the moisture and its effects on the flowability of the powder.

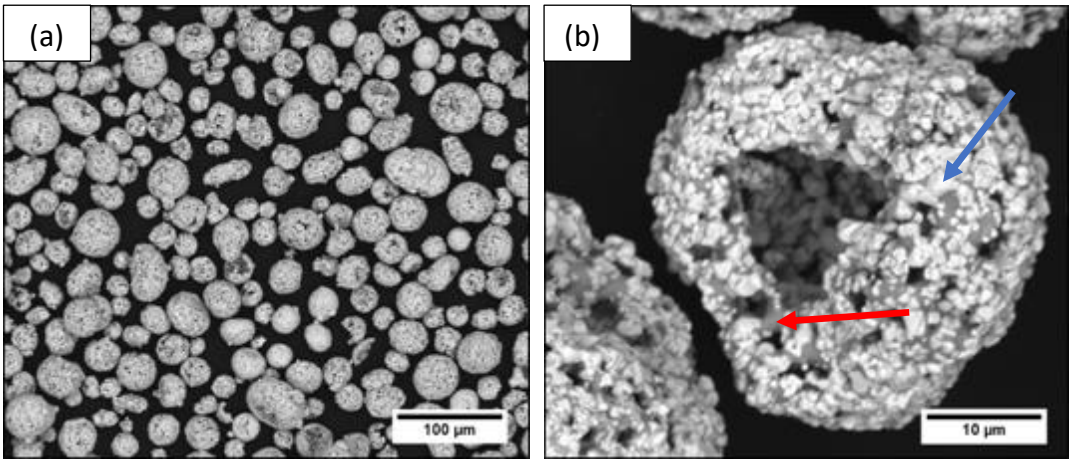


*Figure 49. BSE micrographs of Amperit 518 (WC-12Co) agglomerated and sintered powders in low magnification (a) and high magnification (b). Brighter areas are WC grains (marked with blue arrow) while dark grey areas are the cobalt binder matrix*

Feedstock flow rates given in the next section for WC-Co powder and GNP suspensions are used to calculate the required suspension concentration (which is 0.3 wt.%) to achieve a WC-Co + 1 wt.% GNPs in the deposited coatings. 1 wt.% of GNPs in the final coating composition is planned for this study. According to the literature, addition of GNPs at higher concentration leads to degradation of properties. In addition, in a very similar study performed with alumina showed improved performance by incorporating 1 wt.% of GNPs in the final composition [90]. Furthermore, suspension with higher GNP concentrations leads to cloaking issue of the injector. Different GNP concentrations were not used in this study. However, two different GNPs were chosen in this study to investigate the effect of surface area and particle sizes on the mechanical properties and hence the wear performance. Deionised water-based suspensions of graphene nanoplatelets (labelled as GNP1 in this study) and graphene nanoplatelets aggregates (labelled as GNP2 in this study) were prepared using 0.3 wt. % of each powder. GNP1 has 6-8 nm nominal thickness, 5 µm average lateral size and a specific surface area of 118.8 $m^2/g$. GNP2 consist of varied submicron sized particles with a specific surface area of 300 $m^2/g$. Secondary electron (SE) micrographs of both GNP powders are shown in Figure 50. Both GNP powders have angular flake shaped morphology. However, GNP2 powder is more agglomerated as a result of its high specific surface area,

hence greater forces of attraction. Sodium dodecyl sulphate, SDS (product no. 71725, Sigma–Aldrich, United Kingdom) was added as a surfactant to promote dispersion of the GNPs. The amount of surfactant added was 1 wt. % of the GNPs used. The suspensions were stirred using a FB-505 Ultrasonic Processor (Fischer scientific, United Kingdom) which operates at 20 kHz with a two second pulse every five seconds for one hour.

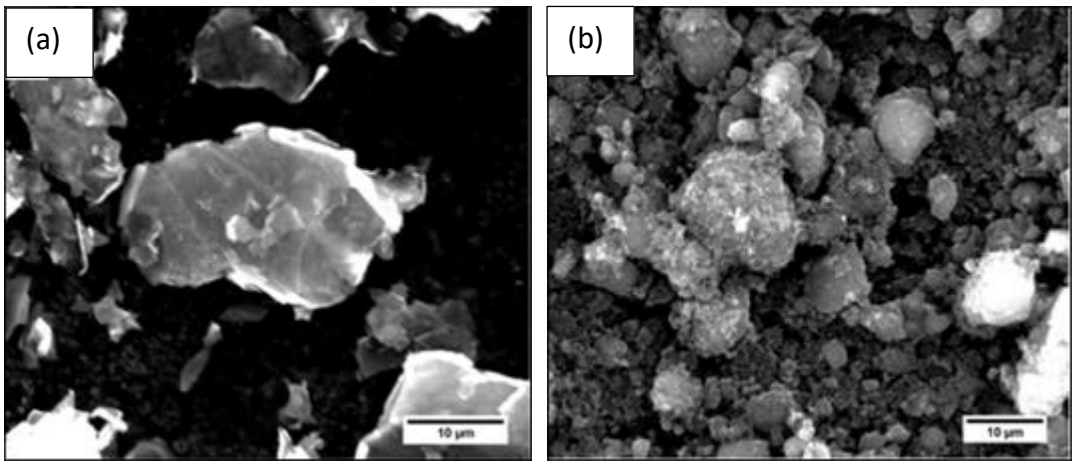


*Figure 50. SE micrographs of GNP1 (a) and GNP2 (b) powders. Both powders have angular flake shapes however GNP2 powder is more densely packed and agglomerated as a result of higher specific surface area.*

AISI 304 stainless steel substrates with dimensions of 60 x 25 x 2 mm with nominal composition Fe-19.0Cr-9.3Ni-0.05C (all in wt. %) were used as substrates. Substrate surfaces were grit blasted with a blast cleaner from Guyson (Dudley, United Kingdom) at 3 bars with F100 brown aluminium oxide particles (0.125-0.149 mm). Prior to thermal spray, the substrate surfaces were cleaned with industrial methylated spirit (IMS) and compressed air.

### 5.3.2 Coating Deposition

Coatings were deposited onto the grit blasted stainless steel substrates with a TopGun SS (GTV GmbH, Germany) HVOF thermal spray system. A custom attachment for the HVOF thermal spray gun shown in Figure 51 was used for radial injection of the GNP1 and GNP2 suspensions. Amperit 518 powder was injected axially into the 22 mm long combustion chamber where the combustion between hydrogen and oxygen takes place, at a rate of 40 g/min. Hydrogen and oxygen flow rates were 660 l/min and 229 l/min respectively, which gives rise to a 75 kW and 70% stoichiometric flame. A hydrogen rich combustion was chosen to minimise the effect of WC decarburization during the thermal spray. Substrates were

attached onto a rotating carousel with a diameter of 260 mm and positioned at a 300 mm stand-off distance. Stand-off distance, oxygen and fuel flow rates were optimised from the literature and the previous work done on HVOF thermal spray setup at the University of Nottingham for each suspension or powder compositions depending on their melting temperature, particle size and density. The carousel rotates with a speed of 73 rpm during the spray runs which gives rise to a 1 m/s linear velocity for the attached substrates. Simultaneously, the spray gun moves vertically with a traverse speed of 5 mm/s, which leads to a 4 mm overlap between tracks from subsequent passes [26]. GNP suspensions were injected at a rate of 170 ml/min radially through an injector with internal duct diameter of 450 µm pointing at 10 mm from the nozzle exit along the flame axis and 15 degrees downstream to the flame direction, as an optimised set of parameters from a previous project [32]. WC-Co powder flow rate, GNP1 and GNP2 suspensions flow rates were optimised to achieve a WC-Co + 1 wt. % GNP1 and WC-Co + 1 wt.% GNP2 in the as-sprayed composite coatings. Three different runs were performed, the first one was just axially injecting Amperit 518 powder to obtain a WC-Co coating as a reference sample. Two more runs were performed by introducing the radial injection of GNP1 and GNP2 suspensions respectively to deposit composite coatings (WC-Co + GNP1 and WC-Co + GNP2).

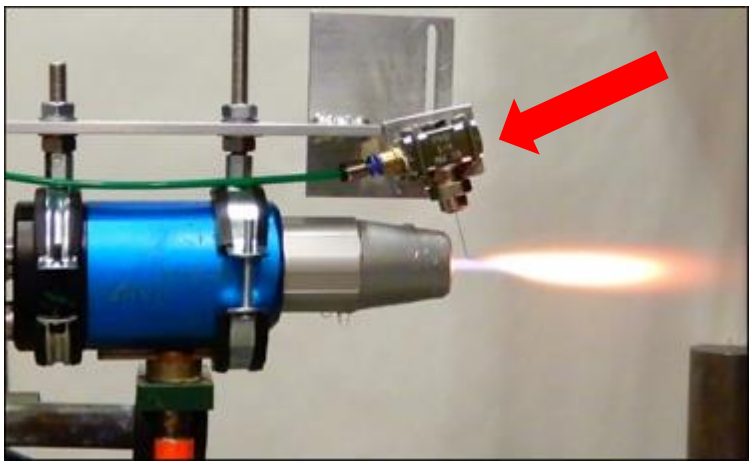

*Figure 51. Image showing the GTV HVOF TopGun with the custom attachment for radial injection indicated with the arrow, where the injector was pointing 10 mm from the nozzle exit and 15° downstream.*

### 5.3.3 Wear Test

The top surface of the coatings was ground via a metal bonded diamond grinding disc of 20-micron particle size which corresponds to a grit size of ~P900. This process was followed by fine polishing in the order of Abracloth and Planocloth in the presence of 9- and 1-micron water-based diamond suspension, respectively. Final polished surfaces had surface roughness values ($R_a$) in the range of 0.02-0.05 µm. Unlubricated rotational sliding wear tests were performed using a rotary tribometer with a ball on disc arrangement (Ducom Instruments, The Netherlands). Tribological performance of polished coatings was investigated at a 60 N load against 6 mm alumina (99.9% aluminium oxide) and tungsten carbide (WC - 6 wt. % Co) counter body (referred to as WC) balls (Dejay distributions, United Kingdom) which resulted in 10 mm diameter circular wear tracks. Both counter surfaces had a surface finish of 0.038 µm. Supplier provided hardness values were 91 in Rockwell A scale for tungsten carbide and 81 in Rockwell 45 N scale for alumina. Vickers hardness conversions for WC is ~1550 HV and ~2000 HV for alumina. Samples were rotated at 100, 200 and 300 rpm against the stationary balls which gives rise to 52, 105 and 157 mm/s linear speeds, respectively. Tests were performed for a total sliding distance of 1 km. The loading condition, sliding speed and counter body materials were chosen to investigate an operating envelope where GNPs within the coating can lead to formation of the tribofilm. Two different counter bodies and 3 different sliding speeds were chosen to form deeper wear tracks. Formation of deeper wear tracks can increase the chances of GNPs embedded in the coating cross section to be exposed during the wear tests and formation a tribofilm. Hence effect of GNPs on both mechanical properties and lubrication can be studied. Duplicate tests were conducted for all conditions. Coefficient of friction (CoF), which has an accuracy of 0.02 ± 1%, was plotted against sliding distance.

2D transverse line profiles of each wear track were measured at four different points using Talysurf Form 50 contact profilometer (Taylor Hobson, United Kingdom) together with a diamond stylus with a tip radius of 2 µm and lateral resolution of 0.5 µm. Mountains map software was used to analyse these line profiles to calculate the cross-sectional area of the wear tracks, then these were converted into volume loss by multiplying with the circumference of the circular tracks which is the total length of the wear track [130,206]. In total eight different points were used to calculate the average and standard error of the mean

for each sample. Material volume loss on the counter body was calculated (from two different measurements – one from each test) by following the assumption of spherical cap of material removal method reported in the studies [5], and [6]. Specific wear rate of both the coatings and the counter bodies was calculated from the volume loss by dividing it by applied force and total sliding distance.

### 5.3.4 Material Characterisation

Cross sectional analysis (microstructure, thickness and porosity) of the deposited coatings, and observations of the morphology of the feedstocks and the worn surfaces were performed with a Quanta 600 scanning electron microscope, SEM (FEI, The Netherlands) in both SE and BSE modes with 20 kV accelerating voltage, a spot size of 5 and a working distance of 13 mm. Combined EDX software (Bruker, USA) was used for elemental composition analysis. Cross sectional samples of the coatings were prepared by cutting the samples with a diamond cutting disk, followed by sequential silicon carbide (SiC) grinding and diamond polishing with a final grit size of 1 µm. Porosity analysis of the coatings was performed on 5 different BSE micrographs for each coating obtained from the SEM at 2000X magnification from the centre of the coatings which gives rise to an area of 70 µm x 60 µm. Contrast threshold function on ImageJ software [208] was applied to the micrographs according to ASTM E2109 standards to estimate the percentage area fraction of the pores in each BSE micrograph. An average porosity along with the standard mean error was reported in all cases.

X-ray diffraction (XRD) was performed on coatings top surface and WC-12Co powder to analyse the phase changes upon the thermal spray. A Bruker D8 Advance diffractometer (Bruker, USA) with Cu $K_\alpha$ radiation (1.5406 Å) in θ-2θ Bragg-Brentano geometry was used with a step size of 0.02˚and a time per step of 0.1 s. in the 20° ≤ 2θ ≤ 100° range. To quantify the decarburization, carbide retention index was calculated for each coating and the values are presented in Table *6*. Index of carbide retention was calculated using the equation 1 and intensities of WC, $W_2C$ and W peaks at 35.6°, 39°, 40.5° respectively [209].

$$\frac{Iwc}{Iwc + Iw2c + Iw} \quad (eq.1)$$

A LabRAM HR spectrometer (Horiba Jobin YVON, Japan), modified by addition of an automated xyz stage (Märzhäuser, Germany) was used to perform Raman spectroscopy. Before the spectra collection, the instrument was calibrated using a standard Si (100) reference band at 520.7 $cm^{-1}$ and the Rayleigh line at 0 $cm^{-1}$. Spectra were obtained by using a red laser with wavelength of 660 nm (for cross section) and a green laser which has a wavelength of 532 nm (for worn surfaces) together with a 300 µm pinhole and an objective yielding 100X magnification. Two different wavelengths were used to avoid the fluorescence effect. Green laser usage on cross sections disturbs the 2D peak, which is important for proving the presence of GNPs. On the other hand, red laser usage on the worn surface disturbs the whole spectrum range. A 25% laser filter was applied to attenuate the intensity at the sample. A 300 lines/mm rotatable diffraction grating was employed for scanning a range of Raman shifts during each acquisition. The detection of signals to create spectra was done with a Synapse detector (Horiba, Japan). Each individual spectrum was collected for 20 seconds and repeated for 3 times to eliminate artefacts (cosmic spikes) generated by cosmic rays and to improve signal to noise ratio. Spectra were corrected by applying linear baseline subtraction to eliminate any residual fluorescence by using Labspec 6 software (Horiba Jobin YVON, Japan) and normalised. Presented spectra for worn surfaces are an average of 5 different spectra from each of the coatings' corresponding wear track surfaces.

The coating microhardness was measured via a Vickers microhardness indenter (Buehler, USA) on polished cross sections. 500 gf with a dwell time of 10 seconds was applied to create 5 indents in the centre of the coatings, parallel to the substrate. An average hardness value with standard mean error was reported in all cases.

## 5.4 Results

### 5.4.1 Coating Characterisation

The XRD diffractogram in Figure *52* shows Amperit 518 powder was composed of hexagonal WC (PDF 00-051-0939) and cubic cobalt (PDF 00-15-0806) phases. The WC phase is still the dominant phase after the thermal spray. However, $W_2C$ (PDF 01-071-6322) and elemental W (PDF 00-004-0806) phases were formed during the thermal spray process. In addition, a slightly broad diffuse peak between the 37°-45° 2θ is also present in the coatings

which is a sign of decarburisation and amorphisation. In addition, the calculated carbide retention index value for all three coatings was 0.67.

All three coatings had achieved a good bonding with the substrates and their thicknesses were all in the same range (105-110 μm) as it can be seen from the SE micrographs of the cross sections in Figure 53. The thickness of each coating was measured from the cross-section micrographs at 5 different locations, and values are presented in Table *6*. Incorporation of the GNPs led to a more porous coating in both cases. Dark areas and lines on the BSE micrographs of the cross sections shown in Figure 53, represent pores and cracks. The existence of the pores was also confirmed by SE micrographs (not shown). Porosity in both composite coatings was measured by the method described in section 2.3 and the values are presented in Table *6*. Brighter areas marked with red arrows represent the binder rich W (splats of molten metal) due to high atomic weight of tungsten. Angular shaped tungsten carbide grains are also visible in all cross sections. Both WC-Co and WC-Co + GNP1 coatings have the same Vickers hardness of ~1190HV, however WC-Co + GNP2 coatings hardness reduced to ~880HV.

Raman spectra were collected from both GNP incorporated coating cross sections shown in Figure 54. Both Raman spectra were dominated by 3 bands. Those bands are D, G and 2D bands present at ~1350, ~1600 and ~2650 $cm^{-1}$ Raman shifts, respectively. D band arises from stretching while G band arises from expansion / contraction of $sp^2$ hybridized carbon-carbon bonds in hexagonal rings or chains. They can be present in carbides as well however, 2D band is a characteristic band of graphene and only present in graphene and graphite containing materials [192,193].

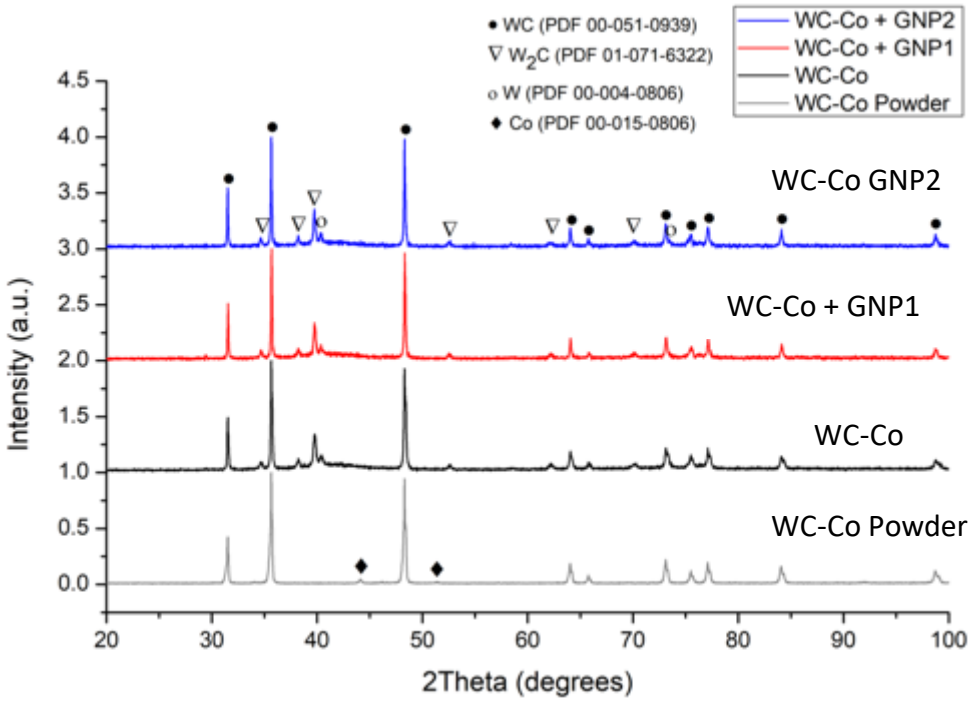


*Figure 52. XRD diffractograms of the Amperit 518 (WC-12Co) powder feedstock, as-sprayed WC-Co coatings and both GNP1 and GNP2 incorporated composite coatings.*

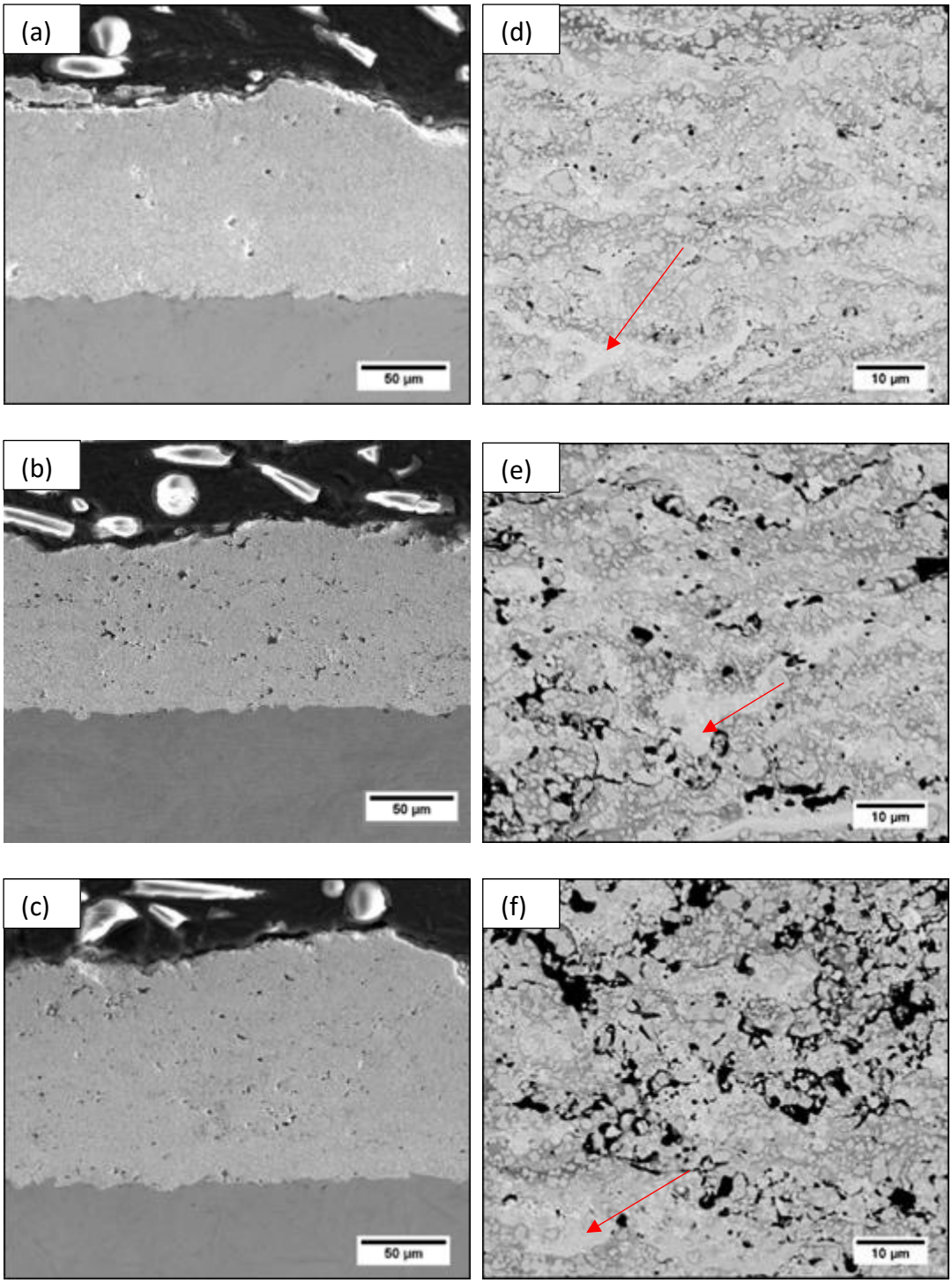


*Figure 53. On the left, SE micrographs of (a) WC-Co, (b) WC-Co + GNP1 and (c) WC-Co + GNP2 coating cross sections in low magnification. On the right, BSE micrographs of (d) WC-Co, (e) WC-Co+GNP1 and (f) WC-Co + GNP2 coating cross sections in high magnification. Darker areas represent pores and cracks while brighter areas are W heavy grain, marked with arrows on BSE micrographs.*

*Table 6. Summary of coatings properties including thickness, porosity and hardness.*

| Coating Properties | | | | |
|---|---|---|---|---|
| Samples | Thickness (µm) | Porosity (%) | Vickers Hardness ($HV_{0.5}$) | Carbide Retention Index |
| WC-Co | 110 ± 2 | 0.6 ± 0.1 | 1191 ± 57 | 0.67 |
| WC-Co + GNP1 | 106 ± 9 | 3.8 ± 0.6 | 1193 ± 60 | 0.69 |
| WC-Co + GNP2 | 106 ± 7 | 2.2 ± 0.4 | 880 ± 71 | 0.67 |

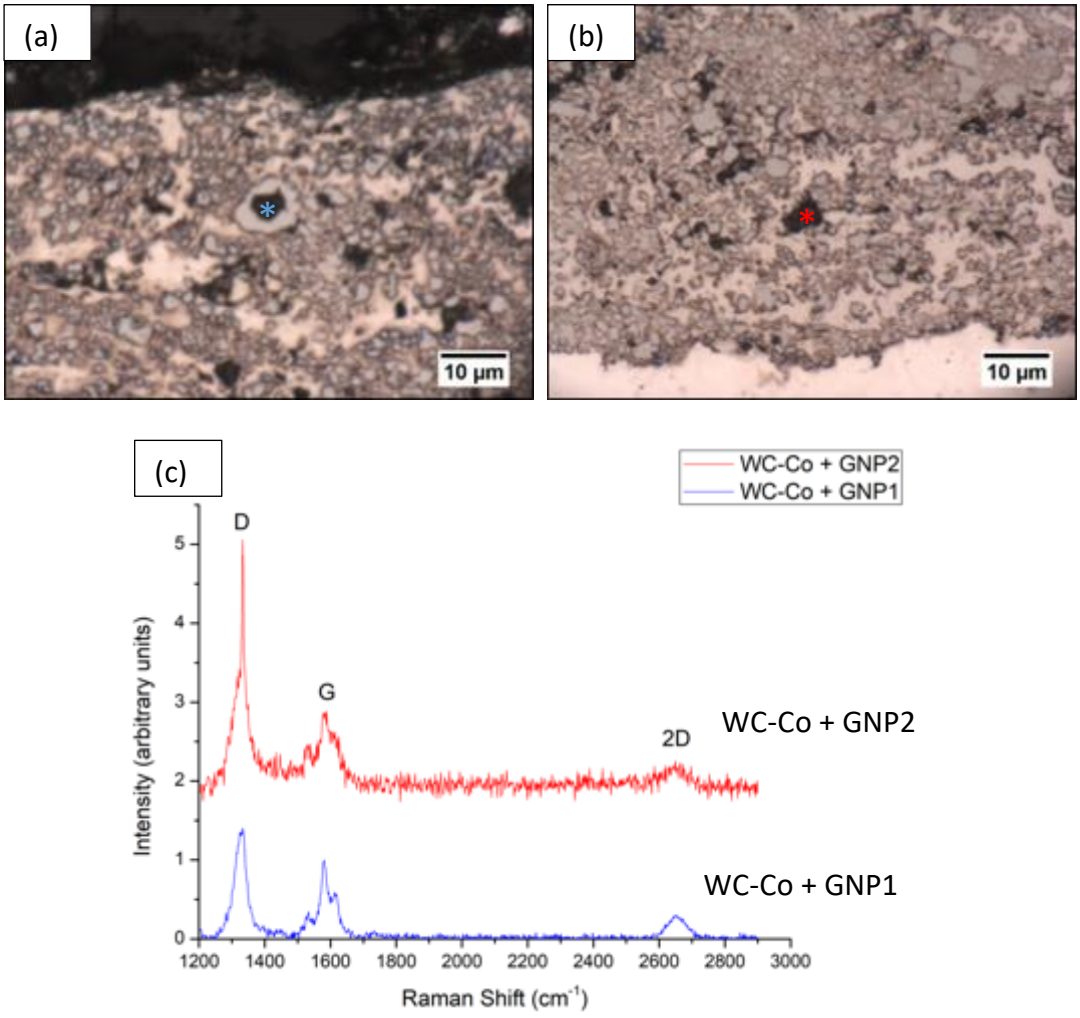


*Figure 54. Optical microscope images of (a) WC-Co + GNP1 and (b) WC-Co + GNP2 coating cross sections are shown and marked areas represent the points where corresponding Raman spectra were obtained. Spectra have been baseline corrected for fluorescence, normalised to the intensity of the G band for ease of comparison and shifted along the y-axis for clarity.*

### 5.4.2 Wear Performance

Coefficient of friction behaviour of all three coatings against WC and alumina counter body are given in Figure *55* and Figure *56*, respectively. There is not an obvious trend in the coefficient of friction graphs as a result of GNP incorporation to the WC-Co matrix. For instance, against the WC counter body at 100 rpm Figure *55*(a) WC-Co + GNP2 coating has higher steady state CoF (~0.6) while WC-Co + GNP1 coating has similar CoF as reference WC-Co coating (~0.4). On the other hand, steady state CoF for WC-Co + GNP1 coating is the highest (~0.6) while WC-Co + GNP2 coating has similar to reference (~0.4) during the repetition tests at the same condition in Figure *55*(d).

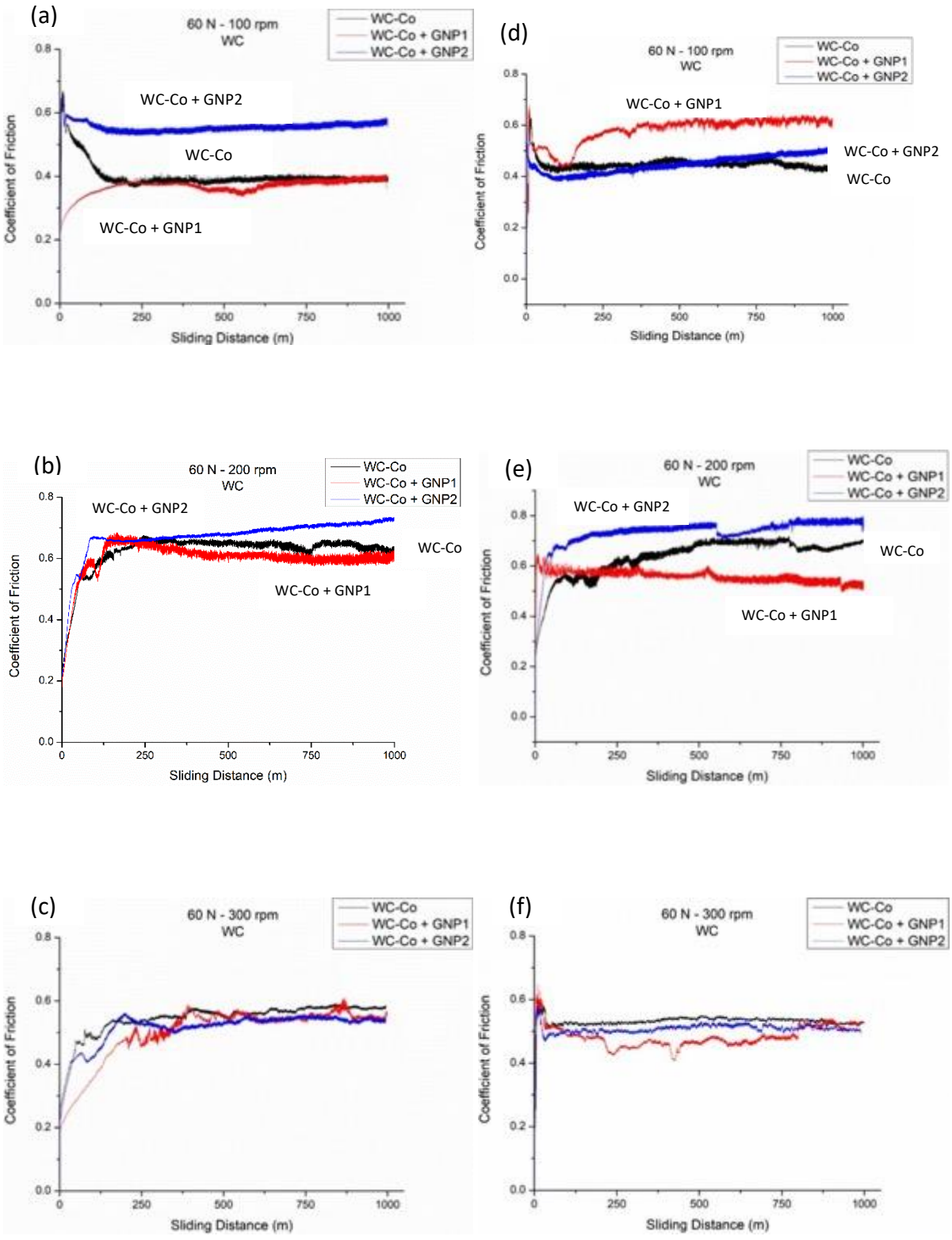


Figure 55. Coefficient of friction graphs for all three coatings against WC counter body from both test 1 and test 2. On the left graphs obtained during test 1 at 100 (a), 200 (b), and 300 (c) rpm. On the right, graphs obtained during test 2 at 100 (d), 200 (e), and 300 (f) rpm.

Furthermore, against the alumina counter body CoF for GNP incorporated coatings are similar to the reference coating. The only exception to that is the repetition tests performed at 100 rpm in Figure *56*(d) where both GNP incorporated coatings achieve nearly 0.2 lower CoF compared to the reference WC-Co coating after a significant running in period for the WC-Co + GNP1 coating. The only noticeable effect of sliding speed on the CoF behaviour is the slight increase in CoF values of all three coatings at 200 rpm against both counter bodies. Measured CoF values against alumina counter body of all three coatings are slightly higher than their counterparts against WC counter body. This difference is expected as each counter body has different hardness and composition, which can lead to different wear mechanisms and surface deformation, hence roughness. Running in periods are also present in CoF graphs of all coatings in all cases. Running in periods for coatings against alumina counter body are shorter in distance compared to their counterparts obtained against WC counter body. Against alumina counter body running in periods are always shorter than 100m and mostly limited to the first few meters of the wear test. On the other hand, most of the running in periods are 250 meters against the WC counter body. Another difference in the running in periods is the shape of the CoF curve. CoF values during the running in periods against the alumina counter body have a really sharp increase to the highest values in the first few meters then gradually decreases and stabilises. However, this is not the only trend existing in CoF graphs obtained against WC counter body. In many cases, CoF values increase gradually then stabilises around the peak value for the rest of the tests. The reason for different types of running in periods is associated with a number of changes in the tribosystem such as surface roughness, surface work hardening, oxide film formations and subsurface defect structure. CoF graphs starting with a low CoF value and gradually increasing toward a stable CoF (such as, WC-Co+GNP1 against WC counter body at 100 rpm in test 1) suggests smoother contact surfaces. On the other hand, graphs starting with a higher CoF value and gradually decreasing towards a stable CoF or reaching a peak then decreasing to a stable value ( such as WC-Co against WC counter body at 100 rpm in test 1) suggest rougher contact surfaces [210]. Overall, neither GNP1 nor GNP2 incorporation improves the CoF performance of the coatings. In addition, there is no sign of lubrication due to GNP exposure, hence only the WC-Co reference coatings worn surface characterisations was performed via SEM micrographs to analyse the wear mechanisms and effect of both speed and counter surface on the wear mechanism.

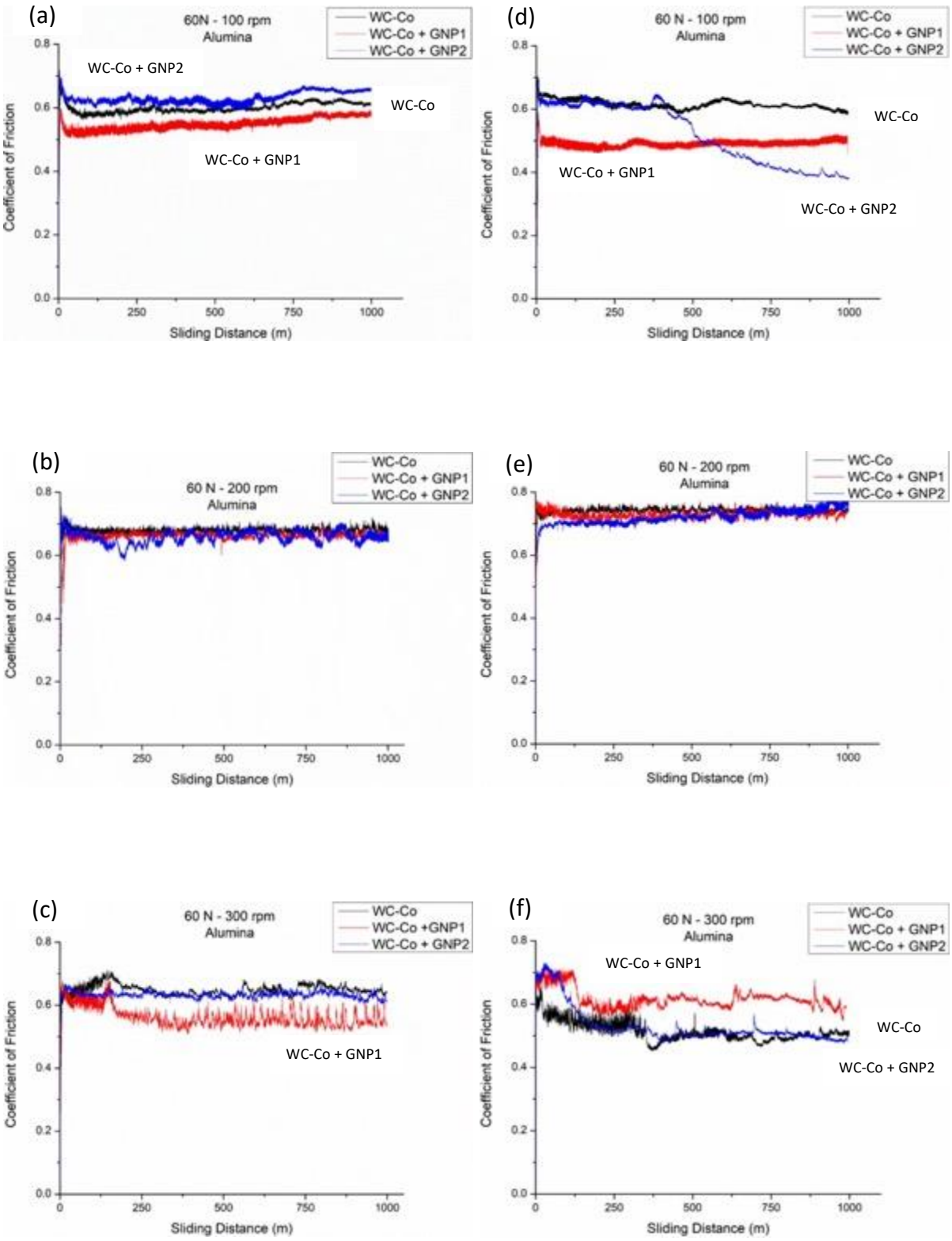


*Figure 56. Coefficient of friction graphs for all three coatings against Alumina counter body from both test 1 and test 2. On the left graphs obtained during test 1 at 100 (a), 200 (b), and 300 (c) rpm. On the right, graphs obtained during test 2 at 100 (d), 200 (e), and 300 (f) rpm.*

Averaged specific wear rates of coatings of all three coatings in all cases, corresponding counter bodies and also combined wear rates are given with the standard error of the mean in Figure *57*. Against the WC counter surface, WC-Co + GNP1 coating has a lower average specific wear rate compared to the reference WC-Co coating in all speeds Figure *57*(a). However, the difference in average wear rates is all in the range of standard error of the mean except at 100 rpm. Large error ranges obtained which recommend the inhomogeneities inside the wear tracks. The inhomogeneities around the contact point at the top of the coatings can affect the wear rates and cause large error ranges. The WC-Co + GNP2 coating has a lower average wear rate than the reference coating at 200 rpm only, which, is also the lowest wear rate achieved by a significant margin for this set of tests. On the other hand, average specific wear rates of the WC counter bodies Figure *57*(b) are reduced in both WC-Co +GNP1 and WC-Co + GNP2 coatings in all speeds. However, range of error bars was increased significantly when the rotational speed increased to 200 and 300 rpm, as the wear becomes more aggressive. In addition, an effect of sliding speed on average wear rate is not observed. Against the alumina counter surface Figure 57(d), both GNP containing coatings have lower average specific wear rates than the reference coating at all speeds. The difference in average wear rates is all in the range of standard error of the mean except for WC-Co + GNP2 coating at both 200 and 300 rpm. Alumina counter surface average specific wear rates Figure 57(e) also follow the same trend as coating specific wear rates. The effect of sliding speed is more obvious when alumina counter body was used, as increasing the sliding speed leads to higher average specific wear rates, this increase is only marginal between 100 and 200 rpm. However, at 300 rpm, the reference WC-Co coating and the WC-Co + GNP1 coatings exhibit a significant increase in average specific wear rates, which is not observed for the WC-Co + GNP2 coating. When the combined average specific wear rates Figure 57(c) and Figure 57(f) are taken into account both GNP1 and GNP2 incorporation improved the wear performance in all three sliding speeds and against both WC and alumina counter surfaces. In summary, against WC counter bodies GNP1 incorporation improved the wear resistance of both the coating and the counter surface, while GNP2 incorporation mostly improved the wear resistance of the counter surface. Against alumina counter bodies both GNP1 and GNP2 incorporation improved the wear resistance of both the coatings and the counter surfaces with WC-Co + GNP2 at 300 rpm showing the biggest improvement over the baseline. However, the main improvements were obtained at 100 rpm against WC counter body by

both GNP1 and GNP2 incorporation and by GNP2 at both 200 and 300 rpm against alumina counter body. Although there was a wide range of error for the wear rates, these obtained a lower wear rate outside the range of errors.

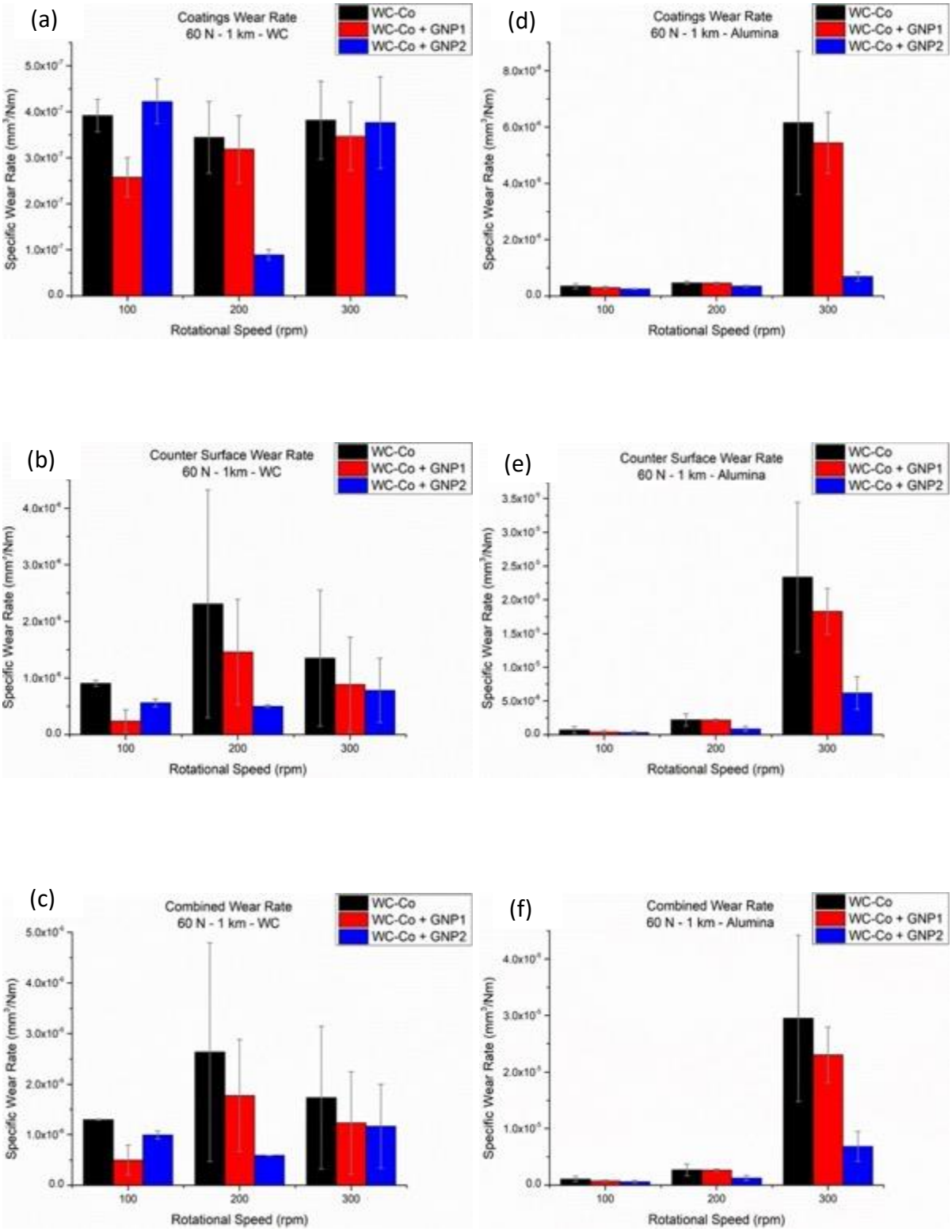


*Figure 57. The specific wear rate values with standard error of the mean for all coatings obtained from averaging results of test 1 and test 2. On the left specific wear rates of the coatings against WC counter surface (a), specific wear rates of the WC counter body (b) and combined specific wear rates (c). On the right specific wear rates of the coatings against alumina counter body (d), specific wear rates of the alumina (e) and combined specific wear rates (f).*

### 5.4.3 Worn Surface Characterisation

Wear tracks which were created by the WC counter surface at 100, 200 and 300 rpm in both SE and BSE micrographs are shown in Figure 58. At 100 rpm in SE micrograph, some parts of the coatings top surface still have smooth regions (marked with blue arrow). While, some areas were deformed by removal of flake shaped particles, where delamination regions (marked with red arrow) were formed. In the BSE micrographs, these delamination regions correspond to a darker grey contrast. EDX analysis shown in Table *7* on the area marked with a red dot shows oxygen and tungsten are the main elements present with small amounts of cobalt. This suggests tungsten (III) oxide, $WO_3$ formation and cracks can be seen around those oxides. Smooth regions cannot be seen on the surface at 200 rpm where nearly all parts of the wear track deformed. Once the rotational speed was increased to 300 rpm, the surface was aggressively damaged as it can be seen from the pull outs, cracks and fractures forming on the surface. Wear tracks which were created by the alumina counter surface at 100, 200 and 300 rpm in both SE and BSE micrographs are present in Figure 59. A similar trend was observed here as well. Increasing rotational speed from 100 rpm to 200 rpm was slightly increased the damage on the surface, while at 300 rpm the surface was again aggressively damaged. EDX analysis performed on the area marked with a red dot shows higher concentration of oxygen and also the presence of aluminium. This suggests, alumina particle transfer from the counter body to the wear track top surfaces and the amount was increased with the rotational speed. Cracks were not observed around and within the oxides in BSE micrographs this time. In both cases, delamination regions and the formed pits are clearly seen on the wear track surfaces. In the case of WC counter surface, formed pits were filled with oxides of tungsten as a result of triboxidation. On the other hand, against alumina counter surface pits were filled with transferred alumina particles. Both GNP containing coatings have wear track surfaces similar to the presented micrographs in this study and presence of GNPs has not been observed on the wear track surfaces. Therefore, those micrographs were not reported in this study.

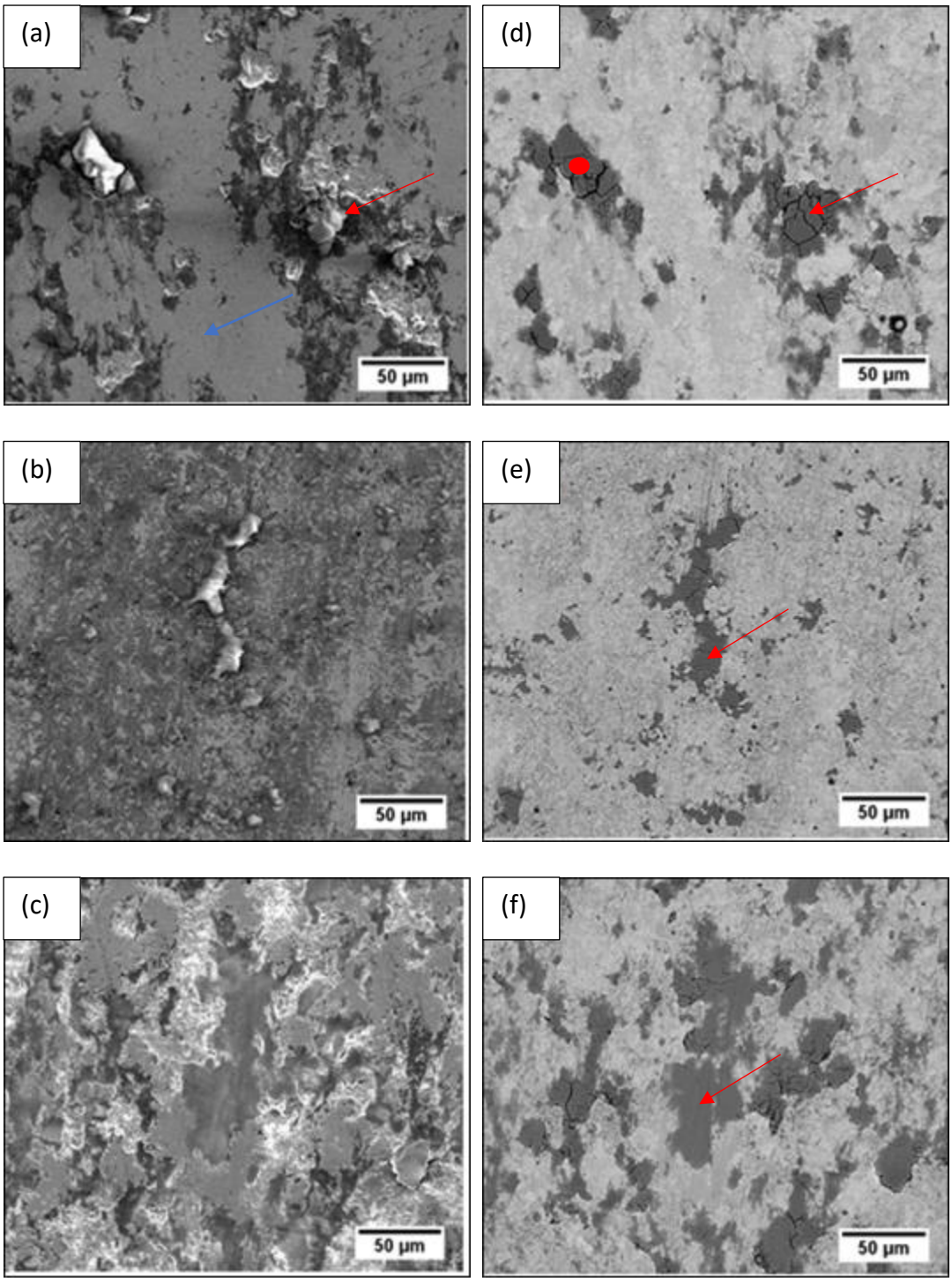


*Figure 58. On the left, SE micrographs of WC-Co wear tracks against WC counter surface at 100 rpm (a), 200 rpm (b), and 300 rpm (c).On the right, BSE micrographs of the same areas at 100 rpm (d), 200 rpm (e), and 300 rpm (f). Dark grey areas on BSE micrographs marked with red arrows represent $WO_3$ phases. Cracking around those phases can also be seen in BSE micrographs. Blue arrow on image (a) represents smooth region while red arrow represents delamination region.*

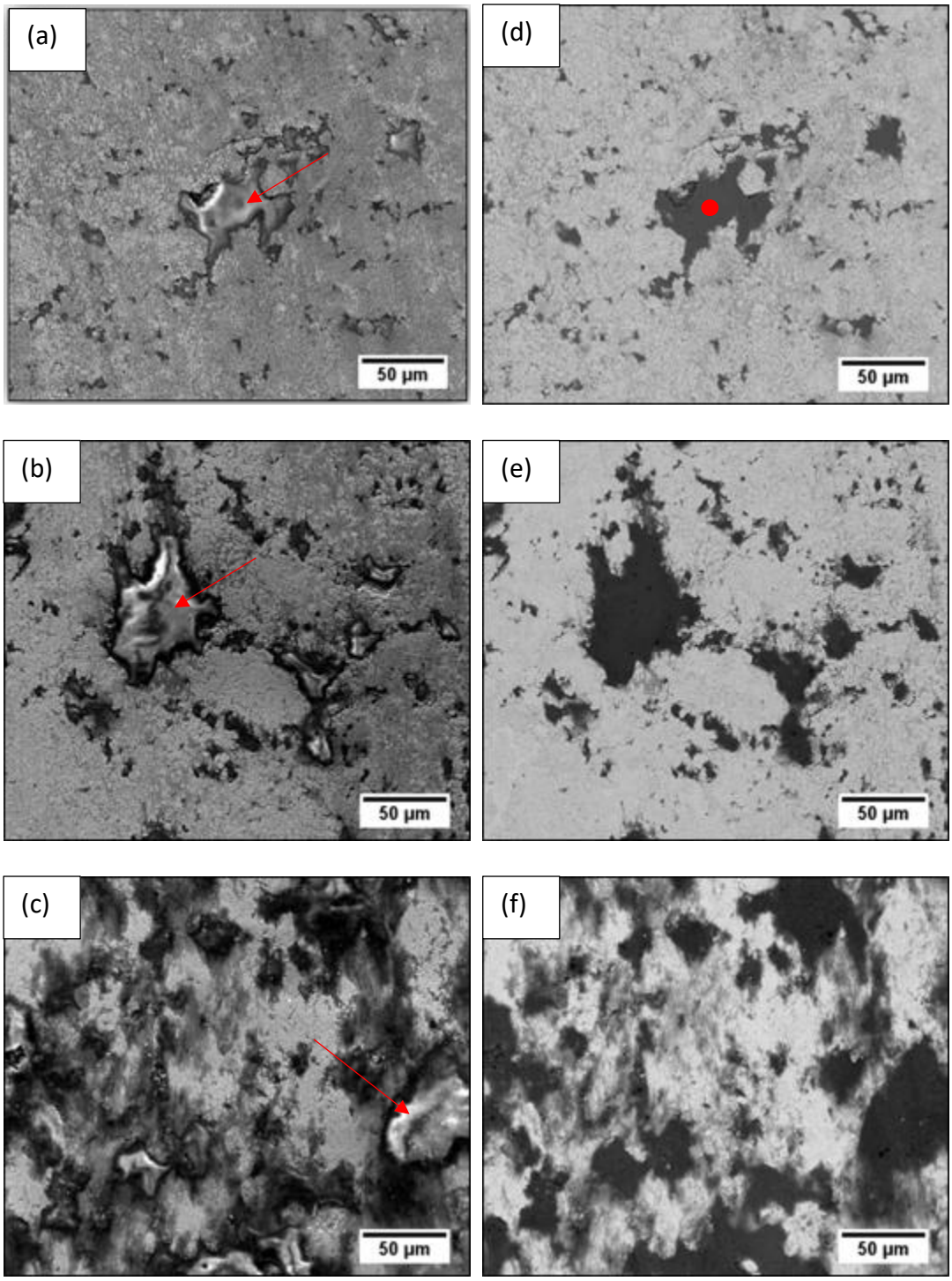


*Figure 59. On the left, SE micrographs of WC-Co wear tracks against alumina counter surface at 100 rpm (a), 200 rpm (b), and 300 rpm (c).On the right, BSE micrographs of the same areas at 100 rpm (d), 200 rpm (e), and 300 rpm (f). Alumina particles transferred from the counter surface can be seen on SE micrographs marked with red arrows. Dark grey areas on BSE micrographs represents alumina and other complex oxides formed during the wear tests*.

*Table 7: Elemental composition obtained by EDX from marked areas inside the wear tracks shown by red dots in Figure 10 and Figure 11.*

| Elements | Elemental composition (wt. %) | |
|---|---|---|
| | *WC Counter Body* | *Alumina Counter Body* |
| W | 74.1 | 41.5 |
| Co | 4.9 | 7.9 |
| O | 21.0 | 37.4 |
| Al | Na. | 13.2 |

Raman spectra obtained from all three coating wear tracks formed with the WC counter body at three different speeds are shown in Figure 60. Spectra were dominated by seven bands Two of those bands are D and G bands from carbides present at 1350 $cm^{-1}$ and 1600 $cm^{-1}$ respectively. The rest of the bands present are oxide bands arising from tungsten (III) oxide $WO_3$ (800 $cm^{-1}$) and cobalt tungstate, $CoW0_4$ (700 $cm^{-1}$,875 $cm^{-1}$ and 975 $cm^{-1}$). In addition, the band observed at the lowest Raman shift (250 $cm^{-1}$) is also arising from oxides and according to the literature it can be from either $WO_3$ or $CoWO_4$. Furthermore, no noticeable trend was present in Raman spectra as the ratio between the carbide and oxide bands fluctuate at different speeds and in different coatings, same as the average specific wear rate data. Raman spectra obtained from all three coating wear tracks formed with the alumina counter body at three different speeds are present in Figure 61. These spectra were nosier than the previous ones. As there is a material transfer and also a grooving wear mechanism taking place, wear surfaces were rougher which affects the signals to noise ratios. Spectra were dominated by four bands this time. D and G bands for the carbides are still present at the same Raman shifts. Remaining two other bands are the oxides present on the wear track surface. $WO_3$ band at 800 $cm^{-1}$ is still present in this case, however it integrates into a bigger oxide band at 900 $cm^{-1}$ Raman shifts. This band tentatively assigned as a complex oxide which probably includes aluminium and cobalt oxides and a different oxide of tungsten. The band around 950 $cm^{-1}$ is corresponds to double bond between tungsten and oxygen [211]. This also suggest change in structure of tungsten oxides found against WC counter body compared to the ones formed against alumina counter body. There is a trend present in these Raman spectra which is compatible with the trend for the average specific wear rates. Increasing the

rotational speed from 100 to 200 rpm does not have a significant effect; however, at 300 rpm, the ratio of the carbide bands to oxide bands decreases significantly which suggests surfaces deformed more aggressively and covered with more oxides instead of carbides. Another noticeable trend is in all cases WC-Co + GNP2 coating has the highest carbide to oxide ratios and also it is the coating that worn less in all cases. This again confirms the theory of wear track surfaces being predominantly carbides instead of oxides. 2D band at ~2650 $cm^{-1}$ Raman shift could not be plotted to comment about presence of GNPs on the wear tracks, because of the fluorescence effect.

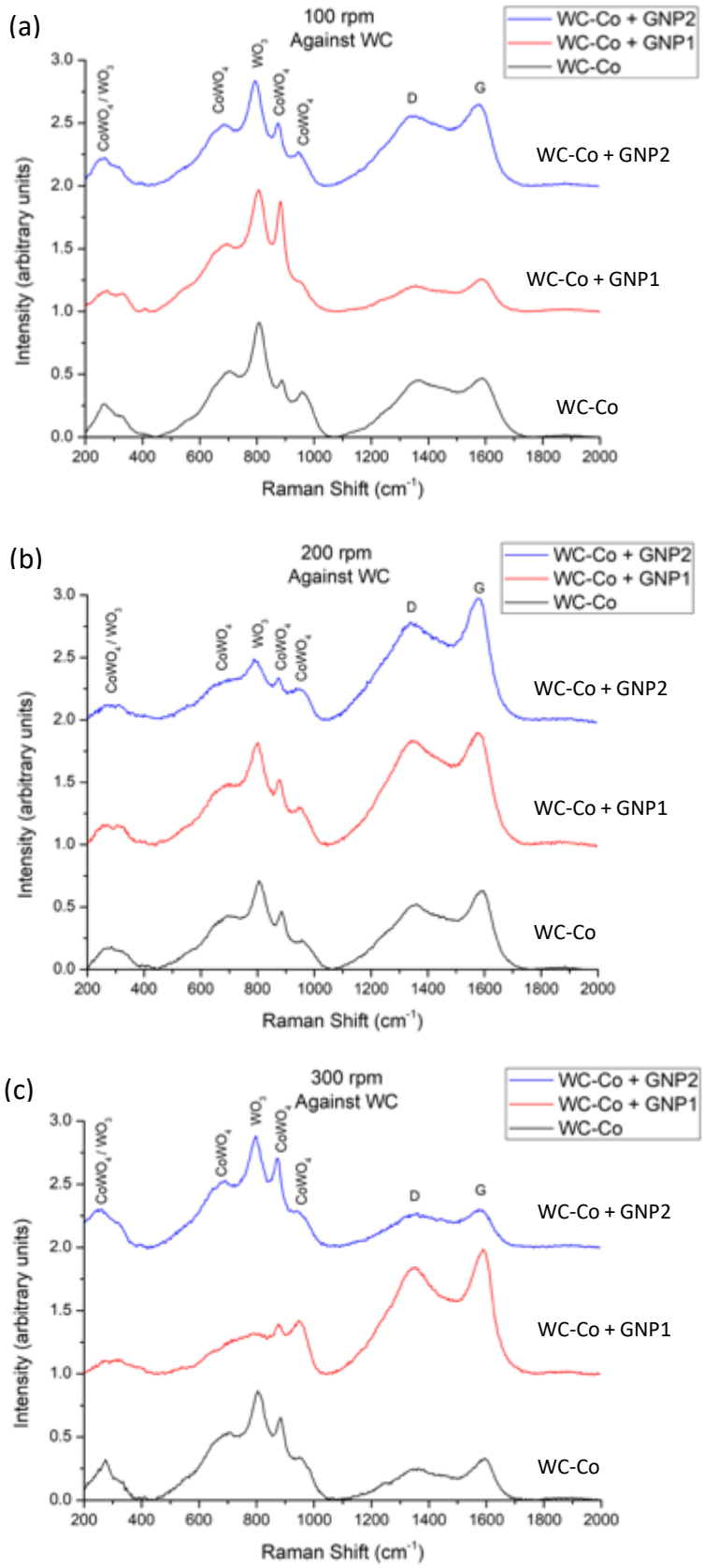


*Figure 60. Raman spectra obtained from wear tracks created by the WC counter body at 100 (a), 200 (b) and 300 (c) rpm.*

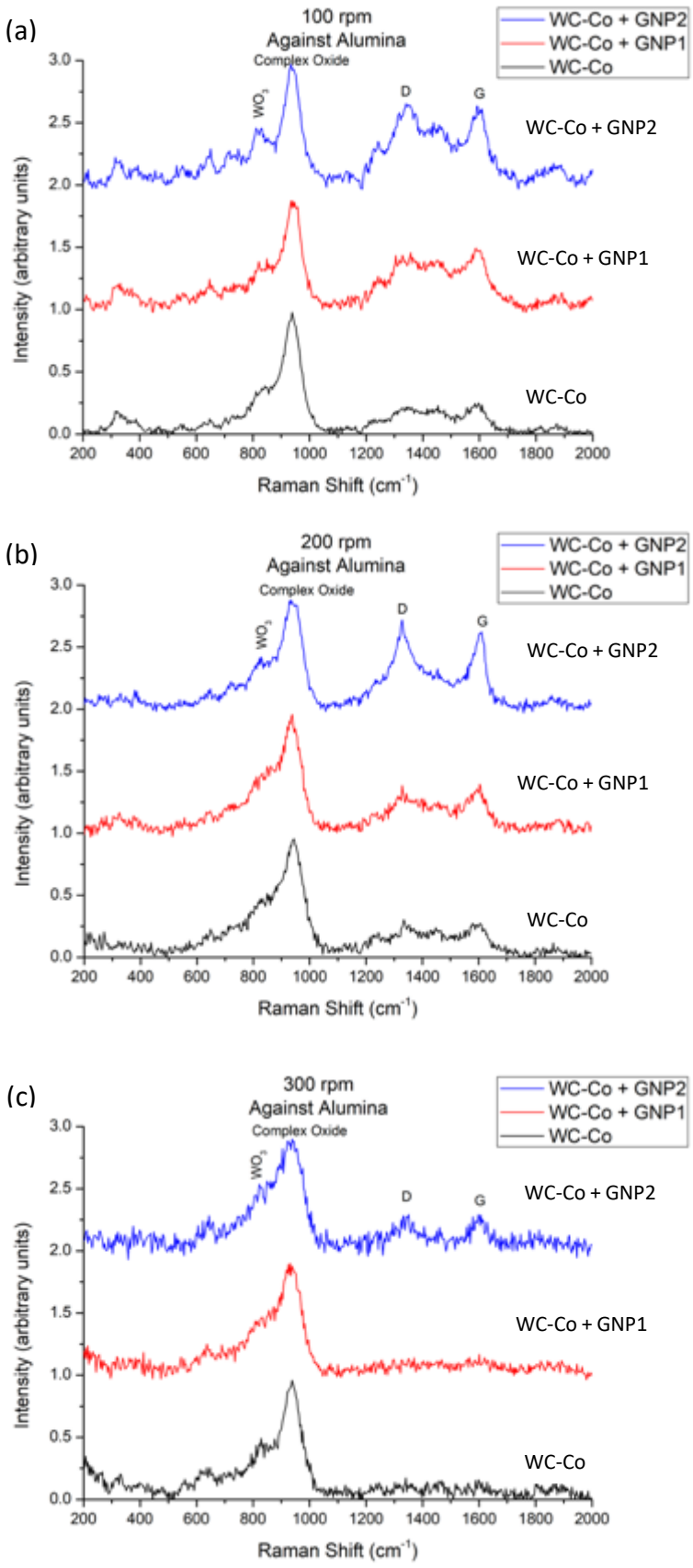


*Figure 61. Raman spectra obtained from wear tracks created by the alumina counter body at 100 (a), 200 (b) and 300 (c) rpm.*

## 5.5 Discussion

### 5.5.1 Coating Microstructure

Microstructural evolution of the WC-Co coatings deposited by HVOF thermal spray process has been studied extensively in another study [131]. Decarburization of WC-Co and formation of unwanted $W_2C$ and W phases formed as a result of high temperature and the oxygen rich nature of the thermal spray system. WC-Co particles heat up although they spend very little time inside the hot gas jet and cobalt melts. WC phases dissolves in molten Co and C also escapes from the system as a result of oxidation into CO. Fast cooling rates of splats formed on the substrates causes the formation amorphous and / or nanocrystalline binder phase which leads the formation of the broad diffuse peak between the 37°-45° 2θ angles in the coatings. Furthermore, precipitation of $W_2C$ and W phases also takes place as a result of carbon loss during the spray [129–132]. The calculated carbide retention index value (0.67) and presence of W phases inside the coatings proves a higher level of decarburization during the thermal spray process. The presence of GNPs did not noticeably affect the carbon retention index. Liquid fuelled HVOF thermal sprayed WC-Co coatings are supposed to have less decarburization and undesirable phase changes [18] because, in liquid fuelled HVOF thermal spray systems powder is injected after the combustion chamber. In this study, hydrogen gas is used as a fuel and gas fuelled HVOF thermal spray systems axially inject the powder into the combustion chamber which subjects the powder to high temperatures during the process. The presence of GNPs was confirmed by Raman, which means GNPs survived the thermal spray process. As a result of the radial injection, GNPs spent a reduced amount of time in the hotter, central part of the flame, which also reduces the chances of oxidation. In addition, in other studies where GNPs were axially injected into the combustion chamber, these GNPs still managed to survive in that condition without changing their unique structure [32,90,191,205].

### 5.5.2 Effect of GNPs on Coating Properties

GNP incorporation slightly reduced the thickness of the deposited coatings and increased the surface roughness which led to a slightly larger scatter around the mean value of the thickness than the WC-Co reference coating. In addition, GNPs prevents the bonding between successive splats which led to the formation of pores and cracks inside the coatings cross section. WC-12Co powder was in a molten or semi-molten phase during the thermal

spray, while GNPs conserved their shape and form. GNP particles positioned themselves between successive splats which prevented the interlocking mechanism between them, and pores were created around GNPs. Raman spectra shown in Figure 54 confirm this theory as the characteristic 2D band of GNPs at 2650 $cm^{-1}$ is present inside the pores of both composite coatings' cross sections. The WC-Co + GNP1 coating has the highest porosity, but it still has the same hardness as the reference coating. On the other hand, nearly 25 % reduction in hardness of WC-Co + GNP2 coating was observed. Hardness measurements were performed by using a 500 gf (5N) load. This load was chosen as it creates indents with measurable diagonals without cracking in the middle of coating cross section. However, it is relatively high to form the indent within a single splat [132]. Therefore, porosity and the bonding strength between the successive splats can affect the hardness value of the coatings. Although both coatings are porous only GNP2 incorporation reduces the hardness suggesting that the GNP particle sizes, and surface areas are the main contributor on the hardness and hence on bonding between the splats. GNP2 has a higher specific surface area leading to more forces of attraction so bigger aggregates of GNP particles. This can create bigger / wider pores which can explain the reduced hardness and bonding strength between splats.

### 5.5.3 Wear Performance

#### 5.5.3.1 Effect of Sliding Speed

Coefficient of friction values for all coatings, generally against both counter bodies increased as the rotational speed increased from 100 rpm to 200 rpm, and then decreased at 300 rpm. There are a few exceptions such as WC-Co coating against WC during the first test, as a result of high sensitivities to small changes such as humidity, temperature and coating inhomogeneities. Increasing rotational speed from 100 to 200 rpm causes more damage, deformation and asperity formations on the surface leading to a slightly rougher surface, and as a result CoF increases. However, at 300 rpm the surface undergoes severe deformation and becomes significantly rougher as CoF decreases compared to 200 rpm (Figure 55 and Figure 56). The speed influences the interface temperature during a wear test and at higher speeds only limited amount of heat can be conducted away from the interface. Higher interface temperature leads to rapid growth of oxides as a result of chemical reactivity and also reduces the mechanical strength of asperities and near surface materials, which reduces the effect of increased surface roughness on the CoF behaviour [212]. Increasing the

rotational speed did not have a noticeable impact on the wear rates when a WC counter body was used; however, a trend related to the speed was observed against the alumina counter body, there is a direct proportional relationship between the rotational speed and specific wear rate. There was a sharp increase in wear rate at 300 rpm, which was a result of the brittle nature of the alumina. At 300 rpm, alumina counter body deforms catastrophically, which leads to a massive increase in the contact area and more alumina transfer from the counter body to the coating. Increase in contact area made the wear tracks wider, while more alumina transfer created more ploughing grooves on the surface and made the wear tracks deeper. As the wear tracks are getting deeper and wider at the same this leads to more than five times increase in specific wear rate. The WC-Co + GNP2 coating was the only exception to that, which will be explained in the section 5.5.3.3

#### 5.5.3.2 Effect of Counter Bodies

Now looking into the effect of Counter bodies, CoF values obtained against alumina counter body are slightly higher than the ones obtained against WC counter body. This is an expected result as both materials lead to different wear mechanisms and similar results reported in another study [213]. Using different counter bodies changes the type of wear mechanisms taking place. Against WC counter body in all coatings and at all speeds, $WO_3$ phase was obtained on the wear track surfaces. As a result of contact stresses, coatings were pulled out at the contact area around the weakly bonded splats and decarburised areas, leaving behind pits. Pulled out materials oxidise into $WO_3$, as a result of friction and heat generation between the coating and the counter body. This oxidised wear debris fills the pits formed on the surface [214,215]. However, against alumina counter body, top surface of the coatings is mostly covered with aluminium oxide particles suggesting a material transfer taking place between the bodies in contact. Alumina grains pulled out during the wear test as a result of intergranular and / or transgranular crack propagation depending on the grain sizes, when the critical contact pressure was reached [216]. During the wear tests against the alumina counter body, weakly bonded splats and decarburised areas were pulled out. [217,218]. This leaves behind small pits which were filled with the alumina debris in this study. However, there is no paste or tribofilm formation observed such as the one mentioned in [218].

#### 5.5.3.3 Effect of GNPs

Broad error ranges obtained for wear rates affected by the inhomogeneity of the coatings as a result of GNP addition. Plastic deformation and hence wear rate is dependent on localised properties such as subsurface defects at the contact point, porosity, the formation of cracks, grain pull outs and surface roughness. The presence of the randomly distributed pores and crack as a result of GNP addition, around the contact area can lead to higher wear rates, however, the presence of GNPs around the contact area can also lead to exposure of GNPs and formation of GNP tribofilm or a solid-state lubricant which can reduce the wear rates."The fluorescence effect in Raman masks the 2D peak, if there is any, which could be used to confirm the presence of GNPs inside the wear tracks. This limitation prevents conclusive comments to be made on the presence of GNPs inside the wear tracks and formation of a lubricative tribofilm. However, CoF graphs do not show a reasonable reduction which suggests there was no lubrication as a result of GNPs, or the amount of GNPs exposed during the tests were so small that it is not enough to create a tribofilm and protect the surfaces in contact. In addition, the wear tracks formed during the test were not deeper than 10 microns which reduces the chances of GNP exposure from the underlaying layers of the deposited coatings. Although tribofilm formation or the lubricative ability of GNPs are not observed, the significant improvement obtained in WC-Co + GNP2 coating at 300 rpm against alumina counter body is a result of GNP addition. Incorporation of GNPs introduces porosity and reduces the hardness of WC-Co +GNP2 coatings which makes it 25% softer than the other two coatings. As this coating is softer than the others, less deformation is happening on the alumina counter body. Therefore, the contact area between the surfaces remains smaller and less material transfer between the surfaces prevents the damage of the coatings.

## 5.6 Conclusion

In this study, composite coatings of WC-Co with graphene nanoplatelets were produced by using two different feedstocks simultaneously via hybrid injection HVOF thermal spray. Using two different feedstocks eliminates the powder mixing and / or suspension preparation stages before the thermal spray. This also allows to spray submicron sized particles in a suspension together with micron sized powders. There was a significant amount of decarburization and dissolution of WC-Co during the process. Both composite coatings have a porous microstructure and Vickers microhardness of WC-Co + GNP2 was reduced by 25%.

However, the wear performance of both coatings is promising. Both composite coatings showed improved wear performance against alumina counter surface at all speeds and also counter surfaces were less damaged as well. Against WC counter body just WC-Co + GNP1 coating wore less than the reference WC-Co coating in all three cases. However, when combined wear rates are considered, both coatings outperformed the reference one in all cases again against WC as well. Wear rates obtained against WC in all three speeds and against alumina in both 100 rpm and 200 rpm are relatively in the same range. However, against alumina at 300 rpm there was a significant increase in wear rates. Different wear mechanisms hence different oxide formations took place as a results of different counter bodies Furthermore, rotational speed did not have a significant effect on the wear rate unless it reaches to a critical level which causes catastrophic deformation of ceramic alumina counter surface. Neither lubricative ability of GNPs nor tribofilm formation were observed, which suggested that the wear performance improved due to alteration of mechanical properties as a result of GNP addition. This study suggests, GNP incorporation into WC-Co coatings has promising results for improving the wear performance of the popular WC-Co cermet coatings used in many industries. Further work on optimising the amount of GNPs present inside coatings are required to analyse if increased number of GNPs inside the coatings can contribute the GNP pull out and tribofilm formation to contribute further into wear resistance properties.

## 5.7 Acknowledgements

This work was supported by the Engineering and Physical Sciences Research Council [Grant Number EP / M50810X/ 1]. This work was supported by Rolls – Royce plc; in the form of a CASE Ph.D. studentship. The authors thank the Nanoscale and Microscale Research Centre (nmRC) for providing access to instrumentations. The authors also acknowledge John Kirk at the University of Nottingham for conducting the HVOF thermal spray.

# Chapter 6: CoCrAlY + hBN composite coatings deposited by high velocity oxy fuel (HVOF) thermal spray for high temperature (900 °C) wear

## 6.1 Abstract

In this study, CoCrAlY powder was mixed with submicron-sized hBN powder to produce composite CoCrAlY + hBN coating using a liquid-fuelled HVOF thermal spray. The effect of hBN addition on the microstructure and mechanical properties of the coating was investigated. The presence of characteristic hBN band around ~ 1350 $cm^{-1}$ Raman shifts confirms the survival of hBN during the thermal spray process. The results showed that hBN addition reduced the thickness and surface oxide formations of the coating during thermal spray by affecting the in-flight characteristics of the CoCrAlY powder in the flame. Although the microhardness of the coating was not affected by the hBN addition, its fracture toughness was reduced. The wear performance of the coatings was investigated in an unlubricated sliding wear test using a ball on disc setup at a high temperature (900°C). The results showed that hBN addition reduced the wear resistance of the coating due to reduced fracture toughness. Brittle deformation and fracture was the main mechanism observed on the worn surfaces for composite coating, while plastic deformation was observed in the reference CoCrAlY worn surfaces. The hBN addition prevented the formation of surface oxides powder during thermal spray. Therefore, hBN can be used to spray powders that are sensitive to oxidation, phase segregation or decarburisation.

Keywords: HVOF; hBN; Nanocomposite; thermal spray; wear; coating

## 6.2 Introduction

Hexagonal Boron Nitride (hBN) is a well-known solid lubricant with a similar layered structure to graphite and is sometimes referred to as white graphite. hBN has a very low density, chemical inertness, high melting point, low friction, high oxidation and wear resistance. Hexagonal boron nitride is the preferred solid lubricant for high-temperature applications to improve wear resistance and reduce the coefficient of friction (CoF) as it outperforms other solid lubricants such as; graphite and molybdenum disulphide [38,110]. It is widely used as an additive to improve the high temperature performance of the coatings

deposited via various techniques such as; electrodeposition, laser cladding and thermal spray. The addition of hBN into the coatings increased the mechanical properties once its concentration was optimised. In addition to improvements in mechanical properties, hBN particles acted as a solid lubricant and reduced the coefficient of friction at high temperatures and hence improving the wear resistance of the composite coatings [38,111–114].

MCrAlY coatings are used in high-temperature oxidation and corrosion resistance of underlying alloy in gas turbines. M refers to a metal that can be Nickel, Cobalt or a combination of both [123–125]. NiCoCrAlY coatings usually have higher oxidation and corrosion resistance than the NiCrAlY coatings, and CoCrAlY coatings are mainly used for cobalt-based superalloys to improve sulphur corrosion resistance [147,152]. MCrAlY coatings can be deposited via various thermal spray techniques, including air plasma spray, low-pressure plasma spray, vacuum plasma spray, high-velocity oxy-fuel (HVOF) thermal spray, and cold spray. However, HVOF thermal spray is favourable over plasma spray for MCrAlY coating deposition due to fewer defects, oxide content, and higher bond strength [147–151].

Thermal spray is a popular and widely used coating deposition technique in the industry for deposition of wear, erosion and corrosion-resistant coatings. It is a cost-effective, fast and reliable way of depositing dense coatings with various microstructures at different thickness ranges. It also allows the usage of various feedstock materials such as; nanostructured powders, suspension and solution precursors [10,33,219,220]. In thermal spray, a stream of feedstock particles is injected into the flame and converted into a molten and/or semi-molten state in the flame that is deposited onto a substrate as a result of plastic deformation upon impact at high velocity. There is a wide range of thermal spray techniques available, and they are classified by way of heat source and feedstock types. High-velocity oxy-fuel (HVOF) thermal spray is a process where oxygen and fuel are used to create a supersonic combustion jet. In HVOF thermal spray, the fuel can be either a gas (hydrogen, ethylene, propane, etc.) or a liquid (kerosene). These are injected into a combustion chamber together with oxygen, where an ignition initiates combustion and the exhaust gas travel through a nozzle. Depending on the type of HVOF spray, feedstock powders are injected either radially inside the barrel (after the combustion chamber) or axially inside the combustion chamber [7,120]. HVOF thermal spray is the preferred method over many other thermal spray processes such as plasma spraying to deposit dense, well-bonded metallic coatings with a lower degree of

decomposition. The combustion in an HVOF torch generates higher particle velocities with lower temperatures than other thermal spray processes [120,221]. Therefore, the degree of oxidation, decomposition and decarburisation of the feedstock materials are lower, which can directly impact the mechanical properties of the deposited coatings [140,202,203].

In this study, CoCrAlY and hBN powders were mixed to form a unique powder to use as a feedstock material. A composite CoCrAlY + hBN coating and a reference CoCrAlY coating were produced using a liquid-fuelled HVOF thermal spray. This composite coating was chosen to obtain the combined high oxidation and corrosion resistance of CoCrAlY and high temperature wear resistance and self-lubricating ability of hBN. The microstructure of the deposited coatings was analysed and compared. Properties of the coatings such as microhardness, porosity and oxide content were investigated, and the effect of hBN addition on these properties was studied. Following this analysis, the tribological performance of both coatings at an elevated temperature, using the ball on disc wear test arrangement, was studied. The wear performance of the coatings and the effect of hBN addition on the performance was investigated.

## 6.3 Materials & Methods

### 6.3.1 Powder Feedstock & Coating Deposition

Two different powders were used as feedstock in this study. A gas atomised cobalt, chromium, aluminium and yttrium (CoCrAlY) metal powder (Amdry 920, Oerlikon Metco, Switzerland), with a chemical composition of 67.0-58.5 wt. % Cobalt (Co), 27.0-31.0 wt. % Chromium (Cr), 5.0-7.0 wt. % Aluminium (Al), 1.0-3.0 wt. % Silicon (Si), and 0.05-0.5 wt. % Yttrium (Y). The CoCrAlY powder had a spheroidal morphology and 38 ± 5.5 µm nominal particle size distribution, stated by the supplier. A hexagonal boron nitride (hBN) powder (Henze, Germany) with 98.5% purity was selected as the 2D additive to form a composite powder together with CoCrAlY. The hBN powder had a 20 $m^2/g$ specific surface area and median grain size ($D_{50}$) of 2.0 µm, stated by the manufacturer.

CoCrAlY + 1 wt. % hBN composite powder was prepared according to a novel procedure that allows the incorporation of nanomaterials into cermet powders [222]. CoCrAlY and hBN powders were added into a 95% distilled water and 5% acetic acid aqueous solution, which had a pH of 3. The amount of hBN added was 1 wt. % of the CoCrAlY used. The mixture was

stirred at 1500 rpm for 1 hour, then dried in a cabinet to evaporate the acidic aqueous solution. The obtained composite powder was also dried overnight inside a drying cabinet at ~100°C before the thermal spray to eliminate the moisture and increase the flowability of the powder. Powder flowability was measured according to the ASTM standards B 213-03, which is the time taken to flow a 50 g sample of powder from calibrated orifice funnel (diameter = 2.54mm). Only 1wt. % hBN was used in this study. According to the literature review chapter addition of higher weigh percentages of 2D materials causes degradation of mechanical properties. In addition, their extremely low density lead to flowability and cloaking issues during the thermal spray. Therefore, 1 Wt.% was chosen as it has worked on the previous chapters with GNPs.

AISI 304 stainless steel substrates with dimensions of 60 x 25 x 2 mm with nominal composition Fe-19.0Cr-9.3Ni-0.05C (all in wt. %) were used as substrates. Substrate surfaces were grit blasted with a blast cleaner from Guyson (Dudley, United Kingdom) at 6 bars with F100 brown aluminium oxide particles (0.125-0.149 mm). Before thermal spray, the substrate surfaces were cleaned with industrial methylated spirit (IMS) and compressed air.

Coatings were deposited onto the grit-blasted stainless-steel substrates with a Met-Jet L4 (Metallisation Ltd, England) liquid-fuelled HVOF thermal spray system. Detailed explanations about this thermal spray setup and schematic can be found in other studies [223,224]. Two different spray runs were performed with different feedstock powders. CoCrAlY powder was injected at a rate of 70.4 g/min for the first run to deposit reference CoCrAlY coatings. Later, CoCrAlY + 1 wt. % hBN mixed powder was injected at a rate of 60.8 g/min to deposit CoCrAlY + hBN composite coating. Oxygen and kerosene flow rates used were 878 l/min and 445 ml/min, respectively. These flow rates led to a 100% oxygen stoichiometric ratio [223]. A 100% stoichiometric ratio is the optimum amount or ratio for a complete combustion reaction, where all the reagents are consumed. Combustion gases and the metal powder were accelerated towards the substrates through a nozzle, which has a length of 100 mm. Substrates were attached to a rotating carousel with a diameter of 260 mm and positioned at a 355 mm stand-off distance. The carousel rotated with a speed of 73 rpm during the spray runs which gives rise to a 1 m/s linear velocity for the attached substrates. Simultaneously, the spray gun moves vertically with a traverse speed of 5 mm/s, which leads to a 4 mm overlap between tracks from subsequent passes [26].

### 6.3.2 Wear Test

Unlubricated rotational sliding wear tests were performed at an elevated temperature (900°C). A rotary tribometer with a ball on disc arrangement, equipped with a built-in furnace (Ducom Instruments, The Netherlands) was used for the tests. 6 mm alumina (99.9% aluminium oxide) balls (Dejay distributions, United Kingdom) were used as counter bodies, which have a surface finish of 0.038 µm and hardness value of 91 on the Rockwell A scale (~2000HV) as stated by the supplier. Circular wear tracks of 10 mm diameter were created onto the deposited coatings under varying loading conditions (10 N and 30 N). Both as-sprayed samples, which had a surface roughness ($R_a$) value of 5.65 ± 0.08 µm were rotated at 100 rpm against the stationary counter body, giving a linear speed of 52 mm/s. Each test was performed for 2 hours and 39 minutes to reach a total sliding distance of 500 m. Therefore, high temperature exposure of the coatings was 2 hours 39 minutes. Once the tests were completed, coatings were cooled down to room temperature. Two tests were conducted for each condition. As the coating is much softer than the counter body and the testing will be performed at elevated temperatures, lower loading conditions ( 10 N and 30 N ) were chosen compared to the previous chapter.

The volume loss of each wear track was measured at four different points using a Talysurf Form 50 contact profilometer (Taylor Hobson, United Kingdom) along with a diamond stylus with a tip radius of 2 µm and lateral resolution of 0.5 µm. Mountains map software (Digital Surf, France) was used to calculate the cross-sectional area of the wear tracks from the line profiles, which were converted into volume loss by multiplying by the circumference of the circular tracks, which is the total length of the wear track [130,206]. In total, eight different points were used to calculate the average and standard error of the mean for each sample. The specific wear rate of both the coatings was calculated from the volume loss, dividing it by applied force and total sliding distance.

### 6.3.3 Feedstock, Coating & Worn Surface Characterisation

Microstructural characterisation of the powder feedstocks, the deposited coatings and the worn surfaces were performed with a Quanta 600 scanning electron microscope, SEM (FEI, The Netherlands) in both secondary electron (SE) and backscattered electron (BSE) modes with 10 kV and 20 kV accelerating voltages, using a spot size of 5 and a working distance of 13 mm. Cross sectional samples of the coatings were prepared by cutting the

samples with a diamond cutting disk, followed by sequential silicon carbide (SiC) grinding and diamond polishing with a final grit size of 1 μm. Cross sectional sample for the powder was prepared by hot mounting the powder in the resin and following the same grinding and polishing sequence mentioned above. Both porosity analysis and the oxide content of the coatings were performed on 5 different BSE micrographs for each coating obtained from the SEM at 2000X magnification from the centre of the coatings, which gives rise to an area of 70 μm x 60 μm. Oxides were identified as darker grey phases on the BSE micrographs. The contrast threshold function on ImageJ software [208] was applied to the micrographs according to ASTM E2109 standards to estimate the percentage area fraction in each BSE micrograph. An average value for both porosity and oxide content and the standard error were reported in all cases.

X-ray diffraction (XRD) was performed on the CoCrAlY powder feedstock, CoCrAlY + hBN mixed powder, deposited coatings and the coatings' top surface after the high temperature wear test to analyse the phase changes. A Bruker D8 Advance diffractometer (Bruker, USA) in θ-2θ Bragg-Brentano geometry was used, the diffractograms were acquired with Cu $K_\alpha$ radiation (1.5406 Å) setting a step size of 0.02˚and a time per step of 0.1 s. in the 20° ≤ 2θ ≤ 100° range.

Raman spectroscopy was performed on a LabRAM HR spectrometer (Horiba Jobin YVON, Japan), modified by the addition of an automated xyz stage (Märzhäuser, Germany). A standard Si (100) reference band at 520.7 $cm^{-1}$ and the Rayleigh line at 0 $cm^{-1}$ was used to calibrate the instruments before the spectrum collection. Spectrum was obtained from the as-sprayed coating top surface by using a green laser which has a wavelength of 532 nm together with a 300 μm pinhole and an objective yielding 100X magnification. A 300 lines/mm rotatable diffraction grating was employed for scanning a range of Raman shifts during each acquisition. A Synapse detector (Horiba, Japan) was used to detect the signals to create the spectrum. The spectrum was collected for 20 seconds and repeated 3 times to eliminate artefacts (cosmic spikes) generated by cosmic rays and to improve the signal to noise ratio. The linear baseline subtraction function was used on Labspec 6 software (Horiba Jobin YVON, Japan) to correct the spectrum and eliminate any residual fluorescence.

The coating microhardness was measured via a Vickers microhardness indenter (Buehler, USA) on polished cross-sections. 300 gf load with a dwell time of 10 seconds was

applied to create 5 indents in the centre of the coatings, parallel to the substrate. The average hardness value with the standard error was reported in all cases. Fracture Toughness of the coatings was measured using the indentation fracture toughness (IFT) method together with the palmqvist crack model described by Evans and Wilshaw, which [225] was also used in the literature for HVOF thermal sprayed coatings [214,226]. The same microhardness instrument was used by increasing the loads to form indents with cracks on the polished cross-sections. Indents for fracture toughness measurements led to cracks in CoCrAlY + hBN coating cross-section under 500gf (~5N) load, but CoCrAlY coating did not have any crack even at higher loads up to 20N.Further increase in load was not possible as the indents were starting to be wider than the thickness of the coating.

## 6.4 Results & Discussion

### 6.4.1 Feedstock & Coating Characterisation

CoCrAlY powder cross-section and morphology were studied by using (BSE) micrographs shown in Figure 62(a and b). The metal powder had a spheroidal morphology, and the particle size was varied from 10 to 50 µm, which is in line with the stated nominal particle size distribution (38 ± 5.5 µm) by the supplier. The powder was free from porosities and there was only one phase present, as there were no different contrasts present in the BSE micrographs. XRD diffractogram shown in Figure 64 (a) also confirmed the presence of a single phase in the CoCrAlY metal powder, which was the crystalline CoCr phase. The hBN powder morphology was studied by using the secondary electron (SE) micrographs shown in Figure 62 (c and d). The powder had flake-like shapes and the particle size was varied from a few microns up to 20 microns. The stated median grain size (D50) was 2 µm; however, particles tended to agglomerate into bigger chunks, which is common in 2D and nano-materials such as graphene and hBN [54,219,227]. The XRD diffractogram shows the hBN powder only consisted of the BN phase (Figure 64(a). The manufactured CoCrAlY + 1 wt. % hBN mixed powder morphology was studied by using both BSE and SE micrographs as shown in Figure 62(e and f). Both spheroidal CoCrAlY and flake hBN powder morphologies were conserved during the powder mixing process. hBN particles in the mixture were labelled by blue arrows shown in Figure 62(e and f). XRD diffractograms for both mixed powder and CoCrAlY metal powder were the same, and only the CoCr phase was detected in the mixed powder due to the detection limit of XRD. BN phases were not present in the mixed powder

XRD diffractogram as only 1 wt. % hBN powder was used. Both morphology and XRD analysis confirmed the powder mixing process did not alter the initial starting powders. Although neither the morphology nor the structure of the CoCrAlY metal powder was changed during the mixing process, the addition of hBN reduced the flowability of the powder. 21.5 seconds were needed for 50 g CoCrAlY powder to flow from the calibrated orifice funnel with a diameter of 2.54mm. In the case of CoCrAlY + hBN mixed powder, the time increased to 36.5 seconds, nearly an increase of 70%. In another study performed on mixing hBN with $Ni_3Al$ metal powder, a reduction of powder flowability was also observed due to the presence of hBN [114]. Reduction in flowability explains the lower powder injection rate during the thermal spray of CoCrAlY + hBN mixed powder, as all other parameters were kept constant.

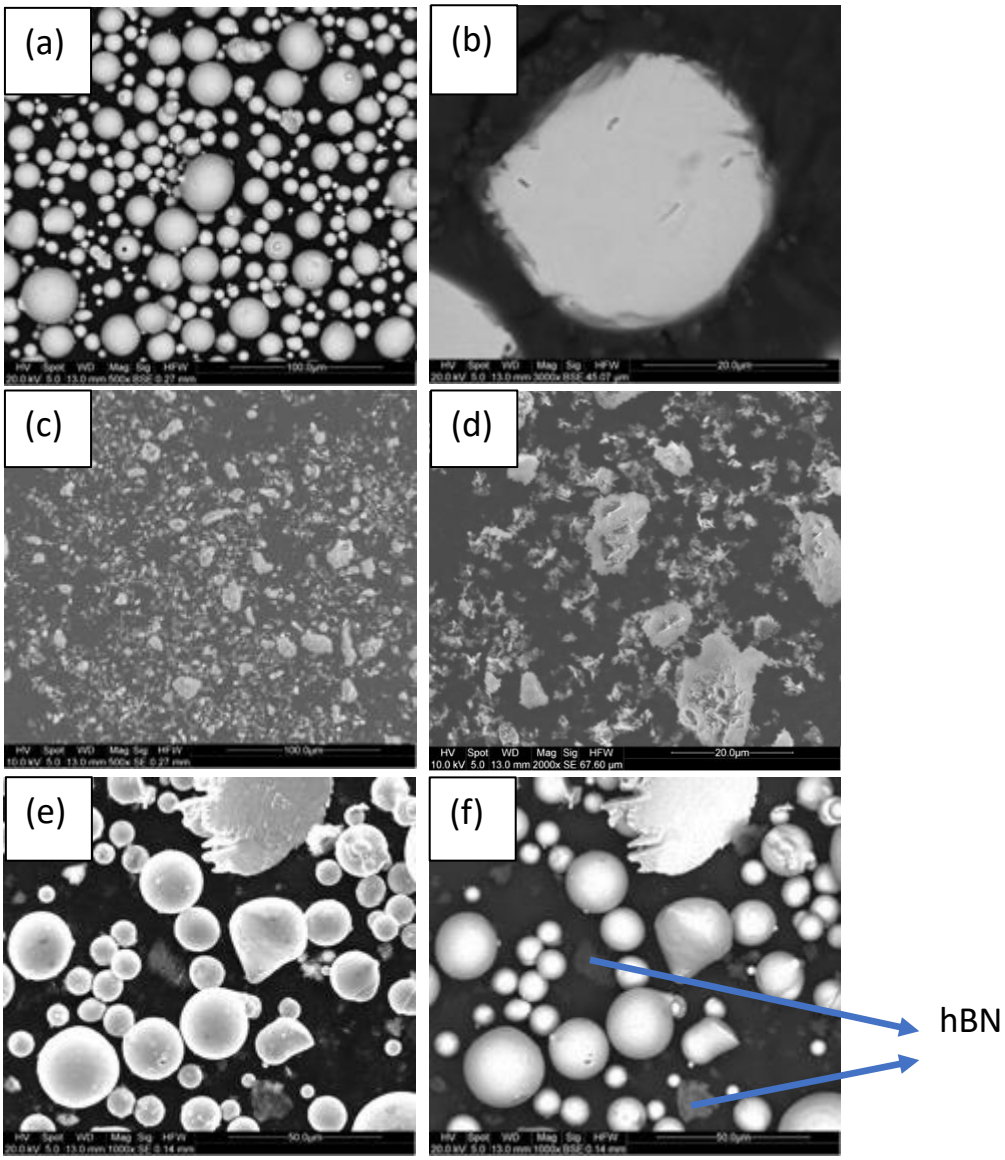


*Figure 62: BSE micrographs showing the CoCrAlY powder morphology (a) and cross section (b), SE micrographs of hBN powder in both low (c) and (d) high magnification and CoCrAlY + 1 wt. % hBN mixed powder in SE (a) and BSE (b) micrographs.*

Raman spectrum obtained from the as-sprayed CoCrAlY + hBN coating is shown in Figure 63. The band is present around ~ 1350 $cm^{-1}$ Raman shifts are the characteristic band of hexagonal boron nitride [228]. The presence of this band confirms the survival of hBN during the thermal spray and the presence of hBN in the coating microstructure. BSE micrographs showing the cross-section of the coating are shown in Figure 66. Both CoCrAlY and CoCrAlY + hBN coatings showed a good bonding interface with the substrates but the CoCrAlY coating was nearly 4 times thicker than the CoCrAlY + hBN composite coating (Figure

62 (a and d)). The CoCrAlY coating had a thickness of ~ 275 µm while the thickness of the composite coating was ~ 75 µm.

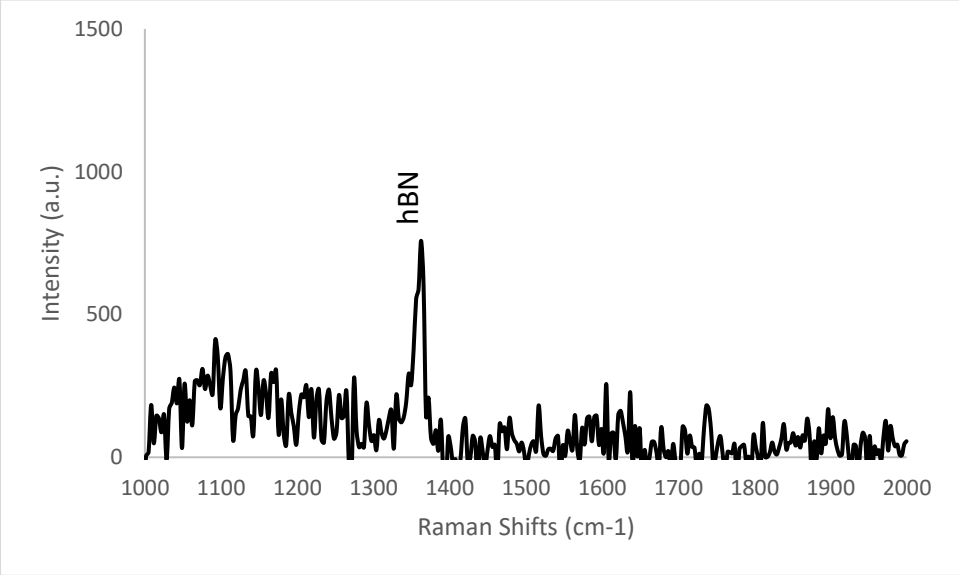


*Figure 63: Raman spectrum obtained from as-sprayed CoCrAlY + hBN coating top surface. The band present around 1350 cm-1 Raman shifts is the characteristic band of hBN*

Phase segregation took place during the coating deposition as can be seen from the as-sprayed XRD diffractogram (Figure 64 (b)). CoCrAlY powder, which consists of the CoCr solid solution phase only was in a molten / semi-molten state as a result of heating during the spray process. Upon impact with substrate and rapid solidification, Cobalt was formed and present in the XRD, together with the CoCr phase. The main cobalt and CoCr phase peaks around 45° two theta are wider for CoCrAlY coating and the XRD diffractogram is noisier than the CoCrAlY + hBN. The peaks for the $CoCr_2O_4$ spinel oxide were also present on the CoCrAlY coating XRD diffractogram which was not found in the CorCrAlY + hBN coating. $CoCr_2O_4$ spinel oxide peaks were slightly shifted, which suggests there was a mixture of Co, Cr and possibly Al instead of just pure Co and Cr in the spinel oxide. XRD diffractograms for both coatings obtained from the ground top surface are shown in Figure 65. Both CoCr and Co phases are still present in coatings. In addition, CoCrAlY coating XRD still has wider and nosier peaks compared to CoCrAlY + hBN. On the other hand, $CoCr_2O_4$ spinel oxide peaks disappeared, which confirms the $CoCr_2O_4$ spinel oxides are present only on the surface. Wider peaks and the presence of

surface oxide peaks suggest a higher degree of heating, melting, formation of amorphous phases during the CoCrAlY coating deposition. In addition to the XRD findings, there were more splats in larger diameter sizes (incompletely melted powder particles) present in the CoCrAlY + hBN composite coating cross-section than in the CoCrAlY coating cross-section (Figure 66(b and e)). This also suggests a higher degree of heating and melting during CoCrAlY coating deposition. As a result of the high specific surface area (20 $m^2/g$) of hBN, most of the energy provided by the flame was used by hBN particles and CoCrAlY powder did not experience the same amount of heating in flight. Combining reduced powder flowability and heating during the thermal spray of CoCrAlY + hBN mixed powder explains the reduced thickness in the coating. Particles with a lower momentum and lower degree of melting deform less upon impact with the substrate, which is critical for splat formation and bonding between successive splats to form a thicker coating [7,120]. Reduction in inter splat bonding was also observed in another study performed on a thermally sprayed $Ni_3Al$ + hBN composite coating once the concentration of hBN reached a critical point [114]. In addition, hBN will mostly be at the boundaries between CoCrAlY particles, and due to its lubricating ability does not promote bonding. Both CoCrAlY and CoCrAlY + hBN coatings had pores (black contrast) and oxides (darker grey contrast) inside their cross-section, shown in Figure 66 (b and e).

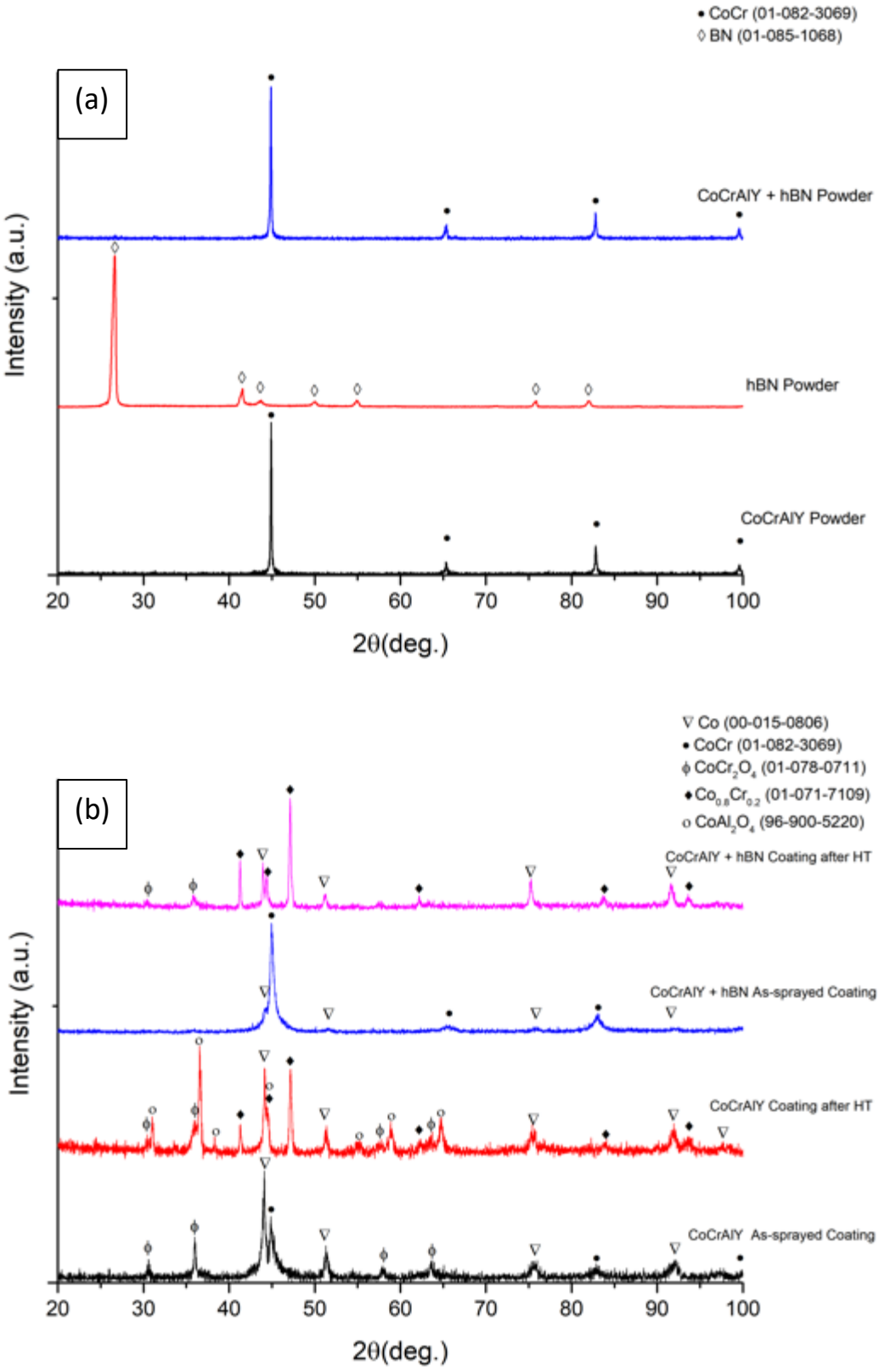


*Figure 64: XRD diffractograms of both the powder feedstocks used in thermal spray (a) and deposited coatings as-sprayed and after HT wear tests (b)*

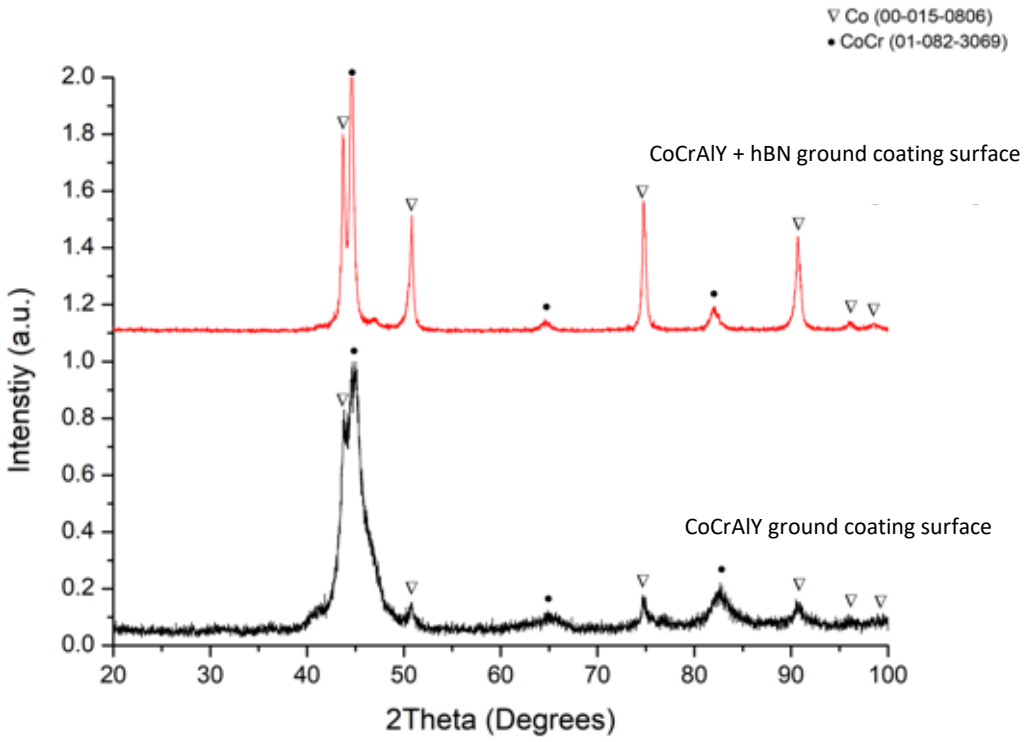


*Figure 65: XRD diffractograms of both CoCrAlY and CoCrAlY + hBN coatings after grinding the top surface*

Coating properties, including Vickers microhardness, porosity and oxide content in the coating cross-section are given in

Table 8. The estimated porosity content for CoCrAlY was (0.23 ± 0.04) %. The addition of hBN increased the porosity content to (0.33 ± 0.08) %. The presence of larger diameter splats and lower particle velocity and temperatures mentioned above can explain the slight increase in porosity. Both coatings had similar oxide phase content inside the coating cross-section. (5.54 ± 0.25) % and (5.68 ± 0.58) % for CoCrAlY and CoCrAlY + hBN, respectively. The microhardness of the CoCrAlY coating was 520 ± 22 HV0.3 and 547 ± 15 HV0.3 for CoCrAlY + hBN composite coating. The addition of hBN did not affect the oxide content in the cross-sections and the microhardness. In addition, the coatings deposited in this study achieved higher microhardness values compared to another study where the hardness was around 445 HV0.3 [229]. The fracture toughness of CoCrAlY + hBN was (2.17 ± 0.28) $MPa.m^{(1/2)}$. The CoCrAlY coating did not fracture even under higher loads. The higher fracture toughness of CoCrAlY coating was due to the formation of strong bonds between the splats. Strong splat bonding has a major influence on the fracture toughness of thermal spray coatings. As mentioned above, the addition of hBN reduced the heating and acceleration of the particles

during thermal spray due to lower flowability of the hBN powder, which affects the splat formation and reduces the bonding between successive splats.

| Coating Properties | CoCrAlY | | CoCrAlY + hBN | |
|---|---|---|---|---|
| | As - Sprayed | After HT | As- Sprayed | After HT |
| Porosity (%) | 0.23 ± 0.04 | 0.08 ± 0.01 | 0.33 ± 0.08 | 0.30 ± 0.03 |
| Oxide Phases (%) | 5.54 ± 0.3 | 7.52 ± 0.9 | 5.68 ± 0.6 | 7.34 ± 0.4 |
| Vickers Hardness (HV0.3) | 520 ± 22 | 701 ± 12 | 547 ± 15 | 707 ± 13 |
| Fracture Toughness ( $MPa.m^{1/2}$ - @500gf≃ 5N) | Na. | Na. | 2.17 ± 0.28 | 2.61 ± 0.13 |

*Table 8:Coating properties both in as-sprayed and after HT conditions.*

To study the effect of temperature on the microstructure, high magnification BSE micrographs of both coating cross-sections away from the wear test zone after the high temperature wear test, are shown in Figure 66(c and f). In addition, XRD micrographs of coatings top surfaces after HT wear and away from the wear test zone are shown in Figure 64(b). The number of oxide phases present in both coatings cross-sections increased, and there was the formation of precipitates in the microstructure, after high temperature exposure. The area underneath the $CoCr_2O_4$ spinal oxide peaks in the CoCrAlY coating XRD diffractogram increased after high temperature exposure, and the peaks from another new spinel oxide, $CoAl_2O_4$ were detected. As a result of the oxidation during high-temperature exposure, the ratio of Co to Cr in the CoCr phase was changed, which led to the transformation of cubic CoCr into hexagonal $Co_{0.8}Cr_{0.2}$. After the high temperature exposure, the starting metal powder was completely transformed as none of the phases present in the CoCrAlY metal powder was present in the coating anymore. The CoCrAlY + hBN composite coating was also oxidised, and $CoCr_2O_4$ spinel oxide peaks were formed, which were not present in the as-sprayed coating top surface. Although the CoCrAlY + hBN composite coating oxidised, the intensity of the main Co peak and the $CoCr_2O_4$ spinel oxide peaks were much lower than the corresponding peaks present in the as-sprayed CoCrAlY coating. Estimated

oxide phase content in both coating cross-sections was increased from 5.54 % to 7.52 % for the CoCrAlY coating and from 5.68 % to 7.34 % for the CoCrAlY + hBN composite coating. The phase transformation of cubic CoCr into hexagonal $Co_{0.8}Cr_{0.2}$ was also present in the CoCrAlY + hBN composite coating. This phase was only present after the high temperature exposure of the coatings but not after the oxidation during the thermal spray process. This suggests, that for the formation of that particular phase, much slower oxidation and cooling were required; hence, there was enough time for thermal equilibrium to be reached for the formation of this new phase. The formation of precipitates in both coatings cross-sections after high-temperature exposure was the precipitation of this new hexagonal $Co_{0.8}Cr_{0.2}$ phase, as it is the only phase that was not present in both coatings before high-temperature exposure. The microhardness of both coatings was also increased the same as the estimated oxide phase content; from 520 HV0.3 to 701 HV0.3 for the CoCrAlY coating and from 547 HV0.3 to 707 HV0.3 for the CoCrAlY + hBN composite coating. This suggests the formation of new oxide phases as a result of high-temperature exposure improved the microhardness of both coatings. Furthermore, recrystallisation of the amorphous phases produced during the thermal spray and increased density of the coatings due to heat treatment also improves the microhardness of the coating [230]. In addition, the fracture toughness of the CoCrAlY + hBN coating increased by 20%, from 2.17 $MPa.m^{1/2\ to}$ 2.67 $MPa.m^{1/2}$, but the CoCrAlY coating still did not form any cracks after high temperature exposure.

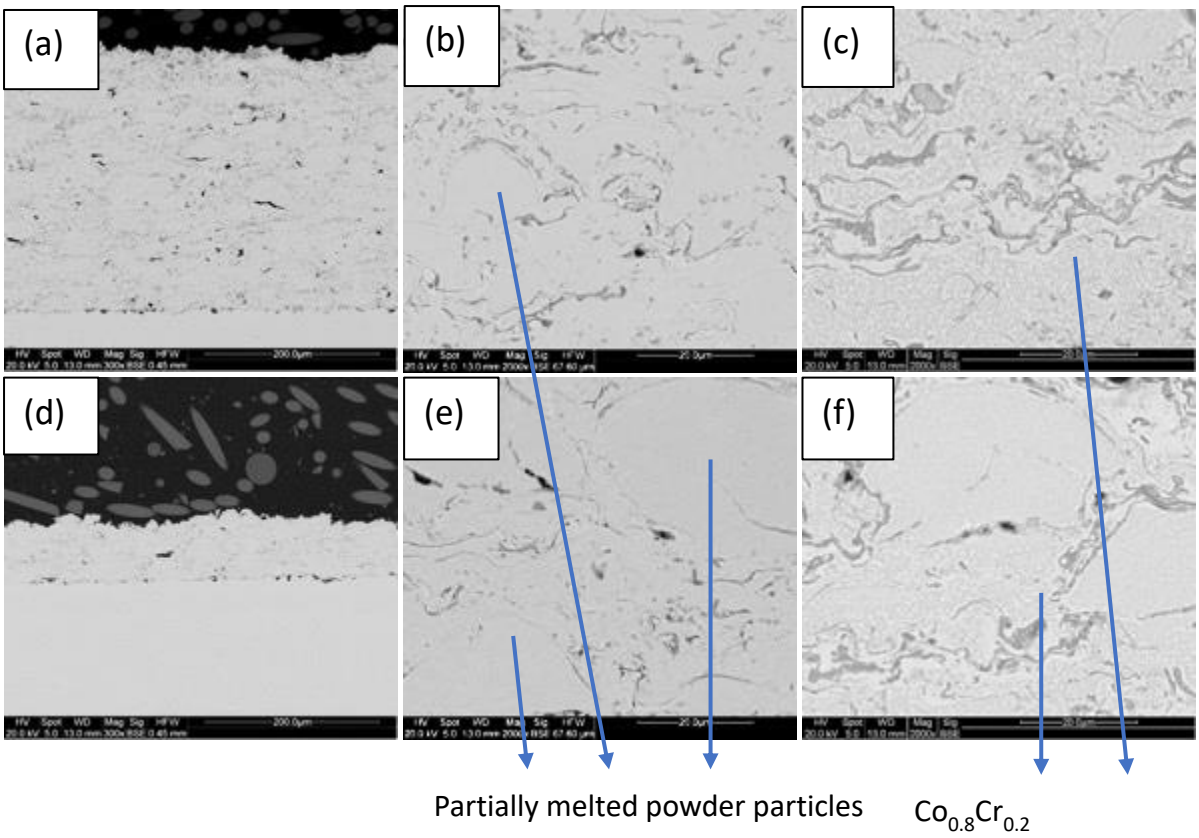


*Figure 66: BSE micrographs of the CoCrAlY coating cross-section in lower magnification (a), higher magnification (b) and after heat treatment (c). BSE micrographs of the CoCrAlY + hBN coating cross-section in lower magnification (d), higher magnification (e) and after heat treatment (f).*

### 6.4.2 Wear Performance

The wear performance of the coatings against the load was investigated under two different loading conditions, 10 N and 30 N. Figure 67 shows the specific wear rates of both CoCrAlY reference coating and CoCrAlY + hBN composite coating against the loads. The addition of hBN increased the specific wear rate of the composite coating by order of magnitude compared to reference CoCrAlY coating under both loading conditions. The specific wear rate was increased from 2.9 x $10^{-6}$ $mm^3$/Nm to 8.5 x $10^{-5}$ $mm^3$/Nm at 10 N load and from 5.0 x $10^{-5}$ $mm^3$/Nm to 1.5 x $10^{-4}$ $mm^3$/Nm at 30 N load. The increase in specific wear rate was expected due to the reduced fracture toughness. The addition of hBN led to crack formation at 300 gf in the composite coating; however, the reference coating did not crack even under increased loading conditions. In addition, the effect of loading was the same for both coatings; increasing the load from 10 N to 30 N led to an increase in specific wear rate

of an order of magnitude. Specific wear rate of CoCrAlY coating was increased from 2.9 x $10^{-6}$ $mm^3$/Nm to 5.0 x $10^{-5}$ $mm^3$ and from 8.5 x $10^{-5}$ $mm^3$/Nm to 1.5 x $10^{-4}$ $mm^3$/Nm for CoCrAlY + hBN composite coating. An increase in the applied load increases the contact area which leads to more material removal. A change in specific wear rate as a result of change in loading suggests a change in wear mechanism. Another study performed on hBN incorporated composite coatings also showed that the addition of hBN increased the wear rate of the coating from room temperature to 800 [113]. However, a few more studies reported improved wear resistance as a result of hBN incorporation in coatings as the test temperature increased from ambient temperature to 600 °C [111,112,114].

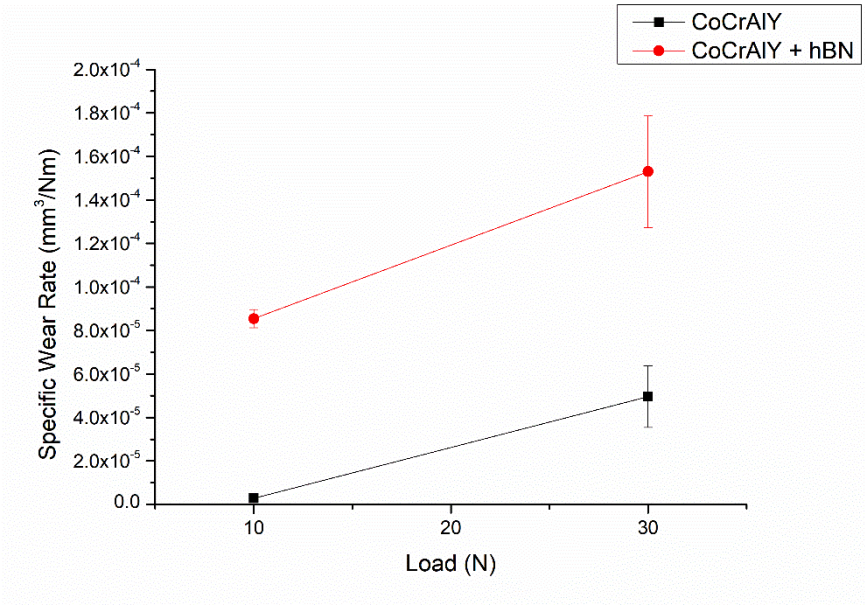


*Figure 67: Specific wear rate of both CoCrAlY and CoCrAlY + hBN coatings against the applied load.*

The coefficient of friction (CoF) for both coatings at 10 N and 30 N load are shown in Figure 68. CoF under 10 N load was 0.2 for CoCrAlY reference coating and 0.4 for CoCrAlY + hBN coating. The CoF was increased by 0.2 (from 0.2 To 0.4) under 10 N load as a result of hBN addition. As the fracture toughness of the composite coating was lower than the reference one, there was more material removal which formed the third body abrasive particles, and a rougher worn surface was formed. The wear track formed on the CoCrAlY coating was not uniform as the 10 N load was not high enough to deform the surface compared to the CoCrAlY + hBN coating, which can also influence the difference in CoF pattern. Under 30 N load, the material removal and surface roughness were already high enough in the reference CoCrAlY coating, the fact that hBN addition decreased fracture

toughness did not affect CoF. On the other hand, the other wear and friction studies performed on hBN incorporated composite coatings showed improved CoF behaviour regardless of the wear resistance and mechanical properties of the deposited coatings [111–114].

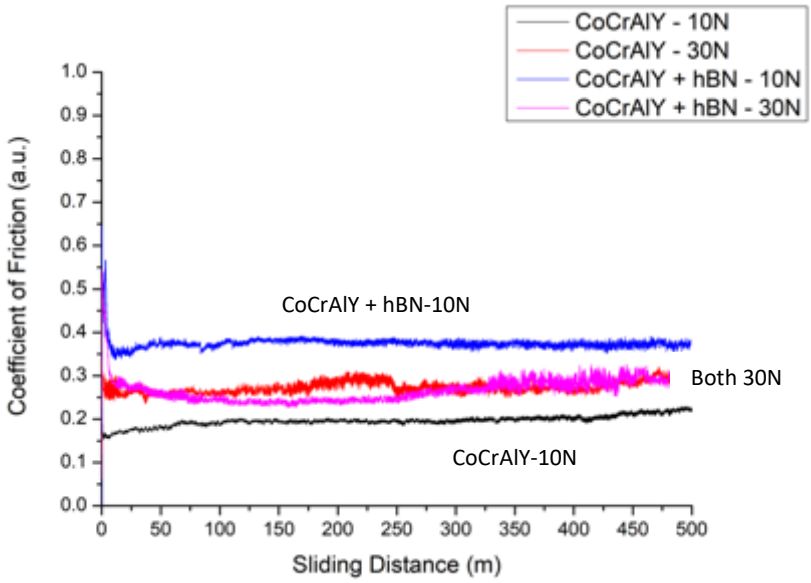


*Figure 68: The averaged coefficient of friction graphs for both CoCrAlY and CoCrAlY + hBN coatings under 10 N and 30 N loading conditions against alumina counter body.*

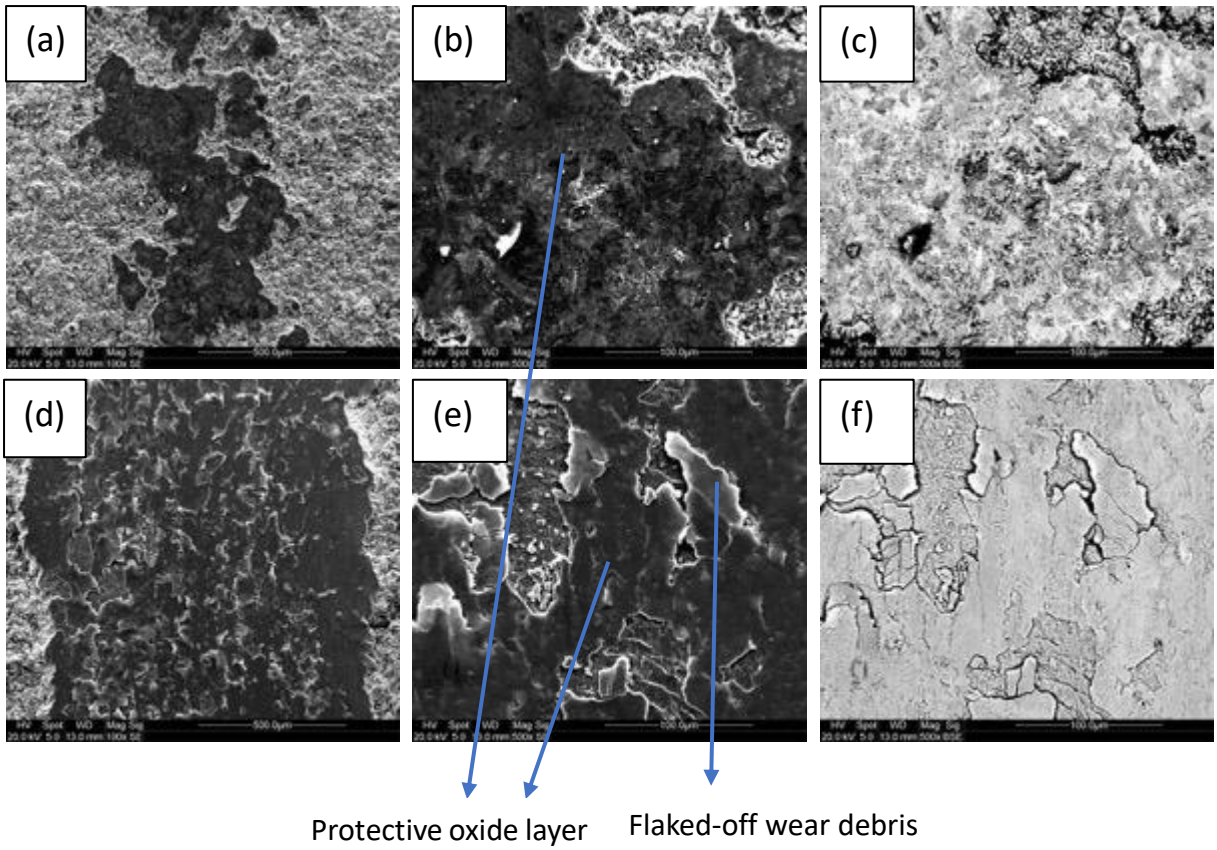


*Figure 69: Micrographs of the CoCrAlY coatings worn surface against 10 N (a, b, c) and 30 N (d, e, f) SE micrographs showing the wear tracks in lower magnification (a, d). Both SE (b, e) and BSE (c, f) in higher magnification from the centre of wear tracks.*

Worn surfaces formed on CoCrAlY coating and CoCrAlY + hBN under both 10 and 30 N loading conditions are shown in Figure 69 and Figure 70, respectively. The wear track obtained on CoCrAlY coating under 10 N loading was not uniform as the loading condition was not high enough to produce a deep wear track. The surface was partially deformed with some unaffected areas. The wear tracks became uniform and wider as the load increased due to the increased applied pressure on the contact point (Figure 69(a and d)). As a result of friction and high-temperature exposure, a protective oxide layer was formed inside the wear tracks. There were no cracks, delamination or pull-outs on this oxide layer under 10 N loading conditions (Figure 69 (b and c)). However, at 30 N, the applied load was high enough to damage the protective oxide layer, which can also be seen from SEM micrographs as the top layer of the wear track was full of cracks and flaked off wear debri. The removed material from the oxide layer was plastically deformed and flaked off from the wear surface (Figure 69

(e and f)). Therefore, the oxide layer was no longer acting like a protective layer and the wear rate at 30N increased significantly compared to 10 N. The wear track obtained on CoCrAlY + hBN coating under 10 N loading was wider and uniform, more similar to the 30 N wear track of the reference CoCrAlY coating (Figure 70 (a)). The surface was covered with a protective oxide layer again as a result of high-temperature exposure and friction. This oxide layer was already damaged at a 10 N load. As a result of reduced fracture toughness, there were brittle fractures on the wear surface instead of plastic deformations. As a result, abrasive grooves were produced on the worn surface, and there was not any plastically deformed and flaked of wear debri on the surface this time (Figure 70 (b and c)). The wear track depth varied from 60 to 90 microns as the loading increased to 30 N. Coating-substrate interface was reached during this wear test and stainless steel substrate was exposed only at certain points. This can also be seen from the deformation on the wear track surfaces obtained at 30 N (Figure 70 (d, e and f)). However, as the CoF trend did not affect and substrate exposure was only at certain points, the measured wear rate was valid for the coating itself and do not include the wear rate of stainless steel substrate. In addition, it was expected to obtain a higher wear rate of the CoCrAlY + hBN composite coating at 30 N as well, after taking into account the performance at 10 N. Substrate exposure did not influence this high specific wear rate value.

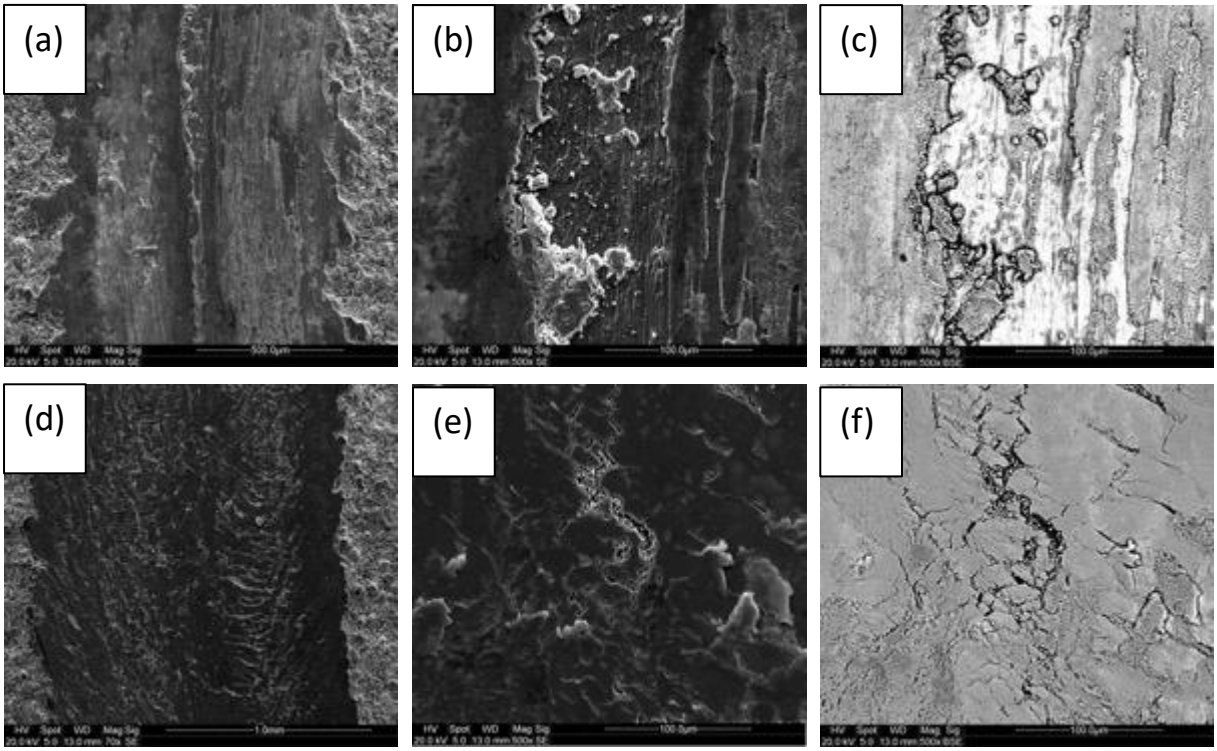


*Figure 70: Micrographs of the CoCrAlY + hBN coatings worn surface against 10 N (a, b, c) and 30 N (d, e, f) SE micrographs showing the wear tracks in lower magnification (a, d). Both SE (b, e) and BSE (c, f) in higher magnification from the centre of wear tracks.*

## 6.5 Conclusion

In this study, CoCrAlY metal powder and sub-micron sized hBN powder were mixed in an acidic aqueous solution. The mixture was dried to obtain a mixed powder and used as a powder feedstock for liquid-fuelled HVOF thermal spray to produce a CoCrAlY + 1 wt. % hBN composite coating. Raman spectrum confirms the survival of hBN during the thermal spray and the presence of hBN inside the deposited coating microstructure. The effect of hBN addition on the microstructure and the mechanical properties of the coating was investigated and compared with a reference CoCrAlY coating. Despite the high temperature capability of hBN, and improve was not achieved as the addition of hBN reduced the flowability and heating profile of the powder during the thermal spray which reduced the flattening of the splats upon impact and weakened the bonding between successive splats. Therefore, a thinner coating with a lower fracture toughness was deposited. Reduced heating also affected the surface oxide formation as the CoCrAlY + hBN composite coating lacks the $CoCr_2O_4$ spinel oxides on the as-sprayed top surface. The addition of hBN did not affect the microhardness

of the coatings but significantly reduced the fracture toughness of the composite CoCrAlY + hBN coating as a result of weak bonding between splats. Reduced fracture toughness affected the wear performance. CoCrAlY + hBN composite coating suffered from brittle fracture and more material loss compared to the plastically deformed CoCrAlY reference coating. This study showed the addition of hBN did not improve either the wear performance or friction behaviour of the coating; however, with further optimisation (changing spray parameters or the concentration of hBN in the final composition) this can be changed. On the other hand, hBN addition prevented the formation of surface oxides during thermal spray. Therefore, hBN can be used to spray powders that are sensitive to oxidation, decarburisation or to eliminate the formation of surface oxides.

## 6.6 Acknowledgements

This work was supported by the Engineering and Physical Sciences Research Council [Grant Number EP / M50810X/ 1]. This work was supported by Rolls – Royce plc; in the form of a CASE Ph.D. studentship. The authors thank the Nanoscale and Microscale Research Centre (nmRC) for providing access to instrumentations. The authors also acknowledge John Kirk at the University of Nottingham for conducting the HVOF thermal spray.

# Chapter 7: High temperature (900 °C) sliding wear of CrNiAlCY coatings deposited by high velocity oxy fuel thermal spray

Publication number = Surface & Coatings Technology 432 (2022) 128063

The coating compositions deposited in this chapter do not include any 2D material. However, the coatings were deposited from a unique and bespoke metal powder that is not commercially available. The wear performance of the coatings deposited in this were tested at both room temperature and high temperature, unlike the other chapters. Hence, the results of this study could be useful to understand the different wear characteristics and the mechanism as a result change in temperature.

## 7.1 Abstract

Nickel based superalloy are in demand for high temperature applications and their corrosion, erosion and wear resistance have been investigated for a long time. Nickel chromium (NiCr) alloys are widely used for corrosion resistant coatings, while chromium carbide nickel chromium (CrC-NiCr) alloys are preferred for wear resistant coatings at high temperature. In this study CrNiAlCY coatings were deposited via a liquid fuelled high velocity oxy fuel (HVOF) thermal spray using two spray parameters and tested as wear resistant coatings. Effects of processing parameters on microstructure and mechanical properties of the coatings were investigated. Results showed that higher oxygen flow rates are critical for obtaining coatings with lower porosity and higher microhardness. Coating with lower porosity and higher hardness was chosen for both room temperature (~24°C) and high temperature (900°C) unlubricated sliding wear tests in a ball on disc setup. The coating was tested against alumina counterbody under 3 different loading conditions (10, 30 and 60 N). The wear rate of the coating was directly proportional to the applied load at room temperature. In the room temperature tests, wear debris was produced, which then oxidised and pushed away to the edges of the wear track. On the other hand, wear debris was smeared on the wear surface at high temperature tests. The surface was oxidised into $Cr_2O_3$ at high temperatures, which acted as a protective layer. Although thermal softening took place at higher temperatures, wear rates under 10 and 30 N were similar to room temperature values due to the protective oxide layer formed on the top surface; however, the oxide layer under 60 N could not withstand the load, started to crack and lost its protective ability.

## 7.2 Introduction

High chromium content nickel-based alloys are widely used in applications as a layer of protective coating, where resistance against high temperature corrosion and wear are required. High chromium content nickel alloys form a continuous $Cr_2O_3$ layer, which is bonded strongly on the surface at high temperatures to protect the alloy from corrosion and wear. In addition, chromium can also form chromium carbides if carbon is present in the alloy mixture. Chromium carbide has a positive impact on matrix strength and hence improves both corrosion and wear resistance. [221,231–236]. Aluminium is another common element used in Nickel based super alloys. Ni-Al intermetallics have high melting points and they increase the resistance to oxidation at elevated temperatures. In addition, $Ni_3Al$ intermetallic acts as a strengthening phase in nickel based superalloys [237–239].

Thermal spray is a popular and widely used coating deposition technique in the industry for deposition of wear, erosion and corrosion resistant coatings. It is a cost-effective, fast and reliable way of depositing dense and superior quality coatings with various microstructures at different thickness ranges and from different feedstock materials including nanostructured powders, suspension and solutions [10,33,219,220]. In thermal spray, a stream of feedstock powder particles is injected into the flame to gain high velocities and temperatures. Particles are converted into a molten and/or semi-molten state in the flame that are deposited onto a substrate as a result of plastic deformation upon impact at high velocities. There is a wide range of thermal spray techniques available, and they are classified by way of heat source and feedstock types. High velocity oxy fuel (HVOF) thermal spray is a process where oxygen and a fuel are used to create a supersonic combustion jet. In HVOF thermal spray, the fuel can be either a gas (hydrogen, ethylene, propane, etc.) or liquid (kerosene) are injected into a combustion chamber together with oxygen, where an ignition initiates combustion and the exhaust gas travel through a nozzle. Depending on the type of HVOF system, feedstock powders are injected either radially inside the barrel (after the combustion chamber) or axially inside the combustion chamber [7,120]. HVOF thermal spray is the preferred method to deposit dense and well-bonded coatings with a lower degree of decomposition from the metallic feedstocks. Combustion in an HVOF torch generates higher particle velocities with lower temperatures than other thermal spray processes such as plasma spraying [120,221].

This prevents the oxidation, decomposition and decarburisation of the feedstock materials, that can reduce the mechanical properties of the deposited coatings [140,202,203].

In this study, a recently developed, unique CrNiAlCY powder was characterised and used as a feedstock for the first time in thermal spray process. CrNiAlCY coatings have been produced by changing spray parameters (oxygen flow rate), using a liquid fuelled HVOF thermal spray. This unique alloy was chosen to obtain the combined high matrix strength, corrosion and wear resistance from both chromium carbide and aluminium – nickel intermetallic phases. The microstructure of the deposited coatings was analysed and compared with the initial powder to investigate the possibility of this unique powder becoming a metallic feedstock powder candidate for thermal spray applications. Properties of the coatings such as microhardness, porosity and oxide content were investigated and the effect of oxygen flow rate on these properties was studied. Following this analysis, the tribological performance of samples showing the best characteristics was studied at room temperature and at an elevated temperature, using the ball on disc wear test arrangement. The wear performance of the coatings during both room temperature and elevated temperature was investigated and compared to understand their mechanisms. Both properties and wear performance of the best performing coating was investigated for possible usage of this recently developed, unique powder to deposit wear resistant coatings in both room temperature and high temperature applications.

## 7.3 Materials & Methods

### 7.3.1 Powder Feedstock & Coating Deposition

A nickel-chromium-aluminium-based metal powder, CrNiAlCY (Oerlikon Metco, Switzerland) was used in this study. The powder is a recently developed, unique composition and is not yet commercially available. The chemical composition of this metal powder is 45.0-50.0 wt. % Chromium (Cr), 39.0-43.0 wt. % Nickel (Ni), 6.5-7.2 wt. % Aluminium (Al), 4.3-4.7 wt. % Carbon (C), 0.14-0.16 wt. % Iron (Fe), 0.13-0.15 wt. % Yttrium (Y) and 0.01 wt. % Silicon (Si). The average particle size ($D_{50}$) of this metal powder is 31.7 µm. The powder was dried overnight inside a drying cabinet at ~100°C before the thermal spray to eliminate the moisture and increase the flowability of the powder. Powder flowability was measured

according to the ASTM standards B 213-03, which is the time taken to flow a 50 g sample of powder from calibrated orifice funnel (diameter = 2.54 mm).

AISI 304 stainless steel substrates with dimensions of 60 x 25 x 2 mm with nominal composition Fe-19.0Cr-9.3Ni-0.05C (all in wt. %) were used as substrates. Substrate surfaces were grit blasted with a blast cleaner from Guyson (Dudley, United Kingdom) at 6 bars with F100 brown aluminium oxide particles (0.125-0.149 mm). Prior to thermal spray, the substrate surfaces were cleaned with industrial methylated spirit (IMS) and compressed air.

Coatings were deposited onto the grit-blasted stainless-steel substrates with a Met-Jet L4 (Metallisation Ltd, England) liquid-fuelled HVOF thermal spray system. Detailed explanation about this thermal spray setup and schematic can be found in other studies [223,224]. CrNiAlCY powder was injected at a rate of 67.5 $g.min^{-1}$. Two different spray runs were performed with changing oxygen flow rate from 749 $l.min^{-1}$ (Run#1) to 878 $l.min^{-1}$ (Run#2) while the kerosene flow rate remained constant at 0.445 $l.min^{-1}$. The higher oxygen flow rate used in Run#2 led to a 100% stoichiometric ratio when combined with 0.445 $l.min^{-1}$ kerosene flow rate. On the other hand, the stoichiometric ratio used in Run#1 was lower than 100% [223]. Stoichiometric ratio is the optimum amount or ratio for a complete combustion reaction, where all the reagents are consumed. Combustion gases and the metal powder were accelerated towards the substrates through a nozzle, which has a length of 100 mm. Substrates were attached to a rotating carousel with a diameter of 260 mm and positioned at a 355 mm stand-off distance. The carousel rotates with a speed of 73 rpm during the spray runs which gives rise to a 1 $mm.s^{-1}$ linear velocity for the attached substrates. Simultaneously, the spray gun moves vertically with a traverse speed of 5 $mm.s^{-1}$, which leads to a 4 mm overlap between tracks from subsequent passes [26].

### 7.3.2 Wear Test

Unlubricated rotational sliding wear tests were performed at room temperature (~24°C) and at an elevated temperature (900°C). Two different rotary tribometers with a ball on disc arrangement (Ducom Instruments, The Netherlands) were used for these tests. The tribometer used for high temperature was equipped with a built-in furnace. 6 mm alumina (99.9% aluminium oxide) balls (Dejay distributions, United Kingdom) were used as counter bodies, which have a surface finish of 0.038 µm and hardness value of 91 in Rockwell A scale

(~2000HV) as stated by the supplier. Circular wear tracks of 10 mm diameter were created onto the deposited coatings under varying loading conditions (10 N, 30 N and 60 N). As-sprayed samples were used during the wear tests which had a surface roughness ($R_a$) value of 5.65 ± 0.08 µm. As-sprayed samples were rotated at 100 rpm against the stationary counter body, giving a linear speed of 52 mm/s. Each test was performed for 2 h and 39 min to reach a total sliding distance of 500 m. Therefore, at elevated temperature wear tests, high temperature exposure of the coatings were 2 h 39 min. Once the tests were completed, coatings were cooled down to room temperature. Two tests were conducted for all conditions.

Volume loss of each wear track was measured at four different points using Talysurf Form 50 contact profilometer (Taylor Hobson, United Kingdom) along with a diamond stylus with a tip radius of 2 µm and lateral resolution of 0.5 µm. Mountains map software (Digital Surf, France) was used to calculate the cross-sectional area of the wear tracks from the line profiles, which were converted into volume loss by multiplying with the circumference of the circular tracks, which is the total length of the wear track [130,206]. In total, eight different points were used to calculate the average and standard error of the mean for each sample. Material volume loss on the counter body was calculated (from two different measurements – one from each test) by following the assumption of the spherical cap of material removal method reported in the studies [140,207]. The specific wear rate of both the coatings and the counter bodies was calculated from the volume loss, dividing it by applied force and total sliding distance.

### 7.3.3 Feedstock, Coating and Worn Surface Characterisation

Microstructural characterisation of the powder feedstock, the deposited coatings and the worn surfaces were performed with a Quanta 600 scanning electron microscope, SEM (FEI, The Netherlands) in both SE and BSE modes with 20 kV accelerating voltage using a spot size of 5 and a working distance of 13 mm. EDX software (Bruker, USA) was used for elemental composition analysis. Cross sectional samples of the coatings were prepared by cutting the samples with a diamond cutting disk, followed by sequential silicon carbide (SiC) grinding and diamond polishing with a final grit size of 1 µm. Cross sectional sample for the powder was prepared by hot mounting the powder in the resin and following the same grinding and polishing sequence mentioned above. Both porosity analysis and the oxide content of the

coatings were performed on 5 different BSE micrographs for each coating obtained from the SEM at 2000X magnification from the centre of the coatings, which gives rise to an area of 70 µm x 60 µm. Oxides were identified as darker grey phases on the BSE micrographs. Contrast threshold function on ImageJ software [208] was applied to the micrographs according to ASTM E2109 standards to estimate the percentage area fraction in each BSE micrograph. An average value for both porosity and oxide content and the standard mean error were reported in all cases.

X-ray diffraction (XRD) was performed on the CrNiAlCY powder feedstock, deposited coatings and the coating top surface after high temperature wear test to analyse the phase changes. A Bruker D8 Advance diffractometer (Bruker, USA) in θ-2θ Bragg-Brentano geometry was used, the diffractograms were acquired with Cu $K_\alpha$ radiation (1.5406 Å) setting a step size of 0.02˚and a time per step of 0.1 s. in the 20° ≤ 2θ ≤ 100° range.

The coating microhardness was measured via a Vickers microhardness indenter (Buehler, USA) on polished cross sections. 300 gf with a dwell time of 10 s was applied to create 5 indents in the centre of the coatings, parallel to the substrate. The average hardness value with the standard error was reported in all cases.

## 7.4 Results & Discussion

### 7.4.1 Feedstock & Coating Characterisation

Both morphology and cross section of the feedstock metal powder were studied by back scattered electron (BSE) micrographs in conjunction with EDX mapping that are shown in Figure 71. The feedstock powder has a spheroidal morphology, as can be seen from the Figure 71a. The powder is free from porosities and it consists of chromium carbide dendrites (grey phases in Figure 71(b)) embedded in a Nickel and Aluminium alloy (light grey phases in Figure 71(b)) binder phase. The EDX mapping given in Figure 71(c, d and e) also confirms the dendric microstructure. XRD diffractogram given in Figure 72 shows the feedstock powder was composed of mainly $Cr_7C_3$ and $Ni_3Al$. The main peak corresponding to $Ni_3Al$ was broad, suggesting that nickel and aluminium alloy binder phase has a lower degree of crystallinity.

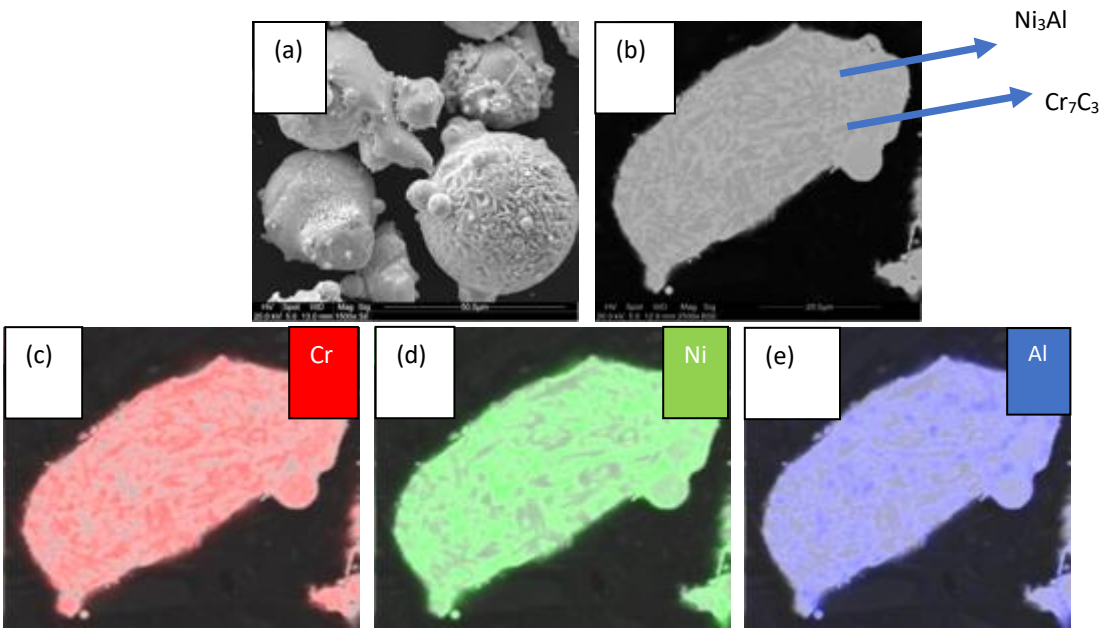


*Figure 71: BSE micrographs showing the CrNiAlCY powder morphology (a) powder cross section (b) and EDX mapping performed on the cross section (c, d and e). Powder has a dendric microstructure confirmed by the EDX. Chromium carbide dendrites, grey phases (c) embedded in a nickel (d) / aluminium (e) alloy binder matrix, light grey phases.*

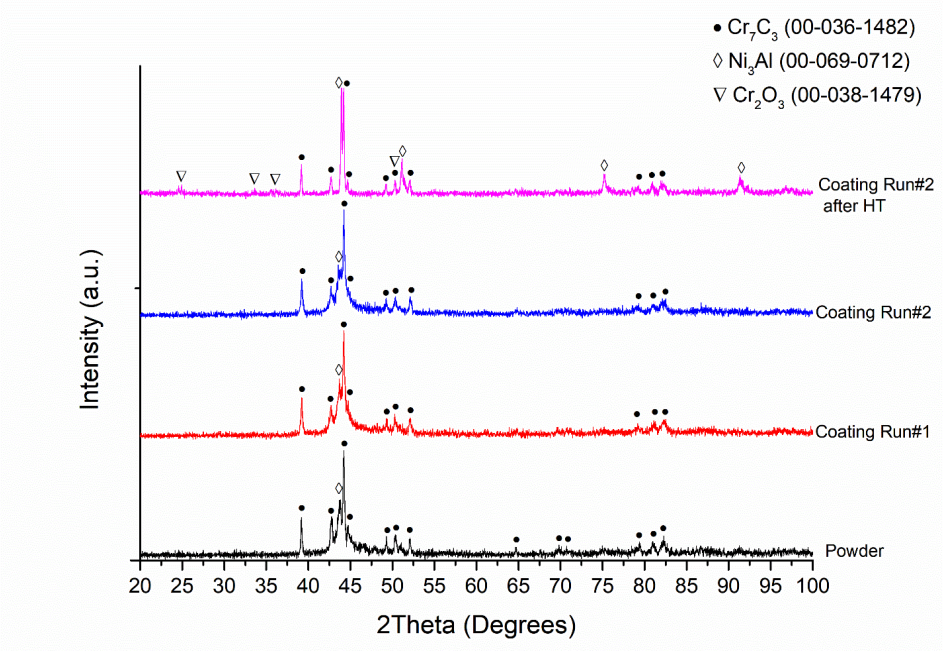


*Figure 72: XRD diffractograms for CrNiAlCY powder, Run#1 coating in as-sprayed condition, Run#2 coating in both as-sprayed and after high temperature exposure conditions.*

BSE micrographs showing cross sections of the coatings produced using different spray parameters (oxygen flow rate 750 l.min$^{-1}$ (Run#1) and 878 l.min$^{-1}$ (Run#2)) are given in Figure 73. Both coatings had similar thickness values ~220 µm and they showed a good bonding with the substrates. Coating properties, including Vickers microhardness, porosity and oxide content, are given in Table 9. Higher porosity content (dark areas) are detected in Run#1 coating compared to Run#2 coating as can be seen from the lower magnification BSE micrographs, Figure 73(a, c). Estimated porosity content confirms this, as Run#1 coating had 1.3 % ± 0.5 porosity while Run#2 had 0.4 % ± 0.1. High magnification BSE micrographs, Figure 73(b, d), show that both coatings had the same microstructure of the powder feedstock with minimal oxidation. Light grey areas represent aluminium and nickel binder phase, while grey areas represent chromium carbide phases and darker grey areas represents the oxides. Estimated oxide phase content via ImageJ was < 1.0%. In this type of HVOF thermal spray system, powder feedstock was injected after the combustion chamber. Therefore, the oxidation of the metallic feedstock is prevented, and low oxide content was expected in the final coating. Liquid fueled HVOF thermal spray is the preferred method in the industry to prevent oxidation and decarburisation of the coatings [18].

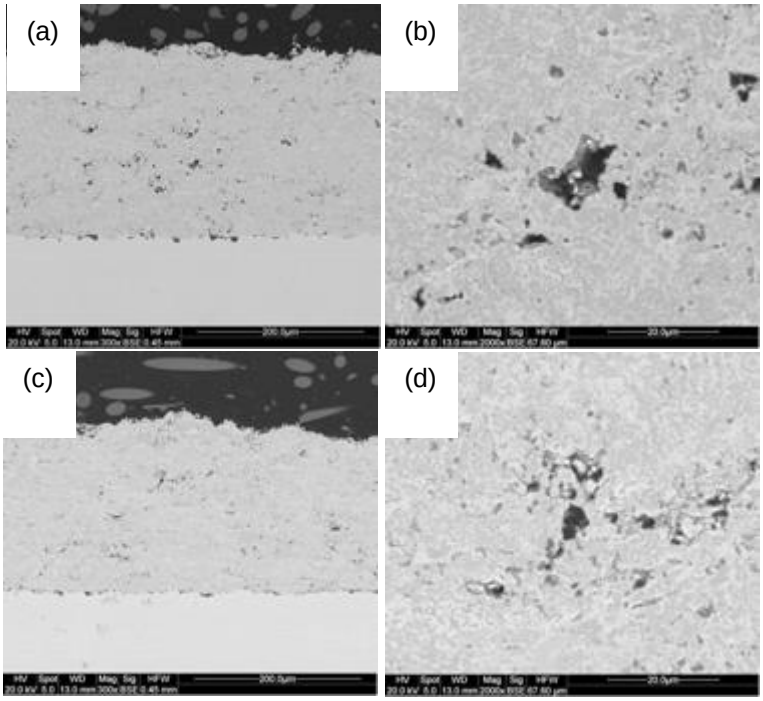


*Figure 73: BSE micrographs of the CrNiAlCY coatings in lower magnification for Run#1 (a) and Run#2 (c) showing uniform thickness and higher magnification for Run#1 (b) and Run#2 (d) showing pores and dendric microstructure of the powder carried on in the coatings as well.*

| Sample | Microhardness (HV0.3) | Porosity (%) | Oxide Phases (%) |
|---|---|---|---|
| Run#1 As-sprayed | 827 ± 15 | 1.3 ± 0.5 | <1.0 |
| Run#2 As-sprayed | 974 ± 23 | 0.4 ± 0.1 | <1.0 |
| Run#2 After HT wear | 825 ± 24 | 0.7 ± 0.2 | 4.0 ± 0.6 |

*Table 9: Vickers microhardness and porosity values of the coatings deposited from both Run#1, Run#2 and after HT wear test on Run#2. The coating deposited by Run#2 has higher hardness and lower porosity; it was chosen for high temperature wear tests. Oxide phases present in the coating cross sections were also analysed for coatings in as-sprayed and after HT wear conditions.*

XRD diffractogram of the as-sprayed coatings shows after thermal spray, chromium carbides remained as $Cr_7C_3$ together with $Ni_3Al$ and there was no oxide peaks present; however, the peaks are slightly broader compared to the powder feedstock. This was expected as the powder was in a molten phase during thermal spray and fast cooling rates of splats formed on the substrates caused the formation of amorphous and / or nanocrystalline phases. XRD diffractograms together with SEM micrographs confirm that the powder had conserved its microstructure during the thermal spray and there was no significant oxidation of the powder.

Microhardness measurements obtained from both coatings shows that the coatings deposited by Run#2 are harder than that of Run#1. Vickers microhardness for Run#2 coatings was 974 ± 23 HV0.3 while for Run#1 it was only 827 ± 15 HV0.3; however, both coatings presented higher hardness values than nanostructured (727.5 HV0.3) and conventional (456.6 HV0.3) NiCr-$Cr_7C_3$ coatings deposited by high velocity air fuel (HVAF) technique [234]. Total gas flow was lower during Run#1 as a result of a lower oxygen flow rate. Therefore, velocity and hence the momentum of the particles exiting the nozzle was lower compared to the Run#2. Particles with a lower momentum deform less upon impact with the substrate, which is critical for splat formation and bonding between successive splats [7,120]. As a result,

coatings deposited by Run#1 lead to a lower degree of particle deformation, producing weaker intersplat bonds and pores. The difference in oxygen flow rates, explains the reason for increased porosity and reduced hardness for coatings deposited by Run#1. Coatings deposited via Run#2 were chosen for both room temperature and elevated temperature wear tests, as they have improved mechanical properties (higher hardness, lower porosity).

To study the effect of temperature on the microstructure without the impact of wear, low and high magnification BSE micrographs of coating Run#2 cross section after high temperature wear test, took far from the wear test zone, are shown in Figure 74. Coating microstructure looks similar after the high temperature exposure, as the chromium carbides in the aluminium nickel binder phase remained unaltered; however, there is another phase present (darker grey), as can be clearly seen from high magnification BSE micrographs. As a result of high temperature exposure, the coatings oxidised and the oxide phases were randomly disturbed as these darker grey phases can be seen throughout the entire coating cross section. Estimated oxide phase content via ImageJ was increased to 4.0% from < 1.0%. XRD diffractogram of the coating after heat treatment also shows the presence of $Cr_2O_3$, which confirms the oxidation during the high temperature exposure. $Cr_7C_3$ and $Ni_3Al$ phases are still present. After the heat treatment, the peaks became narrower as a result of the higher degree of crystallization induced by the temperature. In addition, the intensity of the main $Cr_7C_3$ peak remained the same (44 2theta), and a carbide phase different than the $Cr_7C_3$ did not form. Therefore, $Cr_7C_3$ phase present in the as-sprayed coating did not decarburise after high temperature wear.

After the high temperature exposure, there was a slight increase in porosity content, from 0.4% ± 0.1 to 0.7 % ± 0.2. Pores and cracks were present in the coating microstructure around the oxide phases which, could be the reason for a slight increase in porosity. Microhardness of the coating after heat treatment was reduced to 825 ± 24 HV0.3 from 974 ± 23 HV0.3. Nearly 17 % reduction in microhardness can be explained as a result of thermal softening, increase in porosity and formation of cracks around the oxides. In addition, some studies reported a reduction in hardness values of the coatings after heat treatment as a result of the reduction in residual stress [240], grain growth and lattice strain relaxation [235].

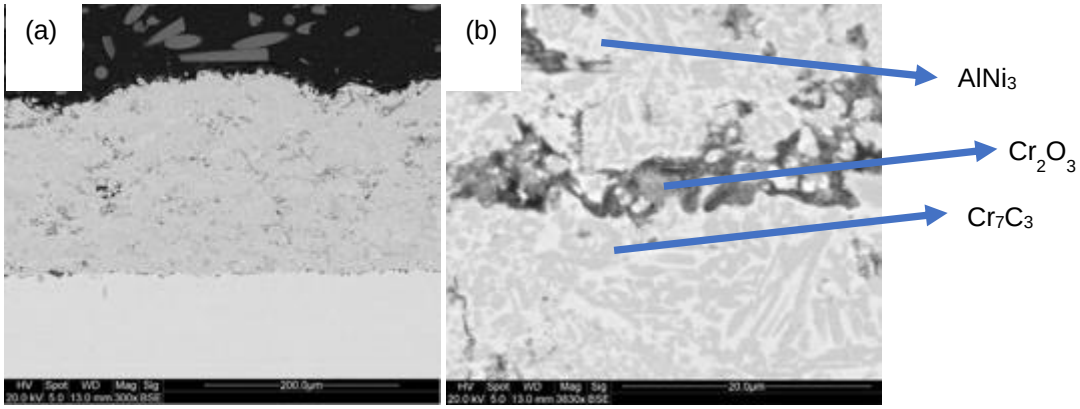


*Figure 74: BSE micrographs of coatings cross section after high temperature exposure in lower (b) and higher (c) magnification. After HT tests, oxide phases were formed in the coating, which can be seen as darker grey phases.*

### 7.4.2 Wear Performance

Wear performance of the coating deposited by Run#2 was investigated under three different loading conditions. Figure 75 shows the specific wear rates of both coating and alumina counterbody balls against the load for both room temperature (RT) and elevated temperature (HT) tests. The specific wear rate of the coating at room temperature tests was doubled when the loading was increased from 10 N to 30 N. Increase in wear rate was continued for 60 N load as well, but not as much as the jump from 10 N to 30 N. Specific wear rate of the coating is directly proportional to the applied load under room temperature conditions. Under high temperature conditions, the specific wear rate of the coating was similar for both 10 N and 30 N loads. However, the specific wear rate was increased significantly when the loading was increased to 60 N. Overall, the coating achieved lower specific wear rates at room temperature tests compared to elevated temperature ones. Materials are softer at elevated temperatures, and it is easier to deform and create wider and deeper wear tracks. Counterbody specifc wear rates were proportional to the loading. Counterbodies lost more material as the loading increased, 30 N at RT was the only exception. Overall, counterbodies used in RT wear tests lost more material than those used in HT tests. It was expected to obtain less material loss against the coatings at HT as the coatings became softer. Counterbody specifc wear rates were an order of magnitude smaller than the coatings specifc wear rates. Alumina has higher hardness compared to the deposited coatings and its properties are stable at the test conditions used in this study. Therefore, it was expected for

alumina counterbodies to be worn less compared to the coatings in both RT and HT wear tests. Figure 76 shows coefficient of friction graphs averaged over the two repeated tests, obtianed from both high temperature and room temperature wear tests under 10 N, 30 N and 60 N loading conditions. CoF values obtained during the high temperature tests were lower than the corresponding room temperature tests. Resistance to the sliding motion was lower as the materials became softer at higher temperatures. CoF value was stabilised around 0.325 - 0.350 within the 500 m sliding distance for 30 N and 60 N loads at high temperature tests. However, at 10 N load, CoF value was stable around 0.2 and it fluctuated between 0.1 - 0.2 before reaching a stable state after 100m sliding distance. The first 100 meters was the bedding-in period where the counter body was creating awear track on the top surface of the coating. This period was longer and not uniform as the 10 N load was not high enough to form a uniform wear track as fast as other loading conditions (30 N and 60 N). On the other hand, CoF values at room temperature tests were more consistent for all three loading conditions. CoF values were reached up to 0.6 at some point during the first 100 m for all 3 loading conditions, then stabilised around 0.50-0.55.

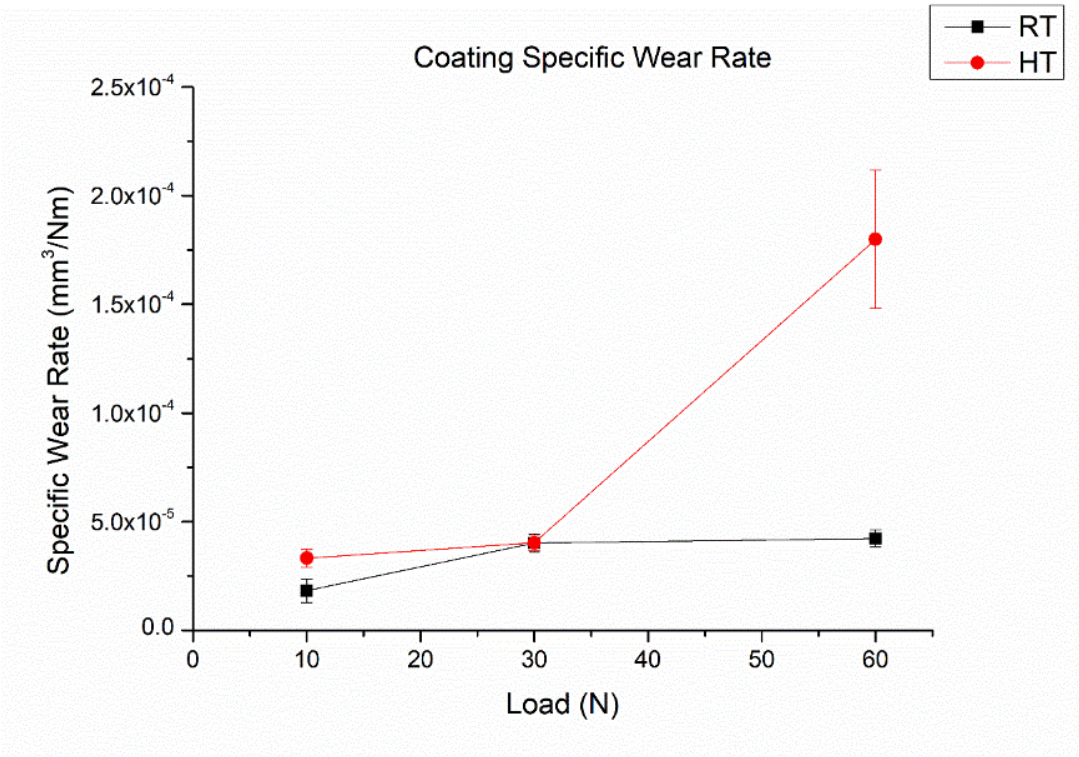


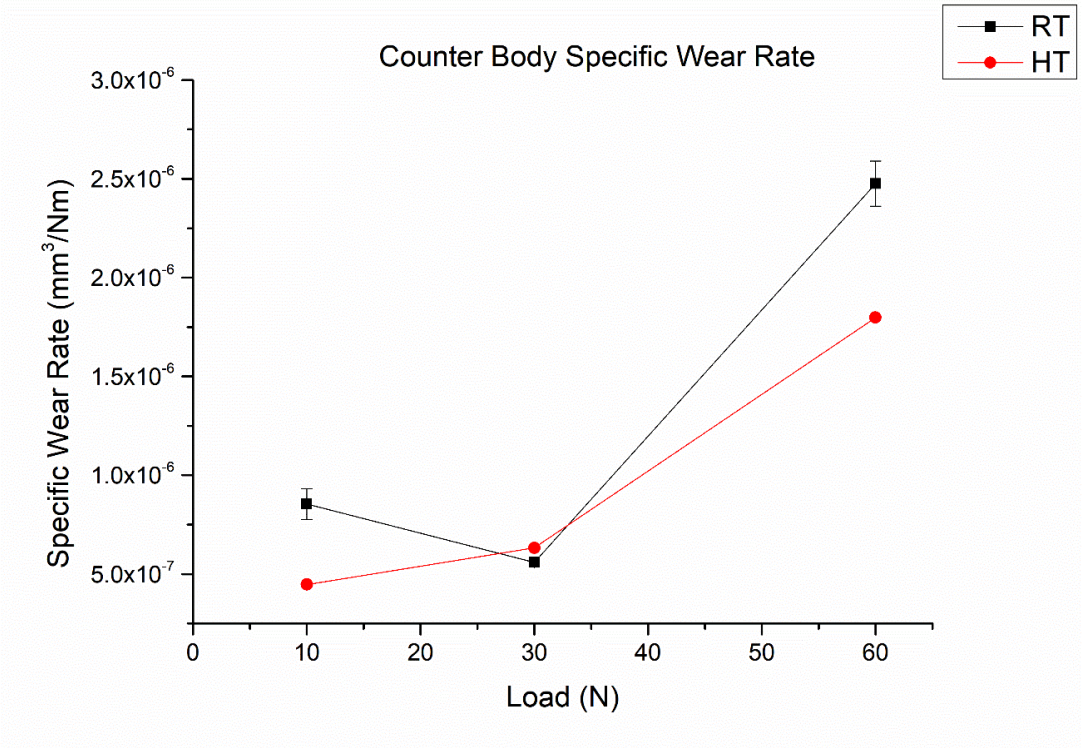


*Figure 75: Specific wear rates of CrNiAlCY coatings at 10, 30 and 60 N in both elevated (900 ˚C) and room (24 ˚C) temperatures and corresponding alumina counterbody specific wear rates.*

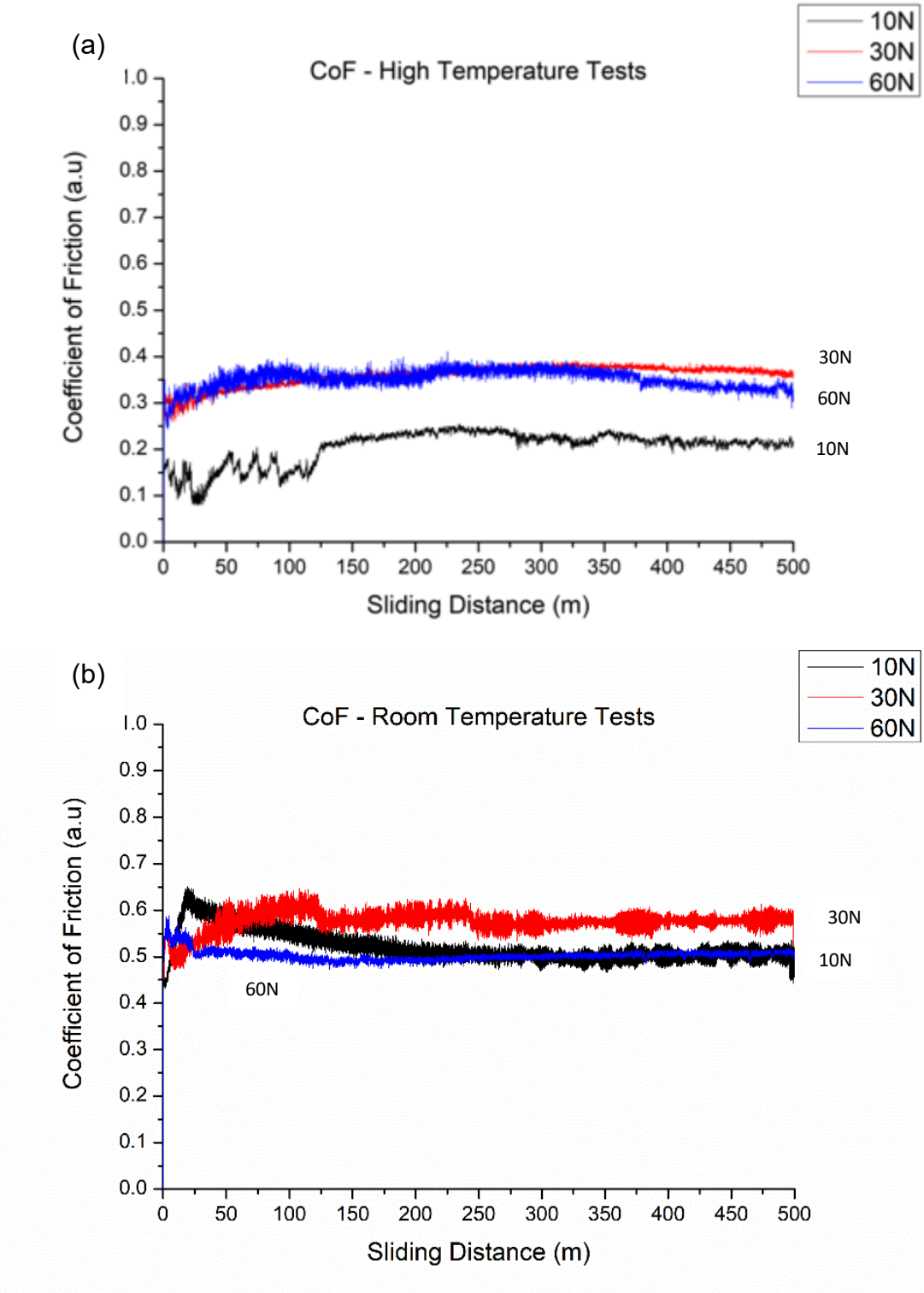


*Figure 76: Coefficient of friction patterns obtained from the wear tests at both high temperature and room temperature wear tests under 10 N, 30 N and 60 N loading conditions*

SEM micrographs in Figure 77 shows worn surfaces on the coatings produced at 10 N Figure 77a, b and c), 30 N (Figure 77 d, e and f) and 60 N (Figure 77 g, h and i) at room temperature wear tests. Wear tracks width at lower magnifications can be seen in Figure 77 (a, d and g) for 10 N, 30 N and 60 N, respectively. Wear track obtained under 10 N loading was not uniform as the loading condition was not high enough to produce a deep wear track. The surface was partially deformed with some unaffected areas. Wear tracks became uniform and wider as the load increased due to the increased applied pressure on the contact point. Worn surfaces at higher magnifications in both SE and BSE modes are shown in Figure 77 (b and c) for 10 N (e and f) for 30 N and (h and i) for 60 N. Under all loading conditions, deformed surfaces were smooth and polished. There was not any crack, or pull-outs observed. Furthermore, wear debris produced during the tests were oxides due to friction and heat generation between the coating and the counterbody [215]. These can be seen as dark phases on the BSE micrographs. In addition, the amount of oxide debris presents inside the wear tracks increased as the loading increased. Oxides were pushed towards the edges of the wear track as they were not strongly bonded to the surface, or there were no pores on the surface to fill with these oxidised debris. 30 N wear track was investigated by EDX and Figure 78 shows the areas where EDX was performed on the BSE micrographs together with both atomic and weight percentages of elements present. Both wear track surfaces and as-sprayed coating has similar elemental composition suggesting that there was no oxidation on the top surface; however, produced wear debris was oxidised as explained above. There was no oxide present inside the wear track surface labelled as point 2 (light grey phases); however, dark grey phases which were labelled as point 3 were rich in oxides.

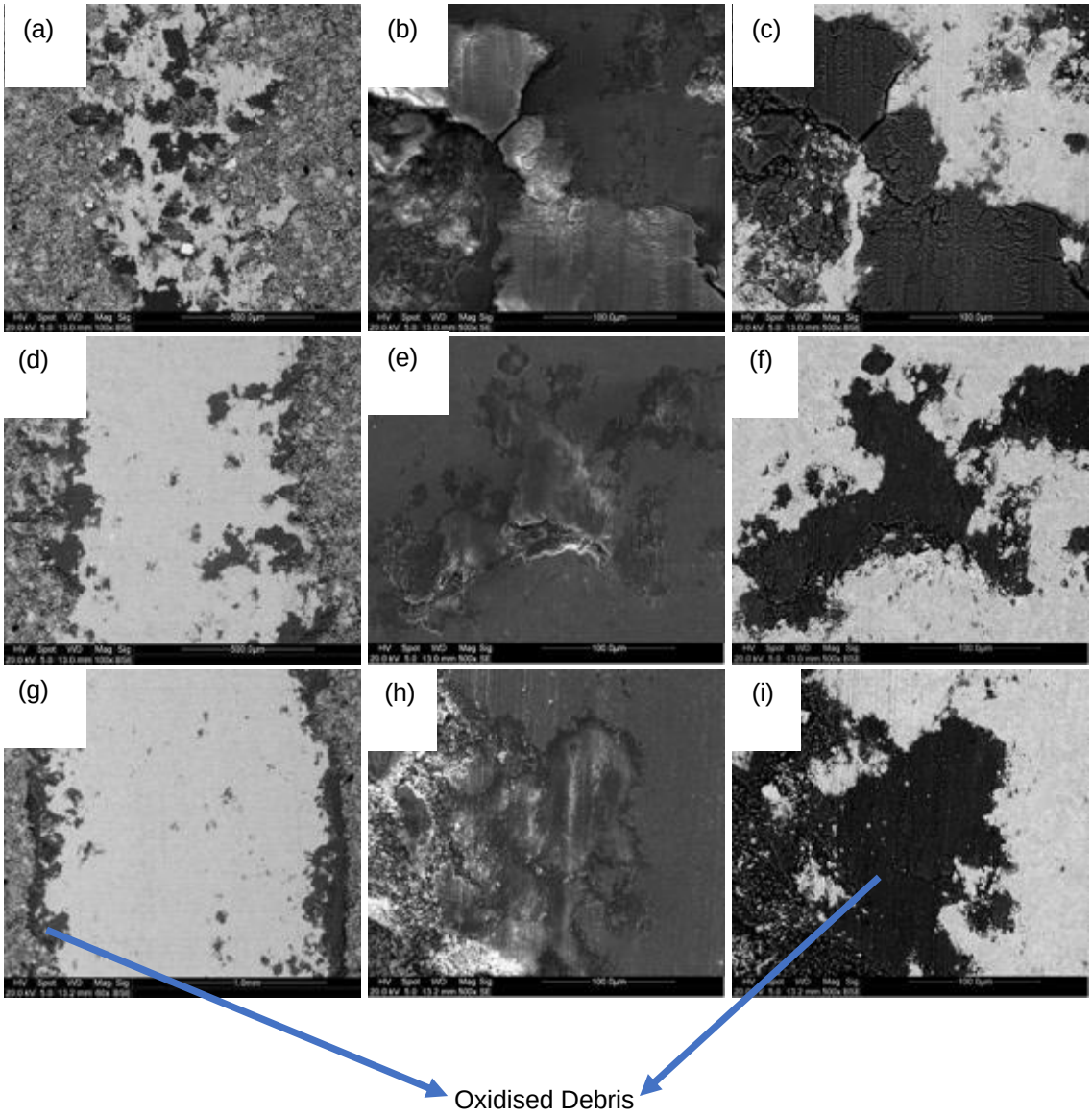


*Figure 77: SEM micrographs of the worn surfaces produced by 10 N (a, b and c) , 30 N (d, e and f) and 60 N (g, h and i) at room temperature wear tests. (a, d and g) shows wear tracks width at lower magnifications, while (b, c, e, f, h and i) shows inside the wear track and deformations at higher magnifications in both SE and BSE modes.*

(a)

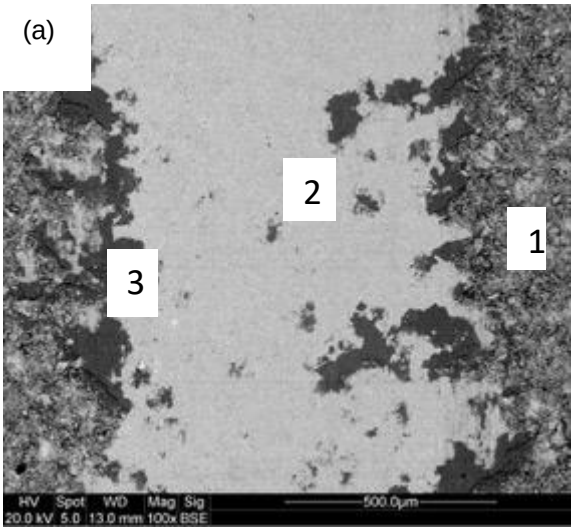


| (b) | Point 1- As-sprayed coating surface | | Point 2 – Inside the wear track | | Point 3- Oxidised wear debris | |
|---|---|---|---|---|---|---|
| Element | wt. % | At.% | wt. % | At.% | wt. % | At.% |
| Ni | 40.4 | 26.7 | 41.5 | 29.3 | 23.1 | 9.4 |
| Cr | 41.8 | 31.1 | 45.6 | 36.3 | 23.3 | 10.5 |
| C | 7.8 | 26.4 | 7.2 | 24.9 | 8.1 | 15.9 |
| O | 2.2 | 5.3 | 0.7 | 1.7 | 41.3 | 60.7 |
| Al | 7.4 | 10.7 | 5.1 | 7.9 | 4.0 | 3.5 |

*Figure 78: BSE micrograph of the wear track produced by 30 N at RT wear test (a). Smooth and light grey areas are inside the wear track and dark grey areas on the edge of the wear track are the oxidised wear debris. Three points are marked and EDX results from those areas are given (b).*

SEM micrographs in Figure 79 shows worn surfaces on the coatings tested at 10 N (Figure 79 a, b and c) , 30 N (Figure 79 d, e and f) and 60 N (Figure 79 g, h and i) at high temperature wear tests. Wear tracks width at lower magnifications can be seen in Figure 79 (a, d and g) for 10 N, 30 N and 60 N, respectively. Wear tracks became wider as the load

increased due to the increased applied pressure on the contact point. Furthermore, worn surfaces had a smoother finish as the load applied increased. Worn surfaces at higher magnifications in both SE and BSE modes are shown in Figure 79 (b and c) for 10 N (e and f) for 30 N and (h and i) for 60 N. Under 10 N and 30 N loading conditions, surface damage looks similar. Worn surfaces were smoother and peeled off coatings smeared on the surface. Dark phases present on the BSE micrographs represent smaller pores. The coating had similar wear rates at both 10 N and 30 N; therefore, it was expected to have similar deformation on the surfaces. An increase in specific wear rate at 60 N can also be seen from micrographs as the surface deformed significantly more compared to the other loading conditions. The surface was dominantly covered with cracks and delamination of the whole coating top surface took place. The wear track tested at 30 N was investigated by EDX and Figure 80 shows the areas where EDX was performed on the BSE micrographs together with both atomic and weight percentages of elements present. Both wear track surfaces and as-sprayed coating surfaces had a higher content of oxides compared to room temperature tests. Oxides on top of as-sprayed coating surface were a result of the exposition to elevated temperatures. The ratio between the atomic percentages of chromium and oxygen suggests the formation of $Cr_2O_3$. This oxide phase was also confirm in XRD diffractogram and reported as the main oxide formed due to high temperature exposure of high chromium content nickel based super alloys in the literature [235,236]. Oxide content inside the wear track surface was slightly higher than the as-sprayed coating surface. Oxidation of the wear track surface resulted from exposure to high temperatures and friction during the wear test. Compared to the room temperature tests, there was not oxidised debris present inside wear tracks. The whole wear track was oxidised during high temperature wear tests and the wear debris produced was smeared onto the surface instead of being pushed towards the edges of the wear track. Elevated temperatures and thermal softening make it easier for the wear debris to bond stronger to the wear track surface. The $Cr_2O_3$ formed at high temperature acts as a protective layer that prevents the deformation on the top surface; that is why the wear rates at both 10 N and 30 N are similar to the room temperature wear tests. However, at 60 N, the applied load was high enough to damage the protective oxide layer, which can also be seen from SEM micrographs as the top layer of the wear track was full of cracks and flakes. Therefore, the oxide layer was no longer acting as a protective layer and the wear rate at 60N increased nearly 3 times compared to the room temperature test.

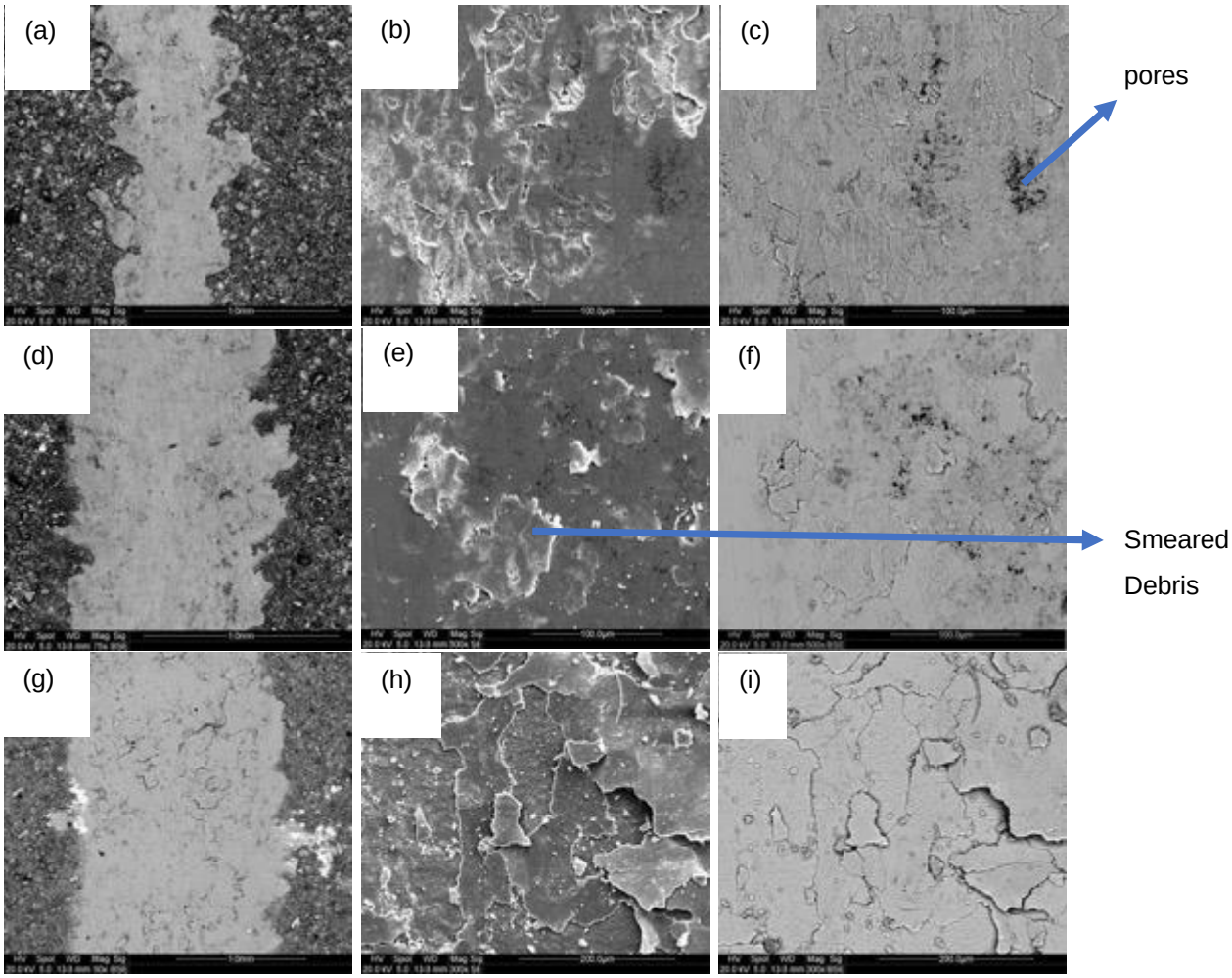


*Figure 79: SEM micrographs of the worn surfaces produced by 10 N (a, b and c) , 30 N (d ,e and f) and 60 N (g, h and i) at high temperature wear tests. (a, d and g) shows wear tracks width at lower magnifications, while (b, c, e, f, h and i) shows inside the wear track and deformations at higher magnifications in both SE and BSE modes.*

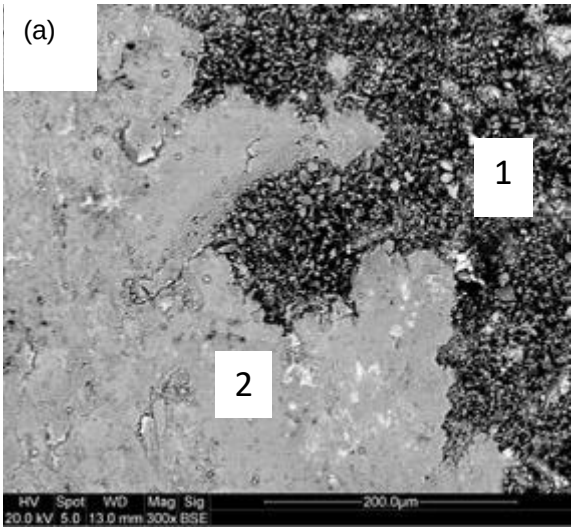


| (b) | Point 1- As-sprayed coating surface | | Point 2 – Inside the wear track | |
|---|---|---|---|---|
| Element | wt. % | At.% | wt. % | At.% |
| Ni | 30.7 | 17.8 | 32.4 | 16.3 |
| Cr | 43.2 | 28.2 | 32.1 | 18.2 |
| C | 3.5 | 9.8 | 5.2 | 12.8 |
| O | 18.3 | 38.8 | 26.3 | 48.4 |
| Al | 4.1 | 5.4 | 4.0 | 4.4 |

*Figure 80: BSE micrograph of the wear track produced by 30 N at HT wear test (a). Smooth and light grey areas are inside the wear track and darker grey areas on the edge of wear track are as sprayed coating top surface. Two points were marked and EDX results from those areas are given (b).*

## 7.5 Conclusion

In this study, a recently developed unique CrNiAlCY metal powder was characterised and tested as a possible feedstock material for coating deposition by HVOF thermal spray. CrNiAlCY coatings were successfully deposited by HVOF thermal spray using two different

oxygen flow rates. Similar coating thicknesses was achieved in both cases and the microstructure of the powder, dendritic chromium carbide grains embedded in an intermetallic aluminium nitride binder matrix was conserved in the coatings. CrNiAlCY coatings deposited using a higher oxygen flow rate (Run#2) achieved increased microhardness and reduced porosity content due to improved mechanical bonding between successive splats. Higher oxygen flow rates are important to achieve higher momentum of particles directed towards the substrate and a higher degree of deformation of splats. Therefore, better mechanical bonding achieved, which leads to denser and harder coatings. However, there was no phase segregation, oxidation or decarburisation in both coating microstructures upon thermal spraying. In addition, coating conserved its microstructure and carbides did not change their forms and decarburise due to high temperature exposure during the high temperature wear tests. These suggest this newly developed unique powder is a good feedstock option for deposition of coatings by HVOF thermal spray for high temperature applications. Wear tests at room temperature showed wear rate increases with the applied loading; however, wear rates at high temperature tests remained similar under 10 N and 30 N loading conditions. The wear rate increased at 60 N only. At room temperature, only wear debris was oxidised and it was pushed away to the edges of the wear track. At higher temperatures, the whole wear surface was oxidised and the wear debris smeared onto the surface instead. $Cr_2O_3$ oxide was formed at high temperatures, which acted as a protective layer and prevented the deterioration of the surface under both 10 N and 30 N load; however, $Cr_2O_3$ could not withstand the 60 N load and started to crack and flaked off.

## 7.6 Acknowledgements

This work was supported by the Engineering and Physical Sciences Research Council [Grant Number EP / M50810X/ 1]. This work was supported by Rolls – Royce plc; in the form of a CASE Ph.D. studentship. The authors thank the Nanoscale and Microscale Research Centre (nmRC) for providing access to instrumentations. The authors acknowledge Heidi Lovelock, Justin Cheney and Jonathon Bracci for supplying the powder. The authors also acknowledge John Kirk at the University of Nottingham for conducting the HVOF thermal spray.

# Chapter 8: General Discussion

The first two studies performed in this thesis were based on achieving improved wear performance and surface protection at room temperature applications by using 2D graphene nanoplatelets suspension. HVOF thermal spray and suspension preparation neither introduced defects nor altered the unique layered structure of the graphene as both $I_D/I_G$ and $I_{2D}/I_G$ band ratios did not change, as shown in Table 10. In addition, a study performed on ceramic nanocomposite coating deposition via S-HVOF thermal spray using GNP suspensions also confirmed the survival of GNPs [90] during the process.

| **Samples** | **$I_D/I_G$** | **$I_{2D}/I_G$** |
|---|---|---|
| As-received GNP | $0.39 \pm 0.03$ | $0.44 \pm 0.07$ |
| GNP Coating | $0.37 \pm 0.11$ | $0.54 \pm 0.08$ |
| GNP wear Track | $2.02 \pm 0.08$ | $0.15 \pm 0.02$ |

*Table 10: Shows both $I_D/I_G$ and $I_{2D}/I_G$ band ratios for as-received GNPs, deposited GNP coating and GNPs from the wear track.*

The deposited GNP film in chapter 4 is not uniform and thick like conventional wear-resistant coatings. The formation of molten or semi-molten particles is key to obtaining a strong bond between the coating and substrate [197]; however, GNPs cannot melt, they are fully oxidised and combust at 600 °C [198,199]. This prevents the formation of a strong bond with the substrate. In similar studies performed via radially injecting the GNP suspension into the thermal spray flame instead of axially into the combustion chamber, led to better deposition efficiency (92% coverage) [32,191]. Radial injection reduces the degradation of GNPs inside the flame as they are subjected to the heat for a reduced amount of time. In addition higher suspension flow rate (170 ml/min) and larger standoff distance (300 mm) were used. In our study, it has been seen that increasing both flow rate and standoff distance increases the area coverage. However, the radial injection doesn't allow the full exploitation of the thrust from the thermal spray flame. Also, a too long stand-off distance could lead to a reduction of the particles velocity and raise problems of gas turbulence. These effects would ultimately lead to a poorer bonding with the substrate.

During the unlubricated sliding wear tests very low CoF values (around 0.1) was achieved due to the presence of GNP tribolfims in the wear track [100]. Layers of GNPs slid over each other due to the presence of weak van der Waals bonds between the layers showing by the schematic given in Figure 81. This motion dissipates the friction force, hence the shear stress acting on the surface is reduced. Coefficient of friction values in between 0.1 and 0.2 were also observed in some studies where graphene was used as a solid lubricant between stainless steel bodies [55,189,190]. Generation of heat due to the contact pressure between the two surfaces led the film to fail after passing through a transition stage, which led to a sudden increase in CoF from ~0.1 to ~0.7. This pattern in dry air only observed in study [190], where solution processed graphene was used as lubricant and lasted less than 100 cycles. However, constant addition of graphene usually prevents this failure but it is not possible in all applications. Deposited GNP film in our study outperformed the solution processed graphene lubricant layer even at higher sliding speed and load used to test the GNP film.

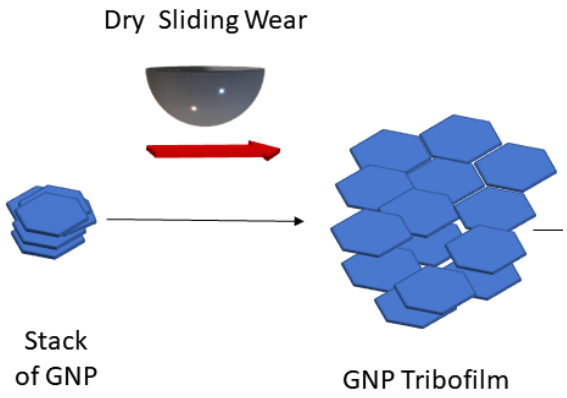


*Figure 81: Schematic diagram showing the formation of GNP tribofilm, as the hexagonal layers slid and position themselves next to each other.*

The generation of heat as a result of the contact pressure between the two surfaces leads to oxidation. The oxygen bonds are formed between the layers. This alters the unique structure and introduces the extrinsic defects via a change of bonding type from $sp^2$ to $sp^3$ hybridization [192,200]. Interatomic hydrogen bonding formed between the layers in oxidised graphene due to the presence of $sp^3$ hybridization. Hydrogen bonding is a stronger interatomic bonding than van der Waals forces, hence the unique self-lubricative ability of

graphene to dissipate the frictional force was prevented. Therefore, the load creates higher in-plane and shear stresses on the film that introduce further defects to the hexagonal structure [55,201]. Once the defects reach a significant amount to alter the structure of graphene, amorphisation of GNP particles occurs.

After studying wear performance of GNP films and their mechanism of action under dry sliding wear, two different GNPs (labelled GNP1 & GNP2) are combined with the conventional WC-Co coating to deposit a composite wear resistant coating . The deposition of WC-Co + GNP composite coatings (WC-Co + GNP1 & WC-Co + GNP2) were achieved by radially injecting the GNP suspension and axially injecting the WC-Co powder, as shown in Figure 82. Radial injection was preferred to eliminate the powder mixing problem, and use the GNPs in the suspension form, which was successful at the previous chapter. In addition, using radial GNP injection reduces the chances of GNPs oxidation. The GNP spent a reduced amount of time in the hotter, central part of the flame. In other studies where GNPs were axially injected into the combustion chamber, GNPs still managed to survive in that condition without changing their unique structure [32,90,191,205].

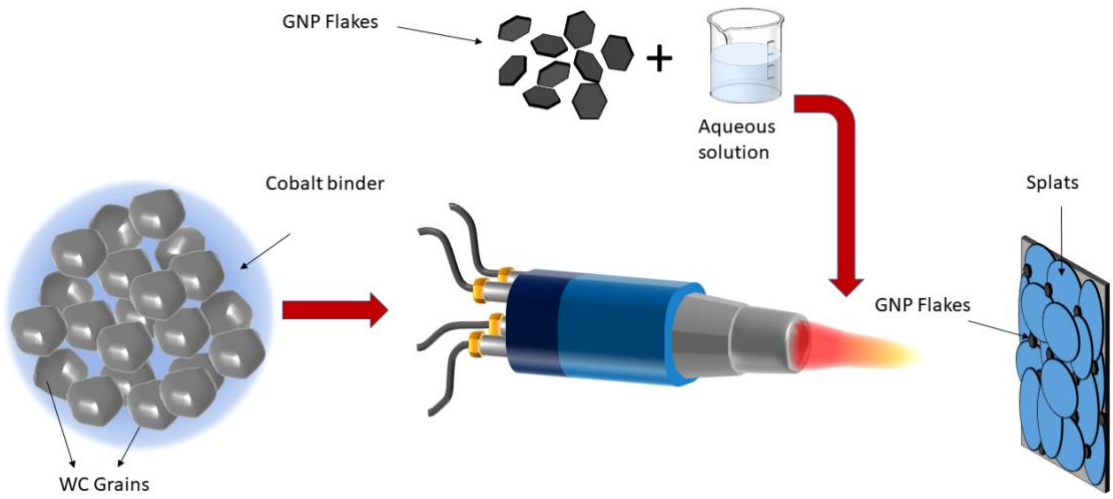


*Figure 82: A schematic diagram showing the coating deposition process*

The 2D characteristic graphene band at the Raman spectra confirms the presence of the GNPs in the composite coatings. In addition to the GNPs, the deposited coatings have $W_2C$ and W phases present in their microstructure as a result of decarburization. WC-Co feedstock particles heat up and cobalt melts because of the high temperatures. WC phases dissolve in molten Co and C oxidises into CO as a result of the oxygen-rich nature of the thermal spray

setup. After carbon loss of $W_2C$ and W phases were precipitated [129–132]. Liquid fuelled HVOF thermal sprayed WC-Co coatings are supposed to have less decarburization and undesirable phase changes [18] because in liquid fuelled HVOF thermal spray systems powder is injected after the combustion chamber. In this study, hydrogen gas is used as a fuel and gas fuelled HVOF thermal spray systems axially inject the powder into the combustion chamber which subjects the powder to high temperatures during the process.

The addition of GNPs increased the porosity for both coatings and lowered the microhardness for only WC-Co + GNP2 coating, given in Table 11. GNP particles positioned themselves between successive splats which prevented the interlocking mechanism and created the pores. The GNP2 incorporation reduces the hardness, suggesting that the GNP particle size and surface area are the main contributors to the hardness and hence bonding between the splats. GNP2 has a higher specific surface area leading to more forces of attraction so bigger aggregates of GNP particles. This can create bigger / wider pores which can explain the reduced hardness and bonding strength between splats. The reduction of mechanical properties as a result of GNP agglomeration were also obtained in other studies where GNPS were incorporated into various matrix materials [65,75,78] .

| **Samples** | **Porosity (%)** | **Vickers Hardness ($HV_{0.5}$)** |
|---|---|---|
| WC-Co | 0.6 ± 0.1 | 1191 ± 57 |
| WC-Co + GNP1 | 3.8 ± 0.6 | 1193 ± 60 |
| WC-Co + GNP2 | 2.2 ± 0.4 | 880 ± 71 |

*Table 11: Porosity and Microhardness of the WC-Co, WC-Co + GNP1 and WC-Co + GNP2 samples.*

The wear performance of the coatings was analysed against two different counter bodies ( alumina and WC) at three different rotational speeds (100 rpm, 200 rpm and 300 rpm). The addition of GNPs did not led to formation of tribofilms in this study compared to the previous chapter as CoF graphs do not show a reasonable reduction. However changing the sliding speed effects the CoF of the coatings. Increasing rotational speed from 100 to 200

rpm causes more damage, deformation and asperity formations on the surface leading to a slightly rougher surface, and as a result, CoF increases. However, at 300 rpm the surface undergoes severe deformation and becomes significantly rougher as CoF decreases compared to 200 rpm. The speed influences the interface temperature during a wear test and at higher speeds, a limited amount of heat can be conducted away from the interface. Higher interface temperature leads to the rapid growth of oxides as a result of chemical reactivity and also reduces the mechanical strength of asperities and near surface materials, which reduces the effect of increased surface roughness on the CoF behaviour [212].

The counter bodies used in the test affected the wear mechanisms of the coatings. Against WC counter body, adhesive wear mechanism took place. There was not any significant change in the specific wear rates due to rotational speed and addition of graphene. This suggests the wear mechanism against WC counter body was same throughout the all tests according the Archard wear law. The Table 12 given below summarises the wear mechanisms seen against WC counter body at all rotational speeds. There was no direct loss of any material from the system. As a result of work hardening and shear, materials pull-outs from the weakly bonded splats and decarburised areas. Pulled-out materials oxidise into $WO_3$, as a result of friction and heat generation between the coating and the counter body. This oxidised wear debris fills the pits formed on the surface due to material pull-outs [214,215]. between the coating and the counter body. This oxidised wear debris fills the pits formed on the surface [214,215].

| Counter-Body | Rotational Speed | Wear Mechanism |
|---|---|---|
| WC | 100 | Adhesive |
| | 200 | Adhesive |
| | 300 | Adhesive |

*Table 12: Wear mechanisms of WC-Co coating against WC counter body at 100, 200 and 300 rpm.*

Against alumina counter body, adhesive wear mechanism took place at both 100 and 200 rpm. The Table 13 below summarises the wear mechanisms seen against alumina counter body at all rotational speeds. Some alumina particles were found on the wear track surfaces. As a result of work hardening and shear, materials pull-outs from the weakly bonded splats

and decarburised areas. This time pits formed on the coating surface were being filled with the alumina debris. Unlike the specific wear rates against WC counter body, the specific wear rate increased significantly at 300 rpm against the alumina counter body. This suggests a change in wear mechanism from adhesive to abrasive wear according to the Archard wear law. The alumina counter body deforms catastrophically due to its brittle nature. Alumina grains underwent intergranular and/or transgranular cracking, when the critical contact pressure was reached [216]. This deformation creates many alumina particles which can act as three body abrasive particles between the surfaces. Abrasive alumina particles created more ploughing grooves on the surface and made the wear tracks deeper.

Unlike the testing against WC counter body, addition of GNPs affected the wear performance against alumina counter body. The WC-Co + GNP2 composite coating had a significantly better wear-resistant performance against the alumina counter body at 300 rpm. The addition of GNP2 introduced pores and reduced the microhardness. As this coating was softer than the others, the alumina counter body deformed less. Therefore, the contact area between the surfaces remains smaller and less abrasive alumina particles were created between the surfaces.

| **Counter-Body** | **Rotational Speed** | **Wear Mechanism** |
|---|---|---|
| Alumina | 100 | Adhesive |
| | 200 | Adhesive |
| | 300 | Abrasive |

*Table 13: Wear mechanisms of WC-Co coating against alumina counter body at 100, 200 and 300 rpm.*

The room temperature wear performance of the GNPs and the GNP incorporated WC-Co composite coatings were extensively studied in this thesis. Promising improvements were obtained in the tribological performance. Therefore, hexagonal boron nitride which has a similar structure to graphene was used for high-temperature wear-resistant coatings for the next study.

CoCrAlY + hBN composite powder was produced before the thermal spray. Both morphology and XRD analysis confirmed the powder mixing process did not alter the initial starting powders. However, the incorporation of hBN into CoCrAlY powder reduced the powder flowability by nearly 70% due to its flake-like shape and agglomeration. In another study performed on mixing hBN with $Ni_3Al$ metal powder, a reduction of powder flowability was also observed due to the presence of hBN [114]. The characteristic Raman band of hBN, present around ~ 1350 $cm^{-1}$, confirms the the presence of hBN in the coating microstructure. The incorporation of hBN reduced the coating thickness and fracture toughness. hBN used in this study has a high specific surface area (20 $m^2/g$) which uses the most of the energy provided by the flame. Therefore, CoCrAlY powder did not experience the same amount of heating and melting in flight. The presence of larger diameter particles in the CoCrAlY + hBN composite coating cross-section together with the elimination of surface oxide peaks also confirms the lower degree of heating and melting as a result of hBN addition. As mentioned before, the momentum of particles and degree of melting is critical for splat formation and strong bonding between successive splats [7,120]. Reduction in inter splat bonding was also observed in another study performed on a thermally sprayed $Ni_3Al$ + hBN composite coating once the concentration of hBN reached a critical point [114]. In addition, hBN will mostly be at the boundaries between CoCrAlY particles, and due to its lubricating ability does not promote bonding. On the other hand, the addition of hBN did not affect the microhardness. The coatings deposited in this study achieved higher microhardness values compared to another study where the hardness was around 445 HV0.3 [229].

The wear performance was investigated at 10 N and 30 N loading conditions.The addition of hBN did not led to formation of tribofilms in this study compared to the chapter 4, as CoF graphs do not show a reasonable reduction. In addition, the reduced fracture toughness as a result of hBN incorporation also increased the specific wear rate of the composite coating by an order of magnitude. Another study performed on hBN incorporated

composite coatings also showed that the addition of hBN increased the wear rate of the coating from room temperature to 800 [113]. However, a few more studies reported improved wear resistance as a result of hBN incorporation in coatings as the test temperature increased from ambient temperature to 600 °C [111,112,114]. The differences between the specific wear rates suggests a change in wear mechanism as a result of hBN incorporation, according to the Archard's wear law. The CoCrAlY coating was plastically deformed and surface has fractures and cracks all over. ON the other hand, the CoCrAlY coating underwent brittle deformation and there were abrasive grooves present on the surface. The Table 14 summarizes the worn surface characteristics for each sample under different loading conditions.

| **Sample** | **Load (N)** | **Worn Surface Characteristics** |
|---|---|---|
| CoCrAlY | 10 | Not a uniform wear track |
| | 30 | Plastically deformed<br>Fractures and cracks |
| CoCrAlY + hBN | 10 | Brittle Deformation<br>Abrasive Grooves |
| | 30 | Reached to the substrate |

*Table 14: Worn surface characteristics of both CoCrAlY and CoCrAlY + hBN coating under 10 N and 30 N loading conditions.*

The last study of this thesis was about depositing high-temperature wear-resistant coating from a unique and recently developed CrNiAlCY powder. The coatings deposited via 100% stoichiometric ratio and higher total gas flow rates achieved higher microhardness and lower porosity content. Higher total gas flow means, higher velocity and momentum of the particles exiting the thermal spray gun; hence stronger bonding between the splats can be achieved. The wear performance of the coating was investigated at both room temperature

and higher temperature against alumina counter body at 10N, 30 N and 60 N loading conditions There was not any significant change in specific wear rates at room temperature test. This suggests the wear mechanism was same throughout the room temperature tests according to the Archard's wear law. On the other hand, the specific wear rates were the same under 10 N and 30 N loading conditions for high temperature wear tests and increased significantly under 60 N load. This suggests the wear mechanism was changed at 60 N load. The wear tracks were uniform and the whole surface was covered with a protective oxide layer. That is also the reason for having similar wear rates to the room temperature tests as the oxide layer protects the surface. However, under 60 N load, the protective oxide layer on top of the wear track was full of cracks and flakes, which suggests the oxide layer was deformed under the load and could not protect the surface anymore.

| **Test Condition** | **Load (N)** | **Worn Surface Characteristics** |
|---|---|---|
| Room Temperature (RT) | 10 | Not a uniform wear track<br>Oxidised debri present |
| | 30 | Uniform and Smooth<br>Oxidised debri pushed towards the edges |
| | 60 | Uniform and Smooth<br>Oxidised debri pushed towards the edges |
| High Temperature (HT) | 10 | Smooth surface<br>Smeared wear debri |
| | 30 | Smooth surface<br>Smeared wear debri |
| | 60 | Rough surface<br>Full of fractures and cracks |

*Table 15: Worn surface characteristics at both room temperature and high temperature wear tests under 10 N, 30 N and 60 N loading conditions.*

# Chapter 9: Conclusion

The main aim of this study was to deposit unique coating compositions with 2D materials via a high velocity oxy-fuel thermal spray for improved wear performance at both room temperature and high temperature (900 °C) applications. 2D Graphene nanoplatelets (GNP) films and composite WC-Co + GNP coatings were deposited for room temperature applications to replace WC-Co coatings. For high temperature and oxidation resistant applications, CoCrAlY + hBN composite coatings were deposited to improve the hardness and wear resistance of the CoCrAlY coatings. In addition, a recently developed bespoke CrNiAlCY powder was used to deposit a new coating composition for high temperature wear applications. Four different studies were performed to reach the aim and complete the objectives of this thesis. A summary of the key findings are given below;

The deposited GNP film via HVOF from GNP suspensions offers significant tribological solutions in the form of a slid lubricant. The self-lubricative ability of the GNPs allows the layers to slide over each other, increases the area coverage, forms a tribofilm and dissipates the energy. However, GNPs started to lose their structural integrity, hence the unique self-lubricative ability was lost. Oxide bonds were formed between the layers as a result of heat generation during the wear tests. The addition of oxygen bonds changed the bonding type of the GNP films. Once those changes reach a critical level which is enough to cause the hexagonal structure of the graphene to change into amorphous carbon, the film fails. Results of this chapter suggest the bonding between the substrate and the film, the thickness and the area coverage of the films have a minor influence on the tribological performance of the deposited GNP films. However, the oxidation of the GNPs during the process and deformation of the unique hexagonal structure have a major effect on the tribological performance.

After a detailed investigation of GNPs films, a hybrid injection HVOF thermal spray setup was used to incorporate GNPs into WC-Co systems. All coatings showed promising tribological solutions against two different counter surfaces (alumina & WC) at three different speeds (100, 200 & 300 rpm). Changing the speed and the counter surface did not have a major influence on the specific wear rate values, different oxides were obtained on the worn surfaces as a result of different counter surface materials. Wear tests performed at 300 rpm against the alumina counter surface is the only exception where there was a large increase in specific wear rates were obtained. These conditions cause the catastrophic failure of the

ceramic alumina counter surface. This increases the contact area and the amount of third body abrasive particles present in the system. The combination of the increased contact surface and the higher amount of abrasive particles lead to a massive increase in wear volume. There was no tribofilm or GNPs present in the wear tracks, which suggests improved performance was due to alteration of mechanical properties as a result of GNP addition.

Following the previous studies, hBN was incorporated into CoCrAlY systems to deposit unique composite coating via HVOF for improved high temperature wear performance. The presence of the characteristic Raman band of hBN around ~1350 $cm^{-1}$ Raman shifts confirms the survival of hBN during the thermal spray and the presence of hBN inside the deposited coating microstructure. Reduced powder flow and heating during the HVOF thermal spray, as a result of hBN addition lowers the momentum of particles in flight. Therefore, reduced splat flatting and poor bonding were obtained. Hence, the fracture toughness was reduced, which in turn lowered the wear performance of the composite CoCrAlY + hBN coating. Further optimisation is required to achieve an improved tribological solution via hBN incorporation. Reduced heating also eliminated the formation of surface oxides on the CoCrAlY + hBN composite coating. The elimination of surface oxides due to the hBN addition offers an alternative method of coating deposition from materials that are sensitive to oxidation and decarburisation.

A recently developed bespoke CrNiAlCY metal powder was used to deposit thermal sprayed wear-resistant coatings. The microstructure of the powder consisted of dendric chromium carbide grains embedded in an intermetallic aluminium nitride binder matrix that was conserved in the coatings. The wear performance of the coatings was analysed at both room temperature and high temperature at three different loading conditions (10 N, 30 N & 60 N). At room temperature tests, the specific wear rate was only increased when the loading increased from 10 N to 30 N, as a 10 N load was not sufficient enough for the formation of a uniform wear track. The produced wear debris was oxidised and pushed towards the edges of the wear track. On the other hand, the specific wear rate was increased sharply when the loading was increased to 60 N at high-temperature tests. During the high-temperature wear, the whole surface was oxidised into a $Cr_2O_3$ layer, which could not withstand the 60 N load, it started to crack, flaked off and as a result the wear mechanism was changed.

# Chapter 10: Future work

This study showed that unique coatings compositions including 2D materials such as graphene and hBN can be deposited via HVOF thermal spray process. However, further research can be carried out on these coatings to optimise the wear performance of the coatings.

For GNP films, the addition of oxygen bonds changed the bonding type of the GNP films. Once those changes reach a critical level which is enough to cause the hexagonal structure of the graphene to change into amorphous carbon, the film fails. Therefore, further work to delay or prevent the oxidation during the wear and deformation of the structure can be crucial to improve the performance of GNP containing composite coatings or films. For WC-Co + GNP composite coatings, further work on optimising the amount of GNPs present inside coatings are required to analyse if an increased number of GNPs inside the coatings can contribute to the GNP pull out and tribofilm formation to contribute further to wear resistance properties. On the other hand, the incorporation of hBN was not promising as much as graphene. However, with further optimisationvia (changing spray parameters or the concentration of hBN in the final composition of the coating, this can be improved.

# Bibliography


[1] K. Holmberg, A. Erdemir, Influence of tribology on global energy consumption, costs and emissions, Friction. 5 (2017) 263–284. https://doi.org/10.1007/s40544-017-0183-5.

[2] Thermal Spray Market | 2021 - 26 | Industry Share, Size, Growth - Mordor Intelligence, (n.d.). https://www.mordorintelligence.com/industry-reports/thermal-spray-market (accessed January 20, 2022).

[3] M. Oge, A.C. Karaoglanli, M.B. Celik, Room and high temperature wear behaviors of steelmaking slag coating and WC-reinforced composite coatings, Surf. Coatings Technol. 399 (2020) 126162. https://doi.org/10.1016/J.SURFCOAT.2020.126162.

[4] Thermal Spray Coatings Market Size To Expand At 6.5% CAGR Between 2019-2029: Fact.MR - Coatings World, (n.d.). https://www.coatingsworld.com/contents/view_market-research/2020-03-31/thermal-spray-coatings-market-size-to-expand-at-65-cagr-between-2019-2029-factmr/ (accessed March 23, 2022).

[5] K.S. Novoselov, A.K. Geim, S. V. Morozov, D. Jiang, Y. Zhang, S. V. Dubonos, I. V. Grigorieva, A.A. Firsov, Electric field in atomically thin carbon films, Science (80-. ). 306 (2004) 666–669. https://doi.org/10.1126/science.1102896.

[6] J.R. Davis, 5.1 Splat, Handb. Therm. Spray Technol. (2004). https://app.knovel.com/hotlink/khtml/id:kt008JAK83/handbook-thermal-spray/splat.

[7] L. Pawlowski, The Science and Engineering of Thermal Spray Coatings: Second Edition, Sci. Eng. Therm. Spray Coatings Second Ed. (2008) 1–626. https://doi.org/10.1002/9780470754085.

[8] J.R. Davis, 6.1 Flame Spray, Handb. Therm. Spray Technol. (2004). https://app.knovel.com/hotlink/khtml/id:kt008JAKH5/handbook-thermal-spray/flame-spray.

[9] J.R. Davis, 1.1 Characteristics of Thermal Spray Coatings (Ref 1), Handb. Therm. Spray Technol. (2004). https://app.knovel.com/hotlink/khtml/id:kt008JAI47/handbook-

thermal-spray/characteristics-thermal.

[10] D. Tejero-Martin, M. Rezvani Rad, A. McDonald, T. Hussain, Beyond Traditional Coatings: A Review on Thermal-Sprayed Functional and Smart Coatings, J. Therm. Spray Technol. 28 (2019) 598–644. https://doi.org/10.1007/s11666-019-00857-1.

[11] M. Oksa, E. Turunen, T. Suhonen, T. Varis, S.P. Hannula, Optimization and Characterization of High Velocity Oxy-fuel Sprayed Coatings: Techniques, Materials, and Applications, Coatings 2011, Vol. 1, Pages 17-52. 1 (2011) 17–52. https://doi.org/10.3390/COATINGS1010017.

[12] P. Fauchais, Understanding plasma spraying, J. Phys. D. Appl. Phys. 37 (2004) R86. https://doi.org/10.1088/0022-3727/37/9/R02.

[13] P. Fauchais, A. Vardelle, B. Dussoubs, Quo vadis thermal spraying?, J. Therm. Spray Technol. 2001 101. 10 (2001) 44–66. https://doi.org/10.1361/105996301770349510.

[14] P.L. Ke, Y.N. Wu, Q.M. Wang, J. Gong, C. Sun, L.S. Wen, Study on thermal barrier coatings deposited by detonation gun spraying, Surf. Coatings Technol. 200 (2005) 2271–2276. https://doi.org/10.1016/J.SURFCOAT.2004.07.107.

[15] T.S. Sidhu, S. Prakash, R.D. Agrawal, State of the Art of HVOF Coating Investigations—A Review, Mar. Technol. Soc. J. 39 (2005) 53–64. https://doi.org/10.4031/002533205787443908.

[16] J.R. Davis, 4. Introduction to Coatings, Equipment, and Theory, Handb. Therm. Spray Technol. (2004). https://app.knovel.com/hotlink/khtml/id:kt008JAK1B/handbook-thermal-spray/introduction-coatings.

[17] M.I. Boulos, P.L. Fauchais, J.V.R. Heberlein, Combustion Spraying, (2021) 235–302. https://doi.org/10.1007/978-3-030-70672-2_7.

[18] R. Schwetzke, H. Kreye, Microstructure and properties of tungsten carbide coatings sprayed with various high-velocity oxygen fuel spray systems, J. Therm. Spray Technol. 8 (1999) 433–439. https://doi.org/10.1361/105996399770350395.

[19] F.-L. Toma, A. Potthoff, L.-M. Berger, C. Leyens, Demands, Potentials, and Economic Aspects of Thermal Spraying with Suspensions: A Critical Review, J. Therm. Spray

Technol. 24 (n.d.). https://doi.org/10.1007/s11666-015-0274-7.

[20] Z.G. Ban, L.L. Shaw, Characterization of thermal sprayed nanostructured WC-Co coatings derived from nanocrystalline WC-18wt.%Co powders, J. Therm. Spray Technol. 2003 121. 12 (2003) 112–119. https://doi.org/10.1361/105996303770348564.

[21] M. Li, P.D. Christofides, Feedback Control of HVOF Thermal Spray Process Accounting for Powder Size Distribution, (n.d.). https://doi.org/10.1361/10599630418086.

[22] V.L. Tellkamp, M.L. Lau, A. Fabel, E.J. Lavernia, Thermal spraying of nanocrystalline inconel 718, Nanostructured Mater. 1–8 (1997) 489–492. https://doi.org/10.1016/S0965-9773(97)00107-4.

[23] M. Li, P.D. Christofides, Modeling and analysis of HVOF thermal spray process accounting for powder size distribution, Chem. Eng. Sci. 58 (2003) 849–857. https://doi.org/10.1016/S0009-2509(02)00616-4.

[24] A. Killinger, P. Müller, R. Gadow, What Do We Know, What are the Current Limitations of Suspension HVOF Spraying?, J. Therm. Spray Technol. 24 (n.d.). https://doi.org/10.1007/s11666-015-0264-9.

[25] L. Pawlowski, Suspension and solution thermal spray coatings, Surf. Coatings Technol. 203 (2009) 2807–2829. https://doi.org/10.1016/j.surfcoat.2009.03.005.

[26] M. Bai, H. Maher, Z. Pala, T. Hussain, Microstructure and phase stability of suspension high velocity oxy-fuel sprayed yttria stabilised zirconia coatings from aqueous and ethanol based suspensions, J. Eur. Ceram. Soc. 38 (2018) 1878–1887. https://doi.org/10.1016/j.jeurceramsoc.2017.10.026.

[27] (54) HYBRID METHODOLOGY FOR PRODUCING COMPOSITE, MULTI-LAYERED AND GRADED COATINGS BY PLASMASPRAYING UTILIZING POWDER AND SOLUTION PRECURSOR FEEDSTOCK, (2013).

[28] S. V Joshi, G. Sivakumar, Hybrid Processing with Powders and Solutions: A Novel Approach to Deposit Composite Coatings, J. Therm. Spray Technol. 24 (n.d.). https://doi.org/10.1007/s11666-015-0262-y.

[29] S. Björklund, S. Goel, S. Joshi, Function-dependent coating architectures by hybrid powder-suspension plasma spraying: Injector design, processing and concept validation, Mater. Des. 142 (2018) 56–65. https://doi.org/10.1016/J.MATDES.2018.01.002.

[30] F. Cipri, F. Marra, G. Pulci, J. Tirillò, C. Bartuli, T. Valente, Plasma sprayed composite coatings obtained by liquid injection of secondary phases, Surf. Coatings Technol. 203 (2009) 2116–2124. https://doi.org/10.1016/J.SURFCOAT.2008.09.029.

[31] S. Chadha, • R Jefferson-Loveday, • F Venturi, • T Hussain, A Computational and Experimental Investigation into Radial Injection for Suspension High Velocity Oxy-Fuel (SHVOF) Thermal Spray, (n.d.). https://doi.org/10.1007/s11666-019-00888-8.

[32] F. Venturi, T. Hussain, Radial Injection in Suspension High Velocity Oxy-Fuel (S-HVOF) Thermal Spray of Graphene Nanoplatelets for Tribology, J. Therm. Spray Technol. 29 (2020) 255–269. https://doi.org/10.1007/s11666-019-00957-y.

[33] K. Derelizade, F. Venturi, R.G. Wellman, A. Kholobysov, T. Hussain, Wear performance of graphene nano platelets incorporated WC-Co coatings deposited by hybrid high velocity oxy fuel thermal spray, Wear. 482–483 (2021). https://doi.org/10.1016/j.wear.2021.203974.

[34] S. Nigam, S.S. Mahapatra, S.K. Patel, Effect of stand-off distance in thermally sprayed copper coating, Https://Doi.Org/10.1080/02670844.2019.1581690. 35 (2019) 826–832. https://doi.org/10.1080/02670844.2019.1581690.

[35] M.F. Hasan, J. Wang, C.C. Berndt, Effect of Power and Stand-Off Distance on Plasma Sprayed Hydroxyapatite Coatings, Http://Dx.Doi.Org/10.1080/10426914.2013.811730. 28 (2013) 1279–1285. https://doi.org/10.1080/10426914.2013.811730.

[36] R. Goswami, H. Herman, S. Sampath, X. Jiang, Y. Tian, G. Halada, Plasma sprayed MoMo oxide nanocomposites: synthesis and characterization, Surf. Coatings Technol. 141 (2001) 220226.

[37] J. Alcalá, F. Gaudette, S. Suresh, S. Sampath, Instrumented spherical micro-indentation of plasma-sprayed coatings, (2001). www.elsevier.com/locate/msea (accessed

February 9, 2022).

[38] S. Zhang, J. Zhou, B. Guo, H. Zhou, Y. Pu, J. Chen, Friction and wear behavior of laser cladding Ni/hBN self-lubricating composite coating, Mater. Sci. Eng. A. 491 (2008) 47–54. https://doi.org/10.1016/j.msea.2007.12.015.

[39] S. Deshpande, S. Sampath, H. Zhang, Mechanisms of oxidation and its role in microstructural evolution of metallic thermal spray coatings—Case study for Ni–Al, Surf. Coatings Technol. 200 (2006) 5395–5406. https://doi.org/10.1016/J.SURFCOAT.2005.07.072.

[40] K. Voleník, V. Novák, J. Dubský, P. Chráska, K. Neufuss, Properties of alloy steel coatings oxidized during plasma spraying, Mater. Sci. Eng. A. 234–236 (1997) 493–496. https://doi.org/10.1016/S0921-5093(97)00241-4.

[41] R.A. Neiser, M.F. Smith, R.C. Dykhuizen, Oxidation in Wire HVOF-Sprayed Steel, J. Therm. Spray Technol. 7 (1998) 537–545. https://doi.org/10.1361/105996398770350765.

[42] N.P. Padture, M. Gell, E.H. Jordan, Thermal barrier coatings for gas-turbine engine applications, Science. 296 (2002) 280–284. https://doi.org/10.1126/SCIENCE.1068609.

[43] K.T. Scott, Plasma sprayed coatings, (1988). https://doi.org/10.1038/SCIENTIFICAMERICAN0988-112.

[44] H. Herman, N.R. Shankar, Survivability of thermal barrier coatings, Mater. Sci. Eng. 88 (1987) 69–74. https://doi.org/10.1016/0025-5416(87)90068-1.

[45] R. McPherson, A review of microstructure and properties of plasma sprayed ceramic coatings, Surf. Coatings Technol. 39–40 (1989) 173–181. https://doi.org/10.1016/0257-8972(89)90052-2.

[46] S.S. Chatha, A. Pal, T. Singh, Performance evaluation of aluminium 6063 drilling under the influence of nanofluid minimum quantity lubrication, J. Clean. Prod. 137 (2016) 537–545. https://doi.org/10.1016/J.JCLEPRO.2016.07.139.

[47] C. Detloff, Coating Microstructures: Understanding the Science Behind Thermal Spray Coatings, TST Eng. Coatings. (2018). https://empoweringpumps.com/tstcoatings-

microstructures-science-thermal-spray-coatings/ (accessed December 12, 2022).

[48] X. Huang, Z. Yin, S. Wu, X. Qi, Q. He, Q. Zhang, Q. Yan, F. Boey, H. Zhang, Graphene-Based Materials: Synthesis, Characterization, Properties, and Applications, Small. 7 (2011) 1876–1902. https://doi.org/10.1002/SMLL.201002009.

[49] R.S. Edwards, K.S. Coleman, Graphene synthesis: relationship to applications, Nanoscale. 5 (2012) 38–51. https://doi.org/10.1039/C2NR32629A.

[50] W. Choi, I. Lahiri, R. Seelaboyina, Y.S. Kang, Synthesis of Graphene and Its Applications: A Review, Crit. Rev. Solid State Mater. Sci. 35 (2010) 52–71. https://doi.org/10.1080/10408430903505036.

[51] D. Wei, Y. Liu, Controllable Synthesis of Graphene and Its Applications, Adv. Mater. 22 (2010) 3225–3241. https://doi.org/10.1002/ADMA.200904144.

[52] P. Avouris, C. Dimitrakopoulos, Graphene: synthesis and applications, Mater. Today. 15 (2012) 86–97. https://doi.org/10.1016/S1369-7021(12)70044-5.

[53] X. Jia, J. Campos-Delgado, M. Terrones, V. Meunier, M.S. Dresselhaus, Graphene edges: a review of their fabrication and characterization, Nanoscale. 3 (2011) 86–95. https://doi.org/10.1039/C0NR00600A.

[54] A. Nieto, A. Bisht, D. Lahiri, C. Zhang, A. Agarwal, Graphene reinforced metal and ceramic matrix composites: a review, Int. Mater. Rev. 62 (2017) 241–302. https://doi.org/10.1080/09506608.2016.1219481.

[55] D. Berman, A. Erdemir, A. V. Sumant, Graphene: A new emerging lubricant, Mater. Today. 17 (2014) 31–42. https://doi.org/10.1016/j.mattod.2013.12.003.

[56] Q.-L. Yan, M. Gozin, F.-Q. Zhao, A. Cohen, S.-P. Pang, Highly energetic compositions based on functionalized carbon nanomaterials, Nanoscale. 8 (2016) 4799–4851. https://doi.org/10.1039/C5NR07855E.

[57] M. Wall, The Raman Spectroscopy of Graphene and the Determination of Layer Thickness, 2011.

[58] RENISHAW, Raman Spectroscopy Explained, RENISHAW -Apply Innov. (2017) 1–44. http://www.renishaw.com/en/raman-spectroscopy-explained--25801.

[59] D.K. Koli, G. Agnihotri, R. Purohit, Advanced Aluminium Matrix Composites: The Critical Need of Automotive and Aerospace Engineering Fields, Mater. Today Proc. 2 (2015) 3032–3041. https://doi.org/10.1016/J.MATPR.2015.07.290.

[60] J. Eliasson, R. Sandstrom, Applications of Aluminium Matrix Composites, Key Eng. Mater. 104–107 (1995) 3–36. https://doi.org/10.4028/WWW.SCIENTIFIC.NET/KEM.104-107.3.

[61] F.H. Latief, E.-S.M. Sherif, A.A. Almajid, H. Junaedi, Fabrication of exfoliated graphite nanoplatelets-reinforced aluminum composites and evaluating their mechanical properties and corrosion behavior, J. Anal. Appl. Pyrolysis. 92 (2011) 485–492. https://doi.org/10.1016/j.jaap.2011.09.003.

[62] F.H. Latief, E.-S.M. Sherif, Effects of sintering temperature and graphite addition on the mechanical properties of aluminum, J. Ind. Eng. Chem. 18 (2012) 2129–2134. https://doi.org/10.1016/j.jiec.2012.06.007.

[63] R. Pérez-Bustamante, D. Bolaños-Morales, J. Bonilla-Martínez, I. Estrada-Guel, R. Martínez-Sánchez, Microstructural and hardness behavior of graphene-nanoplatelets/aluminum composites synthesized by mechanical alloying, J. Alloys Compd. 615 (2015) S578–S582. https://doi.org/10.1016/j.jallcom.2014.01.225.

[64] S.F. Bartolucci, J. Paras, M.A. Rafiee, J. Rafiee, S. Lee, D. Kapoor, N. Koratkar, Graphene-aluminum nanocomposites, Mater. Sci. Eng. A. 528 (2011) 7933–7937. https://doi.org/10.1016/j.msea.2011.07.043.

[65] J.L. Li, Y.C. Xiong, X.D. Wang, S.J. Yan, C. Yang, W.W. He, J.Z. Chen, S.Q. Wang, X.Y. Zhang, S.L. Dai, Microstructure and tensile properties of bulk nanostructured aluminum/graphene composites prepared via cryomilling, Mater. Sci. Eng. A. 626 (2015) 400–405. https://doi.org/10.1016/j.msea.2014.12.102.

[66] S.E. Shin, H.J. Choi, J.H. Shin, D.H. Bae, Strengthening behavior of few-layered graphene/aluminum composites, Carbon N. Y. 82 (2015) 143–151. https://doi.org/10.1016/J.CARBON.2014.10.044.

[67] M. Rashad, F. Pan, A. Tang, M. Asif, Effect of Graphene Nanoplatelets addition on mechanical properties of pure aluminum using a semi-powder method, Prog. Nat. Sci.

Mater. Int. 24 (2014) 101–108. https://doi.org/10.1016/j.pnsc.2014.03.012.

[68] B.L. Mordike, T. Ebert, Magnesium: Properties — applications — potential, Mater. Sci. Eng. A. 302 (2001) 37–45. https://doi.org/10.1016/S0921-5093(00)01351-4.

[69] M. Rashad, F. Pan, A. Tang, M. Asif, M. Aamir, Synergetic effect of graphene nanoplatelets (GNPs) and multi-walled carbon nanotube (MW-CNTs) on mechanical properties of pure magnesium, J. Alloys Compd. 603 (2014) 111–118. https://doi.org/10.1016/j.jallcom.2014.03.038.

[70] M. Rashad, F. Pan, M. Asif, A. Tang, Powder metallurgy of Mg–1%Al–1%Sn alloy reinforced with low content of graphene nanoplatelets (GNPs), J. Ind. Eng. Chem. 20 (2014) 4250–4255. https://doi.org/10.1016/j.jiec.2014.01.028.

[71] M. Rashad, F. Pan, A. Tang, M. Asif, J. She, J. Gou, J. Mao, H. Hu, Development of magnesium-graphene nanoplatelets composite, J. Compos. Mater. 49 (2015) 285–293. https://doi.org/10.1177/0021998313518360.

[72] M. Rashad, F. Pan, H. Hu, M. Asif, S. Hussain, J. She, Enhanced tensile properties of magnesium composites reinforced with graphene nanoplatelets, Mater. Sci. Eng. A. 630 (2015) 36–44. https://doi.org/10.1016/j.msea.2015.02.002.

[73] M. Rashad, F.S. Pan, M. Asif, A. Ullah, Improved mechanical properties of magnesium–graphene composites with copper–graphene hybrids, Mater. Sci. Technol. 31 (2015) 1452–1461. https://doi.org/10.1179/1743284714Y.0000000726.

[74] M. Rashad, F. Pan, A. Tang, M. Asif, S. Hussain, J. Gou, J. Mao, Improved strength and ductility of magnesium with addition of aluminum and graphene nanoplatelets (Al+GNPs) using semi powder metallurgy method, J. Ind. Eng. Chem. 23 (2015) 243–250. https://doi.org/10.1016/j.jiec.2014.08.024.

[75] A. Das, S.P. Harimkar, Effect of Graphene Nanoplate and Silicon Carbide Nanoparticle Reinforcement on Mechanical and Tribological Properties of Spark Plasma Sintered Magnesium Matrix Composites, J. Mater. Sci. Technol. 30 (2014) 1059–1070. https://doi.org/10.1016/j.jmst.2014.08.002.

[76] L.Y. Chen, H. Konishi, A. Fehrenbacher, C. Ma, J.Q. Xu, H. Choi, H.F. Xu, F.E. Pfefferkorn,

X.C. Li, Novel nanoprocessing route for bulk graphene nanoplatelets reinforced metal matrix nanocomposites, Scr. Mater. 67 (2012) 29–32. https://doi.org/10.1016/j.scriptamat.2012.03.013.

[77] M. Li, S.J. Zinkle, Physical and mechanical properties of copper and copper alloys, in: Compr. Nucl. Mater., 2012: pp. 667–690. https://doi.org/10.1016/B978-0-08-056033-5.00122-1.

[78] K. Chu, C. Jia, Enhanced strength in bulk graphene-copper composites, Phys. Status Solidi. 211 (2014) 184–190. https://doi.org/10.1002/pssa.201330051.

[79] J. Dutkiewicz, P. Ozga, W. Maziarz, J. Pstruś, B. Kania, P. Bobrowski, J. Stolarska, Microstructure and properties of bulk copper matrix composites strengthened with various kinds of graphene nanoplatelets, Mater. Sci. Eng. A. 628 (2015) 124–134. https://doi.org/10.1016/j.msea.2015.01.018.

[80] W.J. Kim, T.J. Lee, S.H. Han, Multi-layer graphene/copper composites: Preparation using high-ratio differential speed rolling, microstructure and mechanical properties, Carbon N. Y. 69 (2014) 55–65. https://doi.org/10.1016/j.carbon.2013.11.058.

[81] M. Li, H. Che, X. Liu, S. Liang, H. Xie, Highly enhanced mechanical properties in Cu matrix composites reinforced with graphene decorated metallic nanoparticles, J. Mater. Sci. 49 (2014) 3725–3731. https://doi.org/10.1007/s10853-014-8082-x.

[82] J. Hwang, T. Yoon, S.H. Jin, J. Lee, T.S. Kim, S.H. Hong, S. Jeon, Enhanced Mechanical Properties of Graphene/Copper Nanocomposites Using a Molecular-Level Mixing Process, Adv. Mater. 25 (2013) 6724–6729. https://doi.org/10.1002/ADMA.201302495.

[83] J. Wang, Z. Li, G. Fan, H. Pan, Z. Chen, D. Zhang, Reinforcement with graphene nanosheets in aluminum matrix composites, Scr. Mater. 66 (2012) 594–597. https://doi.org/10.1016/j.scriptamat.2012.01.012.

[84] Z. Xu, X. Shi, W. Zhai, J. Yao, S. Song, Q. Zhang, Preparation and tribological properties of TiAl matrix composites reinforced by multilayer grapheme, Carbon N. Y. 67 (2014) 168–177. https://doi.org/10.1016/j.carbon.2013.09.077.

[85] T. He, J. Li, L. Wang, J. Zhu, W. Jiang, Preparation and Consolidation of Alumina/Graphene Composite Powders, Mater. Trans. 50 (2009) 749–751. https://doi.org/10.2320/matertrans.MRA2008458.

[86] K. Wang, Y. Wang, Z. Fan, J. Yan, T. Wei, Preparation of graphene nanosheet/alumina composites by spark plasma sintering, Mater. Res. Bull. 46 (2011) 315–318. https://doi.org/10.1016/j.materresbull.2010.11.005.

[87] J. Liu, H. Yan, K. Jiang, Mechanical properties of graphene platelet-reinforced alumina ceramic composites, Ceram. Int. 39 (2013) 6215–6221. https://doi.org/10.1016/j.ceramint.2013.01.041.

[88] Y. Fan, L. Wang, J. Li, J. Li, S. Sun, F. Chen, L. Chen, W. Jiang, Preparation and electrical properties of graphene nanosheet/Al2O3composites, Carbon N. Y. 48 (2010) 1743–1749. https://doi.org/10.1016/j.carbon.2010.01.017.

[89] A. Centeno, V.G. Rocha, B. Alonso, A. Fernández, C.F. Gutierrez-Gonzalez, R. Torrecillas, A. Zurutuza, Graphene for tough and electroconductive alumina ceramics, J. Eur. Ceram. Soc. 33 (2013) 3201–3210. https://doi.org/10.1016/j.jeurceramsoc.2013.07.007.

[90] J.W. Murray, G.A. Rance, F. Xu, T. Hussain, Alumina-graphene nanocomposite coatings fabricated by suspension high velocity oxy-fuel thermal spraying for ultra-low-wear, J. Eur. Ceram. Soc. 38 (2018) 1819–1828. https://doi.org/10.1016/j.jeurceramsoc.2017.10.022.

[91] L.S. Walker, V.R. Marotto, M.A. Rafiee, N. Koratkar, E.L. Corral, Toughening in Graphene Ceramic Composites, ACS Nano. 5 (2011) 3182–3190. https://doi.org/10.1021/nn200319d.

[92] O. Tapasztó, L. Tapasztó, M. Markó, F. Kern, R. Gadow, C. Balázsi, Dispersion patterns of graphene and carbon nanotubes in ceramic matrix composites, Chem. Phys. Lett. 511 (2011) 340–343. https://doi.org/10.1016/j.cplett.2011.06.047.

[93] C. Ramirez, F.M. Figueiredo, P. Miranzo, P. Poza, M.I. Osendi, Graphene nanoplatelet/silicon nitride composites with high electrical conductivity, Carbon N. Y. 50 (2012) 3607–3615. https://doi.org/10.1016/j.carbon.2012.03.031.

[94] C. Ramirez, L. Garzón, P. Miranzo, M.I. Osendi, C. Ocal, Electrical conductivity maps in graphene nanoplatelet/silicon nitride composites using conducting scanning force microscopy, Carbon N. Y. 49 (2011) 3873–3880. https://doi.org/10.1016/j.carbon.2011.05.025.

[95] A. Nieto, L. Huang, Y.-H. Han, J.M. Schoenung, Sintering behavior of spark plasma sintered alumina with graphene nanoplatelet reinforcement, Ceram. Int. 41 (2015) 5926–5936. https://doi.org/10.1016/j.ceramint.2015.01.027.

[96] M. Belmonte, C. Ramírez, J. González-Julián, J. Schneider, P. Miranzo, M.I. Osendi, The beneficial effect of graphene nanofillers on the tribological performance of ceramics, Carbon N. Y. 61 (2013) 431–435. https://doi.org/10.1016/j.carbon.2013.04.102.

[97] P. Rutkowski, L. Stobierski, D. Zientara, L. Jaworska, P. Klimczyk, M. Urbanik, The influence of the graphene additive on mechanical properties and wear of hot-pressed Si3N4matrix composites, J. Eur. Ceram. Soc. 35 (2015) 87–94. https://doi.org/10.1016/j.jeurceramsoc.2014.08.004.

[98] H.J. Kim, S.-M. Lee, Y.-S. Oh, Y.-H. Yang, Y.S. Lim, D.H. Yoon, C. Lee, J.-Y. Kim, R.S. Ruoff, Unoxidized Graphene/Alumina Nanocomposite: Fracture- and Wear-Resistance Effects of Graphene on Alumina Matrix, Sci. Rep. 4 (2015) 5176. https://doi.org/10.1038/srep05176.

[99] O. Cedillos-Barraza, S. Grasso, N. Al Nasiri, D.D. Jayaseelan, M.J. Reece, W.E. Lee, Sintering behaviour, solid solution formation and characterisation of TaC, HfC and TaC-HfC fabricated by spark plasma sintering, J. Eur. Ceram. Soc. 36 (2016) 1539–1548. https://doi.org/10.1016/j.jeurceramsoc.2016.02.009.

[100] C. Zhang, A. Nieto, A. Agarwal, Ultrathin graphene tribofilm formation during wear of Al 2 O 3 –graphene composites, Nanomater. Energy. 5 (2016) 1–9. https://doi.org/10.1680/jnaen.15.00027.

[101] H. Porwal, P. Tatarko, R. Saggar, S. Grasso, M. Kumar Mani, I. Dlouhý, J. Dusza, M.J. Reece, Tribological properties of silica–graphene nano-platelet composites, Ceram. Int. 40 (2014) 12067–12074. https://doi.org/10.1016/j.ceramint.2014.04.046.

[102] Y. Yao, Z. Lin, Z. Li, X. Song, K.S. Moon, C.P. Wong, Large-scale production of two-

dimensional nanosheets, J. Mater. Chem. 22 (2012) 13494–13499. https://doi.org/10.1039/C2JM30587A.

[103] L. Liu, L. Xiao, M. Li, X. Zhang, Y. Chang, L. Shang, Y. Ao, Effect of hexagonal boron nitride on high-performance polyether ether ketone composites, (n.d.). https://doi.org/10.1007/s00396-015-3733-2.

[104] K.K. Kim, A. Hsu, X. Jia, S.M. Kim, Y. Shi, M. Hofmann, D. Nezich, J.F. Rodriguez-Nieva, M. Dresselhaus, T. Palacios, J. Kong, Synthesis of monolayer hexagonal boron nitride on Cu foil using chemical vapor deposition, Nano Lett. 12 (2012) 161–166. https://doi.org/10.1021/NL203249A.

[105] S. Majety, X.K. Cao, R. Dahal, B.N. Pantha, J. Li, J.Y. Lin, H.X. Jiang, Semiconducting hexagonal boron nitride for deep ultraviolet photonics, Quantum Sens. Nanophotonic Devices IX. 8268 (2012) 82682R. https://doi.org/10.1117/12.914084.

[106] Z. Liu, L. Song, S. Zhao, J. Huang, L. Ma, J. Zhang, J. Lou, P.M. Ajayan, Direct growth of graphene/hexagonal boron nitride stacked layers, Nano Lett. 11 (2011) 2032–2037. https://doi.org/10.1021/NL200464J.

[107] Y. Kubota, K. Watanabe, O. Tsuda, T. Taniguchi, Deep ultraviolet light-emitting hexagonal boron nitride synthesized at atmospheric pressure, Science. 317 (2007) 932–934. https://doi.org/10.1126/SCIENCE.1144216.

[108] K.K. Kim, A. Hsu, X. Jia, S.M. Kim, Y. Shi, M. Hofmann, D. Nezich, J.F. Rodriguez-Nieva, M. Dresselhaus, T. Palacios, J. Kong, Synthesis of monolayer hexagonal boron nitride on Cu foil using chemical vapor deposition, Nano Lett. 12 (2012) 161–166. https://doi.org/10.1021/NL203249A.

[109] C. Yuan, J. Li, L. Lindsay, D. Cherns, J.W. Pomeroy, S. Liu, J.H. Edgar, M. Kuball, Modulating the thermal conductivity in hexagonal boron nitride via controlled boron isotope concentration, Commun. Phys. 2019 21. 2 (2019) 1–8. https://doi.org/10.1038/s42005-019-0145-5.

[110] A. Lipp, K.A. Schwetz, K. Hunold, Hexagonal boron nitride: Fabrication, properties and applications, J. Eur. Ceram. Soc. 5 (1989) 3–9. https://doi.org/10.1016/0955-2219(89)90003-4.

[111] M. Demir, E. Kanca, İ.H. Karahan, Characterization of electrodeposited Ni–Cr/hBN composite coatings, J. Alloys Compd. 844 (2020) 155511. https://doi.org/10.1016/J.JALLCOM.2020.155511.

[112] X.L. Lu, X.B. Liu, P.C. Yu, S.J. Qiao, Y.J. Zhai, M. Di Wang, Y. Chen, D. Xu, Synthesis and characterization of Ni60-hBN high temperature self-lubricating anti-wear composite coatings on Ti6Al4V alloy by laser cladding, Opt. Laser Technol. 78 (2016) 87–94. https://doi.org/10.1016/J.OPTLASTEC.2015.10.005.

[113] L. Du, C. Huang, W. Zhang, T. Li, W. Liu, Preparation and wear performance of NiCr/Cr3C2–NiCr/hBN plasma sprayed composite coating, Surf. Coatings Technol. 205 (2011) 3722–3728. https://doi.org/10.1016/J.SURFCOAT.2011.01.031.

[114] L. Du, W. Zhang, W. Liu, J. Zhang, Preparation and characterization of plasma sprayed Ni3Al–hBN composite coating, Surf. Coatings Technol. 205 (2010) 2419–2424. https://doi.org/10.1016/J.SURFCOAT.2010.09.036.

[115] J. Tharajak, T. Palathai, N. Sombatsompop, Tribological properties of flame sprayed hexagonal boron nitride/polyetheretherketone coatings, Adv. Mater. Res. 410 (2012) 333–336. https://doi.org/10.4028/WWW.SCIENTIFIC.NET/AMR.410.333.

[116] J. Tharajak, T. Palathai, N. Sombatsompop, Scratch resistance and adhesion properties of PEEK coating filled with h-BN nanoparticles, Adv. Mater. Res. 747 (2013) 303–306. https://doi.org/10.4028/WWW.SCIENTIFIC.NET/AMR.747.303.

[117] J. Tharajak, T. Palathai, N. Sombatsompop, Tribological Properties of Flame Sprayed Hexagonal Boron Nitride/Polyetheretherketone Coatings, Adv. Mater. Res. 410 (2012) 333–336. https://doi.org/10.4028/WWW.SCIENTIFIC.NET/AMR.410.333.

[118] J. Tharajak, T. Palathai, N. Sombatsompop, Scratch Resistance and Adhesion Properties of PEEK Coating Filled with h-BN Nanoparticles, Adv. Mater. Res. 747 (2013) 303–306. https://doi.org/10.4028/WWW.SCIENTIFIC.NET/AMR.747.303.

[119] A. Tozar, İ.H. Karahan, A comparative study on the effect of collagen and h-BN reinforcement of hydroxyapatite/chitosan biocomposite coatings electrophoretically deposited on Ti-6Al-4V biomedical implants, Surf. Coatings Technol. 340 (2018) 167–176. https://doi.org/10.1016/J.SURFCOAT.2018.02.034.

[120] J.R. Davis, Handbook of thermal spray technology. A, 2004. https://app.knovel.com/web/toc.v/cid:kpHTST0006/viewerType:toc (accessed May 31, 2018).

[121] J. Sun, Y. Zhou, J. Deng, J. Zhao, Effect of hybrid texture combining micro-pits and micro-grooves on cutting performance of WC/Co-based tools, Int. J. Adv. Manuf. Technol. 86 (2016) 3383–3394. https://doi.org/10.1007/s00170-016-8452-4.

[122] J. Sun, J. Zhao, Z. Li, X. Ni, Y. Zhou, A. Li, Effects of initial particle size distribution and sintering parameters on microstructure and mechanical properties of functionally graded WC-TiC-VC-Cr3C2-Co hard alloys, Ceram. Int. 43 (2017) 2686–2696. https://doi.org/10.1016/j.ceramint.2016.11.086.

[123] A. Feuerstein, J. Knapp, T. Taylor, A. Ashary, A. Bolcavage, N. Hitchman, Technical and economical aspects of current thermal barrier coating systems for gas turbine engines by thermal spray and EBPVD: A review, J. Therm. Spray Technol. (2008). https://doi.org/10.1007/s11666-007-9148-y.

[124] C.U. Hardwicke, Y.C. Lau, Advances in thermal spray coatings for gas turbines and energy generation: A review, J. Therm. Spray Technol. 22 (2013) 564–576. https://doi.org/10.1007/s11666-013-9904-0.

[125] G. Mauer, D. Sebold, R. Vaßen, MCrAlY bondcoats by high-velocity atmospheric plasma spraying, in: J. Therm. Spray Technol., 2014. https://doi.org/10.1007/s11666-013-0026-5.

[126] R. Ahmed, O. Ali, C.C. Berndt, A. Fardan, R. Ahmed RAhmed, Sliding Wear of Conventional and Suspension Sprayed Nanocomposite WC-Co Coatings: An Invited Review, J. Therm. Spray Technol. 30 (2021) 800–861. https://doi.org/10.1007/s11666-021-01185-z.

[127] H.L. De Villiers Lovelock, Powder/processing/structure relationships in WC-Co thermal spray coatings: A review of the published literature, J. Therm. Spray Technol. 1998 73. 7 (1998) 357–373. https://doi.org/10.1361/105996398770350846.

[128] J.R. Fincke, W.D. Swank, D.C. Haggard, Comparison of the characteristics of HVOF and plasma thermal spray, in: ASM International, Materials Park, OH (United States),

United States, 1994. https://www.osti.gov/biblio/160466.

[129] D.A. Stewart, P.H. Shipway, D.G. McCartney, Abrasive wear behaviour of conventional and nanocomposite HVOF-sprayed WC-Co coatings, Wear. 225–229 (1999) 789–798. https://doi.org/10.1016/S0043-1648(99)00032-0.

[130] P.H. Shipway, D.G. McCartney, T. Sudaprasert, Sliding wear behaviour of conventional and nanostructured HVOF sprayed WC-Co coatings, Wear. 259 (2005) 820–827. https://doi.org/10.1016/j.wear.2005.02.059.

[131] D.A. Stewart, P.H. Shipway, D.G. McCartney, Microstructural evolution in thermally sprayed WC-Co coatings: comparison between nanocomposite and conventional starting powders, Acta Mater. 48 (2000) 1593–1604. https://doi.org/10.1016/S1359-6454(99)00440-1.

[132] Q. Yang, T. Senda, A. Ohmori, Effect of carbide grain size on microstructure and sliding wear behavior of HVOF-sprayed WC-12% Co coatings, Wear. 254 (2003) 23–34. https://doi.org/10.1016/S0043-1648(02)00294-6.

[133] J. Yuan, Q. Zhan, J. Huang, S. Ding, H. Li, Decarburization mechanisms of WC-Co during thermal spraying: Insights from controlled carbon loss and microstructure characterization, Mater. Chem. Phys. 142 (2013) 165–171. https://doi.org/10.1016/j.matchemphys.2013.06.052.

[134] H.L. De Villiers Lovelock, Powder/processing/structure relationships in WC-Co thermal spray coatings: A review of the published literature, J. Therm. Spray Technol. 1998 73. 7 (1998) 357–373. https://doi.org/10.1361/105996398770350846.

[135] P. Chivavibul, M. Watanabe, S. Kuroda, K. Shinoda, Effects of carbide size and Co content on the microstructure and mechanical properties of HVOF-sprayed WC-Co coatings, Surf. Coatings Technol. 202 (2007) 509–521. https://doi.org/10.1016/j.surfcoat.2007.06.026.

[136] Liu, Bai, Chen, Yuan, Effects of Cobalt Content on the Microstructure, Mechanical Properties and Cavitation Erosion Resistance of HVOF Sprayed Coatings, Coatings. 9 (2019) 534. https://doi.org/10.3390/coatings9090534.

[137] M. He, J. Wang, R. He, H. Yang, J. Ruan, Effect of cobalt content on the microstructure and mechanical properties of coarse grained WC-Co cemented carbides fabricated from chemically coated composite powder, J. Alloys Compd. 766 (2018) 556–563. https://doi.org/10.1016/j.jallcom.2018.06.366.

[138] H.E. Exner, J. Gurland, A review of parameters influencing some mechanical properties of tungsten carbide–cobalt alloys, Powder Metall. 13 (1970) 13–31. https://doi.org/10.1179/pom.1970.13.25.002.

[139] C.J. Li, G.J. Yang, Relationships between feedstock structure, particle parameter, coating deposition, microstructure and properties for thermally sprayed conventional and nanostructured WC–Co, Int. J. Refract. Met. Hard Mater. 39 (2013) 2–17. https://doi.org/10.1016/J.IJRMHM.2012.03.014.

[140] J. Pulsford, • S Kamnis, • J Murray, • M Bai, • T Hussain, Effect of Particle and Carbide Grain Sizes on a HVOAF WC-Co-Cr Coating for the Future Application on Internal Surfaces: Microstructure and Wear, J. Therm. Spray Technol. 27 (n.d.). https://doi.org/10.1007/s11666-017-0669-8.

[141] L. Thakur, N. Arora, Sliding and Abrasive Wear Behavior of WC-CoCr Coatings with Different Carbide Sizes, (n.d.). https://doi.org/10.1007/s11665-012-0265-5.

[142] H. Saito, A. Iwabuchi, T. Shimizu, Effects of Co content and WC grain size on wear of WC cemented carbide, Wear. 261 (2006) 126–132. https://doi.org/10.1016/J.WEAR.2005.09.034.

[143] Q. Yang, T. Senda, A. Ohmori, Effect of carbide grain size on microstructure and sliding wear behavior of HVOF-sprayed WC-12% Co coatings, Wear. 254 (2003) 23–34. https://doi.org/10.1016/S0043-1648(02)00294-6.

[144] S. Usmani, S. Sampath, D.L. Houck, D. Lee, Effect of carbide grain size on the sliding and abrasive wear behavior of thermally sprayed WC-Co coatings, Tribol. Trans. 40 (1997) 470–478. https://doi.org/10.1080/10402009708983682.

[145] H. Saito, A. Iwabuchi, T. Shimizu, Effects of Co content and WC grain size on wear of WC cemented carbide, Wear. 261 (2006) 126–132. https://doi.org/10.1016/J.WEAR.2005.09.034.

[146] F.J. Belzunce, V. Higuera, S. Poveda, High temperature oxidation of HFPD thermal-sprayed MCrAlY coatings, Mater. Sci. Eng. A. 297 (2001) 162–167. https://doi.org/10.1016/S0921-5093(00)01239-9.

[147] Y. Han, Z. Zhu, B. Zhang, Y. Chu, Y. Zhang, J. Fan, Effects of process parameters of vacuum pre-oxidation on the microstructural evolution of CoCrAlY coating deposited by HVOF, J. Alloys Compd. 735 (2018) 547–559. https://doi.org/10.1016/J.JALLCOM.2017.11.165.

[148] A. Fossati, M. Di Ferdinando, A. Lavacchi, U. Bardi, C. Giolli, A. Scrivani, Improvement of the isothermal oxidation resistance of CoNiCrAlY coating sprayed by High Velocity Oxygen Fuel, Surf. Coatings Technol. 204 (2010) 3723–3728. https://doi.org/10.1016/J.SURFCOAT.2010.04.059.

[149] P. Richer, A. Zúñiga, M. Yandouzi, B. Jodoin, CoNiCrAlY microstructural changes induced during Cold Gas Dynamic Spraying, Surf. Coatings Technol. 203 (2008) 364–371. https://doi.org/10.1016/J.SURFCOAT.2008.09.014.

[150] M. Di Ferdinando, A. Fossati, A. Lavacchi, U. Bardi, F. Borgioli, C. Borri, C. Giolli, A. Scrivani, Isothermal oxidation resistance comparison between air plasma sprayed, vacuum plasma sprayed and high velocity oxygen fuel sprayed CoNiCrAlY bond coats, Surf. Coatings Technol. 204 (2010) 2499–2503. https://doi.org/10.1016/J.SURFCOAT.2010.01.031.

[151] G.Y. Liang, C. Zhu, X.Y. Wu, Y. Wu, The formation model of Ni-Cr oxides on NiCoCrAlY-sprayed coating, Appl. Surf. Sci. 257 (2011) 6468–6473. https://doi.org/10.1016/J.APSUSC.2011.02.044.

[152] K.H. Kim, S.H. Lee, N.D. Nam, J.G. Kim, Effect of cobalt on the corrosion resistance of low alloy steel in sulfuric acid solution, Corros. Sci. 53 (2011) 3576–3587. https://doi.org/10.1016/j.corsci.2011.07.001.

[153] M. Taheri, Z. Valefi, K. Zangeneh-Madar, Influence of HVOF process parameters on microstructure and bond strength of NiCrAlY coatings, Surf. Eng. 28 (2012) 266–272. https://doi.org/10.1179/1743294411Y.0000000024.

[154] L. Ajdelsztajn, F. Tang, G.E. Kim, V. Provenzano, J.M. Schoenung, Synthesis and

Oxidation Behavior of Nanocrystalline MCrAlY Bond Coatings, (n.d.). https://doi.org/10.1361/10599630522693.

[155] G.H. Tang, G.X. Pei, X.H. Wang, B. Chen, X.L. Zeng, W.J. Cheng, Y.J. Ren, K.H. Wei, Effects of variations in coating materials and process conditions on the thermal cycle properties of NiCrAlY/YSZ thermal barrier coatings, Mater. Sci. Eng. A. 425 (2006) 94–106. https://doi.org/10.1016/J.MSEA.2006.03.043.

[156] Y. Chen, X. Zhao, P. Xiao, Effect of microstructure on early oxidation of MCrAlY coatings, Acta Mater. 159 (2018) 150–162. https://doi.org/10.1016/J.ACTAMAT.2018.08.018.

[157] J. Lu, H. Zhang, Y. Chen, X. Zhao, F. Guo, P. Xiao, Effect of microstructure of a NiCoCrAlY coating fabricated by high-velocity air fuel on the isothermal oxidation, Corros. Sci. 159 (2019). https://doi.org/10.1016/j.corsci.2019.108126.

[158] K. Fritscher, Y.T. Lee, Investigation of an as-sprayed NiCoCrAlY overlay coating - Microstructure and evolution of the coating, Mater. Corros. 56 (2005) 5–14. https://doi.org/10.1002/MACO.200403808.

[159] M.J. Pomeroy, Coatings for gas turbine materials and long term stability issues, Mater. Des. 26 (2005) 223–231. https://doi.org/10.1016/J.MATDES.2004.02.005.

[160] D. Zhang, S.J. Harris, D.G. McCartney, Microstructure formation and corrosion behaviour in HVOF-sprayed inconel 625 coatings, Mater. Sci. Eng. A. 344 (2003) 45–56. https://doi.org/10.1016/S0921-5093(02)00420-3.

[161] M.P. Planche, B. Normand, H. Liao, G. Rannou, C. Coddet, Influence of HVOF spraying parameters on in-flight characteristics of Inconel 718 particles and correlation with the electrochemical behaviour of the coating, Surf. Coat. Technol. 2–3 (2002) 247–256. https://www.infona.pl//resource/bwmeta1.element.elsevier-2dd7b1b9-cd86-33cf-88ae-fc409e849627 (accessed February 14, 2022).

[162] J. Lu, H. Zhang, Y. Chen, X. Zhao, F. Guo, P. Xiao, Effect of microstructure of a NiCoCrAlY coating fabricated by high-velocity air fuel on the isothermal oxidation, Corros. Sci. 159 (2019). https://doi.org/10.1016/j.corsci.2019.108126.

[163] D. Zhang, S.J. Harris, D.G. McCartney, Microstructure formation and corrosion

behaviour in HVOF-sprayed inconel 625 coatings, Mater. Sci. Eng. A. 344 (2003) 45–56. https://doi.org/10.1016/S0921-5093(02)00420-3.

[164] M.P. Planche, B. Normand, H. Liao, G. Rannou, C. Coddet, Influence of HVOF spraying parameters on in-flight characteristics of Inconel 718 particles and correlation with the electrochemical behaviour of the coating, Surf. Coat. Technol. 2–3 (2002) 247–256.

[165] Encyclopedia of Materials Characterization, Encycl. Mater. Charact. (1992). https://doi.org/10.1016/C2009-0-26077-6.

[166] J.I. Goldstein, D.E. Newbury, P. Echlin, D.C. Joy, C. Fiori, E. Lifshin, Scanning Electron Microscopy and X-Ray Microanalysis, (1981). https://doi.org/10.1007/978-1-4613-3273-2.

[167] M.M. Houck, Microscopy (Electron), Encycl. Forensic Sci. Second Ed. (2013) 612–615. https://doi.org/10.1016/B978-0-12-382165-2.00252-X.

[168] N.M. Pirozzi, J. Kuipers, B.N.G. Giepmans, Sample preparation for energy dispersive X-ray imaging of biological tissues, Methods Cell Biol. 162 (2021) 89–114. https://doi.org/10.1016/BS.MCB.2020.10.023.

[169] Raman Spectroscopy | Instrumentation, Introduction & Principle, (n.d.). https://www.mt.com/au/en/home/applications/L1_AutoChem_Applications/Raman-Spectroscopy.html (accessed May 3, 2022).

[170] W.N. Sharpe, ed., Springer Handbook of Experimental Solid Mechanics, (2008). https://doi.org/10.1007/978-0-387-30877-7.

[171] R.E. Smallman, A.H.W. Ngan, Modern Physical Metallurgy: Eighth Edition, Mod. Phys. Metall. Eighth Ed. (2013) 1–697. https://doi.org/10.1016/C2011-0-05565-5.

[172] F. Rickhey, K.P. Marimuthu, J.H. Lee, H. Lee, J.H. Hahn, Evaluation of the fracture toughness of brittle hardening materials by Vickers indentation, Eng. Fract. Mech. 148 (2015) 134–144. https://doi.org/10.1016/J.ENGFRACMECH.2015.09.028.

[173] C. Lee, X. Wei, J.W. Kysar, J. Hone, Measurement of the Elastic Properties and Intrinsic Strength of Monolayer Graphene, Science (80-. ). 321 (2008) 385–388. https://doi.org/10.1126/science.1157996.

[174] A. Sakhaee-Pour, Elastic properties of single-layered graphene sheet, Solid State Commun. 149 (2009) 91–95. https://doi.org/10.1016/j.ssc.2008.09.050.

[175] G.-H. Lee, R.C. Cooper, S.J. An, S. Lee, A. van der Zande, N. Petrone, A.G. Hammerberg, C. Lee, B. Crawford, W. Oliver, J.W. Kysar, J. Hone, High-Strength Chemical-Vapor-Deposited Graphene and Grain Boundaries, Science (80-. ). 340 (2013) 1073–1076. https://doi.org/10.1126/science.1235126.

[176] A.A. Balandin, S. Ghosh, W. Bao, I. Calizo, D. Teweldebrhan, F. Miao, C.N. Lau, Superior Thermal Conductivity of Single-Layer Graphene, Nano Lett. 8 (2008) 902–907. https://doi.org/10.1021/nl0731872.

[177] C. Faugeras, B. Faugeras, M. Orlita, M. Potemski, R.R. Nair, A.K. Geim, Thermal Conductivity of Graphene in Corbino Membrane Geometry, ACS Nano. 4 (2010) 1889–1892. https://doi.org/10.1021/nn9016229.

[178] X. Xu, L.F.C. Pereira, Y. Wang, J. Wu, K. Zhang, X. Zhao, S. Bae, C. Tinh Bui, R. Xie, J.T.L. Thong, B.H. Hong, K.P. Loh, D. Donadio, B. Li, B. Özyilmaz, Length-dependent thermal conductivity in suspended single-layer graphene, Nat. Commun. 5 (2014) 3689. https://doi.org/10.1038/ncomms4689.

[179] A. Rani, S.-W. Nam, K.-A. Oh, M. Park, Electrical Conductivity of Chemically Reduced Graphene Powders under Compression, Carbon Lett. 11 (2010) 90–95. https://doi.org/10.5714/CL.2010.11.2.090.

[180] B. Marinho, M. Ghislandi, E. Tkalya, C.E. Koning, G. de With, Electrical conductivity of compacts of graphene, multi-wall carbon nanotubes, carbon black, and graphite powder, Powder Technol. 221 (2012) 351–358. https://doi.org/10.1016/j.powtec.2012.01.024.

[181] L.M. Hutchings, Triblology, Edward Arnold, London UK, 1992.

[182] Q. Li, C. Lee, R.W. Carpick, J. Hone, Substrate effect on thickness-dependent friction on graphene, Phys. Status Solidi Basic Res. 247 (2010) 2909–2914. https://doi.org/10.1002/pssb.201000555.

[183] Y. Peng, Z. Wang, C. Li, H. Lee, N. Lee, Y. Seo, J. Eom, S. Lee, Comparison of frictional

forces on graphene and graphite Related content Topical Review Izabela Szlufarska, Michael Chandross and Robert W Carpick-Atomic force microscopy and spectroscopy Yongho Seo and Wonho Jhe-Study of nanotribological properties of multilayer graphene by calibrated atomic force microscopy Comparison of frictional forces on graphene and graphite, Nanotechnology. 20 (2009) 6. https://doi.org/10.1088/0957-4484/20/32/325701.

[184] X. Feng, S. Kwon, J.Y. Park, M. Salmeron, Superlubric Sliding of Graphene Nanoflakes on Graphene, (2013). https://doi.org/10.1021/nn305722d.

[185] T. Filleter, J.L. Mcchesney, A. Bostwick, E. Rotenberg, K. V Emtsev, T. Seyller, K. Horn, R. Bennewitz, Friction and Dissipation in Epitaxial Graphene Films, (n.d.). https://doi.org/10.1103/PhysRevLett.102.086102.

[186] Z. Deng, A. Smolyanitsky, Q. Li, X.-Q. Feng, R.J. Cannara, Adhesion-dependent negative friction coefficient on chemically modified graphite at the nanoscale, (2012). https://doi.org/10.1038/NMAT3452.

[187] T. Filleter, R. Bennewitz, Structural and frictional properties of graphene films on SiC(0001) studied by atomic force microscopy, (n.d.). https://doi.org/10.1103/PhysRevB.81.155412.

[188] K.-S. Kim, H.-J. Lee, C. Lee, S.-K. Lee, H. Jang, J.-H. Ahn, J.-H. Kim, H.-J. Lee, Chemical Vapor Deposition-Grown Graphene: The Thinnest Solid Lubricant, 15 (2020) 15. https://doi.org/10.1021/nn2011865.

[189] D. Berman, S.A. Deshmukh, S.K.R.S. Sankaranarayanan, A. Erdemir, A. V. Sumant, Extraordinary Macroscale Wear Resistance of One Atom Thick Graphene Layer, Adv. Funct. Mater. 24 (2014) 6640–6646. https://doi.org/10.1002/adfm.201401755.

[190] D. Berman, A. Erdemir, A. V. Sumant, Few layer graphene to reduce wear and friction on sliding steel surfaces, Carbon N. Y. 54 (2013) 454–459. https://doi.org/10.1016/j.carbon.2012.11.061.

[191] F. Venturi, G.A. Rance, J. Thomas, T. Hussain, A low-friction graphene nanoplatelets film from suspension high velocity oxy-fuel thermal spray, AIP Adv. 9 (2019). https://doi.org/10.1063/1.5089021.

[192] D. Mariotti, V. Švrček, A. Mathur, C. Dickinson, K. Matsubara, M. Kondo, Carbon nanotube growth activated by quantum-confined silicon nanocrystals, J. Phys. D. Appl. Phys. 46 (2013) 122001. https://doi.org/10.1088/0022-3727/46/12/122001.

[193] E.I. Bîru, H. Iovu, Graphene Nanocomposites Studied by Raman Spectroscopy, in: H.I.E.-G.M. do Nascimento (Ed.), Raman Spectrosc., InTech, Rijeka, 2018: p. Ch. 9. https://doi.org/10.5772/intechopen.73487.

[194] C. Ahn, EELS atlas : a reference collection of electron energy loss spectra covering all stable elements, Gatan Inc., Warrendale Pa., 1983.

[195] J. Xie, K. Komvopoulos, Bilayer amorphous carbon films synthesized by filtered cathodic vacuum arc deposition, J. Mater. Res. 31 (2016) 3161–3167. https://doi.org/10.1557/jmr.2016.250.

[196] W.D. Callister, D.G. Rethwisch, Materials Science and Engineering 9th Edition, 2014. https://doi.org/10.1016/j.str.2011.03.005.

[197] L. Pawlowski, The science and engineering of thermal spray coatings, 2008. https://books.google.com/books?hl=en&lr=&id=firIir6iX_AC&oi=fnd&pg=PR7&dq=the+scinece+and+enginnering+of+thermal+spray+coatings+second+ediytion&ots=GTBB3ydWRh&sig=gN9r9oF6RMgOZ2nKK0gQ0rYypkQ (accessed August 8, 2019).

[198] L. Yu, J.S. Park, Y.-S. Lim, C.S. Lee, K. Shin, H.J. Moon, C.-M. Yang, Y.S. Lee, J.H. Han, Carbon hybrid fillers composed of carbon nanotubes directly grown on graphene nanoplatelets for effective thermal conductivity in epoxy composites, Nanotechnology. 24 (2013) 155604. https://doi.org/10.1088/0957-4484/24/15/155604.

[199] S. Colonna, O. Monticelli, J. Gomez, C. Novara, G. Saracco, A. Fina, Effect of morphology and defectiveness of graphene-related materials on the electrical and thermal conductivity of their polymer nanocomposites, Polymer (Guildf). 102 (2016) 292–300. https://doi.org/10.1016/j.polymer.2016.09.032.

[200] F. Banhart, J. Kotakoski, A. V. Krasheninnikov, Structural Defects in Graphene, ACS Nano. 5 (2011) 26–41. https://doi.org/10.1021/nn102598m.

[201] L.-F. Wang, T.-B. Ma, Y.-Z. Hu, H. Wang, Atomic-scale friction in graphene oxide: An

interfacial interaction perspective from first-principles calculations, Phys. Rev. B. 86 (2012) 125436. https://doi.org/10.1103/PhysRevB.86.125436.

[202] C.J. Li, G.J. Yang, Relationships between feedstock structure, particle parameter, coating deposition, microstructure and properties for thermally sprayed conventional and nanostructured WC-Co, Int. J. Refract. Met. Hard Mater. 39 (2013) 2–17. https://doi.org/10.1016/j.ijrmhm.2012.03.014.

[203] C.J. Li, W.Y. Li, Effect of sprayed powder particle size on the oxidation behavior of MCrAlY materials during high velocity oxygen-fuel deposition, Surf. Coatings Technol. 162 (2003) 31–41. https://doi.org/10.1016/S0257-8972(02)00573-X.

[204] F. Venturi, G.A. Rance, J. Thomas, T. Hussain, A low-friction graphene nanoplatelets film from suspension high velocity oxy-fuel thermal spray, AIP Adv. 9 (2019). https://doi.org/10.1063/1.5089021.

[205] K. Derelizade, F. Venturi, R.G. Wellman, A. Khlobystov, T. Hussain, Structural changes of thermal sprayed graphene nano platelets film into amorphous carbon under sliding wear, Appl. Surf. Sci. 528 (2020). https://doi.org/10.1016/j.apsusc.2020.146315.

[206] T. Sudaprasert, P.H. Shipway, D.G. McCartney, Sliding wear behaviour of HVOF sprayed WC-Co coatings deposited with both gas-fuelled and liquid-fuelled systems, Wear. 255 (2003) 943–949. https://doi.org/10.1016/S0043-1648(03)00293-X.

[207] P.H. Shipway, The role of test conditions on the microabrasive wear behaviour of soda-lime glass, in: Wear, Elsevier Sequoia SA, 1999: pp. 191–199. https://doi.org/10.1016/S0043-1648(99)00187-8.

[208] C.A. Schneider, W.S. Rasband, K.W. Eliceiri, NIH Image to ImageJ: 25 years of image analysis, Nat. Methods. 9 (2012) 671–675. https://doi.org/10.1038/nmeth.2089.

[209] C. Lyphout, K. Sato, Screening design of hard metal feedstock powders for supersonic air fuel processing, Surf. Coatings Technol. 258 (2014) 447–457. https://doi.org/10.1016/j.surfcoat.2014.08.055.

[210] P.J. Blau, Running-in: Art or Engineering?, Springer-Verlag New York Inc, 1991.

[211] M.F. Daniel, B. Desbat, J.C. Lassegues, B. Gerand, M. Figlarz, Infrared and Raman study

of WO3 tungsten trioxides and WO3, xH2O tungsten trioxide tydrates, J. Solid State Chem. 67 (1987) 235–247. https://doi.org/10.1016/0022-4596(87)90359-8.

[212] L.M. Hutchings, Triblology, Edward Arnold, London UK, 1992.

[213] J. Pulsford, F. Venturi, S. Kamnis, T. Hussain, Sliding wear behaviour of WC-Co reinforced NiCrFeSiB HVOAF thermal spray coatings against WC-Co and Al2O3 counterbodies, Surf. Coatings Technol. 386 (2020). https://doi.org/10.1016/j.surfcoat.2020.125468.

[214] J. Pulsford, F. Venturi, Z. Pala, S. Kamnis, T. Hussain, Application of HVOF WC-Co-Cr coatings on the internal surface of small cylinders: Effect of internal diameter on the wear resistance, Wear. (2019). https://doi.org/10.1016/j.wear.2019.202965.

[215] G. Straffelini, Wear mechanisms, in: Springer Tracts Mech. Eng., 2015. https://doi.org/10.1007/978-3-319-05894-8_4.

[216] A.K. Mukhopadhyay, M. Yiu-Wing, Grain size effect on abrasive wear mechanisms in alumina ceramics, Wear. 162–164 (1993) 258–268. https://doi.org/10.1016/0043-1648(93)90508-J.

[217] R.I. Blombery, C.M. Perrot, P.M. Robinson, Abrasive wear of tungsten carbide-cobalt composites. I. Wear mechanisms, Mater. Sci. Eng. 13 (1974) 93–100. https://doi.org/10.1016/0025-5416(74)90176-1.

[218] M. Yahiaoui, J.Y. Paris, J. Denape, A. Dourfaye, Wear mechanisms of WC-Co drill bit inserts against alumina counterface under dry friction: Part 1 - WC-Co inserts with homogenous binder phase content, Int. J. Refract. Met. Hard Mater. 48 (2015) 245–256. https://doi.org/10.1016/j.ijrmhm.2014.09.018.

[219] K. Derelizade, F. Venturi, R.G. Wellman, A. Khlobystov, T. Hussain, Structural changes of thermal sprayed graphene nano platelets film into amorphous carbon under sliding wear, Appl. Surf. Sci. 528 (2020). https://doi.org/10.1016/j.apsusc.2020.146315.

[220] T.S. Sidhu, R.D. Agrawal, S. Prakash, Hot corrosion of some superalloys and role of high-velocity oxy-fuel spray coatings - A review, Surf. Coatings Technol. 198 (2005) 441–446. https://doi.org/10.1016/J.SURFCOAT.2004.10.056.

[221] S. Wirojanupatump, P.H. Shipway, D.G. McCartney, The influence of HVOF powder feedstock characteristics on the abrasive wear behaviour of CrxCy–NiCr coatings, Wear. 249 (2001) 829–837. https://doi.org/10.1016/S0043-1648(01)00821-3.

[222] F. Venturi, S. Kamnis, T. Hussain, Internal diameter HVOAF thermal spray of carbon nanotubes reinforced WC-Co composite coatings, Mater. Des. 202 (2021) 109566. https://doi.org/10.1016/J.MATDES.2021.109566.

[223] B. Song, • M Bai, • K T Voisey, • T Hussain, Role of Oxides and Porosity on High-Temperature Oxidation of Liquid-Fueled HVOF Thermal-Sprayed Ni50Cr Coatings, J. Therm. Spray Technol. 26 (n.d.). https://doi.org/10.1007/s11666-017-0531-z.

[224] B. Song, Z. Pala, K.T. Voisey, T. Hussain, Gas and liquid-fuelled HVOF spraying of Ni50Cr coating: Microstructure and high temperature oxidation, Surf. Coatings Technol. 318 (2017) 224–232. https://doi.org/10.1016/j.surfcoat.2016.07.046.

[225] Z. Li, L. Wang, D. Sun, Y. Zhang, B. Liu, Q. Hu, A. Zhou, Synthesis and thermal stability of two-dimensional carbide MXene Ti3C2, Mater. Sci. Eng. B Solid-State Mater. Adv. Technol. 191 (2015) 33–40. https://doi.org/10.1016/j.mseb.2014.10.009.

[226] F. Venturi, J. Pulsford, T. Hussain, A novel approach to incorporate graphene nanoplatelets to Cr2O3 for low-wear coatings, Mater. Lett. 276 (2020) 128283. https://doi.org/10.1016/J.MATLET.2020.128283.

[227] I.M. Joni, R. Balgis, T. Ogi, T. Iwaki, K. Okuyama, Surface functionalization for dispersing and stabilizing hexagonal boron nitride nanoparticle by bead milling, Colloids Surfaces A Physicochem. Eng. Asp. 388 (2011) 49–58. https://doi.org/10.1016/J.COLSURFA.2011.08.007.

[228] T. Kuzuba, K. Era, T. Ishii, T. Sato, A low frequency Raman-active vibration of hexagonal boron nitride, Solid State Commun. 25 (1978) 863–865. https://doi.org/10.1016/0038-1098(78)90288-0.

[229] Y. Itoh, M. Saitoh, M. Tamura, Characteristics of MCrAlY Coatings Sprayed by High Velocity Oxygen-Fuel Spraying System, J. Eng. Gas Turbines Power. 122 (2000) 43–49. https://doi.org/10.1115/1.483173.

[230] L. Liu, H. Xu, J. Xiao, X. Wei, G. Zhang, C. Zhang, Effect of heat treatment on structure and property evolutions of atmospheric plasma sprayed NiCrBSi coatings, Surf. Coatings Technol. 325 (2017) 548–554. https://doi.org/10.1016/j.surfcoat.2017.07.011.

[231] D.J. Branagan, M. Breitsameter, B.E. Meacham, V. Belashchenko, High-Performance Nanoscale Composite Coatings for Boiler Applications, (n.d.). https://doi.org/10.1361/10599630523755.

[232] T.S. Sidhu, S. Prakash, R.D. Agrawal, Hot corrosion and performance of nickel-based coatings, 90 (2006) 41–47. https://about.jstor.org/terms (accessed October 7, 2021).

[233] J. Singh, H. Vasudev, S. Singh, Performance of different coating materials against high temperature oxidation in boiler tubes - A review, Mater. Today Proc. 26 (2019) 972–978. https://doi.org/10.1016/J.MATPR.2020.01.156.

[234] K. TAO, J. ZHANG, H. CUI, X. lin ZHOU, J. shan ZHANG, Fabrication of conventional and nanostructured NiCrC coatings via HVAF technique, Trans. Nonferrous Met. Soc. China. 18 (2008) 262–269. https://doi.org/10.1016/S1003-6326(08)60046-1.

[235] K. Tao, X. Zhou, H. Cui, J. Zhang, Microhardness variation in heat-treated conventional and nanostructured NiCrC coatings prepared by HVAF spraying, Surf. Coatings Technol. 203 (2009) 1406–1414. https://doi.org/10.1016/j.surfcoat.2008.11.020.

[236] K. Tao, X. Zhou, H. Cui, J. Zhang, Preparation and properties of a nanostructured NiCrC alloy coating for boiler tubes protection, Mater. Trans. 49 (2008) 2159–2162. https://doi.org/10.2320/matertrans.MRP2008154.

[237] M. Durand-Charre, J.H. Davidson, The microstructure of superalloys, 2017. https://doi.org/10.1201/9780203736388.

[238] G.A.L.´ Opez, S. Sommadossi, W. Gust, E.J. Mittemeijer, P. Zieba, Phase Characterization of Diffusion Soldered Ni/Al/Ni Interconnections, INTERFACE Sci. 10 (2002) 13–19.

[239] C. Sims, Superalloys II (extrait), Hardcover, J. Wiley & Sons, New York ;;Chichester, 1987. http://books.google.fr/books?id=kqZTAAAAMAAJ (accessed November 1, 2021).

[240] W. Herr, E. Broszeit, The influence of a heat treatment on the microstructure and mechanical properties of sputtered coatings, Surf. Coatings Technol. 97 (1997) 335–340. https://doi.org/10.1016/S0257-8972(97)00196-5.

# Appendix

The runs and parameters shown in chapter 4 are to summarise and explain the main findings of this study. However, there were more thermal spray runs performed to achieve a film with better coverage and durability. Those runs are all given below.

| Spray Runs | Flame Power (kW) | Stand-off Distance (mm) | Suspension Flow Rate (ml/min) | No. of passes | Stoichiometric Percentage (%) | Injector Diameter (mm) | Coverage (%) |
|---|---|---|---|---|---|---|---|
| Baseline | 25 | 85 | 52 | 4 | 85 | 0.3 | 35 |
| Effect of passes | | 85 | 70 | 10 | 85 | 1 | 50-55 |
| Effect of flow rate | | 85 | 125 | 10 | 85 | 1 | 60 |
| Effect of Stoichiometry | | 85 | 125 | 10 | 50 | 1 | No deposition |
| Effect of SoD | | 100 | 125 | 10 | 85 | 1 | 65 |

*Table 16: Spray parameters and percentage area coverage of each run performed by 25kW flame power.*

| Spray Runs | Flame Power (kW) | Stand-off Distance (mm) | Suspension Flow Rate (ml/min) | No. of passes | Stoichiometric Percentage (%) | Injector Diameter (mm) | Coverage (%) |
|---|---|---|---|---|---|---|---|
| Baseline | 50 | 85 | 65 | 10 | 85 | 1 | <5 |
| Effect of SoD | | 170 | 65 | 10 | 85 | 1 | 32 |
| Effect of flow rate | | 170 | 125 | 10 | 85 | 1 | 50-55 |
| Effect of SoD | | 100 | 125 | 10 | 85 | 1 | <5 |
| Effect of SoD | | 125 | 125 | 10 | 85 | 1 | <10 |

*Table 17: Spray parameters and percentage area coverage of each run performed by 50kW flame power*

| Spray Runs | Flame Power (kW) | Stand-off Distance (mm) | Suspension Flow Rate (ml/min) | No. of passes | Stoichiometric Percentage (%) | Injector Diameter (mm) | Coverage (%) |
|---|---|---|---|---|---|---|---|
| Baseline | 75 | 85 | 38 | 2.5 | 85 | 0.3 | No deposition |

Table 18: Spray parameters and percentage area coverage of each run performed by 75kW flame power.